INFORMATION TO USERS

This manuscript has been reproduced from the microfilm master. UMI films the text directly from the original or copy submitted. Thus, some thesis and dissertation copies are in typewriter face, while others may be from any type of computer printer.

The quality of this reproduction is dependent upon the quality of the copy submitted. Broken or indistinct print, colored or poor quality illustrations and photographs, print bleedthrough, substandard margins, and improper alignment can adversely affect reproduction.

In the unlikely event that the author did not send UMI a complete manuscript and there are missing pages, these will be noted. Also, if unauthorized copyright material had to be removed, a note will indicate the deletion.

Oversize materials (e.g., maps, drawings, charts) are reproduced by sectioning the original, beginning at the upper left-hand corner and continuing from left to right in equal sections with small overlaps.

Photographs included in the original manuscript have been reproduced xerographically in this copy. Higher quality 6" x 9" black and white photographic prints are available for any photographs or illustrations appearing in this copy for an additional charge. Contact UMI directly to order.

ProQuest Information and Learning
300 North Zeeb Road, Ann Arbor, MI 48106-1346 USA
800-521-0600

FILAMENTARY MOLECULAR CLOUDS AND THEIR PROLATE CORES

By

JASON D. FIEGE, B.Sc.H, M.Sc.

A Thesis

Submitted to the School of Graduate Studies

in Partial Fulfilment of the Requirements

for the Degree

Doctor of Philosophy

McMaster University

FILAMENTARY MOLECULAR CLOUDS AND THEIR PROLATE CORES

DOCTOR OF PHILOSOPHY
(Physics and Astronomy)

McMaster University
Hamilton, Ontario

TITLE: Filamentary Molecular Clouds and Their Prolate Cores

AUTHOR: Jason D. Fiege, B.Sc., M.Sc. (Queen's University)

SUPERVISOR: Dr. Ralph E. Pudritz

NUMBER OF PAGES: xiv, 252.

Abstract

We develop a model of self-gravitating, pressure truncated, filamentary molecular clouds with a rather general helical magnetic field topology. By comparing with existing observational data, our analysis suggests that the mass per unit length of many filamentary clouds is significantly reduced by the effects of external pressure, and that toroidal fields play a significant role in squeezing clouds. We show that there is an upper limit to the mass per unit length allowed for equilibrium, whose value depends on the strength and character of the magnetic field threading the filament. Clouds that are below this critical mass per unit length are always stable against radial gravitational collapse.

Our theoretical models involve 3 parameters; two to describe the mass loading of the poloidal and toroidal fields, and a third to describe the radial concentration of the filament. We find that many of our models with helical fields are in good agreement with the observed $\sim r^{-2}$ radial density structure of filamentary clouds. Unmagnetized filaments and models with purely poloidal magnetic fields result in steep density gradients that are not allowed by the observations.

We consider the stability of our models against axisymmetric modes of fragmentation. Many of our models fragment gravitationally, although some are subject to MHD-driven "sausage" modes of instability. Our main result is that the toroidal magnetic field helps to stabilize long wavelength gravitational instabilities, but short wavelength MHD "sausage" instabilities result when the toroidal field is sufficiently strong. Many of our models lie in a physical regime where the growth rates of gravitational and MHD instabilities are at a minimum.

We then go on to develop a model of the helically magnetized cores that might originate from finite segments of our filament models. Only modest toroidal fields are required to produce prolate cores, with mean projected axis ratios in the range $0.3 - 1$. Thus, many of our models are in good agreement with the observed shapes of cores (Myers et al 1991, Ryden 1996), which find axis ratios distributed about a mean value in the range $0.5 - 0.6$. We show that the Bonnor-Ebert critical mass is reduced by about 20%, as a result of the helical field in our models.

Acknowledgements

During the past four years, I have benefited enormously from working under the supervision of Ralph Pudritz. His combination of sharp physical insight, scientific knowledge, and enthusiasm for astrophysics continue to amaze me.

I would like to thank Brenda Matthews for many useful discussions regarding her observational data and general aspects of sub-millimetre polarimetry. She also provided technical assistance in the preparation of some of my figures. I am also indebted to Marcel Van Dalfsen, who provided technical assistance with the LaTeX document preparation system on more than one occasion. Thanks also to Kathy Durrell, who helped me by proofreading several chapters.

Thanks are also due to the office staff, especially graduate secretary Jackie Collin, for guiding me through the formalities of submitting this thesis.

My wife's family, John, Elsie, and Melika Ramkissoon have been very supportive for the past three years, and especially in the last few weeks. Their kindness, generosity, and warmth are beyond compare. I also thank my own parents for a solid foundation and strong early influences.

The greatest debt of all is to my wife Annica, whose love, care, and understanding have seen me through this degree and the writing of this thesis. She also compiled and typed all of the references, which helped enormously in my timely completion.

For Annica

Sic ita ad astra...

Contents

1 Introduction 1

2 Observations and Theory of Molecular Clouds in the Milky Way 5

2.1 Observations of Molecular Clouds . . . 5

2.1.1 Molecular Lines . . . 5

2.1.2 Sub-millimetre Observations of Molecular Clouds . . . 10

2.2 Observations of Magnetic Fields in Molecular Clouds . . . 10

2.2.1 Zeeman Observations of Magnetic Field Strengths in Molecular Clouds and Their HI Envelopes . . . 13

2.2.2 Observations of Polarization in Molecular Clouds . . . 16

2.2.3 The Polarized Light of Background Stars . . . 17

2.2.4 The Polarized Far-Infrared and Sub-Millimetre Emission of Dust Grains . . . 18

2.2.5 Ordered Magnetic Fields in Molecular Clouds . . . 19

2.3 The Formation of Molecular Clouds - Spiral Shocks and Supershells . . . 20

2.3.1 Spiral Shocks . . . 20

2.3.2 Supershells . . . 20

2.4 Non-Thermal Motions in Molecular Clouds . . . 22

2.4.1 Non-thermal Pressure . . . 22

2.5 The Origins of Non-Thermal Motions in Molecular Clouds . . . 24

2.5.1 Alfvén Waves . . . 24

2.5.2 Turbulence in Molecular Clouds and the ISM . . . 25

2.5.3 Origins of Turbulence . . . 25

2.5.4 Kolmogorov Turbulence . . . 26

2.5.5 MHD Turbulence . . . 27

2.5.6 Global Properties of MHD Turbulence Simulations . . . 28

2.5.7 Filamentary HI Clouds as Density Fluctuations in a Turbulent ISM 29
2.5.8 Lifetimes of Density Fluctuations 29
2.5.9 Commentary on Simulations of MHD Turbulence 31
2.6 The Surface Pressure on Molecular Clouds 31
2.6.1 The Total Pressure of the ISM 32
2.6.2 HI Clouds and Atomic Envelopes 32
2.7 The Density Structure of Clouds and Clumps 33
2.8 The Internal Structure of Molecular Clouds 34
2.8.1 The Mass Spectrum of Clumps 34
2.9 Self-Gravity in Interstellar Gas Clouds 35
2.9.1 Gravity in Spheroidal and Filamentary Clouds 35
2.9.2 Star Formation in Self-Gravitating Clumps 37
2.10 Jeans Instability and the Fragmentation of Molecular Clouds 37
2.11 Ordered Magnetic Fields in Molecular Clouds - Theoretical Considerations 39
2.11.1 A Virial Analysis of Magnetized Spheroidal Molecular Clouds 39
2.11.2 Clouds Threaded by Purely Poloidal Fields 40
2.11.3 Are Spheroidal Clouds Magnetically Super-Critical or Sub-Critical? 43
2.11.4 Larson's Laws for Molecular Clouds 44
2.11.5 Spheroidal Clouds Threaded by Both Poloidal and Toroidal Fields 46

3 Helical Fields and Filamentary Molecular Clouds 49
3.1 Introduction 50
3.2 Virial Analysis of Filamentary Molecular Clouds 52
3.2.1 Unmagnetized Filaments 56
3.2.2 Magnetized Filaments 57
3.2.3 Surface Pressures on Molecular Filaments 57
3.2.4 Comparison With Observations 58
3.3 Magnetohydrostatic Models of Filamentary Molecular Clouds 61
3.3.1 The Poloidal and Toroidal Flux to Mass Ratios 61
3.3.2 An Idealized Model: Uniform Magnetized Filaments 62
3.3.3 General Equations for Magnetized Filamentary Molecular Clouds 63
3.3.4 Analytic Solutions 65
3.4 Numerical Solutions 67
3.4.1 Numerical Results 67
3.4.2 "Best-Fitting" Models For Magnetized Filamentary Clouds 76

3.5 Discussion . . . 77
3.5.1 Observational Signatures of Helical Magnetic Fields . . . 80
3.6 Summary . . . 81
3.7 Acknowledgements . . . 83

A Derivation of the Virial Equation for Filamentary Molecular Clouds 84

B Bonnor-Ebert Stability of Magnetized Filaments 87
B.0.1 Uniform Clouds . . . 87
B.0.2 Non-Uniform Clouds . . . 88

C Virial Relations and Larson's Laws for Filaments 89

D Mathematical Framework 91

4 Helical Fields and Filamentary Molecular Clouds II - Axisymmetric Stability and Fragmentation 98
4.1 Introduction . . . 99
4.2 General Formulation of the Problem . . . 100
4.2.1 The Polytropic HI Envelope . . . 101
4.3 The Equations of Linearized MHD . . . 102
4.4 Boundary Conditions . . . 104
4.4.1 The Inner Boundary: $r = 0$ . . . 104
4.4.2 The Outer Boundary: $r \to \infty$ . . . 104
4.4.3 The Molecular Filament/HI Envelope Internal Boundary . . . 105
4.5 Dispersion Relations and Eigenmodes . . . 106
4.6 Tests of the Numerical Code . . . 106
4.7 Stability of the Pressure Truncated Ostriker Solution . . . 107
4.8 Stability of Truncated Filaments with Purely Poloidal and Purely Toroidal Fields . . . 112
4.8.1 Poloidal Field Results . . . 113
4.8.2 Toroidal Field Results . . . 113
4.9 Stability of Filamentary Clouds With Helical Magnetic Fields . . . 121
4.10 Discussion and Summary . . . 128
4.11 Acknowledgements . . . 131

A The Equations of Linearized MHD 132

B The Boundary Conditions at the Molecular Filament/HI Envelope Interface 134

C Matrix Representation of the Boundary Conditions 136

5 Dense Cores in Molecular Clouds 140

5.1 Observational Properties of Cores and Bok Globules . . . 142

5.2 Cores are Self-Gravitating . . . 143

5.3 The Shapes of Cores . . . 144

5.4 The Velocity Structure of Cores . . . 145

5.4.1 Rotational Motions in Cores and Bok Globules . . . 146

5.4.2 Random Motions and Thermal Support in Cores and Globules . . . 147

5.5 The Ordered Magnetic Field in Molecular Cloud Cores . . . 149

5.5.1 The Zeeman Effect in Cores . . . 149

5.5.2 Sub-Millimetre and Far Infra-Red Polarimetry in Cores . . . 150

5.6 Spherical Models of Molecular Cloud Cores . . . 152

5.6.1 Bonnor-Ebert Spheres . . . 153

5.6.2 The Singular Isothermal Sphere . . . 153

5.6.3 Polytropic Models of Cloud Cores . . . 154

5.6.4 The TNT Model . . . 156

5.6.5 Multi-Pressure Polytropes . . . 157

5.6.6 The Pure Logatrope . . . 158

5.7 Non-Spherical Models and Ordered Magnetic Fields . . . 159

5.7.1 The Shapes of Cores . . . 160

5.7.2 The Critical Mass of Magnetized Cores . . . 161

5.7.3 The Evolution of Cores by Ambipolar Diffusion . . . 161

5.8 Models of Cloud Cores - Limitations and Possibilities . . . 163

6 Prolate Cores in Filamentary Molecular Clouds 164

6.1 Introduction . . . 164

6.2 The Self-Consistent Field Method . . . 166

6.2.1 Dimensionless Equations . . . 171

6.2.2 Boundary Conditions . . . 172

6.3 Numerical Method . . . 173

6.4 Exploration of the Parameter Space . . . 174

6.4.1 A Gallery of Models . . . 175

6.4.2 Trends in the Model Parameters . . . 181
6.5 Sequences of Models with Varying Mass and External Pressure . . . 185
6.5.1 Effect of Mass . . . 187
6.5.2 Bonnor-Ebert Stability and the Effect of the External Pressure . . . 189
6.6 A Singular Model for Prolate Cores . . . 190
6.7 Discussion and Conclusions . . . 192
6.8 Summary . . . 193
6.9 Acknowledgements . . . 193

A The Mean Projected Axis Ratio and a_4/a Shape Parameter **194**

B Derivation of the Singular Isothermal Model for Prolate Cores **196**

7 Discussion and Summary **199**
7.1 General Discussion of Our Models - Strengths, Weaknesses, and Future Directions . . . 199
7.1.1 The Evolution of Filamentary Molecular Clouds . . . 200
7.1.2 Observational Tests of Our Models . . . 202
7.2 Summary . . . 203
7.2.1 A Model For Helically Magnetized Filamentary Clouds . . . 203
7.2.2 The Fragmentation of Filamentary Clouds . . . 204
7.2.3 Prolate Cores in Filamentary Clouds . . . 205
7.3 Concluding Remarks . . . 206

A Computer Code **208**
A.1 Prolate Cores - Numerical Considerations . . . 208
A.2 Code Listings . . . 211

B Copyright Information **242**

List of Figures

2-1 CO Map of the Orion Region 8

2-2 The Integral-Shaped Filament in ^{13}CO 9

2-3 $850\mu m$ Sub-Millimetre Map of the Integral-Shaped Filament 11

2-4 The Radial Density Profile of the Integral-Shaped Filament from $850\mu m$ Emission 12

2-5 Suggestion of a Helical Field in the L1641 Cloud 15

2-6 Kinetic, Magnetic, and Gravitational Energy Equipartition in Molecular Clouds 16

2-7 The North Polar Spur and a Model for the Magnetic Field of Radio Loop I 22

2-8 Filamentary Structure in Simulations of MHD Turbulence 30

2-9 The Critical Bonnor-Ebert Mass of Magnetized Clouds 43

3-1 Virial Analysis of Magnetized Filamentary Clouds 60

3-2 Schematic Illustration of Flux to Mass Ratios 63

3-3 Structure of Poloidally Magnetized Filaments 68

3-4 Structure of Toroidally Magnetized Filaments 69

3-5 Monte Carlo Exploration of the Parameter Space for Isothermal Filaments 74

3-6 Monte Carlo Exploration of the Parameter Space for Logatropic Filaments 75

3-7 Density Profiles of Isothermal Models 78

3-8 Density Profiles of Logatropic Models 79

4-1 Dispersion Relations for Truncated, Unmagnetized, Isothermal Filaments 108

4-2 Mass Per Unit Length Dependence of Wave Numbers and Growth Rates for Unmagnetized, Pressure-Truncated Filamentary Clouds 109

4-3 The Most Unstable Fragmentation Mode of the Untruncated Ostriker Solution 110

4-4 The Most Unstable Fragmentation Mode of a Truncated Ostriker Solution 111

4-5 Dispersion Relations for Poloidally Magnetized Truncated Filaments 114

4-6 The Dependence of Wave Numbers and Growth Rates on Γ_z for Poloidally Magnetized, Pressure Truncated Filaments . . . 115
4-7 The Most Unstable Mode of a Weakly Magnetized Filament with Poloidal Field Only . . 116
4-8 The Most Unstable Mode of a Strongly Magnetized Filament with Poloidal Field Only . . 117
4-9 Dispersion Relations for Toroidally Magnetized, Truncated Filaments . . . 118
4-10 The Dependence of Wave Numbers and Growth Rates on Γ_z for Toroidally Magnetized Filaments . . . 119
4-11 The Most Unstable Fragmentation Mode of a Toroidally Magnetized, Pressure-Truncated Filament . . . 120
4-12 The Most Unstable Wave Numbers for Helically Magnetized Models . . . 123
4-13 The Growth Rates for Helically Magnetized Models . . . 123
4-14 The Critical Wave Numbers for Helically Magnetized Models . . . 124
4-15 Example of a Gravity-Driven Mode for a Helically Magnetized Model . . . 126
4-16 Example of an MHD-Driven Mode for a Helically Magnetized Model . . . 127
4-17 The Ratio of Fragment Separation to Filament Diameter . . . 128
4-18 The Masses of Fragments . . . 129

5-1 The Shapes of Cores . . . 144
5-2 The Magnetic Field in the Orion KL Region . . . 151
5-3 Density Structure of Isothermal and Polytropic Spheres . . . 154

6-1 Exploration of the Parameter Space of Prolate Core Models . . . 176
6-2 A Gallery of Prolate Core Models . . . 177
6-3 The Distribution of Intrinsic and Mean Projected Axis Ratios for Our Models . . . 178
6-4 The Relationship between the Intrinsic and Mean Projeced Axis Ratios . . . 179
6-5 The Distribution of the a_4/a Shape Parameter . . . 181
6-6 A Representative Core Model with a Weak Toroidal Field . . . 182
6-7 A Representative Core Model with a Strong Toroidal Field . . . 183
6-8 Dependence of the Axis Ratio on the Mass of Cores . . . 184
6-9 Dependence of the Axis Ratio on the External to Internal Pressure Ratio . . . 185
6-10 The Most Massive Core Model . . . 186
6-11 Dependence of the Axis Ratio on M_{tot}/K and M_ϕ/M_{pol} . . . 187
6-12 The Effect of the Mass on the Shapes of Cores . . . 188
6-13 The Effect of the External Pressure on the Shapes of Cores . . . 190
6-14 A Singular Model for Prolate Cores . . . 192

List of Tables

3.1 Observational Data for Filamentary Clouds 59

3.2 Virial Analysis of Filamentary Clouds 60

C.1 The Virial Coefficients for Magnetized Filamentary and Spheroidal Clouds 90

D.1 The Functions H_1 and H_2 for Isothermal and Logatropic Clouds 94

4.1 Wave Numbers and Growth Rates for Unmagnetized, Pressure-Truncated Filamentary Clouds 110

4.2 Wave Numbers and Growth Rates for Poloidally Magnetized, Pressure-Truncated Filaments 113

4.3 Wave Numbers and Growth Rates for Toroidally Magnetized, Pressure-Truncated Filamentary Clouds 118

6.1 Dimensionless Parameters for Models Shown in Figure 6-12 189

6.2 Dimensionless Parameters for Models Shown in Figure 6-13 189

Preface

Most of the original work of this thesis is contained in Chapters 3, 4, and 6. These chapters contain preprints of articles, in their entirety, which have been accepted by refereed journals for publication. The articles contained in Chapters 3 and 4 will be published by the Monthly Notices of the Royal Astronomical Society and the article contained in Chapter 6 will be published by The Astrophysical Journal (see Appendix B). I hereby grant irrevocable, non-exclusive licence to McMaster University and the National Library of Canada to reproduce this material as part of the thesis.

The original ideas developed in these articles are the result of a collaborative effort between myself and my supervisor, Ralph Pudritz. I wrote each of the articles in its entirety, although we made revisions collaboratively during the preparation of the articles for submission and subsequent peer review process. I also performed all analytic and numerical calculations, except for the derivation of the Ostriker (1964) solution for unmagnetized filaments (in Chapter 3), which is entirely by Pudritz. Several additional acknowledgements for useful discussions and comments are found in the first paper.

I wrote all computer code necessary for this work (Appendix A), making extensive use of the mathematical functions and routines in the Matlab language for technical computing.

Chapter 1

Introduction

The molecular clouds in our Galaxy bear little resemblance to the wind-blown, often wispy clouds of the earth's atmosphere. Molecular clouds are cold, magnetized, turbulent, and often gravitationally bound. They range in size from a fraction of a parsec (Bok globules) to hundreds of parsecs (Giant Molecular Clouds) across, and may contain up to $\sim 10^6\ M_\odot$ of molecular, mainly hydrogen, gas (Elmegreen 1985). They are surrounded by the lower density, weakly self-gravitating interstellar medium (ISM), which provides the external pressure that truncates and helps to confine the molecular gas. Molecular clouds are penetrated by the cosmic ray component of the ISM and are bathed in the ultraviolet radiation field of the Galaxy, both of which are responsible for their partially ionized state.

Molecular clouds are exotic objects whose internal structure and dynamics are remarkably rich. They often consist of slender filaments whose lengths range from less than one to several hundred parsecs, clumps on size scales of several parsecs, and dense ~ 0.1 parsec cores. There has even been some suggestion (Elmegreen and Falgarone, 1996) that clouds have a fractal structure on size scales larger than cores. However, there is no doubt that many clouds are organized into filaments and other discrete features, quite apart from any underlying fractal structure that might be present.

One of the most interesting features of molecular clouds is their means of support against self-gravity. It can be shown that thermal pressure can support at most a few tens of solar masses at the extremely low temperatures (typically $\sim 15\ K$) that prevail in molecular clouds (see Section 2.4.1). Therefore, they must be supported by some other means. Our current theoretical understanding suggests that their support is due to magnetic fields and complicated non-thermal motions, whose origins are not fully understood but may involve magnetohydrodynamic (MHD) Alfvén waves or MHD turbulence (see Section 2.4.1). These non-thermal motions, combined with gravitational instabilities and non-isotropic forces due to ordered magnetic fields, all act in concert to produce the extremely complex and textured

internal structure of molecular clouds.

Above all else, stars form in molecular clouds. Molecular clouds would be interesting objects in their own right even if this were not true, but their role as both the environment and raw material of star formation guarantees their fundamental importance in astrophysics. We understand the end products of star formation, namely stars, rather well, but the processes by which they form remain imperfectly understood. An important step in advancing our understanding lies in developing good models of molecular clouds, thus establishing the initial conditions for star formation.

Models of molecular clouds often assume that they are intrinsically spherical objects, in equilibrium between their self-gravity, non-thermal motions, and disordered magnetic fields. However, *filaments* are often the dominant structures in molecular clouds, suggesting that non-isotropic forces might be at work. This observational fact presents several intriguing questions. Why is the gas so filamentary? What is the radial structure of filamentary clouds? What is the geometry of the ordered component of the magnetic field associated with filaments? What are the stability properties of filaments, compared to spheroidal clouds? What are the properties of the cores that form within filamentary clouds? We have developed a model of filamentary clouds and their cores which attempts to answer all of these questions except for the first one, for which we can only offer speculation at present. Our basic strategy is to construct detailed equilibrium models of filamentary clouds and their cores, which we attempt to constrain observationally.

We shall assume that filamentary clouds can be adequately approximated by infinite cylinders. The most general field allowed in cylindrical symmetry has two components; a *poloidal* field component that threads the filament parallel to the axis of symmetry, and a *toroidal* field component that wraps around it, so that the field lines are helical in general. We show in Chapter 3 that helical magnetic fields significantly affect the radial density structure of filamentary clouds. The poloidal field component helps to support the clouds radially against self gravity, while the toroidal field component gently squeezes the filament, thus reducing the support against self-gravity. We show that helical fields can result in an overall confinement of the gas, even for quite modest toroidal fields. One of the most important results of Chapter 3 is that many observed filamentary clouds appear to require this additional confinement if their physical properties are to be understood. We interpret this as indirect evidence for helical fields. [1]

Filaments are also interesting for reasons that concern their stability against radial collapse. We show in Chapter 3 that gravitational instabilities operate very differently in filamentary clouds compared to their spheroidal counterparts. Unlike spheroidal clouds, any filamentary cloud whose mass per unit length is below a critical value (which depends on the internal magnetic field) cannot be made to collapse radially by any amount of external pressure. A comparison of our model with the observations reveals

[1] Some Zeeman observations are also suggestive of helical fields in a massive filamentary cloud in Orion (Heiles 1987, Bally 1989). We discuss this further in Section 2.2.1.

that many molecular filaments fall short of this mass limit, so that wholesale radial collapse is unlikely. Instead, gravitational instabilities in filamentary clouds likely cause them to fragment into long chains of nearly periodic clumps. There are many known examples of fragmented filaments. Prime examples are the enormous filamentary clouds in the Orion region (see Figure 2-1), the "integral-shaped filament" in the Orion A cloud (see Figures 2-2 and 2-3), and the many "globular filaments" in the Schneider & Elmegreen (1979) catalogue. The analysis in Chapter 4 focuses on the fragmentation of our models of filamentary molecular clouds. This analysis provides an estimate of both the lifetimes of filaments and the masses of the fragments that form. Our analysis shows that molecular gas can remain locked up in magnetized filaments for very long times. This has implications for star formation, since fragmentation must precede the formation of cores and their collapse in our model.

A surprising observational fact is that molecular cloud cores and Bok globules appear to be prolate, with mean projected axis ratios (short axis over long axis) of about 0.5 to 0.6. However, most existing theoretical models predict that cores should be flattened, oblate structures as a result of the radial (in cylindrical coordinates) support provided by the poloidal magnetic field perpendicular to the axis of symmetry (see Chapters 5 and 6). We propose that this dilemma might be solved if a helical magnetic field is inherited from a parent filamentary cloud, the basic idea being that the toroidal field component pinches the gas radially while also helping to support the gas in the direction parallel to the axis of symmetry.

The overall intention of this thesis is to present a self-consistent model of filamentary molecular clouds and their cores. It is notable that the helical magnetic structures that we propose offer a unifying solution to two apparently unrelated observations, namely that many filaments appear to be quite far from purely hydrostatic equilibrium, and that their cores are most likely prolate. While none of the evidence that we present should be regarded as absolutely conclusive, it is sufficient to warrant further investigation, both observationally and theoretically. We discuss some of these possible future avenues of research in Chapter 7.

This thesis is written at a time when instrumentation and observational techniques are providing, for the first time, a wealth of data relevant to many aspects of star formation. The most recent major development is the SCUBA bolometer array at the JCMT, which is now providing sub-millimetre continuum maps of unprecedented coverage and resolution of several nearby molecular clouds. When combined with molecular line observations from several telescopes, high quality maps of many cores and filaments will probably soon be in hand. SCUBA is also capable of sub-millimetre polarimetry, which may provide the next major advance in our observational understanding of the magnetic structure of molecular clouds. There is little doubt that we are entering a Golden Age for observations of molecular clouds. It is likely that the next several years, and almost certainly the next decade, will provide a wealth

of data to compare with the theoretical models of molecular filaments and cloud cores that comprise the bulk of this thesis.

Before presenting the original work in this thesis, we review our present understanding of molecular clouds in the next chapter. As we shall see, most of the existing theoretical models pertain to spheroidal models of molecular clouds. This is in sharp contrast to the model of filamentary clouds that we present in Chapter 3, and whose fragmentation properties we determine in Chapter 4. We review observational and theoretical aspects of molecular cloud cores in Chapter 5, and present our new models of prolate magnetized cores in Chapter 6. We include a general discussion of our results in Chapter 7, where we also briefly consider some future directions and possible observational tests of our models. Appendix A provides listings of some of the computer programs used in our analysis.

Chapter 2

Observations and Theory of Molecular Clouds in the Milky Way

The purpose of this chapter is to present an overview of our current observational and theoretical understanding of molecular clouds, and the effects of the interstellar medium (ISM) on their structure. We begin in Section 2.1 with a discussion of molecular line and sub-millimetre observations of molecular clouds. Section 2.2 concerns observations of the Zeeman effect and polarimetry, which are both used to study magnetic fields in molecular clouds. Possible scenarios for the formation of magnetized molecular clouds are considered in Section 2.3. We discuss the non-thermal motions that help to support molecular clouds against their self-gravity in Section 2.4.1, and the possible origins of these motions in Section 2.5. We comment on the surface pressure on molecular clouds in Section 2.6. The internal structure of molecular clouds is discussed in Section 2.8, and the role of self-gravity in Section 2.9. This leads to a discussion of the Jeans instability in molecular clouds in Section 2.10. Finally, we address various theoretical issues concerning the effects of large-scaled ordered magnetic fields on the structure and stability of molecular clouds in Section 2.11.

2.1 Observations of Molecular Clouds

2.1.1 Molecular Lines

The first observations of molecular lines in interstellar gas clouds date back to the late 1930's, when absorption lines from CH, CH^+, and CN vibrational transitions were discovered in the visible spectra of several early type stars (eg. Dunham 1937, Adams & Dunham 1938, See also references in Elmegreen 1985). Molecular hydrogen was detected only in the early 1970's when rocket based observations detected

H_2 ultraviolet absorption lines towards hot stars (Carruthers 1970, Smith 1973). The Copernicus satellite subsequently detected H_2 in numerous interstellar clouds, demonstrating that an appreciable fraction of the hydrogen in dense clouds is in molecular form (see review by Spitzer 1976). Carbon monoxide (CO), which has proven to be an excellent tracer of molecular gas, was first detected in emission by Wilson et al. (1970) in a study of nine galactic HII regions. It was subsequently detected towards the Becklin-Neugebauer object at the heart of the most actively star-forming region of the Orion molecular cloud (Solomon et al. 1971).

Most of our knowledge of the conditions within molecular clouds comes from molecular emission lines at millimetre wavelengths from ^{12}CO, various CO isotopes, and other interstellar molecules. Vibrational and atomic transitions generally cannot be observed in emission because they are not thermally excited at the very low temperatures of $\sim 10 - 20\ K$ that prevail in the molecular gas. However, rotational transitions are of sufficiently low energy that they can be excited at temperatures that are typical of molecular clouds. [1] Unfortunately, molecular hydrogen molecules, which make up $\sim 70\%$ of the gas by mass, do not emit radiation by rotational transitions since they lack a permanent dipole moment. Most ($\sim 28\%$) of the remaining mass is in the form of helium atoms, which likewise do not undergo rotational transitions. Therefore, observations of molecular lines must rely on "tracer" molecules that include heavy elements from the remaining 2% of the mass. Observers must determine the amount of the observed molecule present, and infer the total mass from well-known empirical conversion factors. Naturally, this procedure is sensitive to local chemical inhomogeneities and possible variations of chemical abundances between molecular clouds, which makes it rather difficult to determine masses accurately.

Kinematic information is obtained from the observed Doppler shifts of molecular lines from their rest frame frequencies. [2] Line observations can reveal systematic large scale motions in the gas, such as rotation or translational motions along the line of sight. Perhaps even more importantly, the widths of molecular lines reveal the velocity dispersion of the gas, which determines the combined thermal plus non-thermal support of clouds against their self-gravity.

Despite the difficulties noted above, observers have developed an extensive suite of molecules that probe molecular gas from densities ranging from $\sim 300\ cm^{-3}$ for CO, to $\sim 10^6\ cm^{-3}$ for high density tracer molecules including NH_3, CS, CN, HCN, and H_2CO (see Figure 8 of Genzel 1992). The main

[1] The energy levels of a quantized rigid rotator are given by

$$E = B_e J(J+1) \tag{2.1}$$

where J is the rotational level, and $B_e = \hbar^2/2I$ is the rotational constant in terms of the moment of inertia I of the rigid rotator. For most "heavy top" molecules, including CO, HCN, and CS, $B_e \approx 3 \times 10^{-4}\ eV$, resulting in wavelengths (hc/E) of a few millimetres for the lowest ($J = 1 \rightarrow 0$) rotational transitions (see review Genzel 1992). Also, $E/k \lesssim 10\ K$, which is why these lines can be thermally excited at the low temperatures within molecular clouds.

[2] $\Delta\nu/\nu_0 = -v/c$ where ν_0 is the rest frequency of the line, v is the line of sight velocity component, and c is the speed of light.

factors that determine the usefulness of a given molecular species in a particular application are its optical depth τ, and its critical density and temperature for thermal excitation. Carbon monoxide (^{12}CO) is an abundant, easily excited, and strongly emitting molecule, which is often used to trace molecular gas at low densities. Although ^{12}CO is useful for studying the overall distribution of molecular gas in our galaxy, it becomes optically thick in most applications, therefore providing little information on the internal structure of molecular clouds. Masses also cannot be inferred directly from ^{12}CO observations because the intensity of an optically thick line is not related to the column density of the cloud. [3]

As an example, Figure 2-1 (from Maddalena et al. 1986) shows a very large scale (approximately $30° \times 40°$) ^{12}CO map of the system of molecular clouds in the Orion region. The clouds in this map have an extremely intricate, textured appearance, with several examples of very long filaments. In particular, the two filamentary clouds that pass near the map coordinates $(6^h0^m, 5°)$ and $(6^h36^m, -11°)$, which are respectively called the Northern and Southern Filaments by Maddalena et al. are the largest examples of molecular filaments that we are aware of. Their lengths are respectively $\sim$ 90 *pc* and $\sim$ 300 *pc*, assuming distances of 500 and 900 *pc* to these filaments (Maddalena et al. 1986). The well-known "integral-shaped" filament is located deep ***inside*** of the massive Orion A molecular cloud, which is centred roughly on $(5^h36^m, -6°)$.

In order to probe greater columns of gas, optically thin lines are required, which usually involve less abundant CO isotopes and other molecules of lesser abundance. ^{13}CO is particularly useful for probing intermediate densities, typical of the clumps discussed in Section 2.8 below (eg. Castets et al. 1990). High density tracer molecules such as $C^{18}O$, CS, NH_3, and others are useful mainly for observing the dense *cores* of molecular clouds (see Chapter 5), which are the sites of star formation within molecular clouds (eg. Benson & Myers 1989, Fuller & Myers 1992).

Figure 2-2 (from Castets et al. 1990) zooms in on the densest region of the Orion A molecular cloud to show a ^{13}CO map of the integral-shaped filament discussed above, whose length and extreme slenderness are striking. It is also apparent from this map that the filament is fragmenting into many clumps, strung like beads along the filament. There is evidence for periodic structure in the spacing of the fragments (Dutrey et. al 1991), which is consistent with theoretical predictions of gravitational fragmentation in filamentary clouds (eg. Chandrasekhar & Fermi 1953b, Nakamura 1993, See also Chapter 4). Note that we also show the integral-shaped filament in Figure 2-3, observed in sub-millimetre continuum emission, which we discuss in Section 2.1.2.

[3] Nevertheless, "CO masses" are often reported, which rely on an empirical relation (justified by the virial theorem), between the line width and the mass (eg. Maddalena et al. 1986).

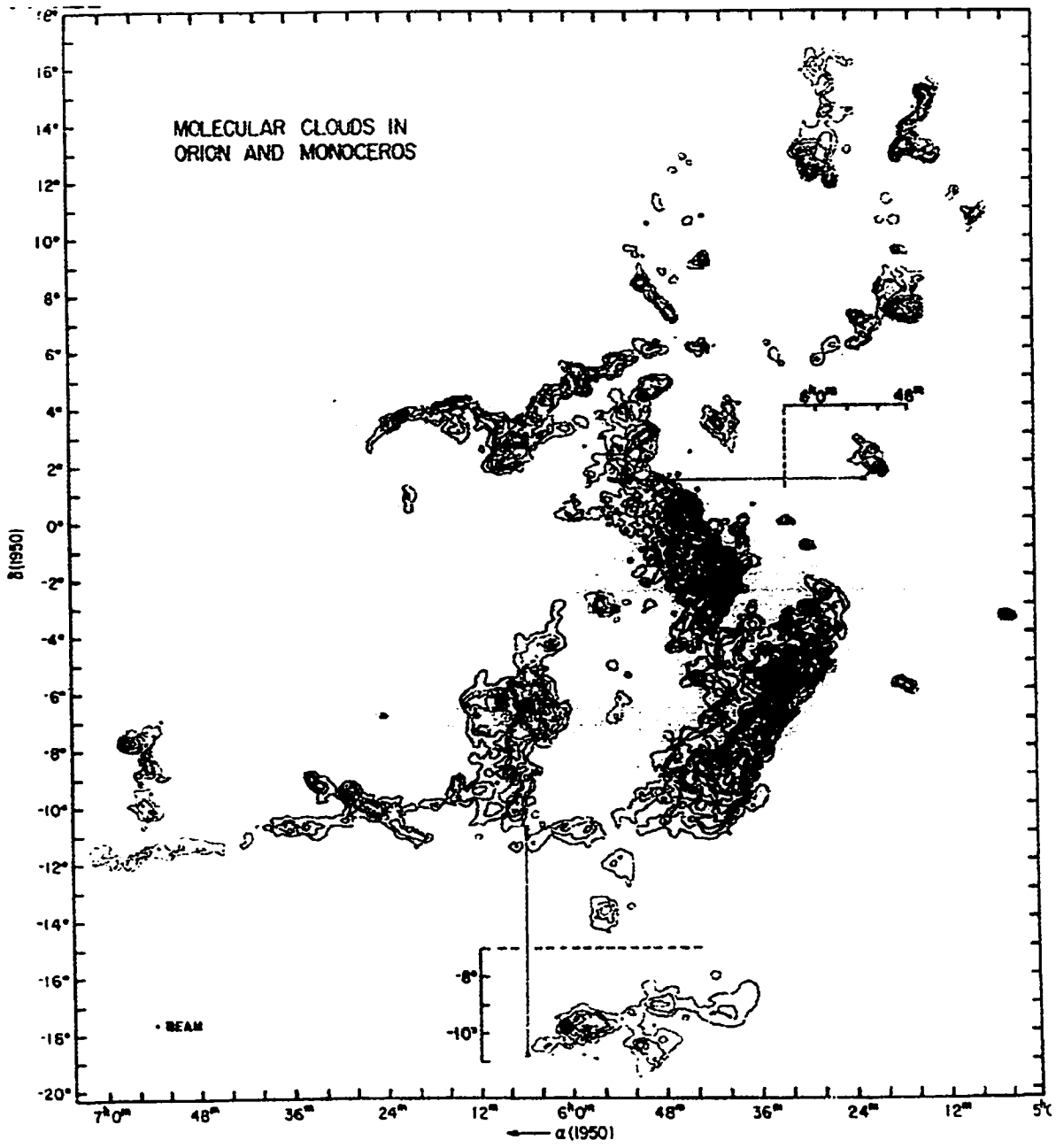

Figure 2-1: Contour map of the integrated intensity of CO emission (W_{CO}) in the Orion region in the velocity range -10 to 20 $km\ s^{-1}$. The two clouds, shown in insets, overlap other clouds in the survey and lie at the positions indicated by arrows. (From Maddalena et al. (1986))

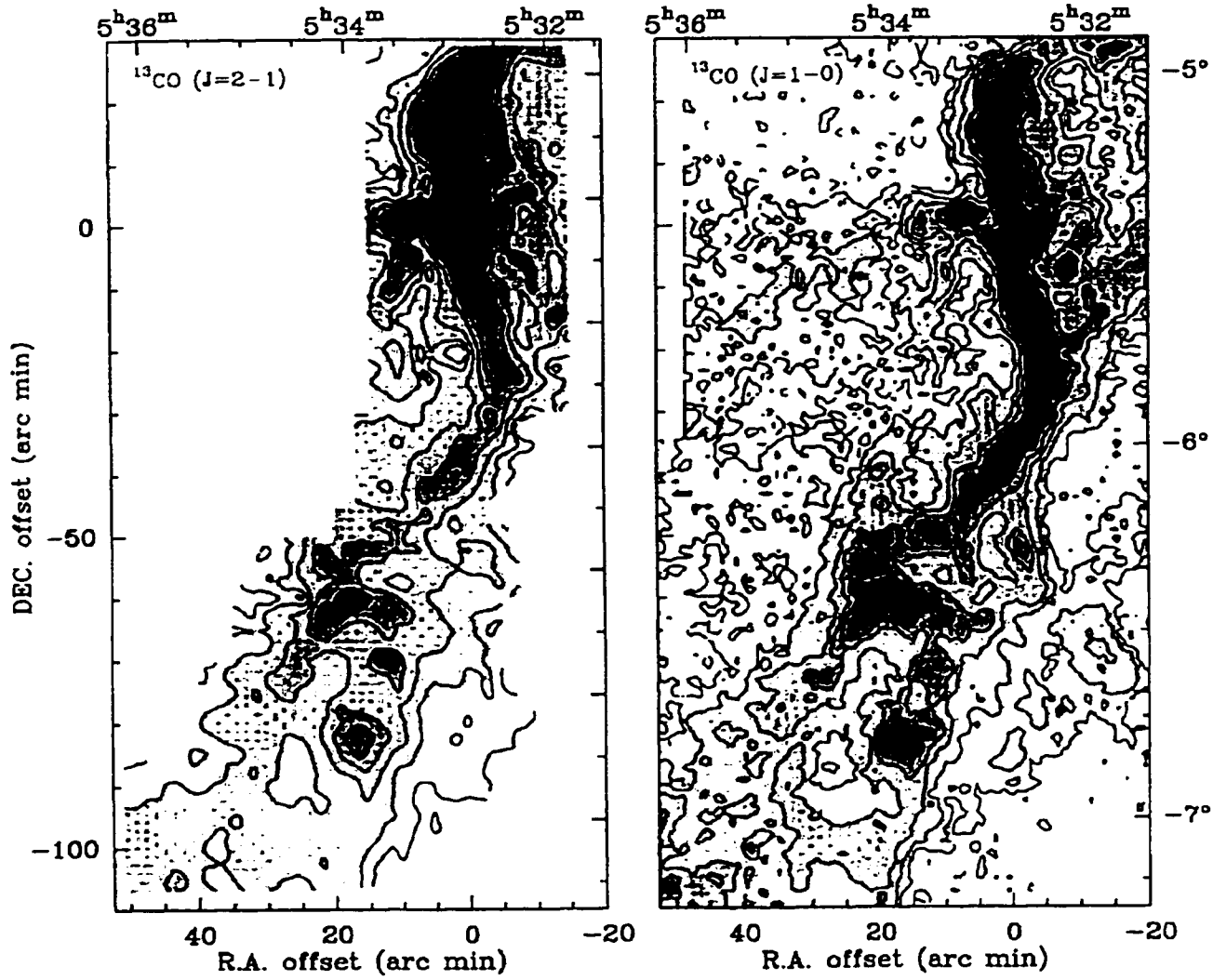

Figure 2-2: (From Castets et al. 1990) **panel (a)** (left): The ^{13}CO $J = 2 \rightarrow 1$ emission of the Orion "integral-shaped" filament. **panel (b)** (right): The $J = 1 \rightarrow 0$ emission (adapted by Castets et al. from Bally et al. 1987).

2.1.2 Sub-millimetre Observations of Molecular Clouds

The second main avenue for studying the structure of molecular clouds is by observing the thermal continuum emission of dust grains, which peaks at sub-millimetre wavelengths. Sub-millimetre continuum observations offer the advantage over other wavelengths that even the densest regions of molecular clouds are usually optically thin, so that sub-millimetre work is not as limited by extinction as observations at optical and near infra-red wavelengths. This fact makes sub-millimetre observations well-suited for measuring the surface densities of dense structures, such as filaments and cores. However, converting from sub-millimetre emission to surface density is complicated by the dependence of blackbody radiation on the generally unknown temperature distribution along lines of sight through the cloud, and the poorly constrained emissivity of dust grains.

Johnstone and Bally (1999) have recently mapped part of the integral-shaped filament, centred on the massive OMC1 star-forming core, in $850\mu m$ and $450\mu m$ emission. We show their $850\mu m$ map in Figure 2-3, where even more intricate filamentary structure is apparent than in the Castets et al. ^{13}CO map (Figure 2-2). It is important to note, however, that the size scales are very different in these maps; the filament observed in ^{13}CO appears more than ten times wider than the same filament observed at $850\mu m$. Figure 2-4 shows radial surface density profiles obtained by Johntone and Bally for three different parts of the filament. These surface density profiles demonstrate that the filament is concentrated radially toward its centre, with an approximately r^{-1} surface density gradient. The density profile is therefore consistent with an r^{-2} power law, in disagreement with the r^{-4} density profile of unmagnetized, isothermal models of self-gravitating filaments (Ostriker 1964). We show in Chapter 3 that many of our models predict r^{-2} density profiles, which might be more consistent with the data.

The main drawback of sub-millimetre continuum observations compared to molecular lines is that no kinematic information is available. We show in Section 2.4 that the velocity dispersion of the gas is important to theoretical models of clouds because it determines the total (thermal plus non-thermal) support of the cloud. Sub-millimetre observations must be accompanied by measurements of spectral line widths if such information is required.

2.2 Observations of Magnetic Fields in Molecular Clouds

Many models of molecular clouds involve dynamically significant, ordered magnetic fields. It is therefore very important, from a theoretical perspective, to obtain as much observational information as possible about the structure of the magnetic field. The most rigorous tests of our models of filamentary clouds and their prolate cores will probably rely heavily on comparisons with such data.

Observationally, our knowledge of magnetic fields in molecular clouds is derived from two main

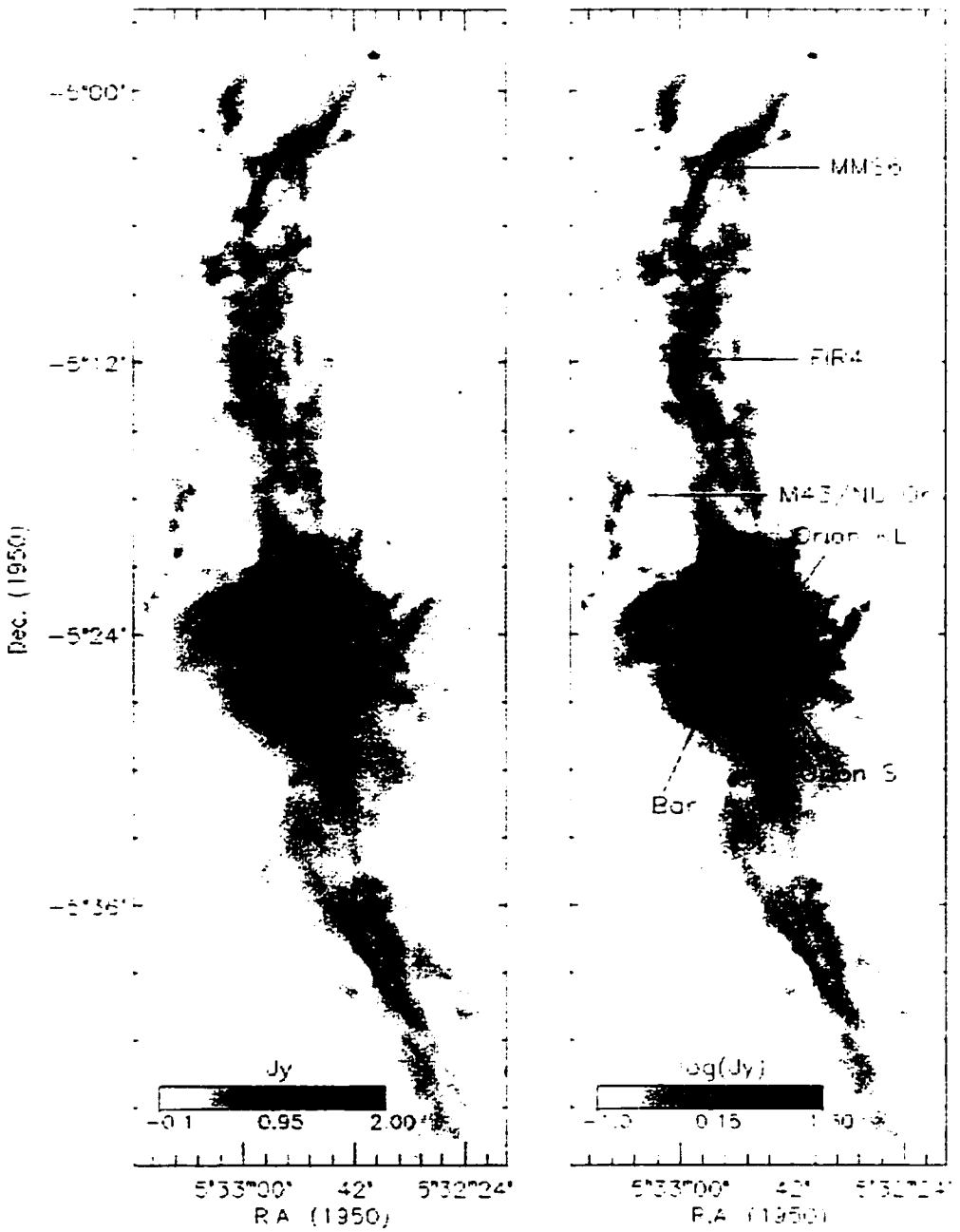

Figure 2-3: (From Johnstone & Bally 1999) The integral-shaped filament in Orion A in 850μm emission. The left panel uses a linear transfer function for the grayscale, while the right panel uses a logarithmic stretch to represent the same data.

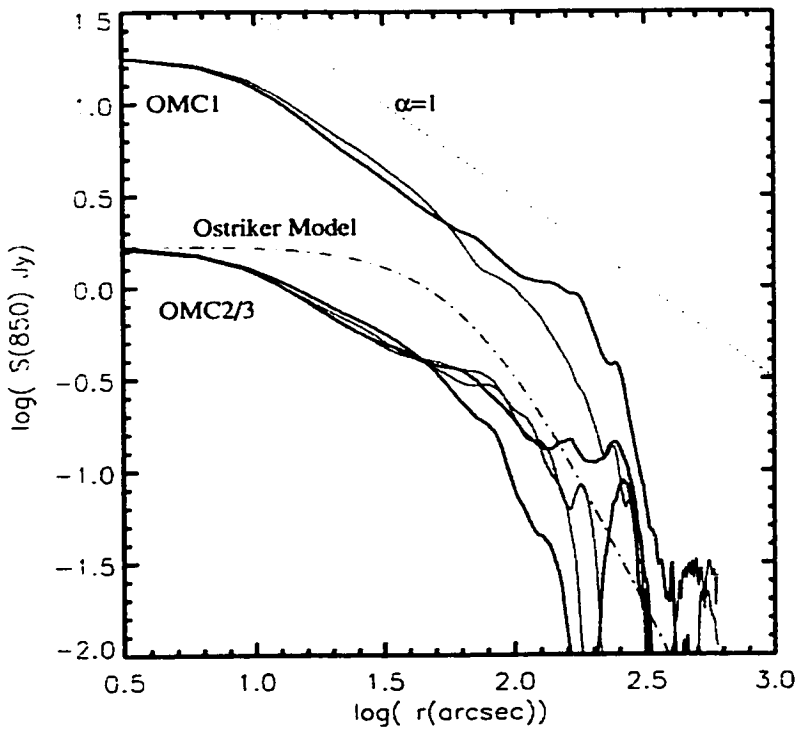

Figure 2-4: (From Johnstone & Bally 1999) The radial density profile of the integral-shaped filament for three different parts of the filament (OMC1, OMC2, and OMC3). The data are not well fit by the Ostriker (1964) model for unmagnetized, isothermal filaments. The dashed line represents an r^{-1} surface density profile, consistent with an r^{-2} density gradient.

sources, which measure complementary components of the magnetic field. First of all, the Zeeman effect is used to directly measure the strength of the line of sight component of the magnetic field within molecular clouds and their HI envelopes. These observations are very difficult and will probably require considerable advancement in instrumentation before detailed maps can be made of the line of sight component of the magnetic field in most molecular clouds. Secondly, optical, near infra-red, and sub-millimetre polarization measurements are now quite commonly being used to measure the direction, but not the magnitude of the component of the magnetic field in the plane of the sky. [4] In this section, we explore these methods in turn to provide an overview of our present observational knowledge of the magnetic field in molecular clouds.

[4] Chandrasekhar and Fermi (1953a) demonstrated that the magnitude of the field can be estimated from the measured dispersion of the polarization angles. However, the method is rather indirect and has only been used by a few authors (eg. Myers & Goodman 1991).

2.2.1 Zeeman Observations of Magnetic Field Strengths in Molecular Clouds and Their HI Envelopes

The Zeeman effect is the splitting of a spectral line that results from the degeneracy-breaking interaction between a magnetic field and the magnetic dipole moment associated with the orbital and spin angular momenta of an electron. Viewed parallel to the magnetic field, the Zeeman effect splits a line into two polarized components of opposite circular polarization, offset by twice the Zeeman shift ν_Z, plus a third unpolarized component.

The Zeeman effect in interstellar gas clouds is much more subtle than in laboratory spectroscopy, since ν_Z is always much smaller than the observed line widths, except for in maser sources (Crutcher et al. 1993). For example, the Zeeman splitting factor $2\nu_Z$ for the HI 21 cm line is only 2.8 $Hz\ \mu G^{-1}$ (Troland & Heiles 1982), which gives a Zeeman splitting of only $\sim 30\ Hz$ for a typical HI field strength of $\sim 10\ \mu G$. This amounts to a velocity shift of only

$$\Delta v = 590 \left(\frac{B}{10\ \mu G}\right)\ cm\ s^{-1}, \tag{2.2}$$

which is less than 1% of the observed line widths in molecular clouds. It is therefore not usually possible to separate the Zeeman components cleanly, and observers must instead measure the Zeeman effect by the variation of the circular polarization across the line. Such observations are challenging because of the smallness of the effect, and several rather subtle instrumental difficulties. (See Troland & Heiles 1982, Troland et al. 1986, and Crutcher et al. 1996 for details.)

One limitation of Zeeman measurements of magnetic fields is that they are sensitive only to the ordered component of the field parallel to the line of sight. Field components that lie in the plane of the sky, or are tangled, are not observable by the Zeeman effect. In fact, any reversal of the line of sight component of the magnetic field within the telescope beam results in a partial cancellation of the Zeeman shift, which can cause Zeeman measurements to underestimate field strengths in some cases (see review by Troland 1990).

Early Zeeman Observations

The Zeeman effect was first detected in the ISM in the HI 21 cm line by Verschuur in 1968, and has subsequently been used by several authors to study the magnetic field in the HI gas associated with molecular clouds. However, 21 cm observations cannot detect the magnetic field within molecular clouds, where the gas is almost entirely molecular (Crutcher et al. 1993). Fortunately, the Zeeman effect is detectable in several molecular species with unpaired electron spins (Elmegreen 1978), most notably OH and CN. The hydroxyl molecule (OH) is a reasonable, though not ideal, tracer of H_2 gas at densities

that are typical of dark clouds, although probably not in dense cores (Crutcher et al. 1993). On the other hand, cyanide molecules (CN) are good high density tracers of H_2 that can be used to probe the magnetic structure of cores (Crutcher et al. 1996, 1999). We further discuss Zeeman observations of cores in Chapter 5.

Zeeman Observations in Orion

Many Zeeman observations have concentrated on the molecular clouds in Orion. Heiles and Troland (1982) first detected the HI Zeeman effect in the atomic clouds associated with the Orion Nebula, finding a 10 μG field. While this is a very small magnetic field by terrestrial standards, Heiles and Troland (1982) showed that the magnetic energy is comparable to, and probably slightly exceeds, the total kinetic energy in non-thermal motions. Both greatly exceed the thermal and self-gravitational energies, which is almost always the case for HI gas (see Sections 2.6 and 2.9).

Heiles (1987) combined previous (Heiles and Troland 1982) HI Zeeman data with new data to map the line of sight component of the magnetic field near the massive L1641 filamentary cloud, which contains the integral-shaped filament discussed in Section 2.1 (see Figures 2-2 and 2-3). The most fascinating aspect of Heiles' map is that the line of sight component of the magnetic field is observed to reverse sign across the filament, which is suggestive of a helical magnetic field threading the HI gas just outside of the L1641 filament (see also Bally 1989). This interpretation is supported by measurements of polarized background starlight in extinction, which suggest that the magnetic field component in the plane of the sky cuts across the filament at an oblique angle (We discuss polarization in Section 2.2.2). Figure 2-5 shows the polarization data overlaid on Heiles' Zeeman map, as well as an illustration of the helical field interpretation of the data. An alternative interpretation has recently been proposed by Heiles (1997), who argues that the observed magnetic structure could be explained by the Eridanus bubble sweeping past a pre-existing filament and stretching magnetic field lines across its surface. This scenario would result in a magnetic structure that would be quite difficult to distinguish from a helical field, so the earlier interpretation is not ruled out.

Zeeman Observations in Other Molecular Clouds

Goodman and Heiles (1994) have searched for the HI Zeeman effect across the face of the Rho Ophiuchus dark cloud complex. The observed field strengths are typically $\lesssim$ 10 μG, with no discernable spatial pattern in their variation. They find comparable kinetic and magnetic energies for most of the positions where a field was detected. Recent detections of the HI Zeeman effect in diffuse clouds (Myers et al. 1995) confirm that magnetic fields are in approximate energy equipartition with non-thermal motions, even for non-self-gravitating clouds.

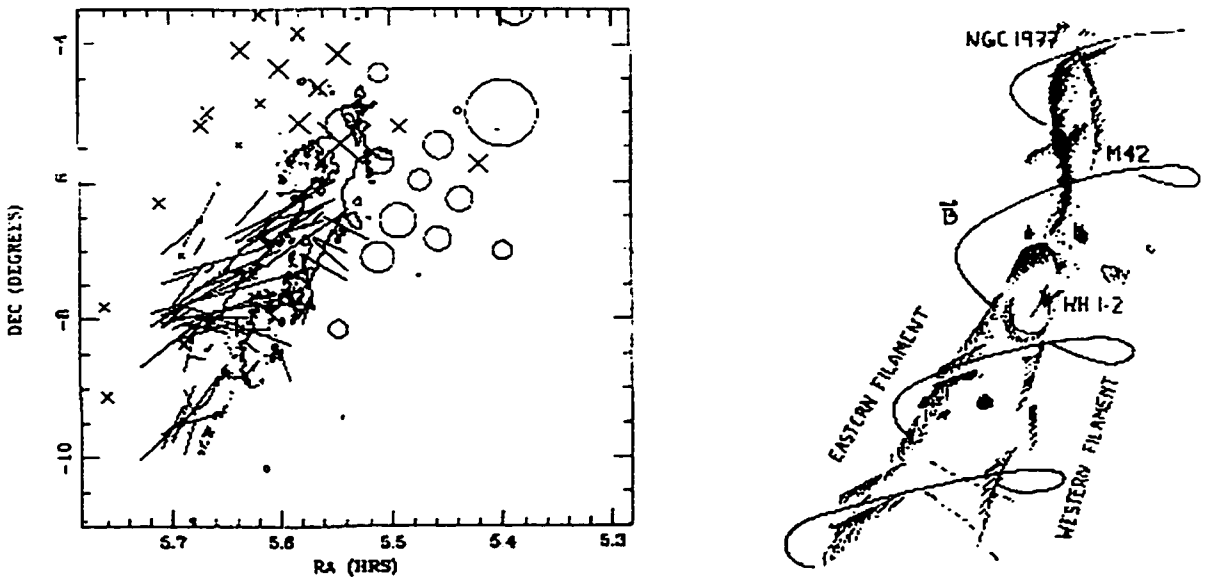

Figure 2-5: (From Bally 1989) **Panel (a)** (left): HI Zeeman data measurements from Heiles (1987) superimposed on the Vrba et al. (1988) optical polarization map, superimposed on an outline of the L1641 ^{13}CO cloud. Circles indicate that the magnetic field coming is out of the page; crosses indicate a field into the page. The sizes of the symbols are proportional to the field amplitude. **Panel (b)** (right): An illustration of the helical field interpretation of the data in panel (a).

Myers and Goodman (1988a,b) give a comprehensive compilation of Zeeman detections in molecular clouds, mostly in molecular lines. They compare the observed strength of the magnetic field with the values predicted by a simple model of molecular clouds which assumes energy equipartition between kinetic, magnetic, and gravitational energies. For this model, the predicted strength of the magnetic field is given by

$$B_{eq} \approx \frac{2}{8 \ln 2} \left(\frac{5}{G}\right)^{1/2} \frac{\Delta v^2}{R}, \tag{2.3}$$

where Δv is the observed line width, G is the gravitational constant, and R is the radius of the cloud. After making a statistical correction to the observed magnetic field B_{obs}, which is necessary because only the line of sight component of the field is measured, they find that the observed field strength $B_{obs} \approx B_{eq}$ within a factor of ~ 2 for their compiled data (see Figure 2-6). This is probably the clearest and most comprehensive observational evidence that magnetic, kinetic, and gravitational energies are in approximate equipartition in molecular clouds.

The fact that magnetic and kinetic energies are found to be nearly in equipartition wherever magnetic fields are measured is strongly suggestive that some kind of global mechanism is at work. [5] We show

[5]The gravitational energy may be less than either the kinetic or magnetic energies for pressure dominated clouds (ie. high latitude clouds).

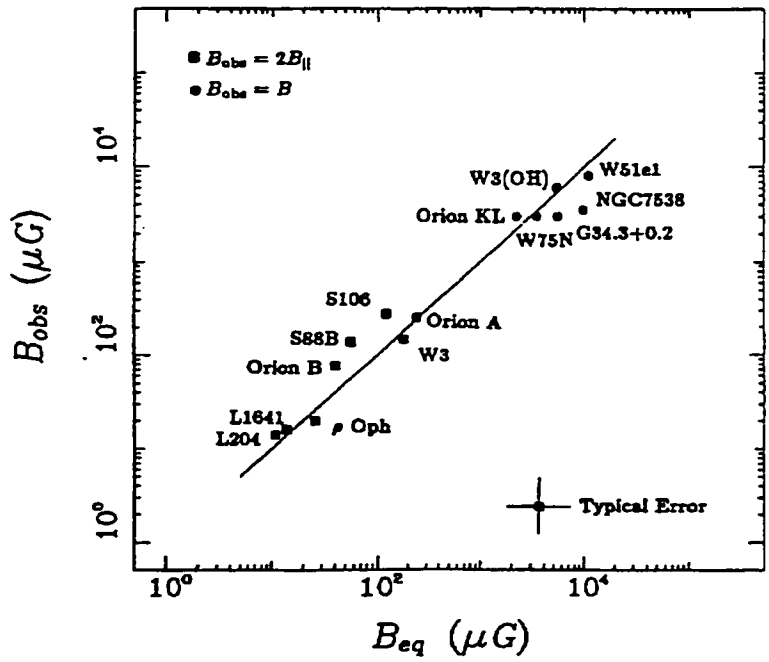

Figure 2-6: (From Myers & Goodman 1988a) A comparison of observed field strengths B_{obs} with the field strength B_{eq} for a model which assumes kinetic, magnetic, and gravitational energy equipartition.

in Section 2.5.1 that equipartition is consistent with non-thermal motions resulting from Alfvén waves. Alternatively, magnetic dynamos resulting from 3-dimensional MHD turbulence might be responsible (Section 2.5.5). Regardless of its origin, equipartition appears to be an observational fact, which we use as a guiding principle in our models of filamentary clouds in Chapter 3.

2.2.2 Observations of Polarization in Molecular Clouds

It has long been known from stellar observations that starlight can appear slightly, but measurably, polarized. It is generally accepted that this observed polarization is due to anisotropic extinction by partially aligned dust grains along the line of sight to the star. More recently, observations have confirmed that the emission of thermal radiation from aligned dust grains at sub-millimetre and millimetre wavelengths is also polarized. It is widely believed that the magnetic field is the main agent responsible for the alignment of grains. A thorough discussion of the conditions required for grain alignment and the mechanisms responsible are well beyond the scope of this thesis, and are in fact an area of active research (eg. Lazarian & Draine 1997, 1999). For our purposes, it is sufficient to accept that there are strong observational and theoretical reasons for believing that grains are predominantly elongated, rapidly rotating, and aligned perpendicular to the local magnetic field, for a wide range of conditions in molecular clouds. Observations of polarized extinction and emission offer a fairly direct method for

probing the geometry of the magnetic field in molecular clouds, which, when combined with Zeeman measurements, can be used to study the 3-dimensional structure of the magnetic field.

2.2.3 The Polarized Light of Background Stars

Most observations of polarization in molecular clouds to date have relied on the polarization of background starlight by aligned grains. These observations have been carried out in the optical and near infrared regions of the spectrum, where absorption and scattering, rather than emission, are the dominant processes. A net polarization of the observed starlight occurs because the scattering and absorption cross-sections are larger in the direction of the major axis than the minor axis for elongated grains. The observed polarization is generally parallel to the component of the magnetic field in the plane of the sky, since grains tend to align with their major axes perpendicular to the field. It is important to realize, however, that the observed polarization is actually due to the combined effects of dust grains along the entire column to the background star. A uniform field in the plane of the sky results in the greatest possible polarization, but variations in the field orientation along the line of sight tend to have a de-polarizing effect.

It is widely appreciated that the dust grains within a molecular cloud are a highly inhomogeneous mixture of grains with different sizes, elongations and compositions (Goodman et al. 1995). The cross section of a grain to starlight depends strongly on the parameter $x = 2\pi a/\lambda$, where λ is the wavelength of observation. Grains are most effective at polarizing starlight when $x \approx 1$. The polarization at a particular observed wavelength is therefore dominated by a subset of the dust grains whose sizes are comparable to λ. Regions along the line of sight that are lacking in appropriately sized grains will not contribute significantly to the observed polarization.

Optical polarization studies are limited to extinctions less than $\sim 2\ mag$, while near infra-red observations can penetrate up to $A_v \sim 40\ mag$ (Weintraub et al. 1999). Well-ordered polarization patterns seen in infra-red are almost always observed to join smoothly onto the optical polarization patterns, which are limited to the low extinction peripheral regions of the clouds (Goodman et al. 1992, 1995, Weintraub et al. 1999). Therefore, the optical and near infra-red observations appear to trace the same large scale field structures.

While the agreement between optical and near infra-red data may seem encouraging at first, there is a serious problem with the interpretation of the polarization as truly representative of the field structure in the *interior* regions of dark clouds. No distortions of the field are observed to be associated with filaments or other dense structures within dark clouds (Goodman et al. 1992). How is it possible that the polarization pattern is so completely oblivious to the presence of dense structures in the gas? On theoretical grounds, a magnetic field that is unaffected by dense structures does not make much sense.

Magnetic fields are essentially frozen to the gas, so that they must squeeze together and bend with the gas when dense structures form within a molecular cloud.

Goodman et al. (1995) rather conclusively show that dust grains within the dense interiors of dark clouds are ineffective at polarizing starlight, so that optical and near-infrared polarimetry provide essentially no information on the field structure inside of dark clouds. This conclusion hinges on the observational fact that the percentage of polarization does not increase with extinction in polarization studies of dark clouds. More precisely, for a set of observed background stars, the polarization is found to increase with extinction, but only until $A_v \approx 1.3 \pm 0.2\ mag$, past which no further increase is observed (Arce et al. 1998, See also review by Weintraub et al. 1999). It is believed that this critical extinction marks a transition from dust grains being "good" at polarizing starlight (ie. elongated and of a size comparable to optical or near infra-red wavelengths) in the outer regions of dark clouds, to being "bad" in their interiors (Weintraub et al. 1999). This result is quite disappointing, since the dense interiors of molecular clouds are the regions of greatest importance for star formation. In the next section, we discuss a relatively new alternative observational technique, which is now beginning to prove its usefulness for determining the field geometry deep within molecular clouds.

2.2.4 The Polarized Far-Infrared and Sub-Millimetre Emission of Dust Grains

The thermal emission of dust grains in molecular clouds peaks in the sub-millimetre region of the electromagnetic spectrum. Sub-millimetre emission is polarized, provided that the grains responsible for the emission are elongated and aligned. This is also true at slightly shorter ($\sim 100\mu m$) far-infrared wavelengths (eg. Novak et al. 1989). However, the orientation of the polarization with respect to the field is opposite that which is obtained in extinction, with the polarization perpendicular to the field component in the plane of the sky. Observations of polarized far-infrared and sub-millimetre emission have the potential, which is yet to be fully realized, of providing a new window for studying the magnetic structure in dark clouds. The first detection of polarized far-infra-red emission is quite recent, dating to a balloon-borne observation of the Orion molecular cloud by Cudlip et al. in 1982. The first detection of polarized sub-millimetre emission was even more recent, by Hildebrand et al. (1984), also in the Orion cloud. Only now are these exciting techniques reaching maturity as a viable tool for the study of magnetic fields in dark clouds, which are much weaker sources than Orion.

Observations of polarization at far-infrared and sub-millimetre wavelengths offer several advantages over optical and near infra-red extinction studies. Most obviously, observations in emission are less prone to confusion effects resulting from foreground and background material, since nearly all of the emission usually originates in the cloud being studied. However, the main advantage is that far-infrared and sub-millimetre observations should succeed at tracing the magnetic structure deep within dark clouds,

precisely where optical and near infra-red observations fail. The polarization in emission is less sensitive to the size of the grains than in absorption, so that essentially all of the grains present contribute to the polarization. Therefore, there should be plenty of grains in the interiors of dark clouds that are "bad" polarizers at optical and near infra-red wavelengths, but perfectly "good" in the far-infrared and sub-millimetre (Goodman et al. 1995).

Far-Infrared and Sub-Millimetre Polarimetry in Molecular Clouds

Far-infrared and sub-millimetre polarimetry is currently feasible only for dense cores and some filaments in molecular clouds. Matthews and Wilson (1999) have used the SCUBA polarimeter to make a remarkable 850 μm map of part of the "integral-shaped filament" in the densest region of the Orion A Molecular Cloud (see Section 2.2.1). Their map shows that the field is well-ordered over the entire length of the part of the filament mapped, with the polarization vectors roughly aligned with the filament. They have also mapped the polarization structure of the numerous cores that are strung along the filament (see also Chini et al. 1997).

It is not known at this time what 3-dimensional field structures might be consistent with their data, since molecular clouds act like 3-dimensional polarizing structures that can sometimes result in counter-intuitive, even surprising, polarization patterns. Carlqvist and Kristen (1997) have modeled the polarization in extinction for simple models of filamentary clouds. They find a surprising "signature" of helical fields, which we discuss in Chapter 3. It seems likely that detailed modeling of polarization patterns, assuming several reasonable magnetic geometries, is the only clear way to ascertain how well and how uniquely any particular model can account for the observational data.

We discuss sub-millimetre and far-infrared polarization maps of cores in Chapter 5.

2.2.5 Ordered Magnetic Fields in Molecular Clouds

At this time, the only safe general conclusion that can be drawn from Zeeman and polarization observations is that remarkably well-ordered magnetic fields exist in molecular clouds, whose strengths are consistent with approximate global equipartition with non-thermal motions in the gas. Therefore, it is justifiable to consider the effects of dynamically significant ordered magnetic fields in theoretical models of clouds and their cores.

2.3 The Formation of Molecular Clouds - Spiral Shocks and Supershells

Having discussed some of the observations of molecular clouds, we briefly pause to consider their origins.

2.3.1 Spiral Shocks

Molecular clouds almost certainly form directly from HI gas in the ISM. It is known that molecular clouds have lifetimes of $\sim 10^7$ *years* (see review by Blitz and Williams 1999), which is much shorter than a Galactic rotation period. Molecular clouds are also known to be strongly concentrated in the arms of spiral galaxies, with very little inter-arm molecular gas present (Heyer and Terebey 1998, Blitz and Williams 1999). Therefore, it is unlikely that most molecular clouds form by the accumulation of molecular "cloudlets" in spiral arms. Rather, it is thought that the passing of a spiral arm can form massive atomic clouds containing up to 10^7 $M_\odot$ of atomic gas, which is presumably gathered and compressed from the inter-arm ISM. These atomic clouds easily provide enough self-shielding from ultraviolet radiation for substantial amounts of molecular gas to form. (Hydrogen molecules are easily dissociated by ultraviolet radiation. We discuss this further in Section 2.6.) Once molecular gas begins to form, it can cool rapidly, primarily by CO rotational line transitions (Goldsmith and Langer 1978), allowing it to gradually contract to form a molecular cloud.

2.3.2 Supershells

Spiral shocks are not the only way to provide the compression of HI gas that seems to be necessary for the formation of molecular clouds. This fact is obvious since irregular galaxies, which often show no evidence of spiral arms, clearly contain molecular clouds that are actively forming stars. There are many other ways of producing thick, highly compressed layers of HI in the ISM. These include supernovae, the bubbles blown by the winds of hot stars, and superbubbles that result from hot star clusters or the combined energy input of several supernovae.

Several nearby molecular clouds are known to be associated with HI loops and arches that might be due to expanding shells (Heiles & Jenkins 1976). For example, the Orion region is encircled by the well-known Barnard's loop. Relatively nearby, there is a prominent HI "hole" whose walls appear to be a dense, expanding shell. This shell coincides with several very young objects, including the Taurus dark clouds, the Pleides cluster, and the Perseus II association, all clearly associated with recent and ongoing star formation (Heiles & Jenkins 1976). It has also been suggested that the giant molecular clouds in Orion, Sco-Cen, and Perseus, along with the Taurus and Ophiuchus dark clouds, may have formed from

compressed gas swept up by the same superbubble that formed the structure known as Lindblad's ring (Elmegreen 1993).

The most spectacular supershell seen in HI 21 *cm* emission is the North Polar Spur, which is part of the larger structure seen in radio continuum emission called Radio Loop 1 (see Figure 2-7, panel a). This enormous structure spans $\sim 120°$ in Galactic longitude and reaches at least 60° above the plane of the Galaxy. It is widely believed that this superbubble is the result of winds from hot stars in the Sco-Cen association.

Heiles and Jenkins (1976) and Heiles (1998) show, from the polarization of background stars, that the Galactic magnetic field is parallel to the North Galactic Spur. Detailed modeling of the polarization over the entire Radio Loop 1 region (Heiles 1998) shows that the observed magnetic field structure is consistent with the field being swept up with the gas into the expanding shell, and stretched over the surface of the bubble. We show Heiles' model superimposed on the polarization data in Figure 2-7 (panel b). Globally, the field lines appear to be well-ordered and stretched along lines of constant longitude. Superbubbles may naturally lead to highly ordered magnetic fields because the tremendous stretching of field lines over an expanding bubble will tend to smooth out disordered field components (Pudritz & Fiege 1999). The magnetic structure in the walls of a bubble should therefore be aligned parallel to the walls and should be quite uniform locally, at any point in the bubble's wall.

The shock on the interior of a supershell is expected to be strongly radiative, so that the shell can cool rapidly (Ferrière, Mac Low, and Zweibel 1991). Shells may therefore be subject to gravo-thermal instabilities. Nagai et al. (1998) have recently performed a stability analysis for slab-like pieces of magnetized shells and demonstrated that the shells must fragment into filaments. They find that the fastest growing modes of instability result in filaments that are perpendicular to the magnetic field for relatively thick shells, but aligned with the field for thin shells.

The models of filamentary clouds that we present in Chapter 3 propose that the magnetic fields threading filamentary clouds might be predominantly helical. A field originally aligned with a filament might become twisted into a helical configuration if the ends are rotated differentially with respect to each other. This might occur in supershells, which collect gas of non-uniform angular momentum from different parts of the Galactic rotation curve.

It should be noted that MHD turbulence could produce a variety of filamentary structures as well (see Section 2.5.5).

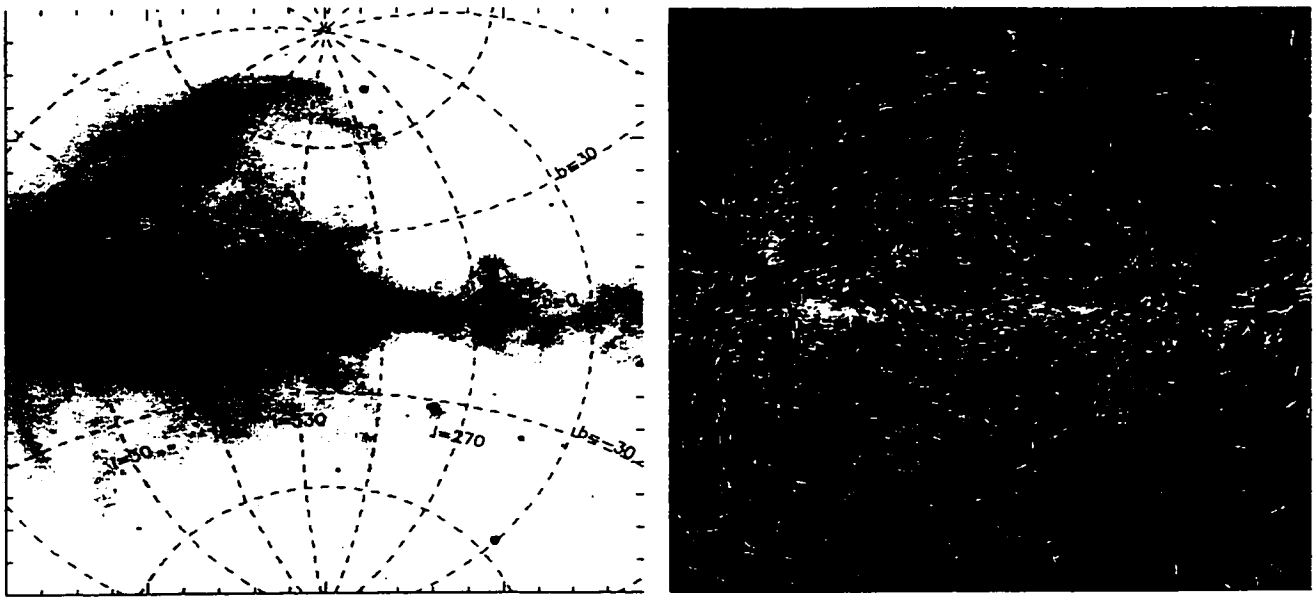

Figure 2-7: (From Heiles 1998) **Panel (a)** (left): The Radio Loop I region of the ISM, observed in 408 MHz radio emission (Adapted by Heiles from Haslam et al. 1983). The North Polar Spur is the large arch above the Galactic plane, which is the dark horizontal band across the centre of the figure. The letters indicate bright radio filaments, which we do not discuss. **Panel (b)** (right): Heiles' model of the Radio Loop I region. The dark dashed lines represent field lines, which are approximately parallel to the white starlight polarization vectors.

2.4 Non-Thermal Motions in Molecular Clouds

2.4.1 Non-thermal Pressure

In Chapter 1, we briefly discussed the seemingly paradoxical dynamical state of molecular clouds, whose thermal pressures are many times too low to support the gas against self-gravity. Molecular clouds maintain their overall equilibrium, in a time-averaged and coarse-grained sense, as a result of non-thermal internal motions plus magnetic support. The precise origins of the motions are not well understood, but we discuss two possibilities, namely Alfvén waves and MHD turbulence, in Section 2.5.

The non-thermal motions within molecular clouds can often be thought of as providing a time-averaged mean field pressure. The non-thermal pressure dominates over the thermal pressure everywhere in molecular clouds and the ISM (ie. the motions are super-sonic), except for in the central regions of dense cloud cores. It is important to realize that non-thermal motions cannot be neglected in any realistic model of molecular clouds. We include non-thermal motions in our models of filamentary clouds and prolate cores through the mean field, effective pressure approach described above.

Implicit to this mean-field interpretation is the assumption that non-thermal motions involve size scales that are smaller than clouds. Some recent simulations of MHD "turbulence" in *atomic* clouds refute

this "micro-turbulent" approximation (see Section 2.5.2). [6] Even so, the success of more conventional models in explaining the observations (eg. Myers & Goodman 1988, See also Sections 2.11.4) suggests that it might be a valid assumption in some cases.

Mestel and Spitzer (1956) first estimated the velocity dispersion required to support a self-gravitating interstellar gas cloud against self-gravity. The virial theorem is given by [7]

$$2K + W = 0, \tag{2.4}$$

where we have ignored magnetic fields and the surface pressure term (We present a more complete analysis in Section 2.11.1 where we retain all terms.). For a spherical cloud of mass M, radius R, and velocity dispersion σ, the gravitational and internal energies (in thermal and non-thermal motions) are respectively given by

$$W = -\frac{3}{5}a\frac{GM^2}{R} \tag{2.5}$$

$$K = \frac{3}{2}M\sigma^2, \tag{2.6}$$

where G is the gravitational constant, and a is a constant of order unity that accounts for the non-uniformity of the cloud.

It is easy to show from equation 2.4 that the expected velocity dispersion is given by

$$\sigma^2 \approx \frac{3\pi}{20}\frac{G\mu m_h N^2}{n}, \tag{2.7}$$

where m_h is the mass of a hydrogen atom, $\mu \approx 2.33$ is the mean atomic weight (relative to hydrogen) of the molecular gas, and n and N are respectively the particle number density and the surface number density (given by $M/(\pi R^2 \mu m_h)$). This formula can be more usefully written in terms of the visual extinction using the relation $A_v = N/(2 \times 10^{21}\ cm^{-2})\ mag$ (Spitzer 1978):

$$\sigma \approx 0.22 \times A_v \left(\frac{n}{1000\ cm^{-3}}\right)^{-1/2}\ km\ s^{-1}, \tag{2.8}$$

where we have normalized by a density that is typical of the interiors of dark clouds. The thermal component of the velocity dispersion is only $\sqrt{kT/\mu m_h} \approx 0.23\ km\ s^{-1}$, assuming a temperature of 15 K. Therefore, the velocity dispersion must be dominated by non-thermal motions in molecular clouds, where $A_v \gg 1$ usually. The support provided by thermal pressure is almost negligible in most

[6] These simulations use the term "turbulence" in an inexact sense. See Section 2.5.2.

[7] Mestel and Spitzer (1956) cast this argument in terms of purely thermal support. However, we generalize their argument to include non-thermal velocity dispersions

molecular clouds. [8]

2.5 The Origins of Non-Thermal Motions in Molecular Clouds

We have discussed the non-thermal motions observed in molecular clouds, but we have not yet addressed the possible *origins* of the non-thermal motions. As we shall see, this is a topic that has been studied for decades and it is also one of tremendous current interest.

There are two competing ideas to explain the non-thermal motions that are observed in molecular clouds. The older of these ideas is that the motions are essentially random and due to some form of MHD turbulence (eg. Mestel & Spitzer 1956). [9] Arons and Max (1975) suggested the alternate view that the motions might be due to relatively ordered MHD Alfvén waves propagating through the gas. We first discuss this latter possibility, leaving the more complicated topic of MHD turbulence for Section 2.5.5.

2.5.1 Alfvén Waves

The non-thermal motions within molecular clouds are generally believed to be magnetic in nature. Arons and Max (1975) first suggested that the motions might be due to the propagation of MHD Alfvén waves through the gas. In their picture, transverse waves propagate along magnetic field lines much like waves on a string under tension. These waves propagate with velocity

$$v_A = \frac{B}{\sqrt{4\pi\rho}}, \tag{2.9}$$

where B is the magnetic field strength and ρ is the density.

Several authors have discussed the fact that Alfvén waves provide an effective isotropic pressure $P \propto \rho^{1/2}$ (eg. Dewar 1970, Pudritz 1990, McKee and Zweibel 1995). If molecular clouds are in a state of rough equipartition between their magnetic and kinetic energy densities, as has often been suggested (Mestel & Spitzer 1956, Myers and Goodman 1988a,b), then $\sigma = v_A/\sqrt{3}$, where σ is the one-dimensional velocity dispersion. Therefore, a key prediction of the Alfvén wave picture is that the observed velocity dispersion within molecular clouds should be supersonic but slightly sub-Alfvénic.

[8] This argument would not hold for magnetically sub-critical clouds, for which the magnetic field is sufficient to support the gas, without any additional pressure support. We discuss magnetic criticality in Section 2.11.2.

[9] Mestel and Spitzer (1956) actually discussed the possibilities of MHD turbulence long before non-thermal line widths had even been observed.

2.5.2 Turbulence in Molecular Clouds and the ISM

Turbulence has also been invoked by many authors as a possible origin for the non-thermal motions observed in molecular clouds. It has become commonplace to categorically describe non-thermal disordered motions in molecular clouds and the ISM as "turbulence", even while recognizing that "astrophysical" turbulence is fundamentally different from the laboratory phenomenon of the same name. Astrophysical turbulence differs from the turbulence studied in terrestrial laboratories for several fairly obvious reasons. First of all, the ISM contains dynamically important magnetic fields, whose non-isotropic stresses greatly increase the complexity of the problem. Secondly, all phases of the ISM are highly compressible so that the traditional Kolmogorov (1941) theory would strictly not apply even in the absence of the field. The turbulence is dominated by shocks because the motions are super-sonic and compressible. Thirdly, radiative transfer is important in the ISM, particularly in dissipating the heat that results from shocks (Vázquez-Semadeni et al. 1999). Finally, turbulence in molecular clouds, and probably some massive HI complexes, operates in a regime where self-gravity is important.

Substantial progress has been made recently by numerical simulations of self-gravitating, MHD turbulence, which are now possible as a result of computational advances (see Vázquez-Semadeni et al. 1999 for a recent review). This new field is important to our models of filamentary molecular clouds for two reasons. First of all, simulations of MHD turbulence show that filamentary structures naturally result from the turbulent flow. Secondly, MHD turbulence is characterized by regions of high kinematic vorticity and magnetic helicity. Therefore, MHD turbulence might provide a feasible way to twist magnetic fields into the helical patterns predicted by our models.

We begin with a brief discussion of the reasons why flows become turbulent, and provide some simple scaling arguments for incompressible, non-magnetic turbulence in Section 2.5.4. We discuss recent simulations of turbulence in the ISM in Section 2.5.5.

2.5.3 Origins of Turbulence

Turbulence can be defined as an irregular and highly chaotic flow that retains an underlying statistical order (Heyer & Brunt 1999). Turbulence occurs because hydrodynamics and magnetohydrodynamics are inherently non-linear phenomena. For small amplitude linear waves, modes of oscillation (ie. waves) are uncoupled so that energy in one mode (ie. one wavelength) does not excite other modes. This is not generally true for finite amplitude waves, however. Because of non-linear couplings between modes, energy rapidly flows out of the originally excited mode, exciting many other modes at both longer and shorter wavelengths. (See Pouquet et al. 1999 for an illustrative example.)

The transition from laminar to turbulent flow is most easily seen by considering the non-magnetic

Navier-Stokes equation of hydrodynamics (ie. the momentum equation in fluid dynamics):

$$\frac{\partial \mathbf{v}}{\partial t} + (\mathbf{v} \cdot \nabla)\mathbf{v} = -\frac{\nabla P}{\rho} + \nu \nabla^2 \mathbf{v}, \tag{2.10}$$

where ν is the kinematic viscosity (in units of $cm^2\ s^{-1}$), and all other quantities are as previously defined. Fluid motions may become turbulent when the non-linear inertial term $(\mathbf{v} \cdot \nabla)\mathbf{v}$ of the Navier-Stokes equation dominates over the linear viscous term. If L is a characteristic length scale for the system, and $\mathbf{v_0}$ is a characteristic velocity, then the inertial term dominates over viscosity whenever $\mathbf{v_0^2}/L \gg \nu \mathbf{v_0}/L^2$. Equivalently, fluids are dominated by turbulence when $R \gg 1$, where R is the Reynolds number defined by

$$R = \frac{\mathbf{v_0} L}{\nu_0}. \tag{2.11}$$

The Reynolds number is extremely high in molecular clouds and the ISM, owing to the large size scales involved.

2.5.4 Kolmogorov Turbulence

We briefly discuss classical Kolmogorov (1941) turbulence, which applies to unmagnetized, incompressible fluids, before discussing the recent simulations of MHD "astrophysical" turbulence described above. Kolmogorov turbulence assumes a quasi-steady state, in which energy injected at large scales cascades to ever smaller scales, until it is finally dissipated by microscopic viscous heating. Kolmogorov turbulence applies to the *inertial range*, between the largest scales of the system and the smallest scales where viscosity is important. The density of the fluid ρ and the rate of viscous energy dissipation per unit mass ϵ (in units of $erg\ g^{-1}\ s^{-1} = cm^2\ s^{-3}$) are the only relevant physical scales in the inertial range. Therefore, they alone must determine the scaling relations between all physical parameters that describe the flow (see Landau & Lifshitz 1989). For example, the velocities v of turbulent eddies must be related to their characteristic sizes by

$$v \sim (\epsilon L)^{1/3}, \tag{2.12}$$

since no other combination of ϵ, ρ, and L has the dimensions of a velocity. It is an observational fact that the line widths Δv of molecular clouds are tightly correlated to their sizes R by a relation that is very similar to equation 2.12. This line width-size relation, which is often called Larson's first law, after its discoverer (Larson 1981), is given by

$$\Delta_v \propto R^{0.38}. \tag{2.13}$$

(See Section 2.11.4, where we discuss Larson's laws in more detail.) It is notable that Larson originally attributed the line width-size relation to turbulence because of the similar scalings in equations 2.12 and

2.13. We discuss an alternate viewpoint in Section 2.11.4.

The energy spectrum $E(k)$ is another important relation for turbulent flows, where k is the wave number $\sim L^{-1}$. Defining $E(k)\ dk$ as the total energy per unit mass in modes with wave number between k and $k + dk$, $E(k)$ is found to have dimensions of $cm^3\ s^{-2}$. Combining this with the dimension of ϵ, it is easy to show that

$$E(k) \sim \epsilon^{2/3} k^{-5/3}. \tag{2.14}$$

The energy spectrum obtained from astrophysical turbulence simulations is often compared with the Kolmogorov $k^{-5/3}$ law, which we further discuss in Section 2.5.6 below.

2.5.5 MHD Turbulence

It is commonly believed (see Bertoldi and McKee 1992 for example) that the Alfvén speed probably represents an upper limit to the velocity dispersion in turbulent molecular clouds and the ISM, because super-Alfvénic turbulence is known to be highly dissipative. The conventional reasoning is that magnetic fields are capable of softening dissipative shocks at sub-Alfvénic velocities, but become ineffective when velocities exceed the Alfvén speed. Therefore, we might expect that $\sigma \approx v_A$. We note that this reasoning predicts approximate equipartition between kinetic and magnetic energies in the ISM and molecular clouds, as is often observed to be the case (eg. Myers & Goodman 1988a,b, See also Section 2.2.1).

However, recent simulations cast doubt on the ability of magnetic fields to limit dissipation by softening sub-Alfvénic shocks (eg. Stone et al. 1998). MHD simulations of turbulent molecular clouds all find that the turbulence rapidly decays, mainly due to the presence of compressive shocks, resulting in a loss of turbulent support. One might ask whether some appreciable fraction of the internal energy of a cloud might be stored in the form of non-compressive Alfvén waves. However, finite amplitude Alfvén waves are coupled to compressive and highly dissipative types of waves in the non-linear regime. Even non-linear Alfvén waves decay as a result of being converted into compressive motions (Stone et al. 1998, see also references therein). If true, these results imply that non-linear motions of any kind must be sustained by a continual injection of kinetic energy to compensate for dissipative losses in molecular clouds and the ISM (eg. Stone et al. 1998). This injection of energy could come from bipolar outflows, stellar winds, supernovae, supershells, or Galactic shear [10] (see review by Vázquez-Semadeni et al 1999, also Bally 1989). Some simulations of turbulence include energy sources that model some of these processes, as we discuss below.

Most simulations of MHD turbulence to date apply only to the atomic phases of the ISM. [11] The most

[10] Shear is included in many simulations, but energy injection at the large scales involved appears to be too inefficient to sustain turbulence (Vázquez-Semadeni et al. 1999)

[11] A notable exception is Stone et al. (1998), who use an isothermal equation of state (in the true sense of constant

detailed simulations of MHD turbulence have been done by Vázquez-Semadeni et al. 1995, Passot et al. 1995, Vázquez-Semadeni et al. 1996, Vázquez-Semadeni et al. 1997, and BVS (ie. various combinations of the same authors, collectively Vázquez-Semadeni et al. hereafter). The phase of the ISM enters their simulations only through the thermodynamics of the gas. The heating is usually assumed to be due to the diffuse ultraviolet radiation of the Galaxy, and point sources of heat from hot OB stars. The gas is assumed to cool radiatively, using a simple model of radiative processes in atomic phases of the ISM. [12]

2.5.6 Global Properties of MHD Turbulence Simulations

The energy spectra that evolve from simulations of MHD turbulence tend to be quite similar the $E(k) \sim k^{-5/3}$ Kolmogorov law, with power laws in the range of -2 to $-5/3$ reported for 2 and 3 dimensional simulations (Vázquez-Semadeni et al. 1999). This is a surprising result, considering the much more complex phenomena involved in astrophysical MHD turbulence. It is also found that simulations tend to evolve toward approximate global energy equipartition between the turbulent magnetic field and the kinetic energy (eg. Stone et al. 1998).

Vázquez-Semadeni et al (1997) show that the clouds which emerge from 2-dimensional turbulence simulations [13] obey Larson's line width size relation quite closely (equation 2.13). We show in Section 2.11.4 below that Larson's laws are also obtained from simple virial arguments, if molecular clouds are near their critical states for radial collapse. The transient clouds that arise from turbulence simulations clearly are not near criticality, so it is surprising that these two very different arguments can both lead to Larson's first law. The simulations do not agree with Larson's second law $\rho \sim R^{-1.1}$ (see Section 2.11.4 below) between the density and size of clouds, however. Hence, the simulations are not in agreement with the observations in this regard.

It must be stressed that the simulations of Vázquez-Semadeni et al. are most applicable to atomic clouds since they do not include cooling functions that are appropriate for molecular gas (ie. all of the clouds are above $100 - 300\ K$, rather than the $\sim 15\ K$ of most molecular clouds). Their applicability to the molecular gas, where Larson's laws are observed to apply, remains to be shown.

---

temperature, as opposed to our usage of "isothermal" to describe a gas of constant velocity dispersion) to model MHD turbulence within molecular gas. However, their simulations do not include self-gravity.

[12] Note that simulations that include stellar heating must incorporate a prescription for star formation, which occurs as a result of gravitational instabilities at scales that are much smaller than a single grid cell. Often, a simple thresholding law is used, which assumes that hot stars form whenever the local density exceeds some prescribed threshold.

[13] Most simulations to date have been two dimensional because the lower computational overhead allows for greater resolution.

2.5.7 Filamentary HI Clouds as Density Fluctuations in a Turbulent ISM

The discrete features that observers call clouds have no special role in this view of ISM as a turbulent, magnetized, self-gravitating, compressible fluid. Clouds are interpreted as finite amplitude density fluctuations that are transient in nature. The most striking feature of the simulations is the dominance of *filamentary* structures, which arise naturally from the turbulent flow (see figure 2-8). This is an extremely interesting result, which might be relevant to our models of filamentary molecular clouds. Although the filaments that arise from the simulations should really be interpreted as HI filaments, it is conceivable that filamentary *molecular* clouds might form within their densest regions. This might provide an important mechanism for producing filamentary molecular clouds, because it is so generic. The drawback of the supershell mechanism for producing filaments, which we discussed in Section 2.3.2, is that supershells result from very special conditions in the ISM. For this reason, it is difficult to believe that all filaments can form as a result of supershells. On the other hand, the diffuse ISM surrounds the entire Galactic disk, and is dominated by non-thermal motions and filamentary structures everywhere that observations have been made. It may be that filaments form naturally by a variety of mechanisms in the ISM.

Vázquez-Semadeni et al. (1999) show that density fluctuations form primarily at the interface between colliding streams of gas. As one might expect, the density structure of the gas is very well correlated with the structure of the velocity field $\mathbf{v}$. In particular, clouds are associated with both the regions of maximum compression, where $\nabla \cdot \mathbf{v} < 0$, and the regions of highest vorticity (maximum $|\nabla \times \mathbf{v}|$). The vorticity arises because most collisions between gas streams are oblique, rather than head-on, resulting in rotational motions (BVS). This might provide a natural mechanism for winding the magnetic field into the helical configurations that our model predicts. However, more 3-dimensional simulations are required to determine whether or not this is a feasible way to generate helical fields. (Of course, this cannot work in 2-dimensional simulations.)

It is reasonable to question the relevance of 2-dimensional simulations to the 3-dimensional turbulence at work in the ISM. In particular, some MHD instabilities (ie. the Balbus-Hawley (1991) instability) and magnetic dynamos, which work to amplify magnetic fields, are inherently three dimensional phenomena, which do not work in two dimensional flows. While suggestive, 2-dimensional simulations cannot provide a convincing picture of real 3-dimensional MHD turbulence.

2.5.8 Lifetimes of Density Fluctuations

We argued in Section 2.3 that GMCs have lifetimes of at least 10^7 yrs, and that these molecular clouds almost certainly form from larger condensations of HI gas. Since many molecular clouds remain

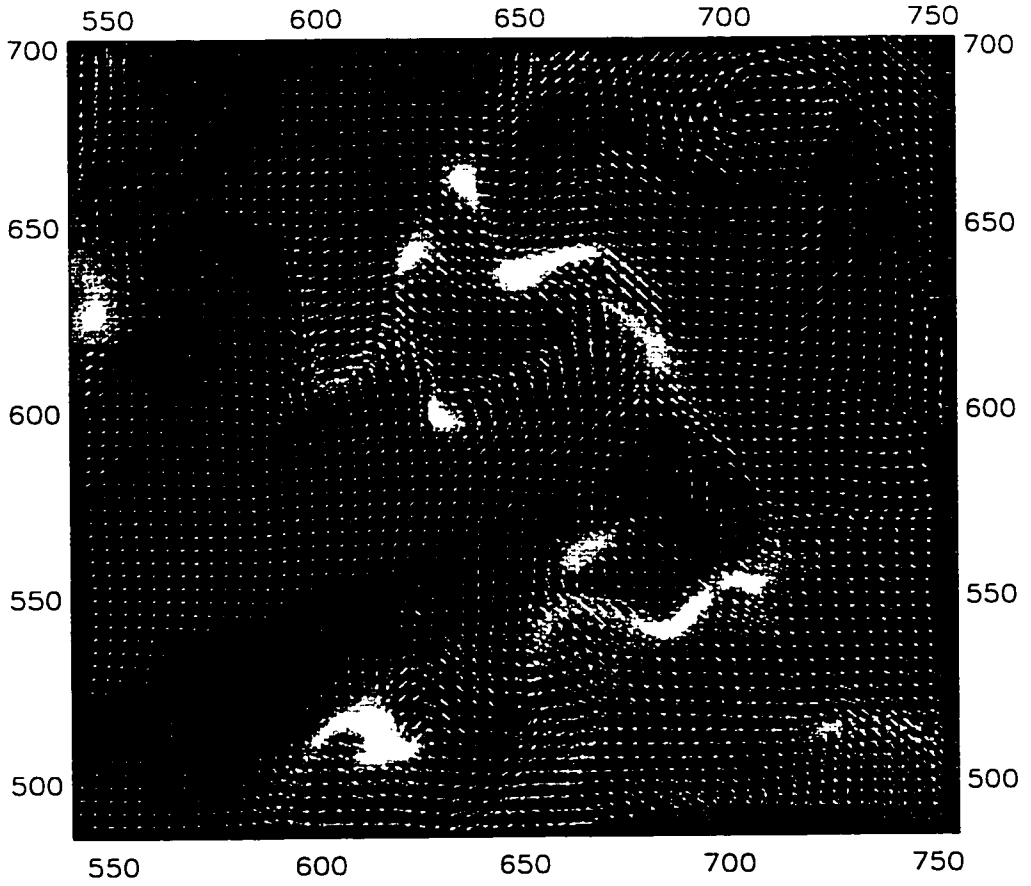

Figure 2-8: (From Ballesteros-Paredes et al. 1999) Filamentary structure in a 2-dimensional simulation of MHD turbulence. The arrows represent the velocity field.

associated with their nascent HI complexes, these also probably live at least $\sim 10^7\ yrs$. How can these long lifetimes be reconciled with the view of clouds as transient density fluctuations? BVS find that the largest clouds that emerge from their simulations live as long as GMCs, before decaying. They also point out that transient clouds need not be disrupted altogether by the turbulent flow. They might instead merge with other clouds, split, or slowly re-expand.

2.5.9 Commentary on Simulations of MHD Turbulence

It is clear that simulations of turbulence in molecular clouds and the ISM have a promising future, and will undoubtedly further our understanding of the extremely non-linear processes at work in these systems. However, there are several challenges that remain to be overcome. Of course, higher resolution, fully 3-dimensional simulations will be obtained with further computational advances. In this way, the applicability of 2-dimensional simulations to a 3-dimensional ISM will be rendered a non-issue. From the perspective of this thesis, however, the principle challenge will be in self-consistently including molecular gas in the simulations. The fact that several authors are *already* attempting to apply their results for atomic gas to molecular clouds is an indication of the need for this kind of work (ie. BVS, Vázquez-Semadeni et al. 1999).

We have argued above that MHD turbulence might provide a reasonable way to produce filamentary clouds, and might even be able to generate the helical fields that our models predict. How then, can equilibrium models of filaments and cores (Chapters 3 and 4 respectively) fit in with this picture of clouds as transient structures in a turbulent ISM? First of all, the simulations show that dense HI filaments can be extremely long lived ($\gtrsim 10^7\ yrs$), which might be aptly described by quasi-equilibrium states. Secondly, our models apply to high density molecular gas, where gravity is much more important than in any region considered by these simulations. Our viewpoint is that molecular filaments and cores are too strongly self-gravitating to evolve as transient fluctuations. Filaments must eventually fragment *gravitationally* into clumps, which may eventually form cores; cores are probably destroyed by the energetic processes (ie. outflows, stellar winds) that are triggered when they collapse to form stars.

2.6 The Surface Pressure on Molecular Clouds

Molecular clouds are truncated by the pressure of the ISM at the surface where the pressure of the molecular gas is equal to that of the external medium. The external pressure also has important consequences for the stability of clouds, which we show in Section 2.11.2 and Chapter 3. However, many models neglect the important role of the external pressure (eg. Nakamura et al. 1993, Gehman et al. 1996). The external pressure is a fundamental ingredient of our models of filamentary clouds, equal in importance

to the magnetic field. We show in the next chapter that the observed properties of filamentary clouds are very difficult to explain, unless they are *both* pressure truncated and magnetized.

2.6.1 The Total Pressure of the ISM

A recent estimate of the total pressure of the ISM at the midplane of the Galaxy is given by Boulares and Cox (1990), who find that

$$P_0 = (2.8 \pm 0.4) \times 10^4 \ K \ cm^{-3}. \tag{2.15}$$

This pressure is divided into contributions from the kinetic ram pressure of the gas ($\sim 1.3 \times 10^4 \ K \ cm^{-3}$), thermal pressure ($\sim 0.2 \times 10^4 \ K \ cm^{-3}$), the magnetic field ($\sim 0.7 \times 10^4 \ K \ cm^{-3}$), and cosmic rays ($\sim 0.7 \times 10^4 \ K \ cm^{-3}$). As usual, the thermal pressure is almost negligible compared to the other pressure components. The contribution due to cosmic rays is important to the overall support of the ISM against the gravitational field of the Galaxy. However, their contribution should not be included in the pressure exerted by the ISM on the surfaces of molecular clouds, because they are energetic particles that penetrate molecular clouds with little transfer of momentum to the gas. The main role of cosmic rays in molecular cloud physics is in maintaining the partially ionized state of molecular gas at high optical depths, where ultraviolet radiation cannot penetrate. Therefore, we are left with a pressure of $\sim 1.8 \times 10^4 \ K \ cm^{-3}$ that is exerted by the ISM on the surfaces of molecular clouds.

2.6.2 HI Clouds and Atomic Envelopes

While the pressure obtained by Boulares and Cox is already an order of magnitude higher than the thermal pressure of the ISM, there is evidence that the pressure in the immediate environs of molecular clouds may be even greater. Molecular clouds are often associated with over-dense atomic clouds that are at a higher pressure than the general ISM. There are generally two types atomic clouds that may be distinguished by whether or not they are bound by self-gravity. The largest HI complexes in our Galaxy, which are located primarily in the inner part of the Galaxy, are massive, gravitationally bound objects that sometimes have dense cores of molecular gas (Elmegreen & Elmegreen 1987). These are to be distinguished from the relatively thin envelopes of atomic gas that are known to surround nearby molecular clouds, which are generally very weakly self-gravitating but are probably bound by the gravitational potential of the molecular clouds.

The best studied example of an atomic envelope is the extensive complex of HI clouds in the Orion region, which has been mapped in 21 cm line emission by Chromey et al. (1989). The total pressure within these HI clouds ranges from $10^{4.5} - 10^5 \ K \ cm^{-3}$, which is several times the average pressure of the ISM at the Galactic midplane. Table 1 in Chromey et al. reveals that the atomic clouds in the

Orion region have very non-uniform internal pressures, contrary to the conventional wisdom that the components of the ISM are in pressure equilibrium (McKee and Ostriker 1977). The pressure exerted on the surfaces of the molecular clouds should therefore be thought of in a *time-averaged* sense, averaging the combined ram pressure effects of colliding HI clouds over the lifetime of a molecular cloud.

From a theoretical perspective, extensive atomic envelopes probably must surround molecular clouds because a sufficiently thick shielding layer of HI is necessary to protect fragile H_2 molecules from the Galaxy's flux of ultraviolet radiation. The formation of molecular clouds is not a well-understood process, but it is known that most H_2 forms from HI on the surfaces of dust grains (Spitzer 1978). Significant amounts of H_2 can accumulate in molecular clouds only when the H_2 formation rate exceeds the rate of photodissociation due to the absorption of ultraviolet radiation. This generally requires a shielding layer of atomic gas with a surface density of $\sim 10^{21}\ cm^{-2}$ (Elmegreen 1993). The observed atomic envelopes may be remnants of the HI gas from which molecular clouds formed, or atomic gas that has accumulated, as a result of the photodissociation of molecular gas. In all likelihood, atomic envelopes may contain a combination of both (Blitz and Williams 1999).

2.7 The Density Structure of Clouds and Clumps

What do we know about the density structure of molecular clouds and their clumps? This important question has been addressed by three very recent studies, which we discuss in this section. The most relevant observational results for our models of filamentary clouds are by Alves et al. (1998) and Lada et al. (1999), who have studied the density profiles of two dark filamentary clouds, namely L977 and IC5146. They found that both clouds are consistent with approximately r^{-2} density profiles. They determined the structure of these clouds by measuring the extinction of background starlight (in the infra-red) as a function of radius. Therefore, their measurements rely only on the assumption that the dust responsible for the extinction is well-mixed throughout the clouds. It is notable that Johnstone and Bally (1999) have also deduced an an r^{-2} density profile for the integral-shaped filament of Orion A, based on observations in the sub-millimetre continuum (See Section 2.1.2).

How do these results compare to models of filamentary clouds? Unmagnetized, isothermal filamentary clouds have a radial density profile of $\sim r^{-4}$ in their outer envelopes (Ostriker 1964). However, our models of isothermal filamentary clouds, which are derived in Chapter 3, have much more shallow density profiles of $\sim r^{-1.8}$ to r^{-2}. We can account for these shallower profiles in our model as due to the effects of the toroidal component of the magnetic field. On the other hand, models that include only the poloidal field have outer density profiles that are steeper than r^{-4}. Therefore, our models are consistent with the observed density profiles only when a helical field is present. As a cautionary note, we emphasize

that our models are not completely general because we assume constant flux to mass ratios for the poloidal and toroidal magnetic fields. Nevertheless, it is encouraging that the simplest case results in good agreement with the observations.

Williams et al. (1995) find that most of the clumps in the Rosette molecular cloud have nearly r^{-2} density profiles. Interestingly, the density gradient steepens only slightly as self-gravity becomes progressively more important from pressure-dominated clumps ($r^{-1.81}$), to gravitationally bound clumps ($r^{-2.05}$), to those that are actively forming stars ($r^{-2.18}$). An r^{-2} profile is expected for strongly self-gravitating isothermal spheres (see Chapter 5), with all parts of the cloud stirred equally by non-thermal motions. However, why such steep gradients should be obtained for pressure-dominated clumps is difficult to explain.

2.8 The Internal Structure of Molecular Clouds

We have already argued that many molecular clouds are highly filamentary. However, *all* known molecular clouds contain extremely complex substructure on scales larger than the dense ~ 0.1 *pc* cores, which are the sites of star formation. Traditionally, clouds are dissected into clumps, which are operationally defined as spatially and kinematically distinct features on a molecular line map. [14] It is likely that some clumps result from the gravitational fragmentation of more uniform structures. We take this view in Chapter 4, where we demonstrate that magnetized, filamentary molecular clouds tend to fragment, forming chains of nearly periodic clumps. Such periodicity has, in fact been noted in many filamentary clouds (Dutrey et al. 1991, Schneider & Elmegreen 1979).

2.8.1 The Mass Spectrum of Clumps

It is well known that the clumps in molecular clouds have a well-defined and apparently quite uniform mass spectrum

$$\frac{dN}{d\ln M} \propto M^{-x}. \tag{2.16}$$

where x is found to vary from $0.6 - 0.8$ between clouds (eg. Loren 1989, see also Blitz and Williams 1999). This is much more shallow than the stellar (Salpeter) initial mass function (IMF), which has $x \approx 1.35$. One consequence of the shallow clump mass spectrum is that most of the mass of a molecular cloud is in its highest mass clumps. This is completely opposite to what is found for the IMF, which is dominated by low mass stars. Patel and Pudritz (1994) argue that this steepening of the mass spectra is a strong confirmation that most clumps form multiple stars (see also review by Pudritz & Fiege 1999).

[14] Naturally, a different definition is required for sub-millimetre continuum observations, where only spatial information is available.

The mass spectrum of clumps has been interpreted as the result of collision-agglomeration processes at work in shaping the internal structure of molecular clouds (eg. Field & Saslaw 1965, Kwan & Valdez 1983, 1987). In such models, distinct clumps of gas move through the interclump medium, building up a realistic spectrum of clump masses by collisional agglomeration. The main limitation of this view of a molecular cloud as a hive of clumps swarming in their combined gravitational potential is that existing calculations do not take into account the large scale structure of the cloud, especially the effects of ordered magnetic fields.

2.9 Self-Gravity in Interstellar Gas Clouds

Molecular and HI clouds vary greatly in the degree to which self-gravity is important. Most molecular clouds are strongly self-gravitating, and are therefore characterized by significant pressure gradients, so that their mean internal pressures are substantially higher than their surface pressures. On the other hand, HI clouds and some molecular clouds (ie. high latitude clouds) are only weakly self-gravitating, with internal pressures that are comparable to their surface pressures. Weakly self-gravitating clouds have much less binding energy, and are therefore more prone to disruption by pressure gradients and flows in the ISM. As a result, such clouds often appear wispy, compared to strongly self-gravitating clouds. We derive criteria for self-gravity to be important to spherical and filamentary clouds below.

Self-gravity works very differently in filamentary clouds, which we model as infinite cylinders, compared to spheroidal clouds. Most importantly, these two geometries give rise to very different stability properties because of an important difference in the way the gravitational energy scales with radius in filaments compared to spheres. This has important consequences for the ways stars must form in filamentary clouds, which we discuss below.

2.9.1 Gravity in Spheroidal and Filamentary Clouds

Theoretical models of molecular clouds that assume virial equilibrium have a long and distinguished pedigree (eg. Chandrasekhar & Fermi 1953b, Mestel & Spitzer 1956, Spitzer 1978, McKee et al. 1993, McKee 1999), as well as a wealth of observational data to suggest that this approximation is often quite justified (eg. Myers & Goodman 1988a,b).

Neglecting the magnetic field and surface pressure for now, the virial theorem for a gas cloud in equilibrium between self-gravity and internal pressure is given by equation 2.4. Expanding equation 2.4, with the help of equations 2.5 and 2.6, we solve for the *virial* mass:

$$M_{vir} = \frac{5\sigma^2 R}{G}, \tag{2.17}$$

where we have assumed that the non-uniformity parameter $a = 1$ for simplicity. Therefore, a sufficient condition for a cloud to be gravitationally bound is that $M \approx M_{vir}$. Observations reveal that this is indeed the case for many molecular clouds, certainly most that are actively forming stars. Most HI clouds, except for some massive HI complexes, appear to be much more weakly self-gravitating (Elmegreen 1993).

An interesting and very important difference is apparent if we consider self-gravitating *filaments*. For filaments, it is most relevant to consider the gravitational and internal kinetic energies per unit length. We show in Chapter 3 that these are respectively given by

$$\mathcal{W} = -m^2 G \tag{2.18}$$

$$\mathcal{K} = \frac{3}{2} m\sigma^2, \tag{2.19}$$

where m is the mass per unit length. We also show in Appendix A of Chapter 3 that the virial theorem for a filamentary cloud, again neglecting surface pressure and magnetic terms, is given by

$$\frac{4}{3}\mathcal{K} + \mathcal{W} = 0. \tag{2.20}$$

Substituting equations 2.18 and 2.19 into equation 2.20, we solve for the *virial mass per unit length*, in analogy to equation 2.17:

$$m_{vir} = \frac{2\sigma^2}{G}. \tag{2.21}$$

The condition for a filamentary cloud to be gravitationally bound is therefore that m must be comaparable to, but not greater than m_{vir}. (Note that $m < m_{vir}$ when there is a surface pressure. See Chapter 3.)

Equation 2.20 has a very interesting property. Notice that m_{vir} does not depend on the radius of the cloud, in contrast to the expression for M_{vir}. Equation 2.21 has no solution when $m > m_{vir}$; therefore, *no equilibrium is possible when the mass per unit length exceeds* m_{vir} (McCrea 1957). This is very different from the behaviour of spheroids, since equation 2.4 can be solved for any choice of mass to obtain the equilibrium radius R of the cloud. Some of these spheroidal equilibria are unstable, however. We further discuss the Bonnor-Ebert stability of spheroidal clouds in Section 2.11.2.

What does this mean for star formation in filamentary clouds? We show in Chapter 3 that $m < m_{vir}$ for many filaments. Therefore, it is unlikely that filaments form stars by wholesale radial collapse to a spindle. Rather, filaments must first fragment to form spheroidal clumps and eventually cores. Some of these might eventually collapse as a result of the Bonnor-Ebert instability.

2.9.2 Star Formation in Self-Gravitating Clumps

An important finding is that some clumps in molecular clouds may *not* be gravitationally bound, even though they exist within clouds which generally are gravitationally bound as a whole (Bertoldi and McKee 1992). Instead, such clumps are confined by the pressure of the interclump medium.

Williams et al. (1995) demonstrated that star formation in the Rosette molecular cloud, which is recognized as a very actively star-forming cloud, is occurring only in strongly self-gravitating clumps. All of the known IRAS infra-red sources are associated with self-gravitating clumps detected in CO and ^{13}CO. This seems to be necessary from a theoretical standpoint since dense cores, in which must star-formation occurs, presumably form by the gravitational fragmentation and contraction of clumps. We discuss cores in detail, in Chapter 5.

If a clump is strongly self-gravitating, its mass seems to be the most important factor determining its star-forming properties. Whether a clump forms no stars, a few isolated stars, or an entire cluster seems to be determined mainly by the mass of the clump. Phelps and Lada (1997) recently detected 7 infra-red clusters in the Rosette molecular cloud, 5 of which had previously been unknown. They demonstrated that *all* seven are associated with, and probably embedded within, massive clumps ($> 200\ M_\odot$) detected in the Williams et al. (1995) study. Another example is the Orion molecular cloud, whose most massive clump, containing $\sim 500\ M_\odot$ of molecular gas, has a star formation efficiency of nearly 40% (Lada 1992, see also review by Pudritz and Fiege 1999).

2.10 Jeans Instability and the Fragmentation of Molecular Clouds

We have already briefly discussed the tendency for filamentary clouds to break up into periodic fragments along the length of the filament. Fragmentation plays an important role in our models because it is the first step in a sequence of events, which ultimately leads to the formation of stars. We study the fragmentation of filamentary clouds in Chapter 4. In many ways, our stability analysis is analogous to the classic Jean's instability, although there are important differences. We briefly discuss Jean's instability as an analogy for the fragmentation of filaments.

It has long been known that a uniform, infinite, self-gravitating, isothermal medium is unstable to gravitational collapse on scales larger than the Jean's length given by [15]

$$\lambda_J = \sqrt{\frac{\pi\sigma^2}{G\rho_0}} \tag{2.22}$$

[15] Jeans (1929) originally considered only thermal support, so that $\sigma^2 = kT/\mu m_h$, where T is the temperature and all other quantities are as defined in the main text. However, his argument easily generalizes to non-thermal support.

(Jeans 1929).

Binney and Tremaine (1994) provide a physical argument and a detailed calculation of the Jeans length, which is based on a *local* perturbation analysis of the medium. However, equation 2.22 can be approximately obtained from the virial theorem (equation 2.4) by setting $M = (4/3)\pi\rho R^3$ and solving for R. Thus, the Jeans length is essentially the size scale on which an uniform medium becomes strongly self-gravitating. The medium tends to break up into fragments of size λ_J, which contain roughly a Jeans mass $M_J = (4/3)\pi\rho(\lambda_J/2)^3$. The timescale on which the instability grows is on the order of a dynamical free-fall time $\sim (G\rho)^{-1/2}$ for wavelengths that are significantly longer than λ_J.

Putting in densities and velocity dispersions that are typical of the molecular gas in dark clouds, we find that the Jeans length and mass are typical of the clumps within molecular clouds:

$$\lambda_J = 1.8\frac{(\sigma/0.5\times10^5\ km\ s^{-1})}{(n/1000\ cm^{-3})^{1/2}}\ pc \tag{2.23}$$

$$M_J = 170\frac{(\sigma/0.5\times10^5\ km\ s^{-1})^3}{(n/1000\ cm^{-3})^{3/2}}\ M_\odot. \tag{2.24}$$

The Jeans mass is clearly much larger than typical stellar masses. Therefore, stars must either form rather inefficiently within self-gravitating clumps, or in a second round of fragmentation. This latter possibility might lead to the formation of clusters.

We note that this argument is almost dangerously simplistic when applied to a medium as non-uniform and highly structured as a molecular cloud. Note in particular that any molecular cloud will almost certainly contain very significant density variations within a region as large as the Jeans length in equation 2.23. The problem is therefore that there is no self-consistent choice for the density in equations 2.23 and 2.24.

Clearly, the classical Jeans instability is an oversimplification of the fragmentation processes at work in our models of filamentary clouds. In Chapter 4, we calculate the general stability properties and fragmentation length scales for our models of magnetized, pressure-truncated, filamentary clouds by looking for *global* modes of instability. We find that many of our filament models fragment on length, mass, and time scales that are roughly of the same order of magnitude as the Jeans instability. However, the helical magnetic field in our models significantly modifies the instability in some cases. Our most intriguing result is that we find a regime where magnetized filaments are very stable against fragmentation. Filaments in these states could live unperturbed for very long times, on the order of

$$\tau_{frag} \approx 5.7\left(\frac{n_c}{10^4\ cm^{-3}}\right)^{-1/2}\ Myr, \tag{2.25}$$

where n_c is the central density of the filament along the axis of symmetry. (See Chapter 4 for the reasons

behind our choice of scaling.)

2.11 Ordered Magnetic Fields in Molecular Clouds - Theoretical Considerations

Molecular clouds exist in an interesting physical regime wherein turbulent pressure, magnetic forces, and gravity are all about equally important (Myers & Goodman 1988a,b). The inclusion of the mean magnetic field in models of magnetized clouds is therefore an important step in developing realistic models. Magnetic models of interstellar gas clouds appear in the literature as early as 1953 in a classic paper by Chandrasekhar and Fermi (1953b), whose analyzed the stability of magnetized filamentary and spherical clouds. [16] Subsequently, Mestel and Spitzer (1956) discussed the stability of interstellar gas clouds in equipartition between their kinetic and magnetic energies. This work is particularly insightful because actual measurements of magnetic fields did not confirm their basic assumption until more than two decades later (eg. Myers & Goodman 1988a,b; also references therein). Subsequently, other analytical models of magnetized clouds have been developed by Stodólkiewicz (1963) and Spitzer (1978). More recently, considerable theoretical effort has gone into developing very detailed numerical models of clouds and cores (Mouschovias 1976a,b, Tomisaka, Ikeuchi, & Nakamura 1988a,b, 1989, 1990, Tomisaka 1991, See also Chapters 3 and 4).

We present a simple virial analysis of magnetized spheroidal molecular clouds in this section, highlighting some of the some of the important differences between filaments and spheroids. We first consider purely poloidal fields in Section 2.11.2, generalizing our results to include helical field configurations in Section 2.11.5.

2.11.1 A Virial Analysis of Magnetized Spheroidal Molecular Clouds

The scalar virial equation, including the magnetic field, is given by

$$2K + \mathcal{M} + W = 0, \tag{2.26}$$

where W is given by equation 2.5, and K is the total kinetic energy, including a surface term due to the external pressure:

$$K = (\langle P \rangle - P_S)V, \tag{2.27}$$

[16] However, the role of magnetic fields in stars was appreciated prior to this time (Schwarzchild 1949, See also references in Chandrasekhar and Fermi 1953b).

where V is the volume of the cloud. The magnetic energy term is quite complicated, containing both volume and surface contributions:

$$\mathcal{M} = \frac{1}{8\pi}\int_V B^2\, dV + \frac{1}{4\pi}\oint (\mathbf{r}\cdot\mathbf{B})(\mathbf{B}\cdot\mathbf{dS}) - \frac{1}{8\pi}\oint B^2\mathbf{r}\cdot\mathbf{dS}. \tag{2.28}$$

In general, we associate the surface S with the surface of the cloud, so that V is its volume. The magnetic energy can be divided into a component $\mathcal{M}_{pol}$ that is due to poloidal magnetic field and a component $\mathcal{M}_{\phi}$ that is due to the toroidal field. We first consider the effect of a purely poloidal field, leaving the discussion of the toroidal component to Section 2.11.5 below.

Spitzer (1978) shows that $\mathcal{M}_{pol}$ can be parameterized as

$$\mathcal{M}_{pol} = b\frac{B_{pol}^2 R^3}{3}, \tag{2.29}$$

where B_{pol} is the poloidal component of the magnetic field and b is a correction factor of order unity that takes into account the non-uniformity of the cloud and the field. It is most useful to express $\mathcal{M}_{pol}$ in terms of the magnetic flux $\Phi = \pi R^2 B_{pol}$ threading the cloud, since the usual assumption of flux-freezing ensures that Φ will be conserved in any radial contraction or expansion of the cloud:

$$\mathcal{M}_{pol} = \frac{b\Phi^2}{3\pi^2 R}. \tag{2.30}$$

2.11.2 Clouds Threaded by Purely Poloidal Fields

Magnetic Criticality

An obvious consequence of equations 2.5 and 2.29 is that the magnetic energy of the poloidal field has the same dependence on radius R as the gravitational energy, but is of opposite sign. Therefore, the overall effect of the magnetic field is to dilute gravity by a constant factor that is independent of the radius or density of the cloud (Mestel & Spitzer 1956). Equating the gravitational and magnetic terms (equations 2.5 and 2.29) of the virial theorem (equation 2.26), the magnetic critical mass is defined by

$$M_{\Phi} = \sqrt{\frac{5b}{9a}}\,\frac{\Phi}{\pi G^{1/2}}. \tag{2.31}$$

The ratio of the magnetic to gravitational energy can be re-expressed in terms of the magnetic critical mass:

$$\frac{\mathcal{M}}{|W|} = \frac{M_{\Phi}}{M}, \tag{2.32}$$

which has a constant value that does not change if the cloud expands or contracts. We note that he concept of magnetic criticality is less useful for filamentary clouds, where the gravitational energy does not scale in the same way as the magnetic energy ($\mathcal{W}$ only depends on the mass per unit length.).

Using equation 2.32, and with the help of equations 2.5 and 2.6, the virial theorem can be re-expressed in the following form:

$$3(\langle P \rangle - P_S)V - \frac{3}{5}a\frac{GM^2}{R}\left(1 - \frac{M_\Phi}{M}\right) = 0. \tag{2.33}$$

Therefore, clouds can be divided into two regimes. Magnetically subcritical clouds, with $M < M_\Phi$, cannot undergo gravitational collapse because the magnetic field alone is sufficient to support the gas against self-gravity. Supercritical clouds, on the other hand, must rely on a combination of magnetic and pressure support to maintain their equilibrium. A critical mass to flux ratio, obtained from equation 2.31 divides these two regimes:

$$\left(\frac{M}{\Phi}\right)_{crit} = 0.13\, G^{-1/2}, \tag{2.34}$$

where the coefficient b/a in equation 2.31 has been replaced by a numerical estimate obtained from detailed numerical calculations (Mouschovias 1976b, Mouschovias & Spitzer 1976)

The Bonnor-Ebert Instability

We rearrange the virial equation (equation 2.33) to give the external pressure as a function of the radius:

$$P_S = \mathcal{A}R^{-3} - \mathcal{B}R^{-4}, \tag{2.35}$$

where $\mathcal{A}$ and $\mathcal{B}$ are constants given by

$$\begin{aligned} \mathcal{A} &= \frac{3M\sigma^2}{4\pi} \\ \mathcal{B} &= \frac{3}{20\pi}aGM^2\left(1 - M_\Phi^2/M^2\right). \end{aligned} \tag{2.36}$$

The constant $\mathcal{A}$ is positive definite, but $\mathcal{B}$ may be either negative, for magnetically subcritical clouds, or positive for supercritical clouds. We observe for this latter case that the external pressure P_S has a maximum possible value for equilibrium.

Setting the derivative of equation 2.35 with respect to R equal to zero, we find that this maximum occurs when the cloud has radius

$$R = \frac{4\mathcal{B}}{3\mathcal{A}} = 0.267a\left(1 - \frac{M_\Phi^2}{M^2}\right)\frac{GM}{\sigma^2}, \tag{2.37}$$

which confirms that there is no maximum surface pressure when a cloud is magnetically sub-critical (ie.

$\mathcal{B} < 0$). The external pressure P_S is obtained by substituting this result into equation 2.35, for which we obtain

$$P_{S,crit} = \frac{27\mathcal{A}^4}{256\mathcal{B}^3} = 3.15\frac{\sigma^8}{a^3G^3M^2}\frac{1}{(1-M_\Phi^2/M^2)^3}. \tag{2.38}$$

It is easy to see that the critical pressure $P_{S,crit}$ tends to infinity as M approaches M_Φ from above. When $M < M_\Phi$, the outward pressure exerted by the frozen-in magnetic field overwhelms gravity, so that no amount of external pressure can result in gravitational collapse. $P_{S,crit}$ is the critical Bonnor-Ebert pressure for magnetized spheroidal clouds. The Bonnor-Ebert critical external pressure for non-magnetic clouds is recovered by equation 2.38 in the unmagnetized limit $M_\Phi = 0$:

$$P_{B.E.} = 3.15\frac{\sigma^8}{a^3G^3M^2}. \tag{2.39}$$

Equation 2.38 can also be thought of as establishing the upper mass limit M_{crit} for equilibrium, given an external pressure P_S. For unmagnetized clouds, the Bonnor-Ebert mass is obtained by solving equation 2.39 for the mass:

$$M_{B.E} = \frac{1.77}{a^{3/2}}\frac{\sigma^4}{G^{3/2}P_S^{1/2}}. \tag{2.40}$$

Exact calculations based on isothermal spheres give the coefficient $1.77/a^{3/2} = 1.18$ (Bonnor 1956). Equation 2.38 cannot be easily inverted to obtain M_{crit}. However, it can be combined with equation 2.39 to obtain

$$M_{crit} = c_1 M_{B.E}\left(1-\frac{M_\Phi^2}{M_{crit}^2}\right)^{-3/2}, \tag{2.41}$$

where c_1 is another numerical correction factor of order unity. [17]

It is useful to rearrange equation 2.41 to obtain a relation between $M_{crit}/M_{B.E}$ and $M_\Phi/M_{B.E}$:

$$\left(\frac{M_\Phi}{M_{B.E}}\right)^2 = \left(\frac{M_{crit}}{M_{B.E}}\right)^2 - c_1^3\left(\frac{M_{crit}}{M_{B.E}}\right)^{4/3}, \tag{2.42}$$

which we plot in Figure 2-9 below $c_1 = 1$. We observe that $M_{crit} = M_{B.E}$ when $M_\Phi = 0$, but becomes nearly equal to M_Φ when $M_\Phi \gg M_{B.E}$. This must be true, because the pressure support is negligible compared to the magnetic support in this limit.

An approximate solution to equation 2.41 has been suggested by McKee (1989):

$$M_{crit} \approx M_{B.E} + M_\Phi, \tag{2.43}$$

which is accurate to $\approx 5\%$ for $M \lesssim 8M_\Phi$ (McKee 1989). This approximate solution is particularly

[17] Tomisaka et al. (1988) find that $c_1 \approx 1.18$ from their numerical solutions.

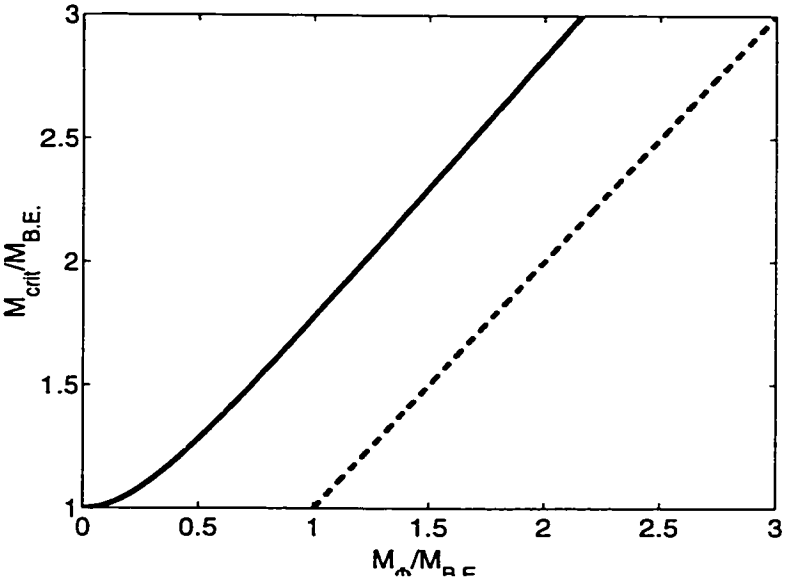

Figure 2-9: We show how the critical Bonnor-Ebert mass M_{crit} varies with the magnetic critical mass M_Φ (solid curve). The dashed curve shows the the critical mass ($= \mathcal{M}_\phi$) for a cloud supported entirely by the magnetic field.

enlightening because it shows how both the pressure and the magnetic field contribute to the overall support of the cloud.

Filaments are Bonnor-Ebert Stable

Filaments have remarkably different Bonnor-Ebert stability properties, compared to their spheroidal counterparts. We show in Chapter 3 that all filamentary clouds that are below a critical mass per unit length m_{vir} (see equation 2.21) are stable in the sense of Bonnor and Ebert. Thus, only the mass per unit length matters for filaments. If $m < m_{vir}$, no amount of squeezing can cause a filament to collapse radially to a spindle-like configuration.

2.11.3 Are Spheroidal Clouds Magnetically Super-Critical or Sub-Critical?

There is a very simple argument which suggests that most spheroidal molecular clouds are probably magnetically super-critical. As we discussed in Section 2.2, there are strong reasons to believe that the non-thermal motions observed in molecular clouds are magnetic in nature and that there is approximate equipartition between the kinetic and magnetic energy terms of the virial theorem. Therefore, we expect that $\mathcal{M} \approx 2\mathcal{K}$, so that $|\mathcal{W}| = 2\mathcal{M}$ by equation 2.26. [18] This result implies that molecular clouds are

[18]This follows from Myers and Goodman 1988b, whose K is the same as our $2\mathcal{K}$. Whether we equate we equate the magnetic energy with the kinetic energy $\mathcal{K}$ or the whole kinetic energy term from the virial theorem $2\mathcal{K}$ is of little

probably super-critical, with $M \approx 2M_\Phi$ by equation 2.32. McKee (1999) arrives at the same conclusion in the context of giant molecular clouds (GMCs), by a similar argument based on equation 2.43.

Physically, this result can be interpreted very simply. If molecular clouds were magnetically sub-critical, then we would require that $\langle P \rangle < P_S$ by equation 2.33, since self-gravity alone would not be sufficiently strong to contain the magnetic field. Gravitational fragmentation and star formation would not likely occur in such a cloud, since the combined effects of gravity and the magnetic field would be globally expansive. Therefore, clouds that are actively forming stars are not likely to be magnetically sub-critical. Also, the velocity dispersion of the gas within a sub-critical cloud would probably be well below the the observed values. A simple example illustrates this point. The external pressure exerted on molecular clouds by their HI envelopes is about $\sim 10^{4.5}\ K\ cm^{-3}$ (see Section 2.6.2). If we assume a mean internal density of $10^3\ cm^{-3}$, which is typical of a dark cloud (see Chapter 3), then the velocity dispersion within the cloud would have to be less than $\sim 0.33\ km\ s^{-1}$, which is barely above the thermal value ($\sim 0.23\ km\ s^{-1}$ for $15\ K$), and certainly well below observed velocity dispersions for dark clouds.

It is not obvious how this argument can be extended to filamentary clouds threaded by helical fields, where the toroidal field component provides a negative contribution to the magnetic energy term in the virial theorem (see Section 2.11.5). Also, this might not be useful, since the concept of magnetic criticality is less useful for filaments than for spheroids.

2.11.4 Larson's Laws for Molecular Clouds

Larson (1981) observationally discovered the following important relations for molecular clouds: [19]

$$\sigma = 1.43 \left(\frac{R}{pc}\right)^{0.38} km\ s^{-1} \tag{2.44}$$

$$\langle n(H_2) \rangle = 6800 \left(\frac{R}{pc}\right)^{-1.10} cm^{-3}. \tag{2.45}$$

The first of these relations is Larson's line width-size relation for molecular clouds, and the second relates the average density $\langle n(H_2) \rangle$ to the radius. These two relations can be combined to obtain

$$\langle N \rangle = 6.5 \times 10^{21} \left(\frac{R}{pc}\right)^{-0.1} cm^{-2}, \tag{2.46}$$

where $\langle N \rangle$ is the average surface density of a molecular cloud. Therefore, observations reveal that molecular clouds have nearly constant average surface densities.

---

consequence to the argument, since the former choice gives the result $M \approx 3M_\Phi$, in agreement with our conclusion that most molecular clouds are supercritical.

[19] We have slightly manipulated Larson's equations 1 and 5 to write them in terms of R instead of length $L = 2R$.

As we discussed in Section 2.5.5, simulations of MHD turbulence are in agreement with equation 2.44), but not equation 2.45. We now present a very different viewpoint by showing that Larson's laws can be explained by the virial theorem in spheroidal clouds if they are near their Bonnor-Ebert critical states, as given by equation 2.41. This was first demonstrated for non-magnetized clouds by Chièze (1987). *However, we show in Chapter 3 that the assumption that all clouds are near criticality is not required to explain Larson's laws if clouds are inherently filamentary.* Therefore, Larson's laws are obtained under less restrictive circumstances for filaments than for spheres.

If molecular clouds are near their Bonnor-Ebert critical states with $M \approx M_{crit}$, then equations 2.37 and 2.40 can be combined to give an expression for their radii:

$$R_{crit} = \frac{0.473 c_1}{a^{1/2}} \sqrt{\frac{(1 - M_\Phi^2/M^2)}{G P_S}} \sigma^2, \tag{2.47}$$

which can be re-arranged to give

$$\sigma \approx 0.64 \frac{a^{1/4}}{c_1^{1/2}} \left(\frac{P_S/k}{10^{4.5}\ K\ cm^{-3}} \right)^{1/4} \left(\frac{R}{pc} \right)^{1/2}, \tag{2.48}$$

where k is Boltzmann's constant and we have assumed that $M \approx 2M_\Phi$ (see Section 2.11.3). This is quite similar to Larson's first law, provided that the surface pressure exerted by the ISM does not vary greatly between clouds.

The second of Larson's laws can be obtained in a straightforward manner by calculating the average surface density of a critical cloud defined by $\Sigma_{crit} \equiv M_{crit}/\pi R_{crit}^2$, where M_{crit} and R_{crit} are given by equations 2.41 and 2.47 respectively. We find that

$$\Sigma_{crit} = \frac{2.52}{c_1\ a^{1/2}} \sqrt{\frac{P_S}{G(1 - M_\Phi^2/M^2)}}. \tag{2.49}$$

This can be re-written in terms of $\langle N \rangle$ to give a relation that is in good agreement with equation 2.46:

$$\langle N \rangle \approx \frac{6.0 \times 10^{21}}{c_1\ a^{1/2}} \left(\frac{P_S/k}{10^{4.5}\ K\ cm^{-3}} \right)^{1/2}, \tag{2.50}$$

where we have again assumed that $M \approx 2M_\Phi$ (Section 2.11.3). It is interesting that Larson's second law predicts that $A_v \approx 3\ mag$ for strongly self-gravitating clouds, assuming that $A_v \approx N/2 \times 10^{21}\ cm^{-2}$ (Spitzer 1978). This is the reason why such clouds generally appear dark on optical plates.

2.11.5 Spheroidal Clouds Threaded by Both Poloidal and Toroidal Fields

We now generalize the discussion of Section 2.11.2 to include the toroidal component of the magnetic field, so that the field lines are helical in general. The simple model that we present in this section parallels our discussion of helically magnetized filamentary clouds in Chapter 3 and prolate cores in Chapter 6.

We require a simple model of the toroidal field so that we can evaluate the integrals in equation 2.28. Consider a thin toroidal flux tube of radius R and cross-sectional area δA (see illustration in Figure 2 of Chapter 3). The mass contained within the flux tube and the toroidal flux threading it are respectively given by

$$\begin{aligned} \delta M &= 2\pi r \rho \delta A \\ \delta \Phi_\phi &= B_\phi \delta A. \end{aligned} \tag{2.51}$$

The toroidal flux to mass ratio (per radian) is therefore given by

$$\Gamma_\phi = \frac{B_\phi}{r\rho}. \tag{2.52}$$

The simplest model for the mass loading of toroidal field lines is obtained by setting $\Gamma_\phi = const.$ This is, in fact, the choice that we make in Chapter 3 to build our models of filamentary molecular clouds, and is the basis for the prolate core models that we construct in Chapter 6.

The magnetic energy associated with the toroidal field is obtained by straightforward evaluation of the integrals in equation 2.28:

$$\mathcal{M}_\phi = -\frac{3}{20\pi^2} d \frac{\Gamma_\phi^2 M^2}{R}, \tag{2.53}$$

where d is another correction factor of order unity. Unlike the poloidal field, the total energy associated with the toroidal field is negative. Therefore, toroidal fields are unlike poloidal fields in that their global effect is to squeeze the gas rather than offer support against self-gravity.

It is most useful to work in terms of the poloidal current associated with the toroidal field. The total current through a cloud is a conserved quantity if we assume that a cloud contracts or expands without dissipation. (We discuss this further in Chapter 6.) By Ampère's law, the toroidal field at the edge of a spherical cloud is related to the total current flowing through the cloud by

$$B_{\phi,S} = \frac{2}{c} \frac{I}{R}. \tag{2.54}$$

Using the definition of Γ_ϕ (equation 2.52), the magnetic energy of the toroidal field (equation 2.53)

becomes

$$\mathcal{M}_\phi = -\frac{16}{15} d \left(\frac{I}{c}\right)^2 R. \tag{2.55}$$

In a recent review, McKee (1999) presented a similar formula in a discussion of the role of the toroidal field in giant molecular clouds (GMCs). He points out that the toroidal field cannot become too large compared with the poloidal field without triggering MHD instabilities. For cylindrical geometries, axisymmetric "sausage" modes are suppressed whenever $B_z > B_{\phi,S}^2/2$, where $B_{\phi,S}$ is the toroidal field at the radial surface of the magnetized plasma (Jackson 1975). Likewise, "kink" modes are stabilized by B_z, so that there is no instability with wavelengths shorter than $\sim 14\ R$, whenever $B_z \approx B_{\phi,S}$. Therefore, stable models should not include toroidal fields that are much stronger than the poloidal field.

By including $\mathcal{M}_\phi$ in the virial equation (equation 2.26), the external pressure is given by

$$P_S = \mathcal{A} R^{-3} - \mathcal{B} R^{-4} - \mathcal{C} R^{-2} \tag{2.56}$$

where $\mathcal{A}$ and $\mathcal{B}$ are as given in equation 2.35 above, and

$$\mathcal{C} = \frac{4}{15\pi} d \left(\frac{I}{c}\right)^2. \tag{2.57}$$

The analysis is substantially simplified if we make the assumption that the correction to equation 2.56 due to the toroidal field is small compared to the other terms. Accordingly, we will work only to first order in $\mathcal{C}$ for the remainder of the analysis.

Differentiating equation 2.56, we find the following quadratic equation for the radius at which the maximum external pressure allowed for equilibrium is obtained:

$$2\mathcal{C} R^2 - 3\mathcal{A} R + 4\mathcal{B} = 0. \tag{2.58}$$

Only one root of this equation leads to a maximum of the pressure. To first order in $\mathcal{C}$, this root is given by

$$R \approx \frac{4\mathcal{B}}{3\mathcal{A}} + \frac{32\mathcal{C}\mathcal{B}^2}{27\mathcal{A}^3}. \tag{2.59}$$

Substituting this into equation 2.56, the critical external pressure (correct to first order in $\mathcal{C}$), is given by

$$P_{S,crit} = P_{S,crit}^{pol} - \frac{8d}{15} P_{\phi,S}, \tag{2.60}$$

where $P_{S,crit}^{pol}$ is the critical pressure with only a poloidal field (equation 2.38), and $P_{\phi,S} = B_{\phi,S}^2/8\pi$ is the

magnetic surface pressure exerted inward on the cloud by the toroidal field $B_{\phi,S}$ at radius R. We have also replaced $\mathcal{A}$, $\mathcal{B}$, and $\mathcal{C}$ by their definitions (equations 2.36 and 2.57). The interpretation of equation 2.60 is straightforward. The toroidal field squeezes the cloud, decreasing the external pressure required for criticality.

The toroidal field also reduces the critical Bonnor-Ebert mass of the core. The critical mass is given by the solution to an equation analogous to equation 2.41, which included only the poloidal field:

$$M_{crit} = \frac{c_1}{\sqrt{1+\frac{8d}{15}P_{\phi,S}}} M_{B.E} \left(1+\frac{M_\Phi^2}{M_{crit}^2}\right)^{-3/2} . \tag{2.61}$$

We note that Habe et al. (1991) also found a reduction of the critical mass, using a formulation based on the Gibb's free energy of a magnetized molecular cloud. This reduction of the critical mass was also noted by Tomisaka (1991).

The general behaviour of the toroidal field in this example carries over to our analysis of helically magnetized filamentary clouds in Chapter 3. There, we show that the toroidal field behaves like a surface pressure that squeezes in on filamentary clouds. (See Jackson 1975, equation 10.46 for an example from plasma physics.) This "pinch" of the toroidal field is an integral part of our models of filamentary clouds and prolate cores. We turn, finally, to a detailed, observationally constrained study of filamentary clouds and their stability to fragmentation in the next two chapters.

Chapter 3

Helical Fields and Filamentary Molecular Clouds

This chapter is a preprint of the paper "Helical Fields and Filamentary Molecular Clouds II - Axisymmetric Stability and Fragmentation" by Fiege J.D. and Pudritz R.E., which has been accepted for publication by the Monthly Notices of the Royal Astronomical Society.

Abstract

We study the equilibrium of pressure truncated, filamentary molecular clouds that are threaded by rather general helical magnetic fields. We first apply the virial theorem to filamentary molecular clouds, including the effects of non-thermal motions and the turbulent pressure of the surrounding ISM. When compared with the data, we find that many filamentary clouds have a mass per unit length that is significantly reduced by the effects of external pressure, and that toroidal fields play a significant role in squeezing such clouds.

We also develop exact numerical MHD models of filamentary molecular clouds with more general helical field configurations than have previously been considered. We examine the effects of the equation of state by comparing "isothermal" filaments, with constant total (thermal plus turbulent) velocity dispersion, with equilibria constructed using a logatropic equation of state.

Our theoretical models involve 3 parameters; two to describe the mass loading of the toroidal and poloidal fields, and a third that describes the radial concentration of the filament. We thoroughly explore our parameter space to determine which choices of parameters result in models that agree with the available observational constraints. We find that both equations of state result in equilibria that agree with the observational results. Moreover, we find that models with helical fields have more realistic density profiles than either unmagnetized models or those with purely poloidal fields; we find that most isothermal models have density distributions that fall off as $r^{-1.8}$ to r^{-2}, while logatropes have density profiles that range from r^{-1} to $r^{-1.8}$. We find that purely poloidal fields produce filaments with steep radial density gradients that are not allowed by the observations.

3.1 Introduction

Observations have revealed that most molecular clouds are filamentary structures that are supported by non-thermal, small-scale MHD motions of some kind, as well as large scale ordered magnetic fields (cf. Schleuning 1998). Nevertheless, virtually all theoretical models assume spheroidal geometry. While spheroidal models are a reasonable geometry for molecular cloud cores, these models cannot adequately describe molecular clouds on larger scales. The goal of this paper is to develop a theory for filamentary molecular clouds including the effects of ordered magnetic fields. It is our intent that this work should elevate filamentary clouds to the same level of understanding as that enjoyed by their spheroidal counterparts (cf. reviews McKee et al. 1993, Heiles et al. 1993). This is an important step in star formation theory because filamentary molecular clouds ultimately provide the initial conditions for star formation. A clear understanding of the initial conditions is necessary if we are to understand the processes by which clouds produce their star-forming cores.

Ostriker (1964) investigated the equilibrium of unmagnetized isothermal filaments; he found that the density varies as $\sim r^{-4}$ in the outer regions. However, this solution is much too steep to account for the observed density profiles in molecular clouds. For example, Alves et al. (1998, hereafter A98) and Lada, Alves, and Lada (1998, hereafter LAL98) use extinction measurements of background starlight in the near infra-red to find r^{-2} density profiles for the filamentary clouds L977 and IC 5146. Johnstone and Bally (1999) have also deduced an an r^{-2} density profile for the integral-shaped filament of Orion A, based on observations in the sub-millimetre continuum.

Most theoretical models for self-gravitating filaments have featured magnetic fields that are aligned with the major axis of the filaments. The pioneering work by Chandrasekhar and Fermi (1953) was the first to analyse the stability of magnetized incompressible filaments with longitudinal magnetic fields. Stodólkiewicz (1963) developed a class of isothermal models in which the ratio of the gas to magnetic pressure (β) is constant. The magnetic field in these models simply re-scales the Ostriker (1964) solution; thus, the steep r^{-4} density profile is preserved. The structure of the Ostriker solution is unchanged by the addition of a uniform poloidal magnetic field. The stability of such models, including the effects of pressure truncation, has subsequently been determined by Nagasawa (1987). Gehman, Adams, & Watkins (1996) have considered the effects of a logatropic equation of state (EOS) on the equilibrium and stability of filamentary clouds threaded by a uniform poloidal field. Unfortunately, these models possess infinite mass per unit length as a result.

Observations suggest that some molecular clouds may be wrapped by helical fields (Bally et al. 1989; Heiles 1987). There is also some observational evidence for helical fields in HI filaments towards the Galactic high latitude clouds (Gomez de Castro, Pudritz, & Bastien 1997). In fact, helical fields represent the most general magnetic field configuration allowed if cylindrical symmetry is assumed. A

few authors have previously modeled filamentary clouds with helical fields. These models are similar to the Stodólkiewicz (1963) solution in that the magnetic pressure is proportional to the gas pressure, so that the density becomes a re-scaling of the Ostriker (1964) solution.

Our analysis replaces the assumption of constant β with the assumption of constant flux to mass loading for the poloidal (eg. Mouschovias 1976, Spitzer 1978, Tomisaka, Ikeuchi, and Nakamura 1988) and toroidal fields. We show that the magnetic field in this case has non-trivial effects on the density distribution, and in fact results in much better agreement with the available data. We also explore the role of the EOS by constructing models using both an "isothermal" EOS, where the total (thermal plus non-thermal) velocity dispersion is assumed constant, and the pure logatrope of McLaughlin and Pudritz (1996, hereafter MP96). The effects of pressure truncation play an important role in our analysis. By including a realistic range of external pressures, appropriate for the ISM, we show that the mass per unit length of our models is significantly decreased from the untruncated value. We also apply the virial theorem to truncated filamentary equilibria threaded by helical fields. We use this equation to compare our models with real filamentary clouds and to establish strong constraints on their allowed magnetic configurations.

How would helical fields arise? All that is required is to twist one end of a filament containing a poloidal field, with respect to the other end. Even if molecular filaments form with an initially axial magnetic field, a helical field is plausibly generated by any kind of shear motion (such as subsequent oblique shocks, torsional Alfvén waves, etc.) that twists the field lines.

It is not the purpose of this paper to examine how helical fields could be generated. The main point of this work is that, having recognized that most molecular clouds are undoubtedly filamentary, magnetized, and truncated by an external pressure, it is of considerable importance to investigate equilibrium models of molecular clouds that contain quite general helical fields and pressure truncation. We employ two main approaches in our theoretical analysis. First, we derive a general virial equation appropriate for pressure-truncated filamentary molecular clouds, which we use to understand the roles of gravity, pressure, and the magnetic field in the overall quasi-equilibrium of filamentary clouds. Second, we develop numerical magnetohydrostatic equilibrium models that can be compared with the internal structure of real clouds.

Our virial analysis demonstrates that poloidal fields always help to support the gas against self-gravity, while toroidal fields squeeze the gas by the "hoop stress" of their curved field lines. Helical fields may either support or help to confine the gas, depending on whether the poloidal or toroidal field component is dominant. We show, in fact, that it is very difficult to understand observed clouds without the notion of helical fields and the confining hoop stresses that they exert upon their molecular gas.

Having found evidence for helical fields from our virial analysis, we construct numerical magnetohydrostatic models of filamentary clouds in order to investigate the internal structure of models that are

allowed by the data. It is noteworthy that our isothermal models with helical magnetic fields always produce density profiles that fall off as $r^{-1.8}$ to r^{-2}, in excellent agreement with the data. We show that the toroidal field component is responsible for the more realistic behaviour, and that purely poloidal fields result in density profiles that fall even more rapidly than r^{-4} in our model. We also consider the pure logatrope of McLaughlin and Pudritz (1996) as a possible effective EOS for the gas. We find that our logatropic models have somewhat shallower density profiles, but many are also in good agreement with the existing data.

A brief outline of our paper is as follows. We first present the results of virial analysis of self-gravitating, pressure truncated, filamentary clouds containing both poloidal and toroidal field (Section 3.2). In Section 3.3, we follow this up with a detailed analysis of the equations of magnetohydrostatic equilibrium describing self-gravitating filaments and discuss important analytic solutions to these. A full numerical treatment of the equations is given in Section 3.4 where we also constrain our 3-parameter models with a wide variety of filamentary cloud data. We discuss these results in Section 3.5 and summarize in Section 3.6.

3.2 Virial Analysis of Filamentary Molecular Clouds

In Appendix A, we use the scalar virial theorem to construct a virial equation appropriate for pressure truncated filamentary clouds containing arbitrary helical fields. After carrying out the manipulations therein, we obtain

$$0 = 2\int P d\mathcal{V} - 2P_S\mathcal{V} + \mathcal{W} + \mathcal{M}, \tag{3.1}$$

where the gravitational energy per unit length is given by

$$\mathcal{W} = -\int \rho r \frac{\partial \Phi}{\partial r} d\mathcal{V}. \tag{3.2}$$

and $\mathcal{M}$ is the sum of all magnetic terms (including surface terms):

$$\mathcal{M} = \frac{1}{4\pi}\int B_z^2 d\mathcal{V} - \left(\frac{B_{zS}^2 + B_{\phi S}^2}{4\pi}\right)\mathcal{V}. \tag{3.3}$$

This equation is appropriate for a non-rotating, self-gravitating, filamentary molecular cloud whose length greatly exceeds its radius. For the remainder of this paper, all quantities written with a subscript S are to be evaluated at the surface of the filament; thus we write that our filament is truncated by an external pressure P_S at radius R_S. We further reserve calligraphic symbols for quantities evaluated per unit length; $\mathcal{W}$ is the gravitational energy per unit length since there are no external gravitational

fields and $\mathcal{V}$ is actually the volume per unit length, or cross-sectional area $\pi {R_S}^2$, of the filament. As we shall now show, $\mathcal{W}$ can be evaluated exactly for a filament of arbitrary internal structure and equation of state. The mass per unit length m of the filament is obtained by simply integrating the density over the cross-sectional area:

$$m = 2\pi \int r\rho(r) dr. \tag{3.4}$$

Poisson's equation in cylindrical coordinates takes the form

$$\frac{1}{r}\frac{d}{dr}\left(r\frac{d\Phi}{dr}\right) = 4\pi G\rho. \tag{3.5}$$

By integrating, we find that the mass per unit length interior to radius r can be written as

$$m(r) = \frac{1}{2G} r \left.\frac{d\Phi}{dr}\right|_r. \tag{3.6}$$

Using this result in equation 3.2, the gravitational energy per unit length can be transformed into an integral over the mass per unit length:

$$\mathcal{W} = -2G \int_0^m m' dm' = -m^2 G. \tag{3.7}$$

It is remarkable that the gravitational energy per unit length takes on the same value regardless of the equation of state, magnetic field, or internal structure of the cloud. The only requirements are those of virial equilibrium and cylindrical geometry. McCrea (1957) gave an approximate formula for the gravitational energy per unit length as $\mathcal{W} = -am^2 G$ (where a is a constant of order unity) based on dimensional considerations; thus, our exact result gives $a = 1$ for all cylindrical mass distributions.

By considering a long filament of finite mass M and length L, we find that the gravitational energy scales quite differently for filaments and spheroids:

$$\begin{aligned} W_{cyl} &= -\frac{GM^2}{L} \\ W_{sphere} &= -\frac{3}{5}a\frac{GM^2}{R}, \end{aligned} \tag{3.8}$$

where a depends on the detailed shape and internal structure for spheroids. It is of fundamental importance that the gravitational energy scales with radius for spheroids, but not for filaments. McCrea (1957) used this point to argue that filaments possess stability properties quite contrary to those of spheroidal equilibria. For spheroids, which best describe molecular cloud cores, the gravitational energy scales as $\sim R^{-1}$. As long as the core is magnetically subcritical, there always exists a critical external pressure

beyond which the gravitational energy must dominate over the pressure support. The equilibrium is unstable to gravitational collapse past this critical external pressure. On the other hand, the gravitational energy of a filament is unaffected by a change in radius. Thus, the gravitational energy remains constant during any radial contraction caused by increased external pressure. If the filament is initially in equilibrium, gravity can never be made to dominate by squeezing the filament; all hydrodynamic filaments initially in equilibrium are stable in the sense of Bonnor (1956) and Ebert (1955).

In Appendix B, we consider the Bonnor-Ebert stability of magnetized filaments. Beginning with a discussion of uniform filaments, we show that a uniform filamentary cloud with a helical field, that is initially in a state of equilibrium, cannot be made to collapse radially by increasing the external pressure. We also give a more general proof which extends the argument to non-uniform filaments of arbitrary EOS. Thus, we conclude that all filamentary clouds, that are initially in a state of equilibrium, are stable against radial perturbations.

The virial theorem for filaments (equation 3.1) is best used to study the global properties of filamentary molecular clouds. It is useful to define the average density, pressure, and magnetic pressure within the cloud as

$$\begin{aligned} \langle \rho \rangle &= \frac{m}{\mathcal{V}} \\ \langle P \rangle &= \frac{\int_{\mathcal{V}} P d\mathcal{V}}{\mathcal{V}} \\ \langle P_{mag} \rangle &= \frac{1}{8\pi \mathcal{V}} \int_{\mathcal{V}} B_z^2 d\mathcal{V}. \end{aligned} \tag{3.9}$$

Quite generally, we may write the effective pressure inside a molecular cloud as $P = \sigma^2 \rho$, where σ is the total velocity dispersion. We emphasize that all of our models take σ to represent the total velocity dispersion, including both thermal and non-thermal components. It is particularly important to note that when we describe an equation of state as "isothermal", we really mean that the total velocity dispersion is constant. The average squared velocity dispersion is defined simply as

$$\langle \sigma^2 \rangle = \frac{\langle P \rangle}{\langle \rho \rangle} = \frac{\int_{\mathcal{V}} \sigma^2 \rho d\mathcal{V}}{\int_{\mathcal{V}} \rho d\mathcal{V}}, \tag{3.10}$$

where the average has been weighted by the mass as in MP96.

With the above definitions, we easily derive a useful form of our virial equation (equation 3.1):

$$\frac{P_S}{\langle P \rangle} = 1 - \frac{m}{m_{vir}} \left(1 - \frac{\mathcal{M}}{|\mathcal{W}|} \right), \tag{3.11}$$

where $\mathcal{M}$ and $\mathcal{W}$ are the total magnetic and kinetic energies per unit length defined in equations 3.2

and 3.3, and m_{vir} is the virial mass per unit length defined by

$$m_{vir} = \frac{2\langle\sigma^2\rangle}{G}. \tag{3.12}$$

We note that m_{vir} is analogous to the the virial mass

$$M_{vir} = \frac{5R\langle\sigma^2\rangle}{G} \tag{3.13}$$

normally defined for spheroidal equilibria. Using the definition of the average magnetic pressure given in equation 3.9, we may write the total magnetic energy per unit length as

$$\mathcal{M} = 2\left(\langle P_{mag}\rangle - P_{mag,S}\right)\mathcal{V}. \tag{3.14}$$

Using this result, along with the expression for the gravitational energy per unit length (equation 3.7) in equation 3.11, we obtain another useful form of the virial equation after some algebraic manipulations:

$$\frac{P_S}{\langle P\rangle} = 1 - \frac{m}{m_{vir}} + \left(\frac{\langle P_{mag}\rangle - P_{mag,S}}{\langle P\rangle}\right), \tag{3.15}$$

where $P_{mag,S}$ is the total magnetic pressure evaluated at the surface of the cloud:

$$P_{mag,S} = \frac{B_{zS}^2 + B_{\phi S}^2}{8\pi}. \tag{3.16}$$

Equation 3.15 makes two important points. First of all, the poloidal component of the magnetic field contributes to the magnetic pressure support of the cloud through $\langle P_{mag}\rangle$. Secondly, the toroidal field enters into equation 3.15 only as a surface term, through $P_{mag,S}$, regardless of the internal distribution of B_ϕ throughout the filament. This "pinch effect" is well known in toroidal field confined plasma, where the mean internal pressure is determined only by the toroidal field at the surface of the plasma (See Jackson equation 10.45 and following discussion.).

All magnetic fields, whether poloidal, toroidal, or of a more complex geometry, are associated with currents that flow within molecular clouds and the surrounding ISM. For a filamentary cloud wrapped by a helical field, the toroidal field component implies the existence of a poloidal current that flows along the filament. A natural question is whether a return current outside of the filamentary cloud completes the "circuit", or whether the poloidal current connects to larger scale structures in the ISM. The answer to this question will likely depend on the mechanisms by which filaments form, which might be addressed by future analysis. If the current returns as a thin current sheet flowing along the surface of the filament, the toroidal field at the surface would be nullified, and so would its confining effects. As we show in

Section 3.2.4, this would make the available data very difficult to understand, indeed. However, in the more general case that the return current is diffuse and extended throughout the surrounding gas, as in the case of protostellar jets (Ouyed & Pudritz 1997), there would be a net magnetic confinement of the filament.

In Appendix C, we derive the virial relations for filamentary molecular clouds analogous to the well known relations for spheroidal clouds (Chièze 1987; Elmegreen 1989; MP96). We show that the two geometries result in differences only in factors of order unity. Most importantly, we use our virial equation 3.1 to show that Larson's laws (1981) are also expected for magnetized filamentary clouds of arbitrary EOS. The reader may consult Table C.1 to compare expressions for m, R, $\langle\rho\rangle$, and Σ for spheroidal and filamentary clouds.

3.2.1 Unmagnetized Filaments

From equation 3.11, we see that unmagnetized clouds obey the following linear relation:

$$\frac{P_S}{\langle P\rangle} = 1 - \frac{m}{m_{vir}}. \tag{3.17}$$

This equation is exact for any unmagnetized filamentary cloud in virial equilibrium regardless of the underlying equation of state or details of the internal structure. Since equation 3.17 contains only quantities that are observable, we have derived an important diagnostic tool for determining whether or not filamentary clouds contain dynamically important ordered magnetic fields.

We can use equation 3.17 to obtain the critical mass per unit length m_h for unmagnetized filamentary clouds. Consider gradually adding mass to a self-gravitating hydrostatic filament. As the mass per unit length increases, the compression due to self-gravity drives the filament to ever increasing internal pressures, while the external pressure remains constant. This process continues until the cloud is so highly compressed that $P_S/\langle P\rangle \to 0$, beyond which no physical solution to equation 3.17 exists. By equation 3.17, this happens when $m = m_{vir}$; thus, the virial mass per unit length plays the role of the critical mass per unit length m_h for unmagnetized filamentary clouds.

For a prescribed EOS, this procedure leads to an unambiguous determination of the value of m_h. Depending on the EOS, the mass per unit length either approaches m_h asymptotically as $P_S/\langle P\rangle \to 0$, or achieves m_h at some finite radius where P_S vanishes.

There is, however, one subtle point that needs to be made. For an isothermal equation of state, we can unambiguously write that $m_h = m_{vir}$. However, the velocity dispersion varies with density for non-isothermal equations of state. Thus, $\langle\sigma^2\rangle$ and hence m_{vir} (by equation 3.12) may vary as the cloud is compressed by self-gravity. The critical mass per unit length m_h is the final value that m_{vir} takes

before radial collapse ensues, while m_{vir} is a quantity that applies equally well to non-critical states.

3.2.2 Magnetized Filaments

When there is a magnetic field present in a filamentary molecular cloud, the critical mass per unit length m_{mag} is significantly modified from the result obtained for unmagnetized clouds in the previous Section. Using the same argument as presented above, a magnetized cloud achieves its critical configuration when $P_S/\langle P\rangle \rightarrow 0$:

$$m_{mag} = \frac{m_{vir}}{1 - \mathcal{M}/|\mathcal{W}|} \tag{3.18}$$

where $\mathcal{M}$ and $\mathcal{W}$ are the total magnetic and gravitational energies per unit length given by equations 3.14 and 3.7. We recall that $\mathcal{M}$ may be either positive or negative, depending on whether the poloidal or the toroidal field dominates the overall magnetic energy. In general, we find that poloidal fields increase the critical mass per unit length beyond m_h for hydrostatic filaments, while toroidal fields reduce the critical mass per unit length below m_h. Physically, the reason for this behaviour is that the poloidal field helps to support the cloud radially against self-gravity, thus allowing greater masses per unit length to be supported. The opposite is true for the toroidal field component, which works with gravity in squeezing the cloud radially.

We may constrain the critical mass per unit length for a filamentary cloud if we have additional information regarding the strengths of the poloidal and toroidal field components. For a nearly isothermal EOS, the magnetic critical mass per unit length is given by

$$m_{mag} \approx m_h \left\{ 1 + \left[\frac{\langle P_{mag}\rangle - P_{mag,S}}{\langle P\rangle} \right] \right\}. \tag{3.19}$$

Since molecular clouds are in approximate equipartition between their magnetic and kinetic energies (Myers and Goodman 1988a,b, Bertoldi and McKee 1992), $\langle P_{mag}\rangle$ is not likely to exceed $\langle P\rangle$ greatly. Therefore, it is unlikely that the magnetic critical mass per unit length m_{mag} would exceed the hydrostatic critical mass per unit length m_h by more than a factor of order unity.

3.2.3 Surface Pressures on Molecular Filaments

Molecular clouds are surrounded by the atomic gas of the interstellar medium (ISM). Like the molecular gas itself, the total pressure of the ISM is dominated by non-thermal motions. The external pressure is extremely important to our analysis since it both truncates molecular clouds at finite radius and helps to confine the clouds against their own internal pressures (see equation 3.11). Boulares and Cox (1990) have estimated the total pressure (with thermal plus turbulent contributions) of the interstellar medium

to be on the order of $10^4\ K\ cm^{-3}$. However, some molecular clouds are associated with HI complexes, whose pressures are typically an order of magnitude higher than the general ISM (Chromey, Elmegreen, & Elmegreen 1989). Therefore, we will be absolutely conservative by assuming that the external pressure on molecular clouds is in the range of $10^{4-5}\ K\ cm^{-3}$. This assumption almost certainly brackets the real pressure exerted on molecular clouds by imposing the total (thermal plus turbulent) pressure of the ISM as a lower bound, and the pressure of large HI complexes as the upper bound.

While the above pressure estimate is appropriate for most filamentary clouds, which are truncated directly by the pressure of the surrounding atomic gas, we note that a second type of filament exists, in which a dense molecular filament is deeply embedded in a molecular cloud of irregular or spheroidal geometry. The best example of this type of filament is the $\int$-shaped filament in the Orion A cloud. In such cases, the external pressure must be estimated using the density and velocity dispersion of the surrounding molecular gas.

3.2.4 Comparison With Observations

We have seen that the magnetic field affects the global properties of filaments only through the dimensionless virial parameter $\mathcal{M}/|\mathcal{W}|$. The virial quantity $\mathcal{M}/|\mathcal{W}|$ provides a very convenient index of whether a cloud is poloidally or toroidally dominated and to what degree. For clouds with positive $\mathcal{M}/|\mathcal{W}|$, the net effect of the magnetic field is to provide support and the field is poloidally dominated (cf. equation 3.11). When $\mathcal{M}/|\mathcal{W}|$ is negative, the net effect of the field is confinement by the pinch of the toroidal field, and the field is toroidally dominated. Since $\mathcal{M}$ is directly compared to the gravitational energy $|\mathcal{W}|$, the magnitude of our virial parameter provides an immediate indication of the importance of the ordered field to the dynamics of the cloud. In Figure 3-1, we have used equation 3.11 to draw contours of constant $\mathcal{M}/|\mathcal{W}|$ as a function of m/m_{vir} and $P_S/\langle P\rangle$. The $\mathcal{M}/|\mathcal{W}| = 0$ (dotted) line represents all helical field configurations, including the unmagnetized special case, which have a neutral effect on the global structure of the cloud. Thus, we see that the diagram is divided into poloidally dominated (dashed lines) and toroidally dominated (solid lines) regions.

Since both m/m_{vir} and $P_S/\langle P\rangle$ are observable quantities, we can constrain our models by locating individual filamentary clouds on this diagram. However, we must first compute m/m_{vir} and $P_S/\langle P\rangle$ for each cloud by the following steps. For each filament, we have found values for the mass, length, radius, and average linewidth from molecular line observations in the literature (see Table 3.1 for references). The mass per unit length m is obtained by dividing the mass of the filament by its length allowing for inclination effects by conservatively assuming all filaments to be oriented within 45° of the plane of the sky. Since the emitting molecule (usually ^{12}CO or ^{13}CO) is always much more massive than the the average molecule in molecular gas, the observed linewidth must be corrected by applying Fuller and

Cloud	Region	M ($M_\odot$)	L (pc)	R_S (pc)	σ (kms^{-1})	Ref.	Notes
L1709	Rho Oph	140	3.6	0.23	0.479	2	1
L1755		171	6.3	0.152	0.526	2	1
L1712-29		219	4.5	0.156	0.534	2	1
DL 2 [a]	Taurus	600	6.4	0.5	1.08	4	4
$\int$-fil. [b]	Orion	5×10^3	13	0.25	1.41	1	2,3
		–	–	0.35	1.13	5	
NF [c]		1.55×10^4	87.3	2.25	1.54	3	1
SF [d]		3.65×10^4	300	2.25	1.29	3	1

[a] Dark lane in Taurus including B18. See Mizuno et al (1995) for a more detailed map.
[b] The $\int$-shaped filament in Orion A.
[c] Northern filament in Orion (See reference).
[d] Southern filament in Orion (See reference).

Table 3.1: We have compiled data on filamentary molecular clouds from several sources. **References:** 1. Bally et al. (1987), 2. Loren (1989), 3. Maddalena (1986), 4. Murphy and Myers (1985), 5. Tatematsu et al. (1993) **Notes:** 1. Little star formation. 2. Dense cores, star formation. 3. Deeply embedded in Orion A cloud. 4. Associated stars.

Myer's (1992) formula:

$$\Delta v_{tot}^2 = \Delta v_{obs}^2 + 8\ln(2)kT\left(\frac{1}{\overline{m}} - \frac{1}{m_{obs}}\right), \tag{3.20}$$

where m_{obs} is the mass of the emitting species, $\overline{m}$ is the mean mass of molecular gas, and T is the kinetic temperature of the gas. For a normal helium abundance $Y = 0.28$, $\overline{m} = 2.33$. We have assumed a temperature of 20 K for the gas; the exact temperature chosen makes only a small difference in Δv_{tot} since the turbulent component of the linewidth always dominates on any scale larger than a small core. The velocity dispersion may be obtained from equation 3.20 by

$$\sigma = \frac{\Delta v_{tot}}{\sqrt{8\ln 2}}. \tag{3.21}$$

We identify σ with $\langle\sigma^2\rangle^{1/2}$ as defined by equation 3.10, since this velocity dispersion is obtained from an average linewidth for the entire cloud. With $\langle\sigma^2\rangle$ known, we compute m_{vir} from equation 3.12, which directly gives us m/m_{vir}. Obtaining the average radius R_S directly from maps, and hence the cross-sectional area $\mathcal{V}$, the average density and internal pressure are then easily obtained using equations 3.9 and 3.10. All that remains to deduce $\mathcal{M}/|\mathcal{W}|$ from equation 3.11 is to estimate the external pressure. Most of the filamentary clouds in our sample are surrounded by atomic gas. Therefore, we conservatively assume the total external pressure to be in the range $10^4 - 10^5$ $K\ cm^{-3}$, as discussed in Section 3.2.3. In fact, the only exception is the $\int$-shaped filament of Orion A, which is deeply embedded in molecular gas. In this case, we have estimated the external pressure from measurements of the density and linewidth in the Orion A cloud (See Table 3.2 for references).

Cloud	m ($M_\odot pc^{-1}$)	m_{vir} ($M_\odot pc^{-1}$)	m/m_{vir}	$\langle P \rangle$ ($10^4 K cm^{-3}$)	P_S ($10^4 K cm^{-3}$)	$P_S/\langle P \rangle$
L1709	35.9	107	0.34	24.3	3.2	0.13
L1755	25.1	129	0.20	46.8	3.2	0.068
L1712-L29	45	132	0.34	82.4	3.2	0.038
DL 2	86.6	547	0.16	63.6	3.2	0.050
$\int$-fil.	355	925	0.38	1.77×10^3	64.8 [a]	0.037
	647	590	1.1	1.05×10^3	64.8	0.062
NF	164	1.11×10^3	0.15	12.1	3.2	0.26
SF	112	777	0.15	5.8	3.2	0.55

[a] Determined from Bally et al. (1987) density estimate and the ^{12}CO linewidth given by Maddalena (1986).

Table 3.2: We have reduced the data of Table 3.1 to obtain m/m_{vir} and $P_S/\langle P \rangle$ for each filament. We assume an external pressure P_S of $10^{4.5 \pm 0.5}$ $K\ cm^{-3}$ for all filaments except the $\int$-shaped filament of Orion A, which is deeply embedded in molecular gas. We also assume that all filaments are oriented within 45° relative to the plane of the sky. We only give central values in the table, but the corresponding error bars are shown in figure 3-1.

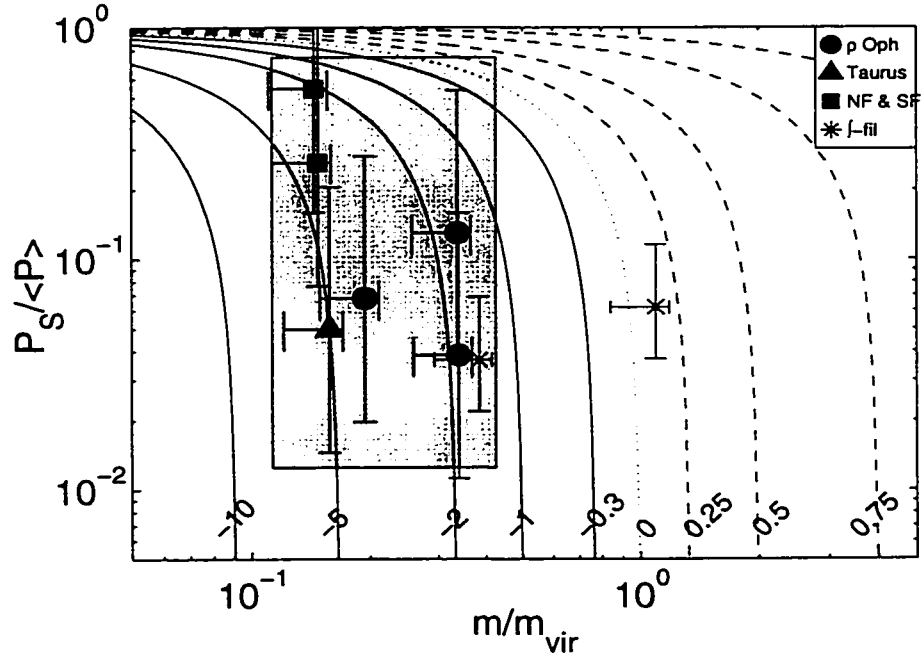

Figure 3-1: Helical field models are compared with the observed properties of real filaments. Curves are shown for various values of the virial parameter $\mathcal{M}/|\mathcal{W}|$. Positive values, corresponding to the dashed curves, indicate that the poloidal field is dominant, while negative values, corresponding to solid curves, indicate that the toroidal field is dominant. The dotted line represents all solutions that are neutrally affected by the helical field (including the unmagnetized solution). The $\int$-shaped filament appears twice, because we have used two independent data sets in our analysis.

Figure 3-1 demonstrates that most filamentary clouds reside in a part of parameter space where

$$\begin{aligned} 0.11 &\lesssim m/m_{vir} \lesssim 0.43 \\ 0.012 &\lesssim P_S/\langle P \rangle \lesssim 0.75, \end{aligned} \tag{3.22}$$

which is indicated by the shaded box in Figure 3-1. Thus, we find that filamentary clouds range considerably in their virial parameters. However, it is remarkable that most of the clouds in our small data set appear to reside in the part of the diagram where $\mathcal{M}/|\mathcal{W}| < 0$. Thus, our virial analysis infers that the magnetic field in at least several filamentary clouds is probably helical and toroidally dominated. Gravity and surface pressure alone appear to be insufficient to radially bind the clouds in our sample. While this means that filaments must be quite weakly bound by gravity, we note that similar results have also been obtained by Loren (1989b) and BM92.

It is natural to wonder to what extent these conclusions could be affected by uncertainties in the observational results. The dominant sources of uncertainty in Figure 3-1 are probably the uncertainties in mass per unit length and surface pressures. However, we have assumed very conservative ranges for the surface pressures and inclination angles of the clouds. We also note that including some rotational support of the filament would necessarily lead to the same conclusion of a helical field.

3.3 Magnetohydrostatic Models of Filamentary Molecular Clouds

The virial treatment of the previous section is perhaps the simplest and most illuminating way to understand the physics and global properties of filamentary molecular clouds. While the virial equations 3.1 and 3.15 are convenient to use, and are in fact exact expressions of magnetohydrostatic equilibrium, the analysis can say nothing of the internal structure of the clouds. This is the importance of the exact analytic and numerical models developed in this section.

3.3.1 The Poloidal and Toroidal Flux to Mass Ratios

We postulate that the magnetic field structure corresponds to that of constant poloidal and toroidal flux to mass ratios Γ_z and Γ_ϕ. The meanings of the flux to mass ratios are illustrated in Figure 3-2, and are defined in the following way. Consider a bundle of poloidal field lines passing through a small cross-sectional area of the filament $\delta\mathcal{V}$. The magnetic flux passing through the surface is $B_z\delta\mathcal{V}$, while

the mass per unit length is $\rho\mathcal{V}$. Thus, the ratio of the poloidal flux to the mass per unit length is

$$\Gamma_z = \frac{B_z}{\rho}. \tag{3.23}$$

Is there an analogous quantity for the toroidal component of the field? In fact the toroidal flux has been defined and is commonly used in plasma physics (Bateman 1978). Here, we consider a bundle of toroidal flux lines with cross-sectional area δA that form a closed ring of radius r centred on the axis of the filament. The mass enclosed by the ring is $2\pi r\delta A$. Thus, we may define the toroidal flux to mass ratio (per radian) as

$$\Gamma_\phi = \frac{B_\phi}{r\rho}. \tag{3.24}$$

The simplest field configuration is that of constant Γ_z and Γ_ϕ. We note that constant Γ_ϕ results naturally if a filament of constant Γ_z and length L is twisted uniformly through an angle ϕ. Then

$$\frac{B_\phi}{B_z} = \frac{r\phi}{L}, \tag{3.25}$$

which leads to the result

$$\Gamma_\phi = \left(\frac{\phi}{L}\right)\Gamma_z. \tag{3.26}$$

We shall always assume constant Γ_z and Γ_ϕ for the remainder of this paper.

3.3.2 An Idealized Model: Uniform Magnetized Filaments

As an illustrative example, it is useful to consider uniform, isothermal filamentary clouds threaded by helical fields of constant Γ_z and Γ_ϕ. In this simple model, the magnetic field is uniform within the filament, but drops to zero outside. By equation 3.24, the toroidal field B_ϕ increases as $\sim r$ within the filament and falls off as $\sim r^{-1}$ in the external medium. Thus, the toroidal field is associated with a constant poloidal current density within the filament.

With the assumption of constant density and the above definitions of Γ_z and Γ_ϕ, equation 3.15 can be expanded to give

$$0 = \left(\sigma^2 - \frac{P_S}{\rho} + \frac{\Gamma_z^2\rho}{8\pi}\right) - m\left(\frac{G}{2} + \frac{\Gamma_\phi^2}{8\pi^2}\right). \tag{3.27}$$

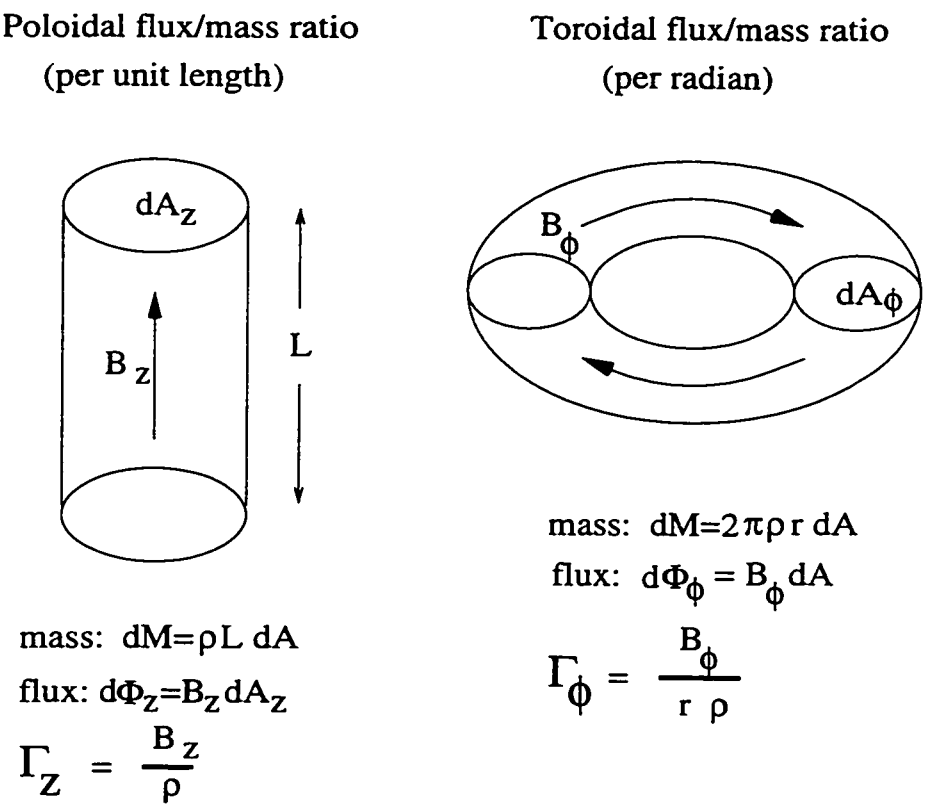

Figure 3-2: A schematic illustration of the poloidal and toroidal flux to mass ratios introduced in equations 3.23 and 3.24.

The critical mass per unit length is obtained by setting $P_S = 0$:

$$m_{mag} = \frac{2\sigma^2 + \Gamma_z^2 \rho/4\pi}{G + \Gamma_\phi^2/4\pi^2}. \tag{3.28}$$

The effects of external pressure and the magnetic field are transparent in this simple model. Pressure and the poloidal field cooperate in supporting the cloud. On the other hand, the toroidal field enters into equation 3.27 in concert with gravity. A filamentary cloud with a helical field would be confined jointly by gravity, external pressure, and the pinch of the toroidal field. Without prior knowledge of the field strength and direction (by molecular Zeeman and polarization observations), the cloud may appear to be unbound by gravity alone.

3.3.3 General Equations for Magnetized Filamentary Molecular Clouds

We consider the equilibrium structure of a non-rotating, self-gravitating molecular cloud with a helical field of constant flux to mass ratios Γ_z and Γ_ϕ. We consider two possible equations of state for the

gas: 1) the "isothermal" equation of state $P = \sigma^2 \rho$ where σ is the total velocity dispersion and 2) the "pure logatrope" of MP96 given by $P/P_c = 1 + A \ln(\rho/\rho_c)$, where P_c and ρ_c are the central (along the filament axis) pressures and densities, and A is a constant. MP96 find $A \simeq 0.2$ for molecular cloud cores. Although their analysis was based only on cloud core data, we shall assume that the same value of A might apply to filamentary clouds as well. We use these two equations of state because they probably bracket the true underlying equation of state for molecular clouds; MHD cloud turbulence probably results in an EOS softer than isothermal (MP96; Gehman et al. 1996), while the pure logatrope is the softest EOS to appear in the literature.

It is convenient to work in dimensionless units where density and pressure are scaled by their central values ρ_c and P_c. We further define the central velocity dispersion by

$$\sigma_c^2 = \frac{P_c}{\rho_c}. \tag{3.29}$$

A natural radial scale is then given by

$$r_0^2 = \frac{\sigma_c^2}{4\pi G \rho_c}, \tag{3.30}$$

which defines the effective core radius of the filament. Finally, we may define natural scales for the mass per unit length and magnetic field:

$$\begin{aligned} m_0 &= r_0^2 \rho_c = \frac{\sigma_c^2}{4\pi G} \\ B_0 &= P_c^{1/2}. \end{aligned} \tag{3.31}$$

Thus, all quantities are written in dimensionless form as follows:

$$\begin{aligned} \tilde{r} &= r/r_0 \\ \tilde{\rho} &= \rho/\rho_c \\ \tilde{m} &= m/m_0 \\ \tilde{P} &= P/P_c \\ \tilde{\sigma} &= \sigma/\sigma_c \\ \tilde{\Phi} &= \Phi/\sigma_c^2 \\ \tilde{B}_z &= B_z/B_0 \\ \tilde{B}_\phi &= B_\phi/B_0 \end{aligned} \tag{3.32}$$

Hereafter, we will only ever refer to Γ_z and Γ_ϕ in their dimensionless forms:

$$\begin{aligned} \tilde{\Gamma}_z &= \sqrt{\frac{\rho_c}{\sigma_c^2}}\left(\frac{B_z}{\rho}\right) \\ \tilde{\Gamma}_\phi &= \frac{1}{\sqrt{4\pi G}}\left(\frac{B_\phi}{r\rho}\right). \end{aligned} \tag{3.33}$$

For brevity, we will drop the tildes for the remainder of this section and the next (except for where ambiguity would result); all quantities hereafter are understood to be written in dimensionless form unless otherwise stated.

Our basic dimensionless equations are those of Poisson

$$\frac{1}{r}\frac{d}{dr}\left(r\frac{d}{dr}\Phi\right) = \rho \tag{3.34}$$

and magnetohydrostatic equilibrium

$$\frac{d}{dr}\left(P + \frac{B_z^2}{8\pi}\right) + \rho\frac{d}{dr}\Phi + \frac{1}{r^2}\frac{d}{dr}\left(\frac{r^2 B_\phi^2}{8\pi}\right) = 0. \tag{3.35}$$

In Appendix D, we construct the mathematical framework to solve these equations numerically for both isothermal and logatropic equations of state. We show that a solution to the dimensionless equations is characterized by three parameters, namely the flux to mass ratios Γ_z and Γ_ϕ defined by equations 3.23 and 3.24, and a third to specify the (dimensionless) radius of pressure truncation. We express this third parameter as a concentration parameter C defined as

$$C = \log_{10}\left(\frac{R_S}{r_0}\right), \tag{3.36}$$

where r_0 is the radial scale defined by equation 3.33. We note that our definition of C is analogous to the concentration parameter $C = \log_{10}(r_t/r_0)$ defined for King models of globular clusters (See Binney & Tremaine 1987). Our concentration parameter differs only in that the tidal radius r_t is replaced by the pressure truncation radius, and our r_0 is smaller by a factor of 3. While we use C primarily as a theoretical parameter, we note that it is in principle observable.

3.3.4 Analytic Solutions

Before discussing numerical solutions, we derive a few special solutions that can be expressed in closed analytic form. Specifically, we discuss the unmagnetized isothermal solution that was found by Ostriker (1964) (a brief derivation is given in Appendix D.). We note that this solution is a special case of a more

general magnetized solution obtained by Stodólkiewicz (1963); for brevity, we shall refer to this solution as the Ostriker solution for the remainder of this paper. We also find a singular solution for logatropic filaments. It is unlikely that either of these special solutions describe real filaments, which are probably magnetized and non-singular, but they do serve as important benchmark results to compare with our more elaborate magnetized models.

The Ostriker Solution: Unmagnetized Isothermal Filaments

The analytic solution for the special case of an unmagnetized isothermal filament is easily obtained using the mathematical framework in Appendix D. It was first given by Ostriker (1964):

$$\rho = \frac{\rho_c}{(1 + r^2/8r_0^2)^2}, \tag{3.37}$$

where we have restored the dimensional units. We note that the density decreases as $\sim r^{-4}$ at large radii. That such steep density profiles have not been observed could be explained by three possibilities: 1) molecular clouds are not isothermal. A softer EOS would give a less steeply falling density at large radius; 2) real clouds contain dynamically important magnetic fields that modify the structure of the filament at large radius; 3) real filaments are always truncated by external pressure. If the filament is truncated before the $\sim r^{-4}$ envelope is reached, such steep behaviour would not be observed. We demonstrate in Section 3.4.1 that either of possibilities 1) or 2) can explain the observed properties of molecular clouds.

Singular Logatropic Filaments

Although we have been unable to find the analogue of the Ostriker solution for the logatropic EOS, we have been successful in finding a singular solution. For this model, we reinterpret ρ_c as the density at some fiducial radius. We postulate a power law solution of the form

$$\rho \propto r^{\alpha}, \tag{3.38}$$

and find that a solution can only be obtained if $\alpha = -1$. The final solution with dimensional units restored is

$$\frac{\rho}{\rho_c} = \sqrt{A}\left(\frac{r}{r_0}\right)^{-1}. \tag{3.39}$$

It is useful to compare our solution with the singular logatropic sphere found by MP96:

$$\frac{\rho_{sphere}}{\rho_c} = \sqrt{2A}\left(\frac{r}{r_0}\right)^{-1}, \tag{3.40}$$

where we have rewritten their solution using our definition of r_0. (Their definition of r_0 differs from ours by a factor of 3. Our definition is the customary choice for filaments.). It is remarkable that both singular logatropic spheres and filaments obey precisely the same power law.

We note that there is no analogous singular power-law model for unmagnetized isothermal filaments.

3.4 Numerical Solutions

We now turn our attention to numerical solutions of equation D.20 using various values of the flux to mass ratios Γ_z and Γ_ϕ. Many of the solutions are shown out to very large radius but may be truncated to reproduce any desired value of the concentration parameter C defined in equation 3.36.

3.4.1 Numerical Results

We have shown in Section 3.2.4 that many filamentary clouds are probably wrapped by helical magnetic fields. However, before considering the most general case of helical fields in Section 3.4.1, we first separately consider the effects of poloidal and toroidal magnetic fields in Section 3.4.1. We note that purely poloidal fields are not allowed by our virial analysis, and purely toroidal fields are probably unrealistic. Neverthess, this is the best way to understand the roles of each field component in our more general helical field models.

Equation D.20 gives the set of differential equations that we integrate to produce our models. The integration was done in a straightforward manner, using a standard Runge-Kutta method.

Models With Purely Poloidal and Toroidal Fields

Figure 3-3 and 3-4 respectively show equilibria threaded by purely poloidal and purely toroidal fields. For both cases, we show the density and pressure profiles, the magnetic structure, and the mass per unit length for isothermal and logatropic filaments. We have also included the velocity dispersion and average velocity dispersion (given by equation 3.10) for the logatropic equation of state.

On each set of figures we have shown the density, pressure, and velocity dispersion structure of the unmagnetized solutions with dashed lines. For isothermal solutions, we have also drawn a line representing the asymptotic r^{-4} behaviour of the Ostriker solution. Similarly, the r^{-1} singular solution has been included on density profiles for logatropic filaments. These power laws are meant as a guide for interpreting the asymptotic behavior of the solutions. We find that our models all have a core-envelope density structure, where the density is nearly constant in the core, but falls off like like a power law in the outer envelope.

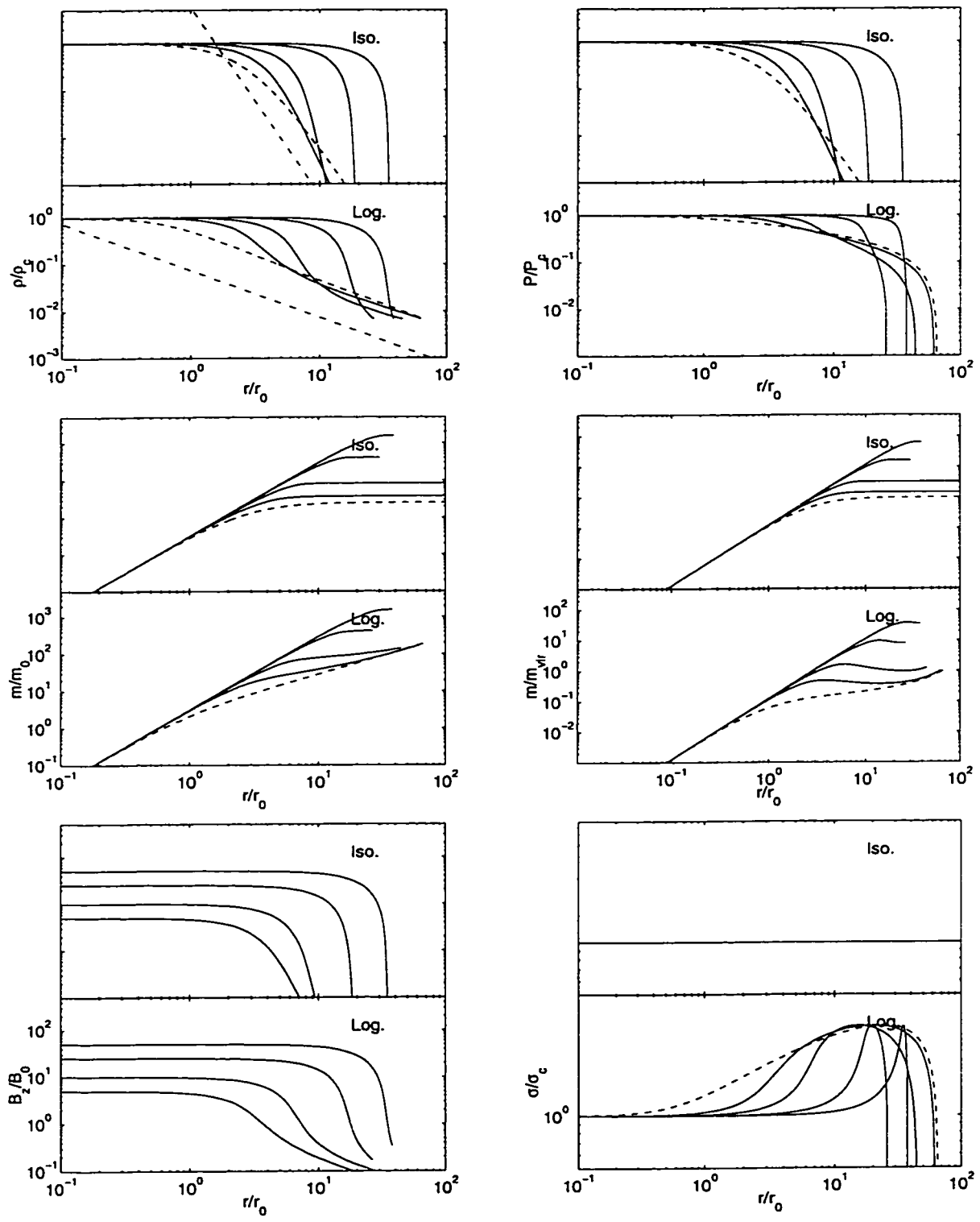

Figure 3-3: Isothermal and logatropic filaments with purely poloidal magnetic field: $\Gamma_z = 0$ (dashed line), 5, 10, 25 and 50. The dot-dashed lines represent the r^{-4} density structure of the Ostriker solution at large radius and the r^{-1} behaviour of the singular logatropic solution.

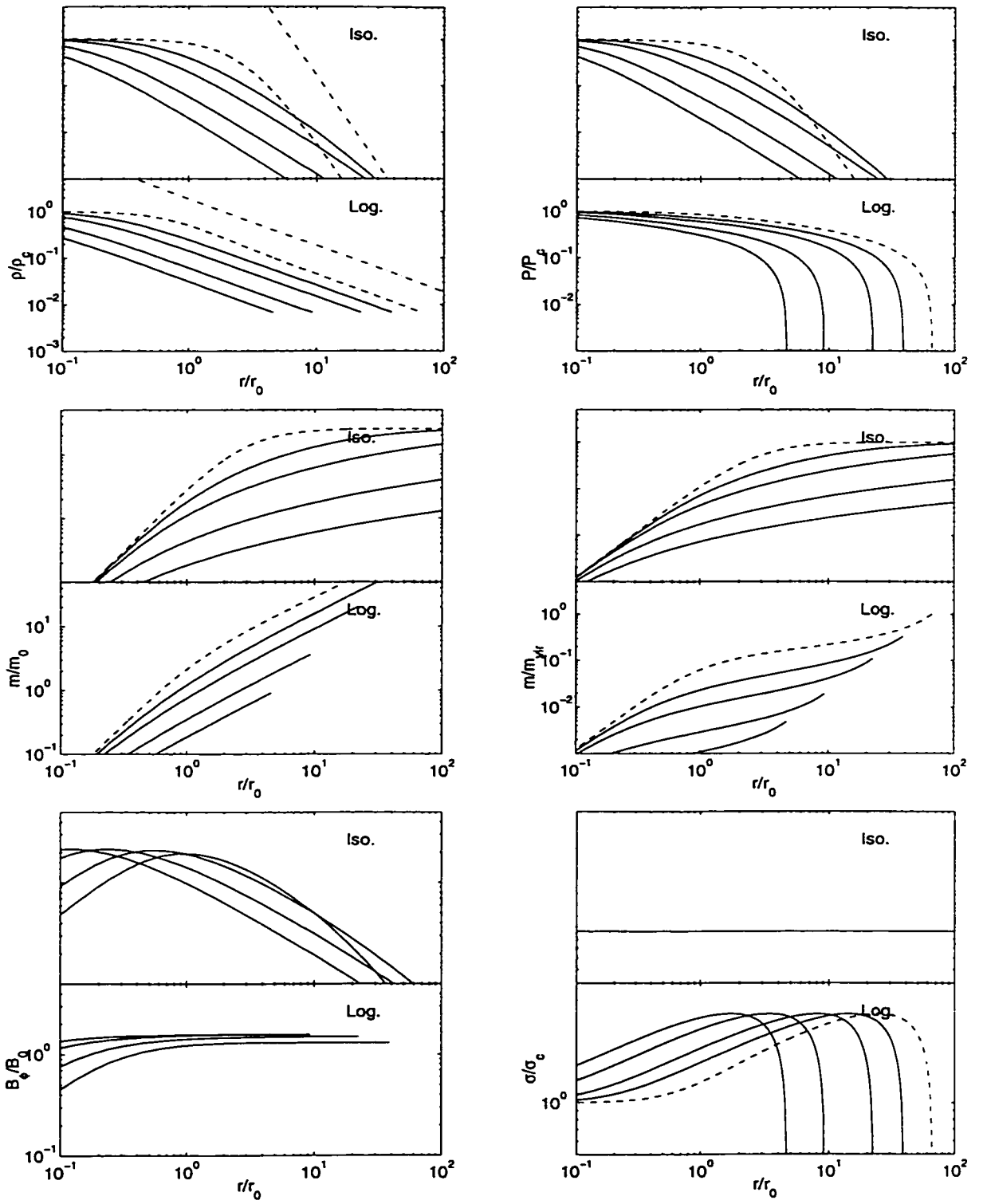

Figure 3-4: Isothermal and logatropic filaments with purely toroidal magnetic field: $\Gamma_\phi = 0$ (dashed line), 5, 10, 25 and 50. The dot-dashed lines have the same meaning as in Figure 3-3.

Comparing the unmagnetized solutions (dashed lines) in Figures 3-3 and 3-4, we observe that the density profile of the unmagnetized logatropic filament is slightly more centrally concentrated than the isothermal Ostriker solution, but falls off much less steeply at large radius. Figures 3-3 and 3-4 show that isothermal and logatropic filaments both tend to finite mass per unit length, although they differ in that isothermal filaments approach the critical mass per unit length only asymptotically as their radii tend to infinity. As discussed in Section 3.2, this limit represents the critical mass per unit length m_h (see Section 3.2.1) beyond which no equilibrium is possible. For the isothermal filament, it is easy to show analytically (from equation 3.37) and we verify numerically that $m_h = 8\pi m_0$, where m_0 is the mass scale defined by equation 3.31. For the unmagnetized logatropic filament, we find numerically that $m_h = 185.8 m_0$. Logatropic filaments can support a greater mass per unit length for equivalent central velocity dispersion σ_c. This is easily understood since the average velocity dispersion $\langle \sigma^2 \rangle^{1/2}$ always exceeds the central value offering more turbulent support to the filament.

Perhaps the most notable feature of logatropic filaments is that they "self-truncate" at finite radius and density $\rho = \rho_c \exp(-1/A)$ where the velocity dispersion and pressure vanish. The logatropic EOS is designed to have a nearly isothermal core and a rising velocity dispersion outside of the core radius. At some point, however, the velocity dispersion turns over and falls to zero. The velocity dispersion could of course never vanish in a real cloud since all real clouds are truncated by finite external pressure. Whether the region of outwardly falling velocity dispersion actually falls within the pressure truncation radius in fits to real clouds is addressed in Section 3.4.2, where we attempt to constrain our models using the observational results of Table 3.2.

Because of the way in which we have defined Γ_z (equation 3.23), B_z is exactly proportional to the density. The toroidal field, however, shows a more interesting structure; B_ϕ always vanishes along the axis of the filament, as it must for the field to be continuous across the axis. We note that the logarithmic radial scale of Figure 3-4 makes the vanishing of B_ϕ at the axis difficult to see in some cases. It also is found to decay at large radius for isothermal filaments since $B_\phi = \Gamma_\phi r \rho \propto r^{-3}$. Hence, there is a single maximum in the toroidal field structure. For logatropic filaments, the r^{-1} asymptotic behaviour of the density implies that $B_\phi = \Gamma_\phi r \rho$ tends to a constant value at large radius. Thus, the toroidal field in logatropic filaments lacks the local maximum found for isothermal filaments.

The effects of poloidal and toroidal magnetic fields on the density structure of isothermal and logatropic filaments are apparent in Figures 3-3 and 3-4. Compared to unmagnetized filaments, the poloidal magnetic field results in a more radially extended core region, and a more rapid fall-off of the density in the outer envelope. For large $\Gamma_z \gtrsim 25 - 50$, the density drops to nearly zero at $30 - 40\ r_0$; the solutions shown in Figure 3-3 appear to end at finite radius because we lose track of the solutions numerically at this point. Toroidal magnetic fields, on the other hand, pinch the core region of the filament to smaller

radial extent, and result in a more gradual decline of the density in the envelope.

It is significant that purely poloidal fields always result in density profiles that are steeper than the r^{-4} behaviour of the Ostriker solution for our models of isothermal filaments. This is also true of logatropic filaments when the field is sufficiently strong. Such steep density profiles have never been observed, so our models of filaments threaded by purely poloidal fields do not match the data. On the other hand, toroidal fields result in $\sim r^{-2}$ outer density profiles that are much more shallow than unmagnetized filaments. This suggests that including a toroidal field component might result in models that agree better with the observations.

We find that the magnetic field has a dramatic effect on the critical mass per unit length m_{mag} of the cloud. For either EOS, a poloidal magnetic field increases m_{mag}, since the poloidal field acts to support the cloud against self-gravity. The toroidal magnetic field works with gravity, thus decreasing the maximum mass per unit length that can be supported. These conclusions are in agreement with our virial results from Section 3.2.

Our analysis shows that all isothermal filaments that are unmagnetized or contain a purely toroidal field tend to the same mass per unit length m_h. We note that this cannot be directly seen in Figures 3-3 and 3-4 since the limit is approached well outside the range of our figures. The existence of this limit is easily explained by our virial equation 3.15 since the toroidal field always tends to zero at large radius for isothermal filaments. The critical mass per unit length m_{mag} clearly cannot be affected, since the toroidal field only enters the virial equation through its surface value. This is not the case for logatropic filaments because B_ϕ tends to a constant value at large radius.

Helical Field Models

In Section 3.2.4, we provided evidence based on our virial analysis that filamentary clouds likely contain toroidally dominated helical magnetic fields. At this point, we shall take a further step by comparing our exact magnetohydrostatic models with the observed properties of filamentary molecular clouds. As we have noted in Section 3.4, a numerical solution is completely determined by the choice of three dimensionless parameters; the flux to mass ratios Γ_z, Γ_ϕ, and the concentration parameter C.

Although R_S can be observed with little difficulty, obtaining an accurate value for C is difficult because of the uncertainty in the core radius r_0. According to equation 3.30, the core radius depends on both the central density and velocity dispersion along the axis of the filament, both of which might be quite uncertain. We can, however, estimate a rough upper bound to C using the data of Table 3.1. We do not know presently whether the central (axial) velocity dispersions of filamentary clouds are dominated by non-thermal motions, as the bulk of the cloud certainly is, or if the velocity dispersions are thermal, as they are in many low-mass cloud cores. Nevertheless, we do know that σ_c must be at

least the thermal value, which is 0.23 $km\ s^{-1}$, assuming a temperature of $15K$. Central densities are probably less than about $10^4\ cm^{-3}$, which is typical of a core. Therefore, equation 3.30 implies that r_0 is probably not less than $\approx 0.04\ pc$. In Table 3.1, we find that $R_S \lesssim 0.5\ pc$ for most (but not all) of the filaments in our sample. Therefore, equation 3.36 implies that most filamentary clouds should have concentration parameters that are less than approximately 1.1. This estimate should be treated with caution, considering the uncertainties and generalizations in our calculation. In particular, we note that larger filaments, such as the Northern and Southern Filaments in the Orion region (See Table 3.1) have radii that are many times larger than the value that we used in our calculation and may, therefore, have concentration parameters that exceed our upper bound.

Three observable quantities shall be required to constrain our theoretical models. We have previously (Section 3.2.4) found the virial parameters $P_S/\langle P\rangle$ and m/m_{vir} to be useful in showing that toroidally dominated helical fields play an important role in the virial equilibrium of filamentary clouds. We use these parameters, as well as a third parameter specifying the ratio of average magnetic to kinetic energy densities to constrain our models. Accordingly, we define a virial parameter

$$X = \frac{M}{K}, \tag{3.41}$$

where M and K are the average magnetic and kinetic energy densities within the cloud defined by

$$\begin{aligned} M &= \frac{\int_V (B_z^2 + B_\phi^2) dV}{8\pi V} \\ K &= \frac{3}{2}\langle\rho\rangle\langle\sigma^2\rangle, \end{aligned} \tag{3.42}$$

and V is the volume of the cloud (not to be confused with $\mathcal{V}$). Myers and Goodman (1988a,b) have provided considerable observational evidence that the average magnetic and kinetic energy densities are in approximate equipartition, with $M \approx K$ to within a factor of order 2. Therefore, we impose the auxiliary constraint that

$$X \approx \mathcal{O}[1] \tag{3.43}$$

for filamentary clouds with realistic magnetic fields. This equipartition of energy has been explained by attributing the non-thermal motions within molecular clouds to internally generated Alfvénic turbulence (BM92). Since super-Alfvénic turbulence is highly dissipative, the Alfvén speed poses a natural limit for the non-thermal velocity dispersion (BM92). Thus, we expect $\sigma \approx v_A$ for molecular clouds. Defining the average squared Alfvén speed as

$$\langle v_A^2\rangle = \frac{\int_0^m v_A^2 dm'}{m}, \tag{3.44}$$

it is easy to show that

$$X = \frac{\langle v_A^2 \rangle}{3\langle \sigma^2 \rangle}. \tag{3.45}$$

Therefore, $X \approx 1$ is a natural result for magnetized clouds supported against gravity by Alfvénic turbulence. In the analysis that follows, we assume that

$$0.2 \leq X \leq 5 \tag{3.46}$$

for all reasonable models and that $0.5 \leq X \leq 2$ is appropriate for our most realistic models.

Monte Carlo Exploration of the Parameter Space

In this Section, we perform a Monte Carlo sampling of our parameter space in order to determine which values of Γ_z, Γ_ϕ, and C result in models that obey all of our constraints. The Monte Carlo exploration is very straightforward. We simply assign random values to the three theoretical parameters and compute helical field models using the mathematical framework of Section 3.3.3. Once a solution has been obtained, we compute m/m_{vir}, $P_S/\langle P \rangle$, and X using equations 3.12, 3.9, and 3.41, from which we easily determine whether or not the solution obeys our constraints. Figure 3-5 shows the results of our exploration for isothermal models, while Figure 3-6 shows the results for logatropic models. Each point in these figures represents a model that obeys our constraints on m/m_{vir} and $P_S/\langle P \rangle$; models that fall outside of these constraints have been discarded.

The grayscale in Figures 3-5a and 3-6a represent different ranges for X. The most likely range of X, with $0.5 \leq X \leq 2$ is shown as the lightest coloured points. The next darkest gray dots represent a less likely, but still possibly allowed range, with $0.2 \leq X \leq 5$, while the darkest gray dots represent models that are outside of these ranges, and therefore have unrealistically large or small magnetic fields. It should be noted that there relatively little overlap between these regions; they map out quite distinct regions on the diagrams. From Figure 3-5a, we find that the allowed ranges for the flux to mass ratios are approximately

$$\begin{aligned} 5 \lesssim \Gamma_\phi &\lesssim 25 \\ \Gamma_z &\lesssim 8 \end{aligned} \tag{3.47}$$

for isothermal filaments with $0.5 \leq X \leq 2$. A somewhat larger region of the parameter space is allowed for filaments with $0.2 \leq X \leq 5$. Comparing with Figure 3-6a, we find that the allowed flux to mass

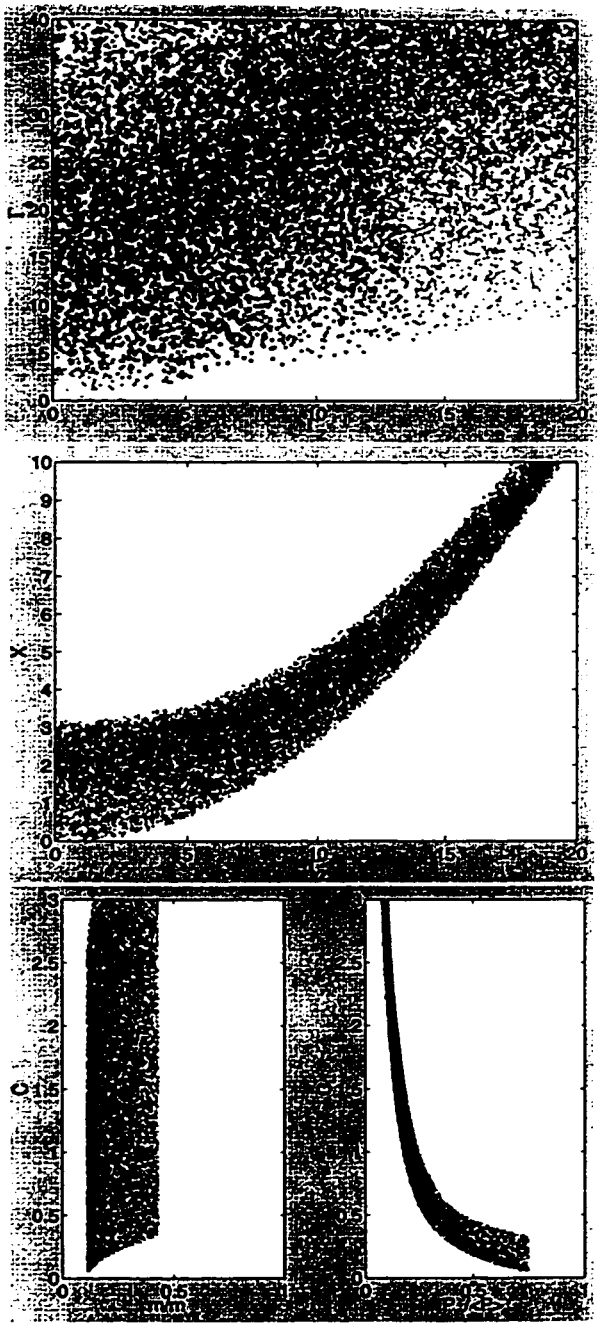

Figure 3-5: Isothermal Models. We show the results of our Monte Carlo exploration for isothermal filaments. Each point on these figures represents a model that obeys the observational constraints given in equation 3.22; thus, we determine which ranges of Γ_z, Γ_ϕ, and C result in models that agree with the available observational data. a) (top) The grayscale represents different ranges for X, as defined in equation 3.41. The most realistic solutions, with $0.5 \lesssim X \lesssim 2$ are shown as white dots. The medium gray dots have $0.2 \lesssim X \lesssim 5$. The dark gray dots represent models that are outside of these ranges with unrealistic magnetic field strengths. b) (middle) We show that X is determined mainly by Γ_z. c) (bottom) We show the allowed ranges of the concentration parameter C. The shading is the same as in a). However, we note that the darkest gray dots are mostly hidden "behind" the medium gray, in this case.

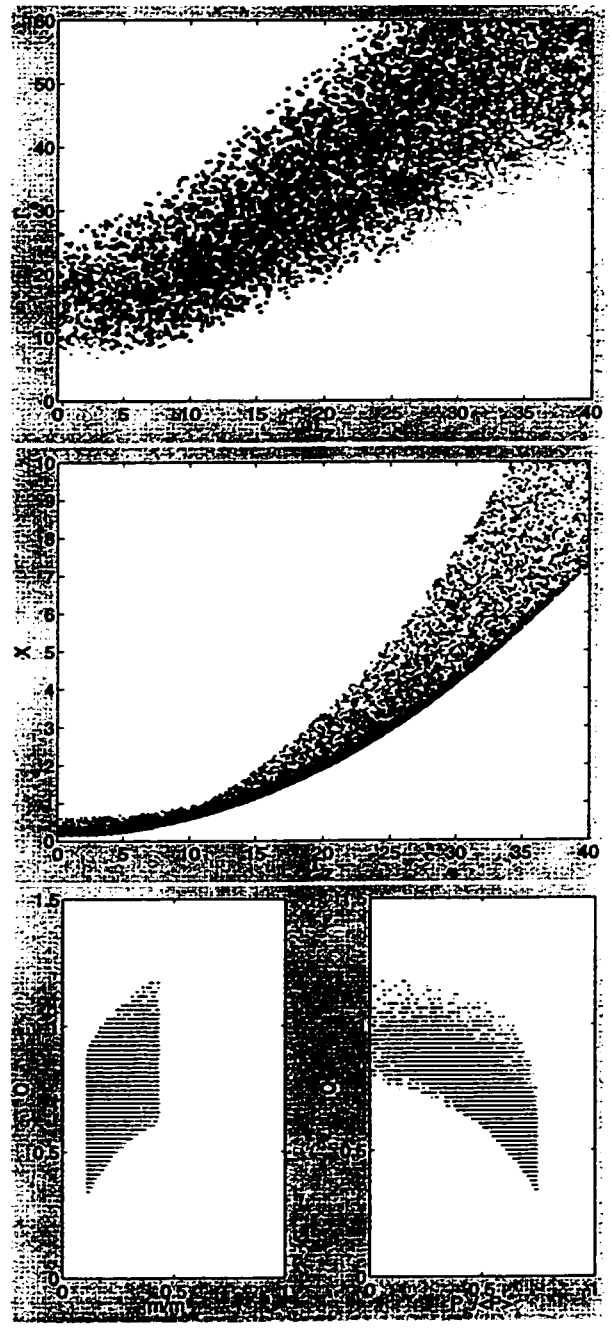

Figure 3-6: Logatropic Models. We show the results of our Monte Carlo exploration for logatropic filaments. The graphs are as described in the caption of Figure 3-5.

ratios are somewhat larger for logatropic filaments, where we find

$$\begin{aligned} 10 \lesssim \Gamma_\phi &\lesssim 40 \\ 10 \lesssim \Gamma_z &\lesssim 20 \end{aligned} \tag{3.48}$$

when $0.5 \leq X \leq 2$. We note that Γ_z is more tightly constrained than Γ_ϕ for both isothermal and logatropic filaments.

In Figures 3-5b and 3-6b, we plot the magnetic parameter X, for the allowed models, against the poloidal flux to mass ratio Γ_z. We find that X has a very strong dependence on Γ_z for both isothermal and logatropic models. Moreover, we find that there is no obvious correlation between X and Γ_ϕ. Since we can regard X as nearly a function of Γ_z alone, the auxiliary constraint on X directly constrains Γ_z. It is for this reason that somewhat tighter constraints are obtained on Γ_z in equations 3.47 and 3.48, than on Γ_ϕ.

Figures 3-5c and 3-6c show the dependence of the concentration parameter C on m/m_{vir} and $P_S/\langle P\rangle$ for models that are allowed by the observations. We find that C may range from 0 to ≈ 3 for isothermal models, but $C \lesssim 1.7$ for most solutions where $0.5 \leq X \leq 2$. Moreover, we find that C correlates rather well with $P_S/\langle P\rangle$, with greater values of $P_S/\langle P\rangle$ corresponding to smaller values of C. We note that most filamentary clouds probably have $C \lesssim 1.1$, considering our discussion in Section 3.4.1. However, we do not enforce this upper bound as a rigid constraint, since further data on the central densities and velocity dispersions of filamentary clouds needs to be obtained in order to make our argument definitive. We find that $C \gtrsim 1$ whenever $P_S/\langle P\rangle \lesssim 0.25$; therefore, isothermal filaments with $C \lesssim 1$ must be subject to external pressures that are at least one fourth of the mean internal pressure. Such relatively high external pressures are well within the range of pressures allowed by equation 3.22. The concentration parameter C is much more restricted for logatropic models, where C may range only from approximately 0.4 to 1.2. As a general trend, we find that C increases slightly with m/m_{vir}, and also as $P_S/\langle P\rangle$ decreases. This is a natural result, since filaments become more radially extended, with greater C, as they become closer to their critical configurations with vanishing $P_S/\langle P\rangle$ and maximum m/m_{vir}.

3.4.2 "Best-Fitting" Models For Magnetized Filamentary Clouds

In Figure 3-7, we show 50 isothermal helical field models that span the range of parameters allowed by equations 3.22 and 3.46. We see that our allowed models possess a number of very robust characteristics. Most importantly, we find that most of our isothermal models have outer density profiles that fall off as $\sim r^{-1.8}$ to r^{-2}, with some of most truncated models having somewhat more shallow profiles. This is most clearly shown in Figure 3-7b, where we have plotted the power law index $\alpha = d\ln\rho/d\ln r$ as a

function of the dimensionless radius r/r_0. We observe that α becomes more negative with increasing radius, but that none of our models ever have density profiles that are steeper than r^{-2}. Thus, we find that our isothermal helical field models have density distributions that are much more shallow than the r^{-4} Ostriker solution. This radical departure from the Ostriker solution is clearly due to the dominance of the magnetic field over gravity in the outer regions. The overall effect of the helical field is to modify the density structure of the Ostriker solution so that a much more realistic form is obtained. In particular, we note that A98 and LAL98 have recently used extinction measurements of background starlight in the near infra-red to show that two filamentary clouds, namely L977 and IC 5146, have r^{-2} density distributions. Our helical field models have density profiles that are essentially the same as those obtained for models with purely toroidal fields in Section 3.4.1. Therefore, we conclude that the outer density distribution is shaped primarily by the toroidal component of the field, in our model. We note, however, that the toroidal field is in fact much weaker than the poloidal field throughout most of a filamentary cloud. In all cases, the basic magnetic structure is that of a poloidally dominated core region surrounded by a toroidally dominated envelope, where the field is relatively weak.

In Figure 3-8, we show a sample of 50 logatropic models that are allowed by our constraints. The main difference between the logatropic models and the isothermal models shown in Figure 3-7 is that there is a much greater variety of allowed density distributions for the logatropes. We find logatropic filaments with density profiles as shallow as r^{-1} and as steep as $r^{-1.8}$. Unlike the isothermal solutions, α does not decrease monotonically. Rather, it usually reaches a minimum value somewhat less than -1 when $r/r_0 \approx 1$ to 3, and increases at larger radii. The result is that the density distribution usually contains a small region where the density falls quite rapidly, which is surrounded by an envelope with a more gentle power law. Many logatropic models have density profiles that are more shallow than the A98 and LAL98 data. However, some logatropic models have density profiles that might agree with the data. The main difference between isothermal and logatropic models is that isothermal filaments produce a nearly "universal" $r^{-1.8}$ to r^{-2} density profile, while logatropic filaments show a much larger range of behaviour.

3.5 Discussion

We show, in Section 3.2.4, that most of the filamentary molecular clouds in our sample have velocity dispersions that are too high for them to be bound by gravity and surface pressure alone. Thus, we find evidence that many filamentary clouds are probably wrapped by helical magnetic fields whose toroidal components help to confine the gas by the hoop stress of the curved field lines. It is important to realize that this conclusion is based on our virial analysis of filamentary clouds (Section 3.2) and is, therefore,

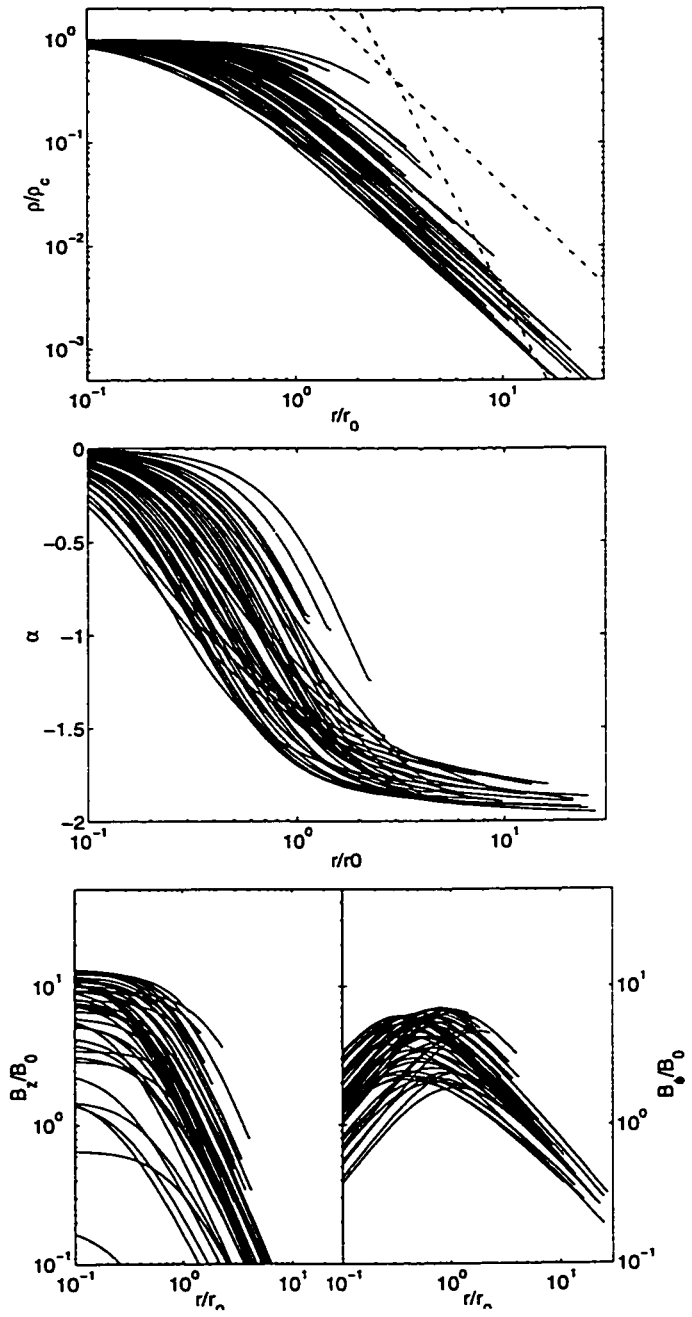

Figure 3-7: We show a sample of 50 isothermal models that span the range of allowed parameters given in equations 3.22 and 3.46. a) (top) We show the density profiles of the models. The dashed lines represent the r^{-4} density profile of the Ostriker solution and an r^{-2} profile, which is in agreement with the observed density profiles of filamentary clouds (Alves et al. (1998), Lada, Alves, and Lada (1998)). b) (middle) We show the how the power law index $d\ln\rho/d\ln r$ behaves with radius. c) (bottom) We show the behaviour of the poloidal and toroidal components of the magnetic field.

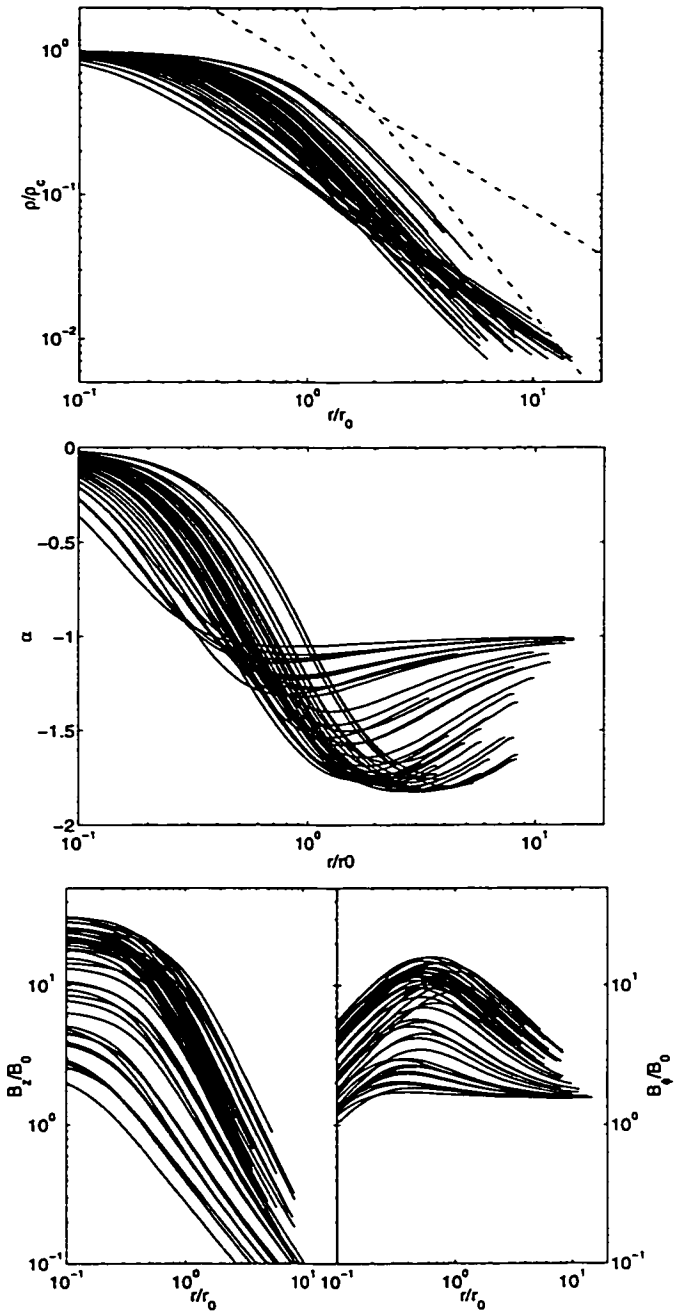

Figure 3-8: We show a sample of 50 logatropic models that span the range of allowed parameters given in equations 3.22 and 3.46. a) (top) We show the density profiles of the models. The dashed lines represent the r^{-4} density profile of the Ostriker solution and an r^{-2} profile, which is in agreement with the observed density profiles of filamentary clouds (Alves et al. (1998), Lada, Alves, and Lada (1998)). b) (middle) We show the how the power law index $d\ln\rho/d\ln r$ behaves with radius. c) (bottom) We show the behaviour of the poloidal and toroidal components of the magnetic field.

independent of either the EOS of the gas or the mass loading of the magnetic field lines. We find that all of the filamentary clouds in our sample have masses per unit length that are much lower than the critical mass per unit length for purely hydrostatic filaments, and that filaments are quite far from their critical configurations, where $P_S/\langle P\rangle \rightarrow 0$ (See equation 3.22.). Thus, star formation in filamentary clouds must involve fragmentation into periodic cores (cf. Chandrasekhar & Fermi 1953), rather than overall radial collapse. We refer to the second paper in our series for a full analysis of this process.

We construct numerical magnetohydrostatic models of filamentary clouds, which we explore thoroughly in Section 3.4.1 using Monte Carlo techniques. We show that both isothermal and logtropic models are consistent with the available observational data. We find that helical fields have profound effects on the outer density profiles of filamentary clouds. While hydrostatic filaments have a density profile that falls off as r^{-4} (see Section 3.3.4), nearly all of our isothermal models with helical fields have much more shallow density profiles that fall off as $r^{-1.8}$ to r^{-2}. The toroidal component of the field is entirely responsible for these shallow density profiles. Logatropic models show a a greater variety of behaviour, with density profiles ranging from r^{-1} to $r^{-1.8}$. We note nearly all of our isothermal models and many of our logatropic models are in excellent agreement with the r^{-2} density profiles of the filamentary clouds L977 and IC 5146, which have recently been observed by A98 and LAL98. Helical fields, rather than the nature of the EOS, seem to explain the data by controlling the density profiles.

The confirmation of helical fields in filamentary clouds will ultimately require direct observations of the field structure using sub-mm polarization and possibly molecular Zeeman observations. Unfortunately, most polarization observations of molecular clouds have been carried out in the optical and near infra-red regions of the spectrum; Goodman et al. (1995) have demonstrated that such measurements are likely a poor indicator of magnetic field direction in cold dark clouds. More promising is the prospect of observing the thermal dust grain emission of dark clouds, which will hopefully become commonplace in the near future with instruments like the SCUBA polarimeter. In emission, we can be assured that any polarization is due to warm dust grains within the cloud being observed. The observational verification of our helical field models for filamentary molecular clouds will need to rely heavily on such observations.

3.5.1 Observational Signatures of Helical Magnetic Fields

Helical magnetic fields present an interesting and unique polarization pattern. One might expect to find polarization vectors aligned with some average pitch angle of the magnetic field. However, Carlqvist (1997) has modeled the polarization pattern of helical magnetic fields and demonstrated that this assumption is incorrect. The signature of a helical field, assuming that the polarization percent remains small and that the cloud is optically thin, is actually polarization vectors that are either aligned with or perpendicular to the filament axis with a possible 90^o change in orientation at some radius. The

reason for this counterintuitive behaviour is that any line of sight through the filament intersects a given radius not once, but twice. Since the order of polarizing elements is unimportant in the limit of small polarization, the combination of any symmetric pair of polarizing elements results in a cancellation of any oblique component of the net polarization. Although Carlqvist's model was done for absorption polarimetry, the same reasoning holds for emission. The overall pattern will only reflect the dominant component of the field along any line of sight; thus, our models predict that the innermost (poloidally dominated) regions of filamentary clouds should be dominated in emission by polarization vectors aligned perpendicular to the filament, while the polarization should be predominantly parallel to the filament in the (toroidally dominated) outer regions.

There is some direct evidence that filamentary clouds contain helical magnetic fields. Optical polarization and HI Zeeman data are consistent with a helical field in the large Orion A filament oriented at an approximately 20° pitch angle relative to the axis of the filament (Bally 1989). While the reliability of the optical polarization data is uncertain due to the reasons discussed above, the Zeeman observations do not suffer such ambiguity. The line of sight component of the magnetic field has been observed to reverse across the L1641 portion of the filament (Heiles 1987, 1989). Such a reversal is very suggestive of a helical field wrapped around the cloud. More recently, Heiles (1997) has suggested that an alternate explanation might be that the shock front of the Eridanus superbubble has swept past the Orion A cloud causing field lines to be stretched over the filament, thus simulating a helical pattern. While Heiles favours this idea, he cannot rule out the older idea that the field is intrinsically helical. Regardless of the true nature of the $\int$-shaped filament, we observe that it is one of the few filaments shown in Figure 3-1 where our models do not actually require a helical field for equilibrium.

3.6 Summary

1. We have applied the virial theorem to filamentary molecular clouds that are truncated by a realistic external pressure and contain ordered magnetic fields. We have collected data on filamentary clouds from the literature. We find that most of the filamentary clouds in our sample are constrained by

$$\begin{aligned} 0.11 &\lesssim m/m_{vir} \lesssim 0.43 \\ 0.012 &\lesssim P_S/\langle P \rangle \lesssim 0.75. \end{aligned} \tag{3.49}$$

We use these observational constraints to show that many filamentary clouds are likely wrapped by helical magnetic fields.

2. We have used our virial equation to derive virial relations for filaments that are analogous to the well-known relations for spheroidal equilibria (Chièze 1987; Elmegreen 1989; MP96). We find that the virial relations for filaments differ from the corresponding relations for spheroids only by factors of order unity.

3. We have studied the stability of filamentary molecular clouds in the sense of Bonnor and Ebert. We find that all filamentary molecular clouds, that are initially in equilibrium, are stable against radial perturbations. Thus, a cloud that is initially in equilibrium cannot be made to undergo radial collapse by increasing the external pressure; the only way to destabilize a filament against radial collapse is by increasing its mass per unit length beyond a critical value that depends on the magnetic field. This critical value is the maximum mass per unit length for which any equilibrium is possible; for purely hydrostatic filaments, the critical mass per unit length is given by $m_h = 2\langle\sigma^2\rangle/G$ (See Section 3.2.1). The poloidal component of the magnetic field increases the critical mass per unit length by supporting the gas against self-gravity. The toroidal field works with gravity in compressing the filament; thus, the toroidal field decreases the critical mass per unit length.

4. We have constructed exact numerical magnetohydrostatic models for filamentary clouds in Sections 3.4 and 3.4.1. We have considered both isothermal and logatropic equations of state, which likely bracket the true underlying EOS for filamentary molecular clouds. The magnetic field structure is more general than in previous studies; we have assumed only that the poloidal and toroidal flux to mass ratios (Γ_z and Γ_ϕ) are constant.

5. Isothermal models with purely poloidal magnetic fields have density profiles that are even steeper than the Ostriker solution; it is unlikely that such models describe real molecular clouds. Toroidal fields result in density profiles that are more shallow than the Ostriker solution (typically r^{-2} profiles), and in better agreement with observations.

6. We have performed a Monte Carlo exploration of our parameter space, in which we randomly sample our parameter space and then determine whether or not the resulting model agrees with the observational constraints (equations 3.22 and 3.46). We find both isothermal and logatropic filaments that are allowed by the data. We find that

$$\begin{aligned} 5 \lesssim \Gamma_\phi &\lesssim 25 \\ \Gamma_z &\lesssim 8 \end{aligned} \tag{3.50}$$

for isothermal filaments, and

$$10 \lesssim \Gamma_\phi \lesssim 40$$

$$10 \lesssim \Gamma_z \lesssim 20 \tag{3.51}$$

for logatropic filaments.

7. Our best-fitting isothermal models have density profiles that fall off as only $\sim r^{-1.8}$ to $\sim r^{-2}$, in contrast to the r^{-4} behaviour of the Ostriker solution. These shallow profiles are entirely due to the effects of the toroidal component of the magnetic field. Thus, our assumption of constant poloidal and toroidal flux to mass ratios is consistent with the observed density profiles for isothermal filaments. The logatropic filaments show a greater variety of density profiles that range from r^{-1} to $r^{-1.8}$. Thus, some of the logatropic filaments may agree with the observed r^{-2} profiles (A98 and LAL98), while others may be somewhat too shallow.

3.7 Acknowledgements

The authors wish to acknowledge Christopher McKee and Dean McLaughlin for their insightful comments, as well as an anonymous referee for useful comments regarding the derivation of our virial results. J.D.F. acknowledges the financial support of McMaster University and an Ontario Graduate Scholarship. The research grant of R.E.P. is supported by a grant from the Natural Sciences and Engineering Research Council of Canada.

Appendix A

Derivation of the Virial Equation for Filamentary Molecular Clouds

The purpose of this Appendix is to derive a useful form of the virial equation for filamentary molecular clouds (equation 3.1), which we use to establish observational constraints on our models in Section 3.2.4. We consider the equilibrium of a long self-gravitating filamentary molecular cloud threaded by a magnetic field that may contain both a poloidal and toroidal component, so that the field lines are helical in general. We apply the usual scalar virial theorem (cf. Spitzer 1978) to a finite cylindrical volume V of the filament, chosen well away from the ends and bounded by a surface S, whose radius coincides with the radius R_S of the cloud and whose length is L:

$$K + M + W = 0 \tag{A.1}$$

where the internal energy (due to thermal plus non-thermal motions), magnetic, and gravitational energies are respectively given by

$$K = 3\int_V P dV - \oint P\mathbf{x}\cdot\mathbf{dS} \tag{A.2}$$

$$M = \frac{1}{8\pi}\int_V B^2 dV + \frac{1}{4\pi}\oint(\mathbf{x}\cdot\mathbf{B})(\mathbf{B}\cdot\mathbf{dS}) - \frac{1}{8\pi}\oint B^2\mathbf{x}\cdot\mathbf{dS} \tag{A.3}$$

$$W = -\int_V \rho\mathbf{x}\cdot\nabla\Phi dV. \tag{A.4}$$

In these formulae, P is the pressure, which is a function of cylindrical radius, P_S is the external pressure at the radial surface of the cloud, $\mathbf{x}$ is a coordinate vector, $\mathbf{B}$ is the magnetic field, and Φ is the gravitational potential.

Considering the contributions from the radial surface and the ends of our cylindrical volume separately, the surface pressure term in equation A.2 can be evaluated as follows:

$$\begin{aligned} \oint P\mathbf{x}\cdot\mathbf{dS} &= 2P_S V + L\int_0^{R_S} 2\pi r P dr \\ &= 2P_S V + \int_V P dV. \end{aligned} \tag{A.5}$$

Therefore, equation A.2 becomes

$$K = 2\int_V P dV - 2P_S V. \tag{A.6}$$

Cylindrical symmetry requires that all derivatives with respect to z must vanish within volume V. The gravitational energy therefore becomes

$$W = -\int_V \rho r \frac{\partial \Phi}{\partial r} dV, \tag{A.7}$$

which we show in Section 3.2 is equal to $-m^2GL$, where m is the mass per unit length of the filament.

The second term of the magnetic energy (equation A.3) contributes only at the ends of our cylindrical volume since $\mathbf{B}\cdot d\mathbf{S} = 0$ everywhere along the sides. This term simplifies to become

$$\begin{aligned} \frac{1}{4\pi}\oint(\mathbf{x}\cdot\mathbf{B})(\mathbf{B}\cdot\mathbf{dS}) &= \frac{L}{4\pi}\int_0^{R_S} 2\pi r B_z^2 dr \\ &= \frac{1}{4\pi}\int_V B_z^2 dV. \end{aligned} \tag{A.8}$$

Similar manipulations allow us to simplify the third term of the magnetic energy:

$$\frac{1}{8\pi}\oint B^2\mathbf{x}\cdot\mathbf{dS} = \frac{1}{4\pi}(B_{\phi S}^2 + B_{zS}^2)V + \frac{1}{8\pi}\int_V B^2 dV, \tag{A.9}$$

where $B_{\phi S}$ and B_{zS} are the field components evaluated at the radial surface of the filament. Combining the three terms of the magnetic energy, we find that

$$M = \frac{1}{4\pi}\int_V B_z^2 dV - \frac{1}{4\pi}(B_{\phi S}^2 + B_{zS}^2)V. \tag{A.10}$$

Inserting equations A.6 and A.10 into the virial equation A.1 and dividing by the length, we obtain equation 3.1, which is a form of the scalar virial theorem that is appropriate for filamentary molecular

clouds.

Appendix B

Bonnor-Ebert Stability of Magnetized Filaments

We have shown, in Section 3.2, that all hydrodynamic filaments, which are initially in equilibrium, are stable in the sense of Bonnor (1956) and Ebert (1955). In this section, we examine the Bonnor-Ebert stability of uniform magnetized filaments.

B.0.1 Uniform Clouds

We begin by considering a radial perturbation of a uniform filament in which the mass per unit length and the velocity dispersion are conserved. Solving equation 3.27 for the external pressure, we easily obtain

$$P_S = \frac{c_\phi}{\mathcal{V}} + \frac{c_z}{\mathcal{V}^2}, \tag{B.1}$$

where

$$\begin{aligned} c_\phi &= m\sigma^2 - m^2\left(\frac{G}{2} + \frac{\Gamma_\phi^2}{8\pi^2}\right) \\ c_z &= \frac{m^2\Gamma_z^2}{8\pi}. \end{aligned} \tag{B.2}$$

Differentiating with respect to $\mathcal{V}$ and simplifying using equations B.1, B.2, 3.23, and 3.9, we obtain

$$\frac{dP_S}{d\mathcal{V}} = -\frac{1}{\mathcal{V}}\left(P_S + P_{mag}\right) < 0 \tag{B.3}$$

for all choices of $\mathcal{V}$ and P_S. We conclude that all uniform filaments in equilibrium (having $m \leq m_{mag}$) are stable in the sense of Bonnor and Ebert.

B.0.2 Non-Uniform Clouds

We now extend the argument to general magnetized filamentary equilibria using the mathematical framework of Section 3.3.3 and Appendix D.

Again we consider a radial perturbation of a filamentary cloud in which the mass per unit length m is conserved. Following MP96, we shall also require that the central velocity dispersion σ_c remain unchanged. Referring to equations 3.31 and 3.33, we may write

$$\tilde{m} = \frac{m}{m_0} = \frac{4\pi G m}{\sigma_c^2}. \tag{B.4}$$

Thus, we see that the dimensionless mass per unit length $\tilde{m}$ is also conserved during the perturbation. Since $\tilde{m}$ is implicitly a function of $\tilde{r}$ alone, the dimensionless radius $\tilde{R_S}$ must remain fixed during the perturbation. Therefore, we find that the radial perturbation takes the form of a simple rescaling of the dimensionless solution with none of the dimensionless variables perturbed whatsoever. With this result in hand, we write

$$\begin{aligned} P_S &= P_c \tilde{P}_S = \sigma_c^2 \rho_c \tilde{P}_S \\ R_S &= \sqrt{\frac{\sigma_c^2}{4\pi G}} \rho_c^{-1/2} \tilde{R_S}, \end{aligned} \tag{B.5}$$

where σ_c, $\tilde{P}_S$, and $\tilde{R_S}$ all remain fixed during the perturbation. Eliminating ρ_c, we obtain the result

$$R_S = \sqrt{\frac{\sigma_c^4}{4\pi G}} (\tilde{P}_S \tilde{R_S}^2)^{1/2} P_S^{-1/2}. \tag{B.6}$$

Since $R_S \propto P_S^{-1/2}$, we find that

$$\frac{dR_S}{dP_S} < 0 \tag{B.7}$$

for all external pressures P_S. Therefore, we conclude that all self-gravitating filaments that are initially in a state of equilibrium (which requires $m \leq m_{mag}$ by equation 3.18), are stable in the sense of Bonner and Ebert.

Appendix C

Virial Relations and Larson's Laws for Filaments

We derive the virial relations for filamentary molecular clouds analogous to the well known relations for spheroidal clouds (Chièze 1987; Elmegreen 1989; MP96). Using equation 3.7 in our virial equation for filamentary clouds (equation 3.1), we write

$$0 = 2m\langle\sigma^2\rangle - 2P_S\mathcal{V} - am^2G + \mathcal{M} \tag{C.1}$$

We have shown in Section 3.2 that the constant a is exactly unity for any filament but we retain the constant in order to compare more directly with the corresponding expressions for spheroidal clouds. Equation C.1 can be rewritten as

$$\alpha_{mag} \equiv a\frac{1-\mathcal{M}/|\mathcal{W}|}{1-P_S/\langle P\rangle} = \frac{m_{vir}}{m} \tag{C.2}$$

where we have introduced the observable virial parameter α_{mag} for filamentary clouds analogous to that of Bertoldi and McKee (1992, hereafter BM92). We may also write

$$\alpha_{mag} = \alpha_{non}\left(1-\frac{\mathcal{M}}{|\mathcal{W}|}\right), \tag{C.3}$$

where α_{non} is just α_{mag} evaluated in the unmagnetized limit:

$$\alpha_{non} = \frac{a}{1-P_S/\langle P\rangle}. \tag{C.4}$$

	C_m	C_R	C_ρ	C_Σ
filament	2	$\sqrt{\frac{2}{\pi}}$	1	$\sqrt{\frac{\pi}{2}}\sec i$
spheroid	$\frac{5}{2}$	$5\sqrt{\frac{3}{20\pi}}$	1	$\sqrt{\frac{20}{3\pi}}$

Table C.1: The coefficients of the virial relations given in equations C.5. We have included a correction $\sec i$ for the projected surface density of filamentary equilibria and defined the effective mass per unit length for a sphere as $m_{sphere} = M/(2R)$.

Equations C.2 and C.4 are easily solved for the mass per unit length m, radius R_S, average density $\langle\rho\rangle$, and surface density Σ. In order to compare with the corresponding results for spheroidal magnetized equilibria (See MP96), we present the results as general expressions with the coefficients written in Table C.1:

$$\begin{aligned} m &= C_m \frac{\langle\sigma^2\rangle}{\alpha_{mag} G} \\ R &= C_R \left(\frac{\alpha_{non} - a}{\alpha_{non}}\right)^{1/2} \frac{1}{\alpha_{mag}^{1/2}} \frac{\langle\sigma^2\rangle}{(G P_S)^{1/2}} \\ \langle\rho\rangle &= C_\rho \left(\frac{\alpha_{non}}{\alpha_{non} - a}\right) \frac{P_S}{\langle\sigma^2\rangle} \\ \Sigma &= C_\Sigma \frac{1}{\alpha_{mag}^{1/2}} \left(\frac{\alpha_{non}}{\alpha_{non} - a}\right)^{1/2} \left(\frac{P_S}{G}\right)^{1/2} . \end{aligned} \tag{C.5}$$

We have included a correction for the inclination i of the filament with respect to the plane of the sky; this only affects the expression for the surface density. These expressions are remarkably similar to those for spheroidal clouds, retaining identical functional forms and differing only by coefficients of order unity. Of course, the mass per unit length of a filament cannot be compared directly to the mass of a spheroid. However, if we define an effective mass per unit length by taking $m_{sphere} = M/(2R)$, the resulting expression again differs from ours by only a numerical factor of order unity.

As long as the external pressure is approximately constant, we find that $\sigma \propto R^{1/2}$ and $\Sigma \propto const \times \sec i$ for filaments. Thus, Larson's laws apply to filamentary clouds, aside from a trivial geometric correction factor to take into account the inclination of the filament with respect to the observer.

Appendix D

Mathematical Framework

In this Appendix, we construct the mathematical framework used to compute the numerical solutions described in Section 3.4. We define the magnetic pressure of the poloidal field P_{mag} and a useful quantity b_ϕ that depends on the toroidal field by

$$\begin{aligned} P_{mag} &= B_z^2/(8\pi) \\ b_\phi &= r^2 B_\phi^2/(8\pi). \end{aligned} \tag{D.1}$$

Defining the effective enthalpy of the turbulent gas by

$$dh = \frac{dP}{\rho}, \tag{D.2}$$

and introducing the magnetic potentials f_z and f_ϕ

$$\begin{aligned} df_z &= \frac{dP_{mag}}{\rho} \\ df_\phi &= \frac{db_\phi}{r^2\rho}, \end{aligned} \tag{D.3}$$

we may write equation 3.35 as

$$\frac{d}{dr}\left(h + \Phi + f_z + f_\phi\right) = 0. \tag{D.4}$$

We are free to specify boundary conditions for each of these potentials along the filament axis; $h = \Phi = f_z = f_\phi = 0$ at $r = 0$. Thus, equation D.4 can be integrated:

$$h + \Phi + f_z + f_\phi = 0. \tag{D.5}$$

It is useful to define a new radial variable by the transformation

$$s = \ln(r/\alpha). \tag{D.6}$$

This transformation is really necessary only to derive a special analytic solution in Section 3.3.4. However, this logarithmic transformation is useful from a numerical standpoint because it improves our ability to calculate solutions quickly and accurately out to very large radii. Under this transformation, equations 3.34 and D.4 can be combined to give

$$\frac{d^2}{ds^2}(h + f_z + f_\phi) = -\Psi, \tag{D.7}$$

where

$$\Psi = r^2\rho = \alpha^2 e^{2s}\rho. \tag{D.8}$$

To solve the differential equation D.7, we must first express h, f_z, and f_ϕ in terms of s and the new quantity Ψ. Applying equation D.2 to the isothermal and logatropic equations of state and integrating, we obtain the following formulas for the enthalpies:

$$\begin{aligned} h_{iso} &= \ln\rho = \ln\Psi - 2\ln\alpha - 2s. \\ h_{log} &= A\left(1 - \frac{1}{\rho}\right) = A\left(1 - \alpha^2 e^{2s}\Psi^{-1}\right). \end{aligned} \tag{D.9}$$

We have also used the definitions of s (equation D.6) and Ψ (equation D.8) to write the final forms of the enthalpies in terms of these variables.

Assuming constant flux to mass ratios Γ_z and Γ_ϕ we derive from equations 3.23, 3.24, and D.1

$$\begin{aligned} P_{mag} = \frac{\Gamma_z^2\rho^2}{8\pi} &= \frac{\Gamma_z^2\Psi^2}{8\pi\alpha^4 e^{4s}} \\ b_\phi &= \frac{\Gamma_\phi^2\Psi^2}{8\pi}. \end{aligned} \tag{D.10}$$

Substituting these relations into equations D.3 and integrating, we obtain

$$\begin{aligned} f_z &= \frac{\Gamma_z^2}{4\pi}(\rho - 1) = \frac{\Gamma_z^2}{4\pi}\left(\frac{\Psi}{\alpha^2 e^{2s}} - 1\right) \\ f_\phi &= \frac{\Gamma_\phi^2}{4\pi}\Psi, \end{aligned} \tag{D.11}$$

where we have applied our boundary conditions that both f_z and f_ϕ vanish along the axis of the filament where $\rho = 1$ and $\Psi = 0$. We have expressed all quantities in equations D.9 and D.11 in terms of s and

Ψ alone. Thus, equation D.7 is closed and can, at least in principle, be solved for Ψ. Since ρ, P_{mag}, and b_ϕ are written in terms of Ψ (equations D.8 and D.10), these quantities may be determined. Finally, the poloidal and toroidal magnetic fields may be obtained from equations D.1.

As a brief example, we show how equation D.7 naturally leads to the Ostriker (1964) solution discussed in Section 3.3.4. From equation D.7, we easily obtain

$$\frac{d^2}{ds^2}(\ln \Psi) = -\Psi \tag{D.12}$$

for isothermal equilibria. This equation can be solved in closed form; the solution is simply

$$\Psi = 2\ sech^2 s. \tag{D.13}$$

Converting back to r and ρ, the equation takes the form

$$\rho = \frac{8/\alpha^2}{(1 + r^2/\alpha^2)^2}. \tag{D.14}$$

The boundary condition at $r = 0$ is $\rho = 1$ in our dimensionless units; therefore, we require that $\alpha = \sqrt{8}$, giving the Ostriker solution of equation 3.37.

It is most convenient for numerical solutions to write equation D.7 as a pair of first order equations. This is best accomplished by writing the gravitational acceleration as

$$g = -\frac{d}{dr}\Phi = -\frac{1}{r}\frac{d}{ds}\Phi. \tag{D.15}$$

Then Poisson's equation 3.34 becomes

$$\frac{1}{r^2}\frac{d}{ds}(rg) = -\rho. \tag{D.16}$$

Note that there is no reason for numerical solutions to retain the constant scale factor α introduced in equation D.6. For the remainder of this section, we will take $\alpha = 1$. With the help of equation D.5 and the definition of Ψ (equation D.8), our numerical system becomes

$$\begin{aligned} \frac{d}{ds}(h + f_z + f_\phi) &= rg \\ \frac{d}{ds}(rg) &= -\Psi, \end{aligned} \tag{D.17}$$

where h, f_z, and f_ϕ are functions of Ψ by equations D.9 and D.11. Thus, equations D.17 can be rewritten as differential equations for Ψ and g. We write these equations explicitly below.

	H_1	H_2
Isothermal	-2	Ψ^{-1}
Logatropic	$-2Ae^{2s}\Psi^{-1}$	$Ae^{2s}\Psi^{-2}$

Table D.1: H_1 and H_2 are the functions related to the enthalpy by equation D.19.

Denoting the derivative $\frac{d}{ds}$ with a prime ($'$), we derive from equations D.3

$$\begin{aligned} f_z' &= \frac{\Gamma_z^2}{4\pi}e^{-2s}(\Psi' - 2\Psi) \\ f_\phi' &= \frac{\Gamma_\phi^2}{4\pi}\Psi'. \end{aligned} \tag{D.18}$$

Using equations D.9, we must calculate h' separately for the isothermal and logatropic equations of state. We note that h' can be written in the general form

$$h' = H_1(s,\Psi) + H_2(s,\Psi)\Psi', \tag{D.19}$$

where the functions H_1 and H_2 are given in Table D.1.

Using equations D.18 and D.19, we express our system of equations D.17 in its final form:

$$\begin{aligned} \Psi' &= \frac{rg - H_1 + \frac{\Gamma_z^2}{2\pi}e^{-2s}\Psi}{H_2 + \frac{\Gamma_\phi^2}{4\pi} + \frac{\Gamma_z^2}{4\pi}e^{-2s}} \\ g' &= -(g + e^{-s}\Psi). \end{aligned} \tag{D.20}$$

Since H_2 is positive definite, this dynamical system is regular on the entire interval $s \in (-\infty, \infty)$.

These equations are now in a form that can be numerically integrated given appropriate initial conditions at the axis of the filament ($r = 0$). The problem arises however that $r = 0$ occurs at $s = -\infty$ in our transformed variable; thus, we start the integration at a small but finite value of r. We expect that ρ tends to a constant value of unity near the axis for any non-singular distribution. From the definition of Ψ (equation D.8), we find that $\Psi_0 \approx e^{2s_0}$ where s_0 is the initial value chosen for s (typically ≈ -10). Recalling that g is the gravitational acceleration, we apply Gauss's law to find the initial value for g:

$$g_0 \approx -\frac{r}{2} = -\frac{1}{2}e^{s_0}. \tag{D.21}$$

References

Alves J., Lada C.J., Lada E.A., Kenyon S.J., Phelps R., 1998, Ap.J., 506, 292

Bally J., Stark A., Wilson R.W., Langer W.D., 1987, ApJ., 312, L45 Bally J., 1989, in Proceedings of the ESO Workshop on Low Mass Star Formation and Pre-main Sequence Objects, ed. Bo Reipurth; Publisher, European Southern Observatory, Garching bei Munchen

Bateman G., 1978, "MHD Instabilities", The MIT Press, Cambridge, Massachusetts

Bertoldi F., McKee C.F., 1992, Ap.J., 395, 140

Bonnor W.B., 1956, MNRAS, 116, 351

Carlqvist P., 1998, Ap.&S.S., 144, 73

Carlqvist P., Gahm G., 1992, IEEE Trans. on Plasma Science, vol. 20, no. 6, 867

Carlqvist P. & Kristen H., 1997, A&A, 324, 1115

Caselli P., Myers P.C., 1995, Ap.J., 446, 665

Castets A., Duvert G., Dutrey A., Bally J., Langer W.D., Wilson R.W., 1990, A&A, 234, 469

Chandrasekhar S., 1961, "Hydrodynamic and Hydromagnetic Stability", Oxford University Press, London

Chandrasekhar S., Fermi E., 1953, Ap.J. 118, 116

Chièze J.P., 1987, A&A, 171, 225

Chini R., Reipurth B., Ward-Thompson D., Bally J., Nyman L.-Å., Sievers A., Billawala Y., 1997, Ap.J., 474, L135

Chromey F.R., Elmegreen, B.G., Elmegreen, D.M., 1989, Ap.J., 98, 2203

Draine B., Roberge W., Dalgarno A., 1983, Ap.J., 270, 519

Dutrey A., Duvert G., Castets A., Langer W.D., Bally J., Wilson R.W., 1993, A&A, 270, 468

Dutrey A., Langer W.D., Bally J., Duvert G., Castets A., Wilson R.W., 1991, A&A, 247, L9

Ebert R., 1955, Z.Astrophys., 37, 217

Elmegreen B.G., 1989, Ap.J., 338, 178

Elmegreen B.G., 1993, in Protostars and Planets III, ed. Levy E.H., Lunine J.I., University of Arizona Press, Tucson, Arizona

Fuller G.A., Myers P.C., 1992, Ap.J., 384, 523

Gehman C.S., Adams F.C., Watkins R., 1996, Ap.J., 472, 673

Gomez de Castro A.I., Pudritz R.E., and Bastien P. 1997, Ap.J., 476, 717

Goodman A.A., Bastien P., Myers P.C., Ménard F., 1990, Ap.J., 359, 363

Goodman A.A., Jones T.J., Lada E.A., Myers P.C., 1995, Ap.J., 448, 748

Hanawa T., et al., 1993, Ap.J., 404, L83

Heiles C., 1987, Ap.J., 315, 555

Heiles C., 1990, Ap.J., 354, 483

Heiles C., 1997, Ap.J.Supp., 111, 245

Heiles C., Goodman A.A., McKee C.F., Zweibel E.G., in Protostars and Planets III, ed. Levy E.H., Lunine J.I., University of Arizona Press, Tucson, Arizona

Hildebrand R.H., 1988, QJRAS, 29, 327

Inutsuka S., Miyama S.M., 1992, Ap.J., 388, 392

Jackson J.D., 1975, "Classical Electrodynamics", John Wiley & Sons, New York

Johnstone D., Bally J., 1999, Ap.J., 510, 49L

Lada C.J., Alves J., Lada E.A., 1999, Ap.J., 512, 250

Loren R.B., 1989a, Ap.J., 338, 902

Loren R.B., 1989b, Ap.J., 338, 925

Maddalena R.J., Morris M., Moscowitz J., Thaddeus P., 1986, Ap.J., 303, 375

McCrea W.H., 1957, MNRAS, 117, 562

McKee C.F., Zweibel E.G., Goodman A.A., Heiles C., 1993, in Protostars and Planets III, ed. Levy E.H., Lunine J.I., University of Arizona Press, Tucson, Arizona

McLaughlin D.E., Pudritz R.E., 1996, Ap.J., 469, 194

Mizuno A., Onishi T., Yonekura Y., Nagahama T., Ogawa H., Fukui Y., 1995, Ap.J.,445, L161

Mouschovias T.Ch., 1976, Ap.J., 206, 753

Murphy D.C., Myers P.C., 1985, Ap.J., 298, 818

Myers P.C., Goodman A.A., 1988a, Ap.J., 326, L27

Myers P.C., Goodman A.A., 1988b, Ap.J., 329, 392

Myers P.C., Goodman A.A., Güsten R., Heiles C., 1995, Ap.J., 442, 177

Nagasawa M., 1987, Prog. Theor. Phys., 77, 635

Nakamura F., Hanawa T., Nakano T., 1993, PASJ, 45, 551

Nakamura F., Hanawa T., Nakano T., 1995, Ap.J., 444, 770

Ostriker J., 1964, Ap.J., 140, 1056

Ouyed R., Pudritz R.E., 1997, Ap.J., 482, 712

Schneider S., Elmegreen B.G., 1979, Ap.J., 41, 87

Schleuning D.A., 1998, Ap.J., 493, 811

Shu F.H., 1992, "The Physics of Astrophysics, Vol. II, Gas Dynamics", University Science Books, Mill Valley, CA

Spitzer L.Jr., 1978, "Physical Processes in the Interstellar Medium", John Wiley & Sons, New York

Stodólkiewicz J.S., 1963, Acta Astron., 13, 30

Strittmatter P.A., 1966, MNRAS, 132, 359

Tomisaka K., Ikeuchi S., Nakamura T., 1993, Ap.J., 326, 208

Uchida Y., Fukui Y., Mizuno A., Iwata T., Takaba H., 1991, Nature, 349, 140

Ungerechts H., Thaddeus P., 1987, Ap.J.Supp., 63, 645

Chapter 4

Helical Fields and Filamentary Molecular Clouds II - Axisymmetric Stability and Fragmentation

This chapter is a preprint of the paper "Helical Fields and Filamentary Molecular Clouds II - Axisymmetric Stability and Fragmentation" by Fiege J.D. and Pudritz R.E., which has been accepted for publication by the Monthly Notices of the Royal Astronomical Society.

Abstract

In Paper I (Fiege & Pudritz, 1999), we constructed models of filamentary molecular clouds that are truncated by a realistic external pressure and contain a rather general helical magnetic field. We address the stability of our models to gravitational fragmentation and axisymmetric MHD-driven instabilities. By calculating the dominant modes of axisymmetric instability, we determine the dominant length scales and growth rates for fragmentation. We find that the role of pressure truncation is to decrease the growth rate of gravitational instabilities by decreasing the self-gravitating mass per unit length. Purely poloidal and toroidal fields also help to stabilize filamentary clouds against fragmentation. The overall effect of helical fields is to stabilize gravity-driven modes, so that the growth rates are significantly reduced below what is expected for unmagnetized clouds. However, MHD "sausage" instabilities are triggered in models whose toroidal flux to mass ratio exceeds the poloidal flux to mass ratio by more than a factor of ~ 2. We find that observed filaments appear to lie in a physical regime where the growth rates of both gravitational fragmentation and axisymmetric MHD-driven modes are at a minimum.

4.1 Introduction

It has long been known that filamentary molecular clouds often have nearly periodic density enhancements along their lengths. One has only to look at the Schneider and Elmegreen (1979) catalogue of filaments to observe many examples of so-called globular filaments, where quasi-periodic cores are apparent. Such periodicity has also been noted along the central ridge of the $\int$-shaped filament of Orion A (Dutrey et al. 1991). The fragmentation of self-gravitating filaments has accordingly received some attention. Given that overdense fragments may eventually evolve into star-forming cores, it is important to have as complete a picture of fragmentation as possible.

Chandrasekhar and Fermi (1953) first demonstrated that uniform, incompressible filaments threaded by a purely poloidal magnetic field are subject to gravitational instabilities, and that magnetic field helps to decrease the growth rate of the instability. More recently, other authors (Nagasawa 1987, Nakamura, Hanawa, & Nakano 1993, Tomisaka 1996, Gehman 1996, etc.) have studied the stability of compressible, magnetized filaments. We perform a stability analysis for the equilibrium models of filamentary molecular clouds that we described in Fiege & Pudritz 1999 (hereafter FP1). Our equilibria are threaded by helical magnetic fields and are truncated by the pressure of the ISM. Most importantly, our models are constrained by observational data and are characterized by approximately r^{-2} density profiles, which are in good agreement with the observational data (Alves et al. 1998, Lada, Alves, and Lada 1998).

We demonstrated in FP1 that most filaments are well below the critical mass per unit length required for radial collapse to a spindle, and that any magnetized filamentary cloud that is initially in a state of radial equilibrium is stable against purely radial perturbations. Here, we consider more general modes of axisymmetric instability to find the growth rates and length scales on which our models may break up into periodic fragments along the axis. We show that our models are subject to two distinct types of instability. The first is a gravity-driven mode of fragmentation, which occurs when the toroidal field component is relatively weak compared to the poloidal. The second type of instability arises when the toroidal magnetic field is relatively strong compared to the poloidal field, and probably represents the axisymmetric "sausage" instability of plasma physics. We find a stability criterion for these modes, which we discuss in Section 4.9. We find that the gravitational and MHD modes blend together at wavelengths that are intermediate between the long wavelengths of purely gravitational modes, and the very short wavelengths of purely MHD-driven instabilities. These intermediate modes, in fact, represent a physical regime in which filamentary clouds fragment very slowly.

Once the process of fragmentation begins, it becomes non-linear on a timescale governed by the growth rate of the instability. We stress that our analysis is linear and, therefore, can say nothing about the non-linear evolution of filamentary clouds. However, the linear stability is important because it de-

termines the dominant length scale for the separation of fragments, and the largest scale for substructure in filamentary clouds. These fragments might eventually evolve into cores. In the present work, we limit our discussion to how the magnetic field configuration and external pressure affect spacing and mass scale of fragments.

We consider only axisymmetric modes here. The analysis of non-axisymmetric modes, most notably the kink instability (cf. Jackson 1975), will be investigated in a separate paper. One might expect fast-growing kink instabilities because of the toroidal character of the outer magnetic field. However, the centrally concentrated poloidal field is much stronger than the peak toroidal field in most of our models; this magnetic "backbone" should largely stabilize our models against the kink instability.

A brief plan of our paper is as follows. In Section 4.2, we discuss the equilibrium state of the molecular filament and atomic envelope, as well the general method of our stability calculations. We derive the equations of motion and all boundary conditions in Sections 4.3 and 4.4. We discuss the general stability properties of filaments in Section 4.5, and the test problems that we used to verify our numerical code in Section 4.6. We discuss the fragmentation of purely hydrodynamic filaments in Section 4.7, and filaments with purely poloidal or toroidal magnetic fields in Section 3.4.1. In Section 4.9, we analyze the stability of the observationally constrained models with helical fields discussed in Paper I. Finally, in Section 4.10, we discuss the significance of our results, and summarize our main findings.

4.2 General Formulation of the Problem

The models described in FP1 involve three parameters, two to describe the mass loading of the magnetic flux lines, and a third to specify the radial concentration of the filament. A Monte Carlo exploration of our parameter space led us to construct a class of magnetostatic models that are consistent with the observations. We use the equations of linearized MHD to superimpose infinitesimal perturbations on these observationally allowed equilibria. In general, we assume that molecular filaments are embedded in a less dense envelope of HI gas. In addition, we assume that the envelope is non-self-gravitating and is in equilibrium with the gravitational field of the filament. Thus, the envelope is most dense at the interface between the molecular and atomic gas, and slowly becomes more rarified with radial distance. There is, in fact, at least one known example of a filament that is embedded in molecular gas of lower density. The $\int$-shaped filament of Orion A is a very dense filament that is presently fragmenting and forming stars. Since its external medium is molecular, our treatment of the external medium as non-self-gravitating strictly does not apply to this case.

We also assume that the poloidal field component (B_z) remains constant in the HI envelope, while the toroidal field component (B_ϕ) decays with radius as r^{-1}, so that the equilibrium state of the atomic

gas is current free. We note that the magnetic field exerts no force in zeroth order in this configuration; thus, equilibrium is determined by hydrostatic balance alone. We model the HI envelope as a polytrope, which we discuss in Section 4.2.1.

Of the authors mentioned in section 4.1, only Chandrasekhar and Fermi (1953) and Nagasawa (1987) considered filaments that are truncated at finite radius. Chandrasekhar and Fermi considered the external medium to be a vacuum, while Nagasawa considered an infinitely hot and non-conducting external medium of zero density but finite pressure. We treat the external medium as a perfectly conducting medium of finite density. By using the most general possible boundary conditions between two perfectly conducting media, we self-consistently solve the equations of linearized MHD in both the molecular filament and the surrounding HI envelope. Our approach allows us to study both the effects of a finite density envelope on the predicted growth rates of the instability, and also to predict what gas motions might arise in the envelope during fragmentation.

4.2.1 The Polytropic HI Envelope

The analysis of Paper I provides the equilibrium state of the self-gravitating molecular filament. However, we must also find an equilibrium solution for the HI envelope. We assume that the envelope is non-self-gravitating and current-free, with both field components continuous across the interface. Thus, the field in the envelope is given by

$$\begin{aligned} B_z &= B_{zS} \\ B_\phi &= B_{\phi S}\left(\frac{r}{R_S}\right)^{-1}, \end{aligned} \tag{4.1}$$

where R_S is the radius of the molecular filament, as defined in Paper I, and B_{zS} and $B_{\phi S}$ are the field components at the surface.

It is required that the total pressure of the gas and magnetic field balance at the interface. Thus the boundary condition on the total pressure is given by

$$\left[P + \frac{B_z^2 + B_\phi^2}{8\pi}\right] = 0, \tag{4.2}$$

where we use square brackets to denote the jump in a quantity across the interface. Since we have assumed that the field components are continuous in our model, the pressure must be continuous also.

The magnetic field exerts no force on the gas in our current-free configuration. Therefore, we may derive the equilibrium structure of the envelope by taking the gas to be in purely hydrostatic balance

with the gravitational field of the molecular filament;

$$0 = \frac{dP_e}{dr} + \rho_e \frac{d\Phi}{dr}, \tag{4.3}$$

where subscript e refers to the HI envelope, and all quantities have their usual meanings. We assume that the gas is polytropic with polytropic index γ_e;

$$\frac{P_e}{P_S} = \left(\frac{\rho_e}{\rho_{e,S}}\right)^{\gamma_e}. \tag{4.4}$$

Pressure equilibrium at the boundary between the molecular filament and the HI gas demands that $\rho_{e,S} = P_S/\sigma_{e,S}^2$, where $\sigma_{e,S}$ is the velocity dispersion of the HI gas just outside the boundary. The gravitational potential outside of a cylindrical filament, with mass per unit length m, is given by

$$\Phi = 2Gm \ln \frac{r}{R_S}, \tag{4.5}$$

where we choose the zero point of Φ to be at the surface of the filament (radius R_S). With the help of equations 4.4 and 4.5, it is easy to solve for the density structure of the HI envelope:

$$\rho_e = \frac{P_S}{\sigma_{e,S}^2}\left(1 - 2\frac{\gamma_e - 1}{\sigma_{e,S}^2 \gamma_e} Gm \ln \frac{r}{R_S}\right)^{\frac{1}{\gamma_e - 1}}. \tag{4.6}$$

The pressure distribution may then be obtained from equation 4.4. We find that the pressure falls very slowly with radius, especially for $\gamma_e < 1$. Generally we will take $0.25 \leq \gamma_e \leq 0.5$ to simulate an atomic envelope that is nearly isobaric out to very large radius.

4.3 The Equations of Linearized MHD

In this Section, we set up the eigensystem of equations governing the motion of a perfectly conducting, self-gravitating, magnetized gas. We assume that all perturbed variables can be expressed as Fourier modes. For example, we write the perturbed density ρ_1 in the form

$$\rho_1(r, z, t) = \rho_1(r) e^{i(\omega t + m\phi + k_z z)}, \tag{4.7}$$

where $m = 0$ for the axisymmetric modes considered in this paper. We note that all quantities are written in dimensionless form using the dimensional scalings introduced in Paper I.

We shall customarily reserve the subscript "0" for equilibrium quantities and "1" quantities in first

order perturbation. In Appendix A, we show that the linearized equations of MHD reduce to the following set of coupled differential equations. The momentum equation combined with induction and continuity equations becomes

$$\begin{aligned} -\omega^2\rho_0\mathbf{v_1} &= \gamma\sigma_0^2\nabla\left[\nabla\cdot(\rho_0\mathbf{v_1})\right] \\ &+ \frac{1}{4\pi}\left\{(\nabla\times\mathbf{B_0})\times\left[\nabla\times\left(\rho_0\mathbf{v_1}\times\frac{\mathbf{B_0}}{\rho_0}\right)\right]\right. \\ &+ \left.\left[\nabla\times\nabla\times\left(\rho_0\mathbf{v_1}\times\frac{\mathbf{B_0}}{\rho_0}\right)\right]\times\mathbf{B_0}\right\} \\ &- \rho_0\nabla(i\omega\Phi_1) + \nabla\Phi_0\nabla\cdot(\rho_0\mathbf{v_1}), \end{aligned} \tag{4.8}$$

and Poisson's equation becomes

$$0 = \nabla^2\varphi_1 + \mathcal{G}\nabla\cdot(\rho_0\mathbf{v_1}). \tag{4.9}$$

where $\varphi_1 = i\omega\Phi_1$. The polytropic index γ is allowed to be discontinuous at the interface between the molecular and atomic gas; in general we define

$$\gamma = \left\{ \begin{array}{ll} 1, & r \le R_S \\ \gamma_e, & r > R_S \end{array} \right\}. \tag{4.10}$$

We have also included a parameter $\mathcal{G}$ in equation 4.9 that allows us to "turn off" self-gravity in the HI envelope, as discussed in section 4.2:

$$\mathcal{G} = \left\{ \begin{array}{ll} 1, & r \le R_S \\ 0, & r > R_S \end{array} \right\}. \tag{4.11}$$

.

Equations 4.8 and 4.9 represent the eigensystem, written entirely in terms of the perturbed momentum density $\rho_0 v_1$ and φ_1. Appendix A shows that equations 4.8 and 4.9 can be finite differenced and written in the form of a standard matrix eigenvalue problem:

$$-\omega^2\Psi = \hat{L}\Psi, \tag{4.12}$$

where $\hat{L}$ is a 4×4 block matrix operator, and Ψ is an "eigenvector" made up of the components of the

momentum density and the modified gravitational potential φ:

$$\Psi = \begin{bmatrix} \rho_0 v_{r1} \\ \rho_0 v_{\phi 1} \\ \rho_0 v_{z1} \\ \varphi_1 \end{bmatrix}. \tag{4.13}$$

It has been shown by Nakamura (1991) that the equations of self-gravitating, compressible, ideal MHD are self-adjoint; thus the eigenvalue $-\omega^2$ of equation 4.12 is purely real, and ω may be purely real or purely imaginary. When ω is real, the perturbation is stable, since it just oscillates about the equilibrium state. On the other hand, when ω is imaginary, the perturbation grows exponentially, and the system is unstable. It is these unstable modes that we are primarily concerned with, since they lead to fragmentation.

4.4 Boundary Conditions

Equation 4.12 does not yet fully specify the eigensystem since boundary conditions have yet to be imposed. There are three radial boundaries in our problem; the first two are obviously the boundaries that occur at $r = 0$ and $r \to \infty$. The third is the internal boundary that separates the molecular filament and the HI envelope. As we discussed in Section 4.3, we cannot directly difference across the interface because the density is discontinuous on that surface. Instead, we specify the appropriate boundary conditions, thus linking the perturbation of the HI envelope to that of the filament.

4.4.1 The Inner Boundary: $r = 0$

The boundary condition at the radial centre of the filament ($r = 0$) is trivial for axisymmetric modes ($m = 0$). Mass conservation demands that $\rho_0 v_r \to 0$, and the perturbed gravitational field $d\Phi_1/dr \to 0$ since the internal mass per unit length vanishes as $r \to 0$.

4.4.2 The Outer Boundary: $r \to \infty$

The outer boundary conditions are that all components of the perturbation vanish at infinity; thus, all components of the momentum density $\rho_0 \mathbf{v_1}$, and the perturbed potential φ_1, must vanish.

It would be difficult to specify these boundary conditions on a uniform grid. Therefore, we employ a non-uniform radial grid spacing defined by the transformation

$$r = S \tan \xi \tag{4.14}$$

where S is a constant scale factor; thus radial infinity is mapped to $\xi = \pi/2$. In practice, we vary ξ over the range $\delta_1 \leq \xi \leq \pi/2 - \delta_2$ for small δ_1 and δ_2, which define the inner and outer boundaries. Thus, our numerical grid extends from nearly zero radius to essentially infinite radius. Our transformation has the benefit of excellent dynamic range; by choosing S appropriately, we can arrange to have most of the grid points (approximately 2/3) inside of the molecular filament, where good resolution is most important, with progressively fewer points in the HI envelope as $r \to \infty$. In practice, we find that the eigensystem is quite insensitive to the choice of δ_2; there is no detectable change in the eigenvalue $-\omega^2$ for δ_2 corresponding to outer radii greater than $\sim 100\, r_0$, where r_0 is the core radius defined in Paper I for filamentary clouds.

4.4.3 The Molecular Filament/HI Envelope Internal Boundary

The most complex boundary in the problem occurs at the interface between the molecular and atomic gas. This surface is a contact discontinuity which moves freely, but through which no material may pass. No material may cross the boundary since this would involve a phase transition between atomic and molecular gas, which requires much longer than the dynamical timescales relevant to our problem. The boundary conditions at the interface are written as follows:

$$[\Phi] = 0 \tag{4.15}$$

$$[\nabla\Phi \cdot \hat{n}] = 0 \tag{4.16}$$

$$[\mathbf{B} \cdot \hat{n}] = 0 \tag{4.17}$$

$$\left[-\left(P + \frac{\mathbf{B}\cdot\mathbf{B}}{8\pi}\right)\hat{n} + \frac{\mathbf{B}}{4\pi}(\hat{n}\cdot\mathbf{B})\right] = 0, \tag{4.18}$$

where square brackets denote the jump in a quantity across the boundary. We note that these jump conditions apply in a Lagrangian frame that is co-moving with the deformed surface. Equations 4.15 and 4.16 demand that the gravitational potential and its first derivative (the gravitational field) must be continuous aross the interface. Equation 4.17 is the usual condition on the normal magnetic field component from electromagnetic theory; it is easily derived from the divergence-free condition of the magnetic field. The final condition, equation 4.18 states that the normal component of the total stress is continuous across the boundary.

Appendix B derives the explicit forms of these equations in terms of the components of Ψ (equation 4.13), and Appendix C shows how the boundary conditions can be included in the matrix eigensystem given by equation 4.12. Equation C.5 gives the final form of our eigensystem, which we solve, in Section 4.5, for various equilibrium configurations. In general, equation C.5 has $4 \times (N-1)$ eigenvalues, where N is the size of each block matrix, but most of these represent stable MHD waves. We generally solve

only for the dominant mode, since fragmentation will be dominated by the fastest growing axisymmetric instability (with largest positive $-\omega^2$). For this reason, our problem is well suited for iterative methods. We solve equation C.5 using the well-known method of shifted inverse iteration (cf. Nakamura 1991).

4.5 Dispersion Relations and Eigenmodes

For any equilibrium state (which may be prepared using the formulation of Paper I), we may determine a dispersion relation for the dominant mode by solving equation C.5 for $-\omega^2$ as we vary the wave number k_z. The wave number specifies the wavelength λ over which the instability operates;

$$\lambda = \frac{2\pi}{k_z}. \tag{4.19}$$

We shall be primarily concerned with the following characteristics of our dispersion relations. 1) $k_{z,max}$ is the wavenumber of maximum instability, which may determine the scale for the separation of fragments by equation 4.19. 2) $-\omega^2_{max}$ is the maximum squared growth rate for unstable modes, and determines the timescale on which the instability operated. 3) $k_{z,crit}$ is the maximum wave number for which a mode is unstable. Therefore, it sets the minimum length scale of the instability. We shall often write $k_{z,max}$, and $k_{z,crit}$, and $-\omega^2_{max}$ in dimensionless form, defined by

$$\begin{aligned} \tilde{k}_{z,max} &= r_0 k_{z,max} \\ \tilde{k}_{z,crit} &= r_0 k_{z,crit} \\ -\tilde{\omega}^2_{max} &= -\omega^2_{max}(4\pi G\rho_c)^{-1}, \end{aligned} \tag{4.20}$$

where tildes are reserved for dimensionless quantities for the remainder of this paper.

4.6 Tests of the Numerical Code

We have tested our code by reproducing some of the dispersion relations given by Nagasawa (1987) and Nakamura (1993). These test problems include the following: 1) the untruncated Ostriker solution (Nakamura), 2) untruncated filaments with purely poloidal, purely toroidal, and helical fields (Nakamura), and 3) pressure truncated filaments with constant poloidal fields (Nagasawa).

Nagasawa assumes that the external medium is non-conducting and infinitely hot, with constant pressure and zero density. Our results are indistinguishable from his when we use his boundary conditions. When we include the effects of perfect MHD (infinite conductivity) and finite density in the external medium, our results converge towards his in the limit of high velocity dispersion $\sigma_e \gtrsim 10 - 100$. At

lower, and more realistic, velocity dispersions ($\sigma_e \approx 5$), we find that the instability is slightly decreased, although the general character of his dispersion relations is preserved. These effects are further discussed in Section 4.7.

4.7 Stability of the Pressure Truncated Ostriker Solution

In this Section, we systematically examine the effects of the density and pressure of the external medium on the stability of hydrostatic filaments. The equilibrium state is the isothermal Ostriker solution discussed in Paper I;

$$\rho = \frac{\rho_c}{[1 + (r/r_0)^2]^2}, \tag{4.21}$$

which may be truncated at any desired radius by the external pressure (see Paper I).

Two independent effects are shown in Figure 4-1; curves 1 to 3 show the effect of varying the density of the external medium, while the solid curves (curves 4 to 8) shows the effect of varying the external pressure, or equivalently the mass per unit length.

We first consider the effect of varying the density of the HI envelope. Equation 4.6 gives the density, as a function of radius, for our polytropic envelope. We note that the density is controlled, mainly, by the velocity dispersion $\sigma_{e,S}$ just outside of the molecular filament. The dashed curves (1 to 3) in Figure 4-1 have been computed using using the same equilibrium solution for the molecular filament (see Table 4.1), but different values for $\sigma_{e,S}$. For all three curves, we have assumed that $P_S/\langle P \rangle = 0.801$ and $m/m_{vir} = 0.199$. We find that envelopes with lower velocity dispersions and higher densities have a slightly stabilizing effect. Although we have taken the external medium to be non-self-gravitating, it responds dynamically and self-consistently to the gravitational field and motions of the molecular filament. As the filament fragments, the deformation of the surface and the changes in the gravitational potential induce motions in the surrounding gas. These motions slightly resist the fragmentation of the filament, because of the finite inertial mass of the envelope. We have also computed one solution, shown as the curve numbered 1, where we have assumed that the external medium is infinitely hot, and of infinitely low density, which is consistent with Nagasawa's (1987) treatment of the boundary conditions (see Section 4.4). It is apparent that dispersion relations computed with fully self-consistent boundary conditions converge to this curve in the limit of high velocity dispersion. In practice, we find essentially no difference when $\sigma_e/\sigma_c \gtrsim 10$.

We now consider the effect of the external pressure, or equivalently, the effect of the mass per unit length. The virial equation from Paper I demonstrates that pressure truncation is equivalent to a

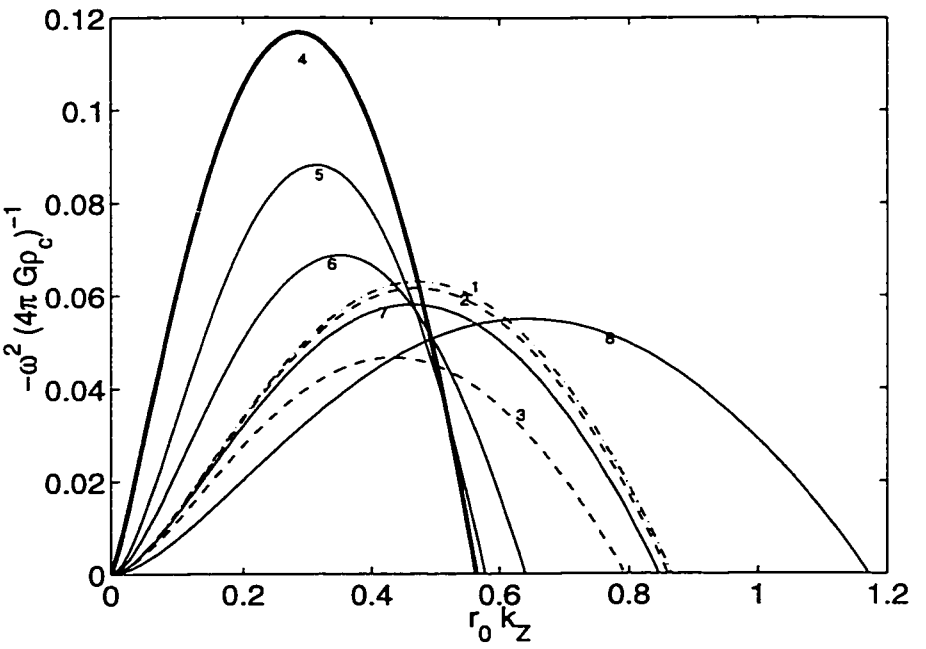

Figure 4-1: We have computed dispersion relations for truncated, unmagnetized, isothermal filaments. The external medium has finite density and a velocity dispersion of $\sigma_e = 5\sigma$ for the solid curves. The curve shown as dot-dashed has an infinitely hot, zero density, external medium. The dashed curves have been computed using external media with velocity dispersions $\sigma_e = 10\sigma$ for the upper curve, and $\sigma_e = 2.5\sigma$ for the lower curve. Table 4.1 summarizes the results shown here.

reduction of the mass per unit length for hydrostatic filaments;

$$\frac{m}{m_{vir}} = 1 - \frac{P_S}{\langle P \rangle}, \tag{4.22}$$

where $m_{vir} = 2\langle\sigma^2\rangle/G$ is the virial mass per unit length. Thus, $P_S/\langle P\rangle$ and m/m_{vir} cannot be varied independently for unmagnetized filaments. The solid lines in Figure 4-1 (curves 4 to 8) show dispersion relations for the truncated Ostriker solution, where we have assumed that the velocity dispersion of the HI envelope just outside of the filament is five times that of the molecular gas (see Table 4.1). We find that more severely pressure truncated filaments, with higher $P_S/\langle P\rangle$ and lower m/m_{vir}, are less unstable than more extended filaments. Thus, pressure truncation suppresses the gravitational instability of the filament. This result is easy to understand. Decreasing the mass per unit length decreases the gravitational force that drives the instability. Therefore, pressure dominated filaments, with external pressure comparable to the central pressure, are more stable than those that are dominated by self-gravity (eg. untruncated filaments).

Figure 4-2 shows how the mass per unit length affects the wave number $k_{z,max}$ and growth rate $-\omega^2_{max}$ of the most unstable mode, as well as the critical wave number $k_{z,crit}$. We find that the growth

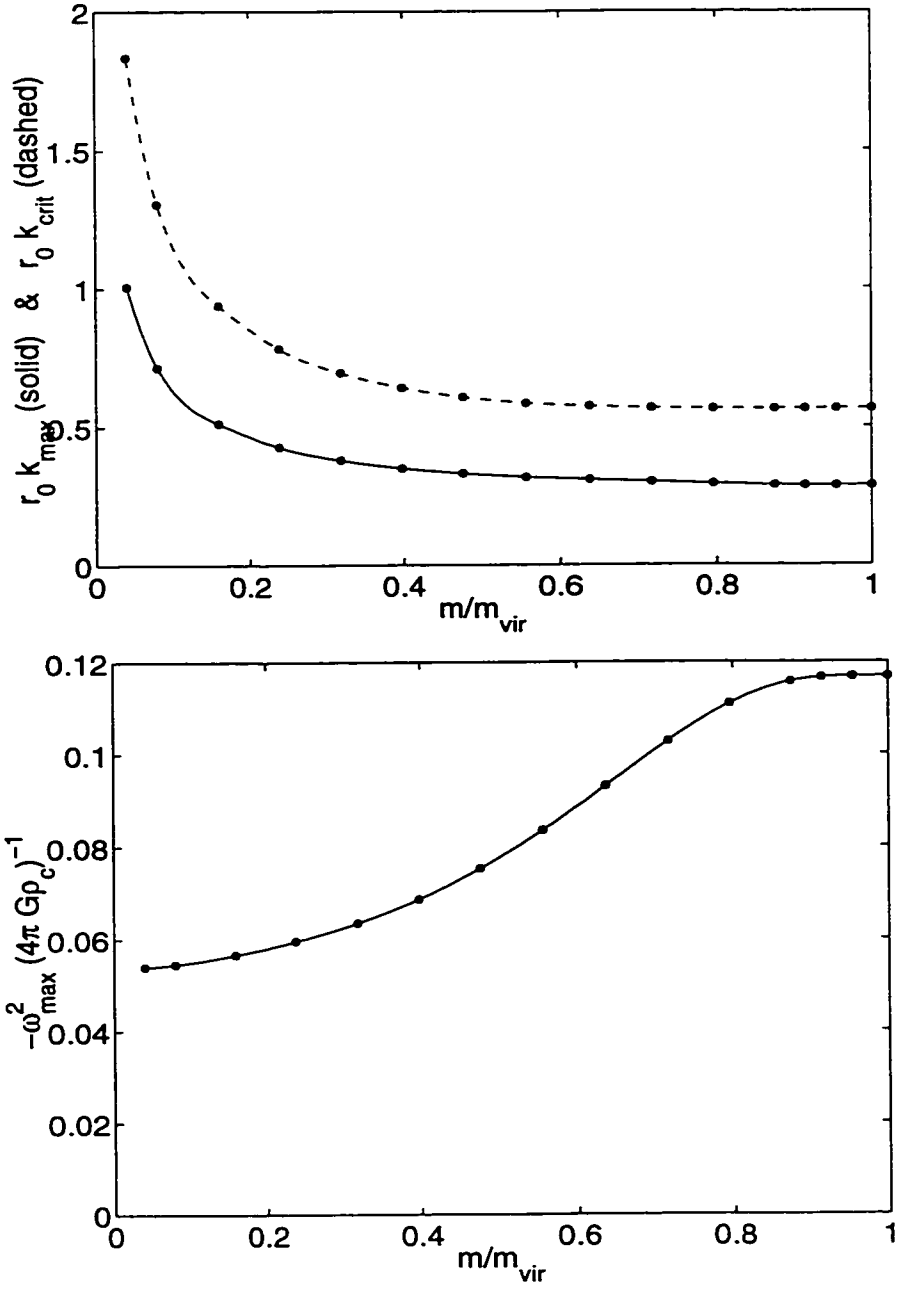

Figure 4-2: We plot the dispersion parameters $k_{z,max}$, $k_{z,crit}$, and $-\omega^2$ for unmagnetized, pressure-truncated filamentary clouds, as a function of m/m_{vir}.

	m/m_{vir}	$P_S/\langle P\rangle$	C	$\tilde{k}_{z,max}$	$-\tilde{\omega}^2_{max}$	$\tilde{k}_{z,crit}$
1	0.199	0.801	0.149	0.472	0.063	0.866 [a]
2	0.199	0.801	0.149	0.47	0.0616	0.861 [b]
3	0.199	0.801	0.149	0.432	0.0467	0.791 [c]
4	1	0	∞	0.285	0.117	0.564
5	0.597	0.403	0.537	0.313	0.0882	0.578
6	0.398	0.602	0.362	0.35	0.0687	0.64
7	0.199	0.801	0.149	0.462	0.0581	0.847
8	0.0995	0.901	-0.027	0.639	0.0549	1.17

[a] Infinitely hot external medium.
[b] "Hot external medium": $\sigma_e = 10\sigma$
[c] "Cold external medium": $\sigma_e = 2.5\sigma$

Table 4.1: We give the wave numbers and growth rates for the fastest growing modes of truncated, unmagnetized filaments (See Figure 4-1). We also give the critical growth rate, beyond which the filament is stable against axisymmetric perturbations. The tildes indicate dimensionless variables, as defined by equations 4.20. The external medium has finite density and a velocity dispersion of $\sigma_e = 5\sigma$, except where otherwise indicated in the footnotes.

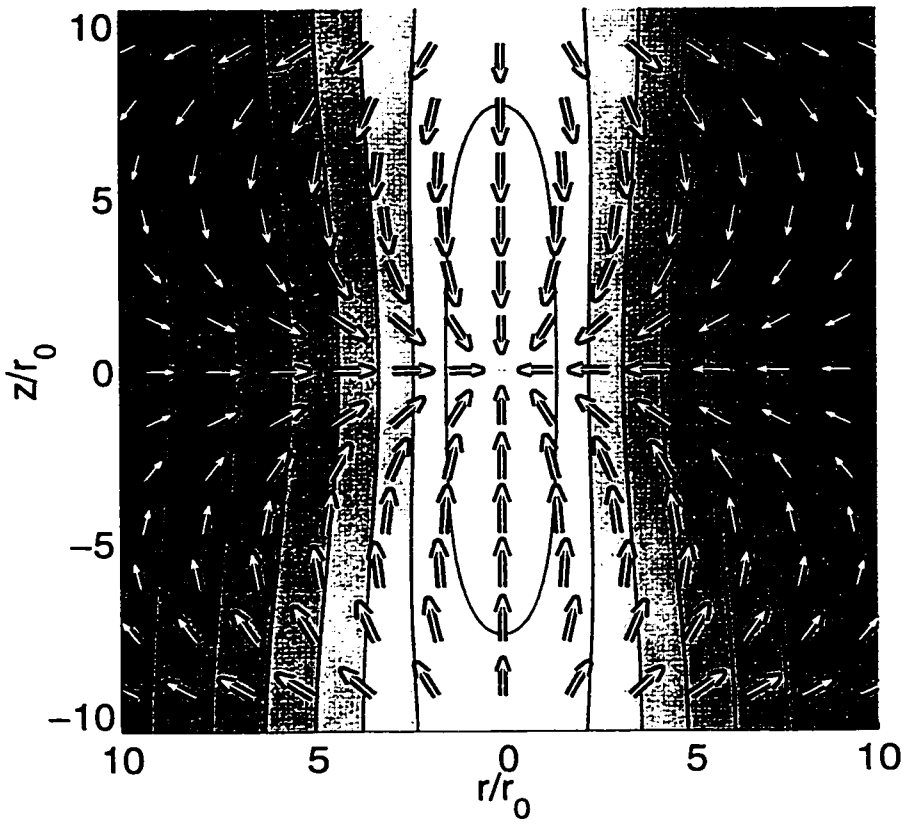

Figure 4-3: We show the eigenmode corresponding to the most unstable mode of the untruncated Ostriker solution ($r_0 k_{z,max} = 0.285$, $-\omega^2(4\pi G\rho_c)^{-1} = 0.117$). The contours show the density, while the arrows show the velocity field. We note that the segment shown is just one wavelength in the periodically fragmenting filament. The arrows are scaled logarithmically with the velocity, as discussed in the text.

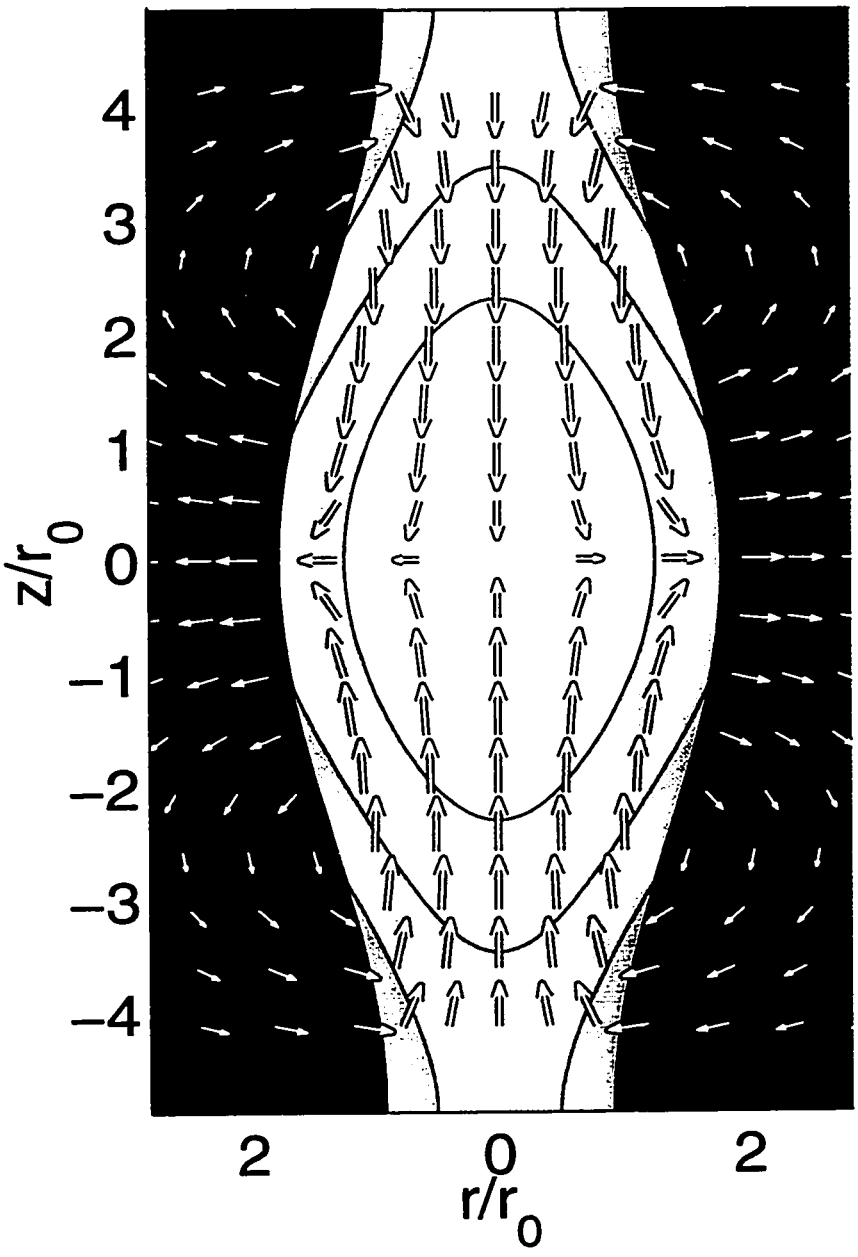

Figure 4-4: We show the eigenmode corresponding to the most unstable mode of a truncated Ostriker model with mass per unit length $m/m_0 = 5$ ($m/m_{vir} = 0.199$). For this mode, $r_0 k_{z,max} = 0.462$ and $-\omega^2(4\pi G\rho_c)^{-1} = 0.449$.

rate is significantly suppressed when $m/m_{vir} \lesssim 0.8$. The wave numbers remain essentially constant until $m/m_{vir} \approx 0.3$. For smaller masses per unit length, the wave number increases, corresponding to fragmentation on smaller length scales.

Two examples of eigenmodes are shown in figures 4-3 and 4-4 for unmagnetized filaments; the first shows the fragmentation of the untruncated Ostriker solution, while the second is significantly truncated ($m/m_{vir} = 0.199$). These figures show a single wavelength in the periodic fragmentation of a filament. We note that the size of the perturbation is greatly exaggerated in these figures, where we typically add a perturbation of $\approx 33\%$ (in peak density) to the unperturbed solution.

The arrows in figures 4-3 and 4-4 show the velocity field, but the scaling is logarithmic due to the large range of velocities that must be shown. Specifically, $arrow\ length \propto log_{10}(1 + \alpha v/\sigma_c)$, where we choose $\alpha \approx 50$. Both cases have purely poloidal velocity fields. The untruncated case shows an asymmetric infall onto the fragment, with almost purely radial infall near the fragments, and some radially outward motions between them. On the other hand, the truncated model shows infall along the axis, but the motions are actually radially outward in the vicinity of the fragment. This is due simply to the outward bulging of the fragment, which can occur because there is no infalling material approaching from the radial direction.

There are interesting motions in the gas outside of the truncated filament shown in Figure 4-4. We observe inward motions, that are driven by external pressure crushing the less dense parts of the filament between fragments. At the same time, the bulging of the filament near the fragments drives a radially outward flow in the surrounding gas. We emphasize that no mass is actually exchanged between the molecular filament and the surrounding atomic gas. Gas flows towards the fragments along the filament axis, which then bulge outwards slightly. This induces circulatory motions in the surrounding envelope in which gas flows away from the fragments and towards the increasingly evacuated inter-fragment regions.

4.8 Stability of Truncated Filaments with Purely Poloidal and Purely Toroidal Fields

Following Paper I, we study the effects of poloidal and toroidal fields separately before considering the more general case of helical fields in Section 4.9. We note that none of the equilibrium models used in this Section fall within the range of observationally allowed models from Paper I. These models are useful, however, in that they provide insight into the roles played by the field components in more general helical field models.

	Γ_z	C	$P_S/\langle P\rangle$	$\tilde{k}_{z,max}$	$-\tilde{\omega}^2_{max}$	$\tilde{k}_{z,crit}$
1	0	0.149	0.801	0.462	0.0581	0.846
2	1	0.146	0.813	0.421	0.0513	0.751
3	2.5	0.133	0.859	0.325	0.0348	0.556
4	5	0.116	0.929	0.254	0.023	0.428
5	10	0.106	0.977	0.225	0.0184	0.377
6	25	0.102	0.996	0.216	0.017	0.362
7	50	0.101	0.999	0.214	0.0168	0.359

Table 4.2: We give the wave numbers and growth rates for the fastest growing modes of truncated filaments with poloidal field only (See Figure 4-5). We also give the critical growth rate, beyond which the filament is stable against axisymmetric perturbations. In all cases, the mass per unit length is $5m_0$ ($m/m_{vir} = 0.199$), which falls within the range of observationally allowed masses per unit length found in Paper I. We have also assumed an external medium which is perfectly conducting and of finite density, with $\sigma_e = 5\sigma$.

4.8.1 Poloidal Field Results

Figure 4-5 shows a sequence of dispersion relations, in which we have varied the poloidal flux to mass ratio Γ_z while holding the mass per unit length constant at $m = 5\ m_0$ ($m/m_{vir} = 0.199$). We observe that the poloidal field has a stabilizing effect on the filament, but that the stabilization saturates for $\Gamma_z \gtrsim 10$. The critical and most unstable wave numbers are decreased by the poloidal field, but this effect also saturates when $\Gamma_z \gtrsim 10$. These results agree qualitatively with those obtained by Nagasawa (1987) for pressure truncated isothermal filaments threaded by purely poloidal fields, although the degree of stabilization is greater in our model. Chandrasekhar and Fermi (1953) also find that poloidal fields stabilize incompressible filaments, but they do not find any saturation of the stabilizing effect. This is especially apparent in Figure 4-6, where we have plotted $k_{z,max}$, $k_{z,crit}$, and $-\omega^2_{max}$ as a funtion of Γ_z.

Figures 4-7 and 4-8 show two eigenmodes corresponding, respectively, to a weak ($\Gamma_z = 1$) and relatively strong ($\Gamma_z = 5$) poloidal field. Naturally, as the poloidal flux to mass ratio increases, and the field strengthens, the gas becomes more tightly constrained to move only along the field lines. When $\Gamma_z \gtrsim 10$, the motions are almost entirely poloidal; further increasing Γ_z has no significant effect on the motions, and, hence, no significant effect on the dispersion relations.

4.8.2 Toroidal Field Results

Finally we consider models in which the magnetic field is purely toroidal. We stress that these models are illustrative only, and certainly do not represent realistic models of filamentary clouds. Figure 4-9 shows a sequence of dispersion relations, in which we have varied the toroidal flux to mass ratio Γ_ϕ while holding the mass per unit length constant at $m = 5\ m_0$ ($m/m_{vir} = 0.199$). We observe that the toroidal field strongly stabilizes the cloud against fragmentation. Contrary to the effects of the poloidal

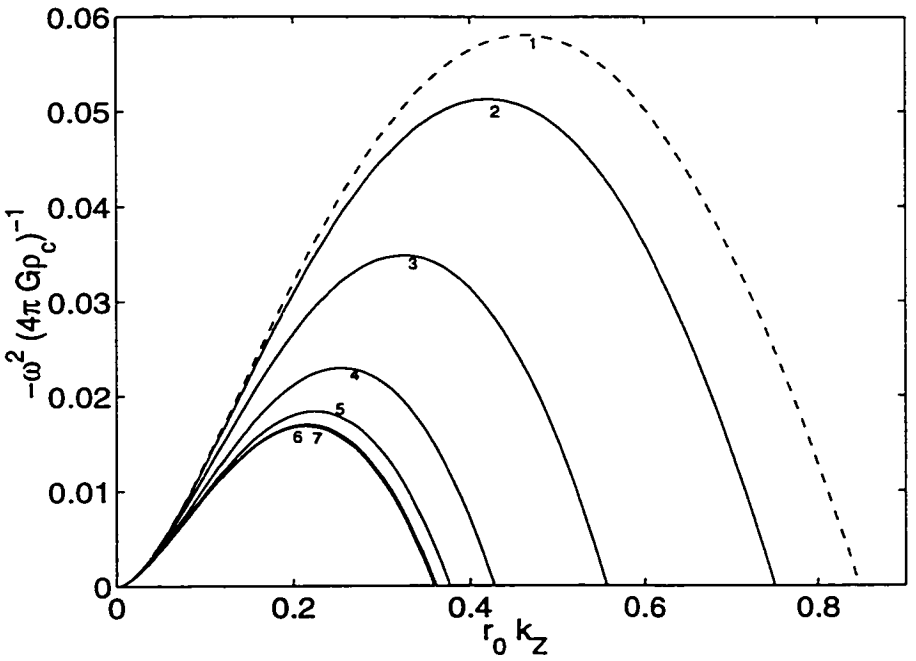

Figure 4-5: We have computed dispersion relations for truncated filaments with poloidal field only. In all cases, the mass per unit length is $5m_0$ ($m/m_{vir} = 0.199$), which falls within the range of observationally allowed masses per unit length found in Paper I. We have also assumed an external medium which is perfectly conducting and of finite density, with $\sigma_e = 5\sigma$. The labeling of the dispersion relations corresponds to the numbering in Table 4.2.

field, the stabilization does not saturate; in fact, the models are completely stable against fragmentation when $\Gamma_\phi \gtrsim 10$. Purely toroidal fields have a stabilizing effect because fragmentation requires a flow of material along the axis of the filament, which must result in substantial compression of the toroidal flux tubes. This results in a gradient in the magnetic pressure $1/8\pi\ \partial B_\phi^2/\partial z$ which resists this motion. When the toroidal flux to mass ratio Γ_ϕ is sufficiently high, the toroidal flux tubes can resist compression and arrest fragmentation altogether. The effects of the varying Γ_ϕ are most readily apparent in Figure 4-10, where we have plotted $k_{z,max}$, $k_{z,crit}$, and $-\omega^2_{max}$ as a function of of Γ_ϕ. We have shown an example of an eigenmode in figures 4-11, where $\Gamma_\phi = 5$. In this case, the toroidal field becomes strongest near the fragments. The gas motions are purely poloidal in both cases, with a "reverse flow" just outside of the filament. As in the purely hydrodynamic case, the gas is pushed radially outward near the fragment, and flows toward the empty regions between them. However, the pinch of the toroidal field restricts the motions to a narrow band just outside the filament.

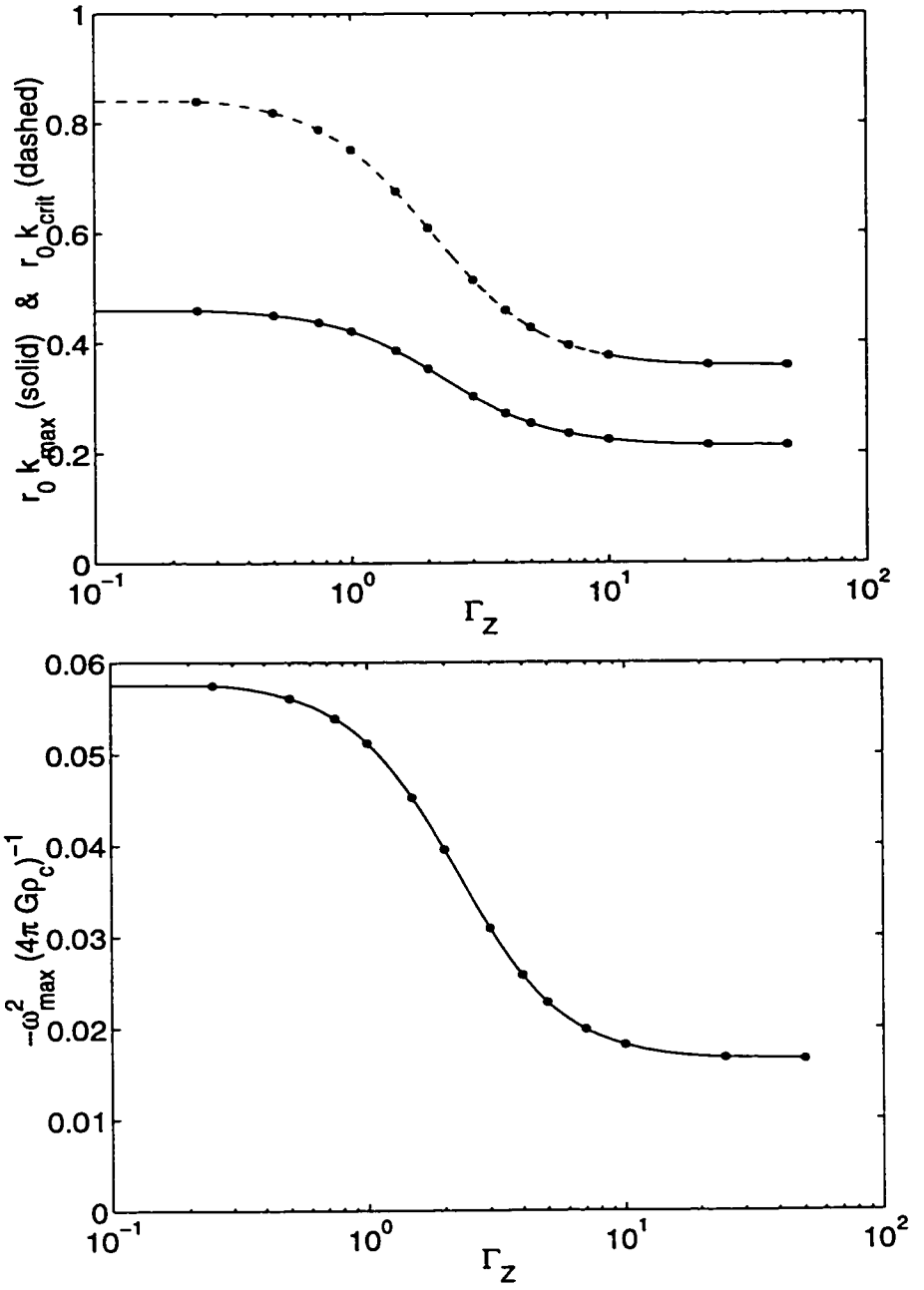

Figure 4-6: We plot the dispersion parameters $k_{z,max}$, $k_{z,crit}$, and $-\omega^2$ for poloidally magnetized, pressure-truncated filamentary clouds ($m = 5m_0$), as a function of Γ_z.

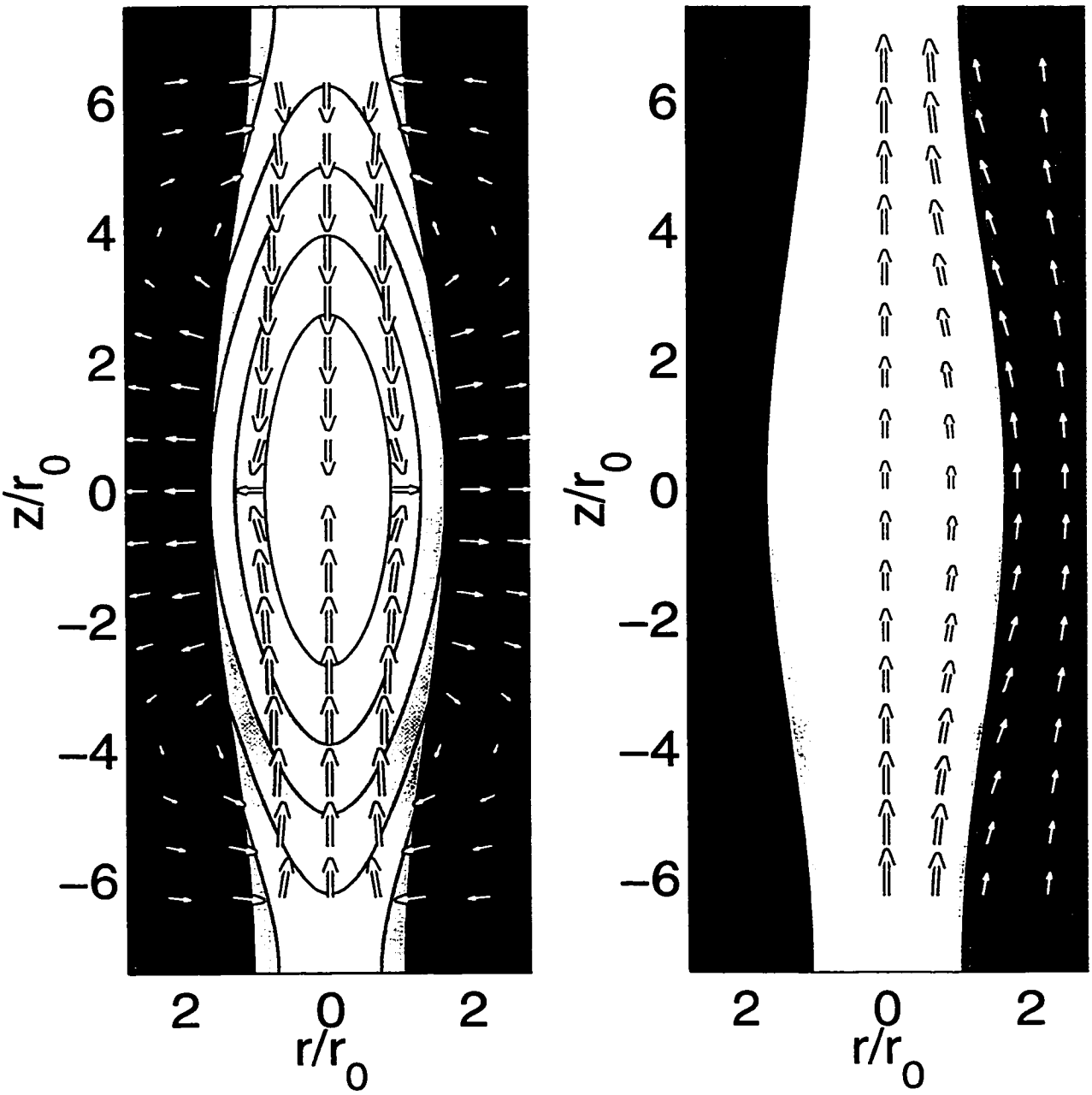

Figure 4-7: We show the eigenmode corresponding to the most unstable mode of a truncated magnetized model with a weak poloidal field ($\Gamma_z = 1$), and mass per unit length $m/m_0 = 5$ ($m/m_{vir} = 0.199$). For this mode, $r_0 k_{z,max} = 0.421$ and $-\omega^2(4\pi G\rho_c)^{-1} = 0.0512$. The figures represent a) (left panel) density contours with superimposed poloidal velocity vectors. We note that there is no toroidal velocity when the field is purely poloidal. and b) (right panel) The magnetic field. We always represent the magnetic field as a split-frame figure, with poloidal field vectors shown on the right, and contours to represent the toroidal field on the left. Since no toroidal field is generated in this case, the left side of the figure is left blank.

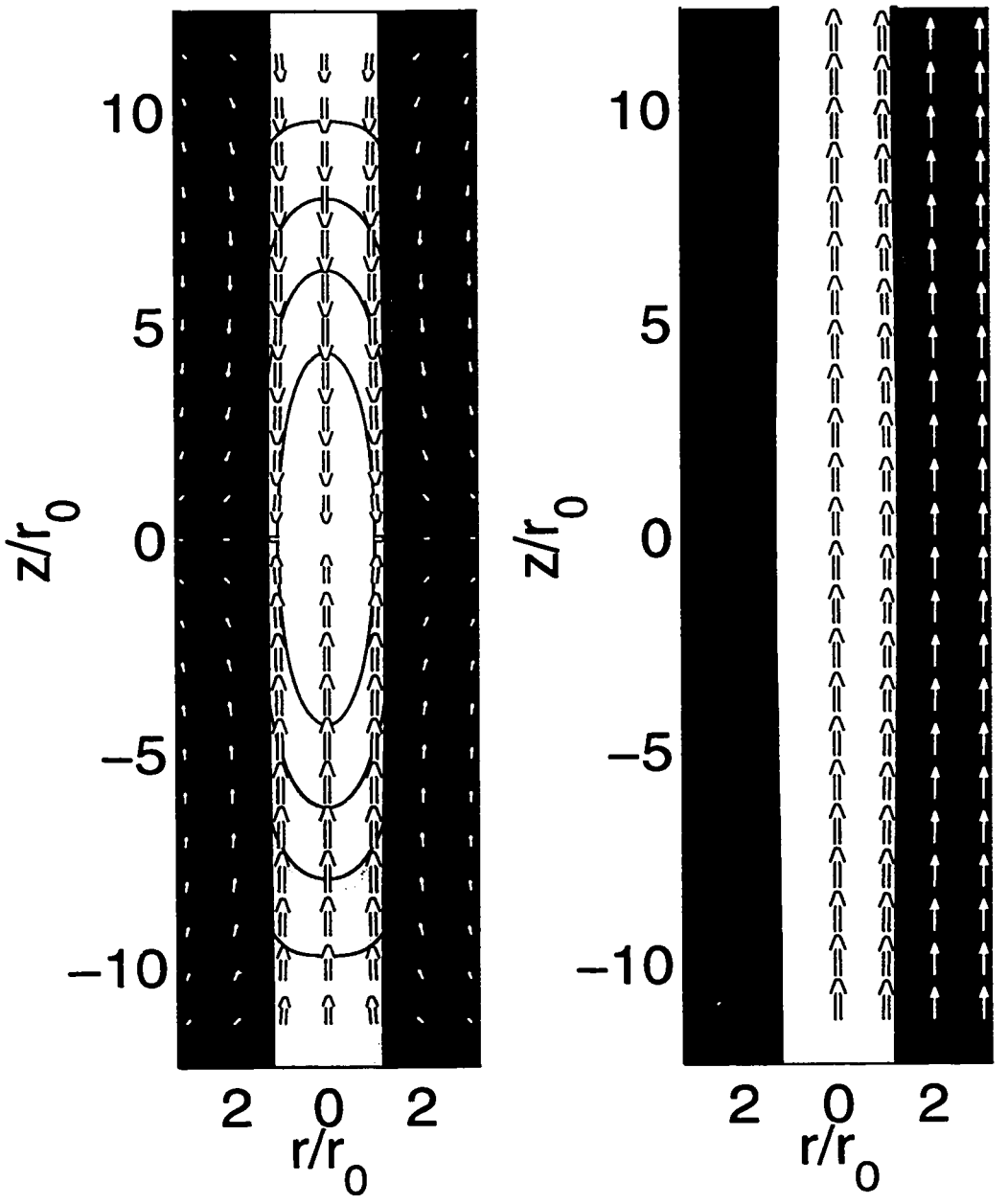

Figure 4-8: We show the eigenmode corresponding to the most unstable mode of a truncated magnetized model with a relatively strong poloidal field ($\Gamma_z = 5$), and mass per unit length $m/m_0 = 5$ ($m/m_{vir} = 0.199$). For this mode, $r_0 k_{z,max} = 0.225$ and $-\omega^2(4\pi G\rho_c)^{-1} = 0.0228$. The figures represent a) (left panel) density contours with superimposed poloidal velocity vectors. We note that there is no toroidal velocity when the field is purely poloidal. and b) (right panel) The magnetic field. We always represent the magnetic field as a split-frame figure, with poloidal field vectors shown on the right, and contours to represent the toroidal field on the left. Since no toroidal field is generated in this case, the left side of the figure is left blank.

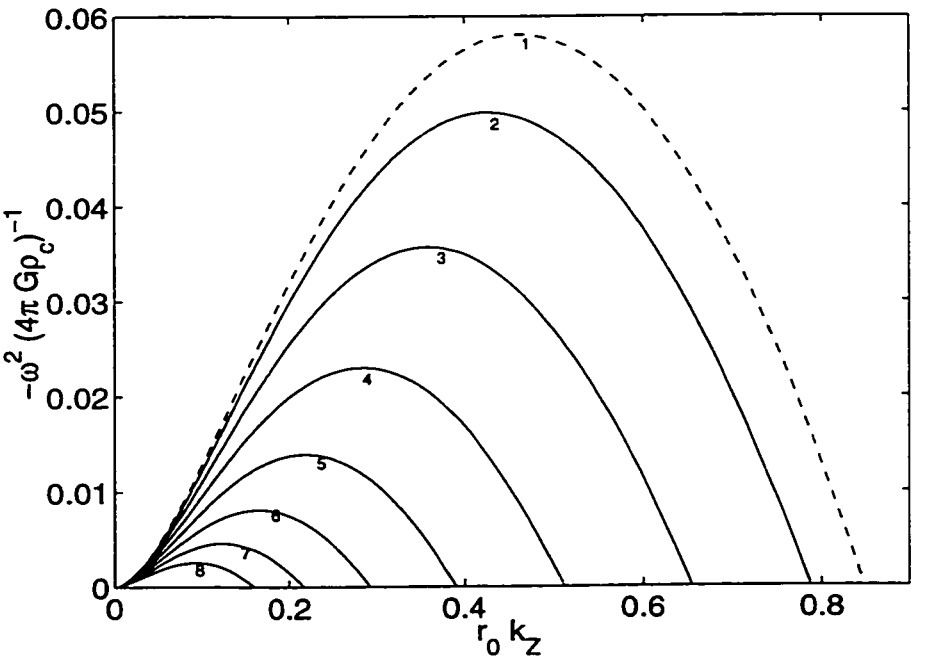

Figure 4-9: We have computed dispersion relations for truncated filaments with toroidal field only. In all cases, the mass per unit length is $5m_0$ ($m/m_{vir} = 0.199$), which falls within the range of observationally allowed masses per unit length found in Paper I. We have also assumed an external medium which is perfectly conducting and of finite density, with $\sigma_e = 5\sigma$. The labeling of the dispersion relations corresponds to the numbering in Table 4.3.

	Γ_ϕ	C	$P_S/\langle P\rangle$	$k_{z,max}$	$-\tilde{\omega}^2_{max}$	$k_{z,crit}$
1	0	0.149	0.801	0.462	0.0581	0.846
2	1	0.162	0.764	0.427	0.0499	0.787
3	2	0.199	0.683	0.358	0.0357	0.655
4	3	0.253	0.598	0.284	0.023	0.513
5	4	0.318	0.523	0.218	0.0139	0.39
6	5	0.392	0.462	0.165	0.00811	0.293
7	6	0.471	0.413	0.123	0.0046	0.217
8	7	0.555	0.372	0.0914	0.00256	0.16

Table 4.3: We give the wave numbers and growth rates for the fastest growing modes of truncated filaments with toroidal field only (See Figure 4-9). We also give the critical growth rate, beyond which the filament is stable against axisymmetric perturbations. In all cases, the mass per unit length is $5m_0$ ($m/m_{vir} = 0.199$), which falls within the range of observationally allowed masses per unit length found in Paper I. We have also assumed an external medium which is perfectly conducting and of finite density, with $\sigma_e = 5\sigma$.

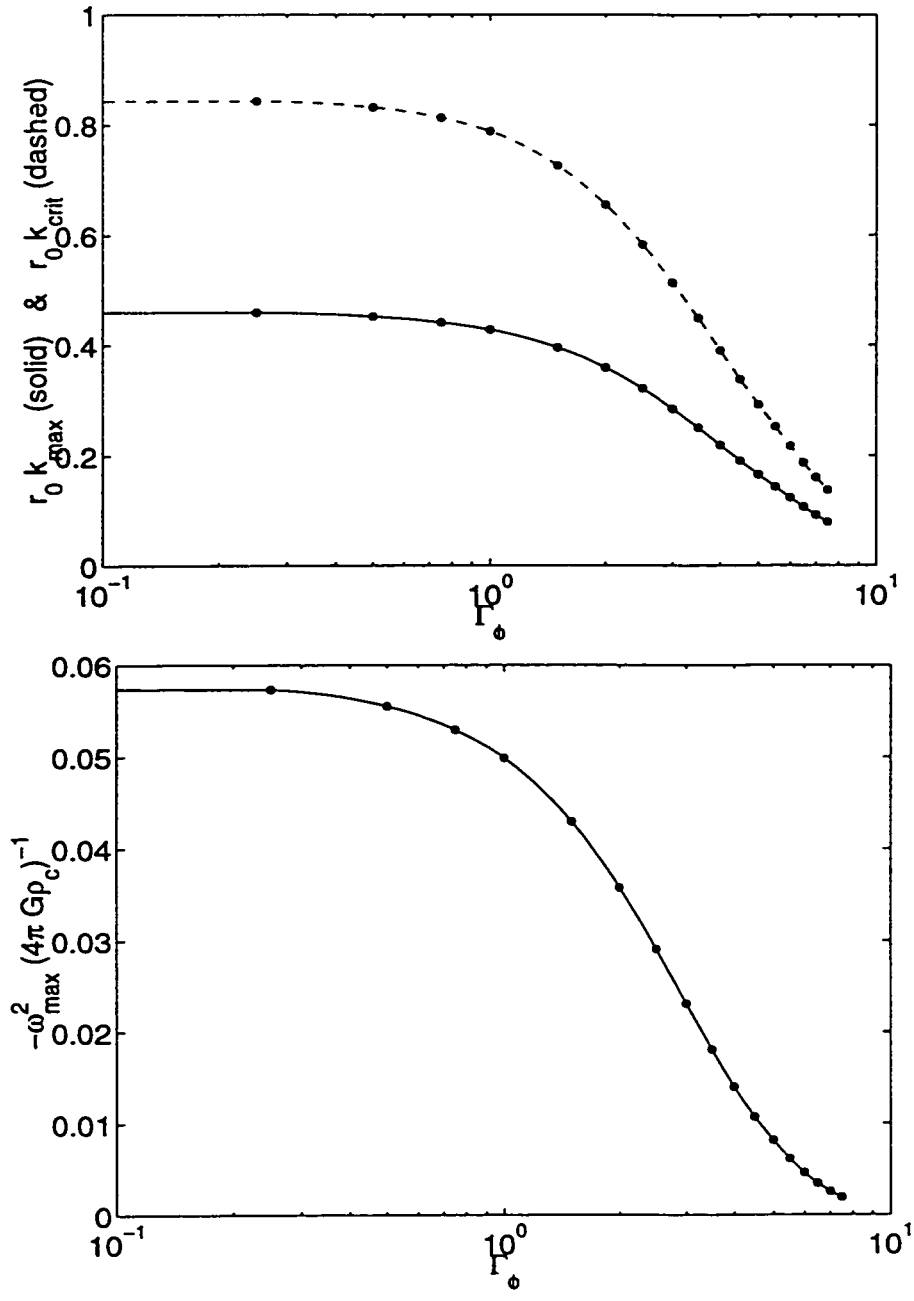

Figure 4-10: We plot the dispersion parameters $k_{z,max}$, $k_{z,crit}$, and $-\omega^2$ for toroidally magnetized, pressure-truncated filamentary clouds ($m = 5m_0$), as a function of Γ_ϕ.

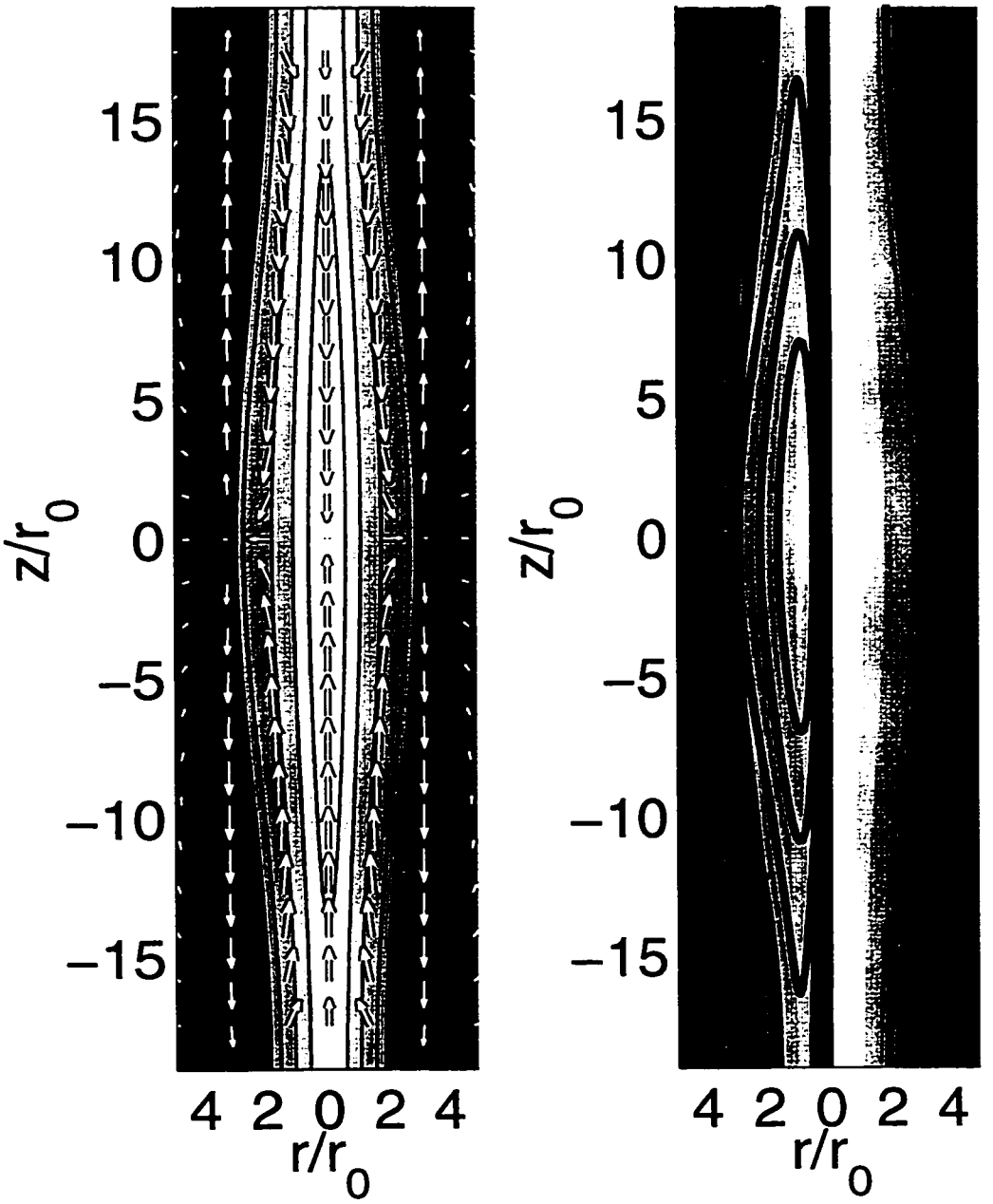

Figure 4-11: We show the eigenmode corresponding to the most unstable mode of a truncated magnetized model with a toroidal field ($\Gamma_\phi = 5$), and mass per unit length $m/m_0 = 5$ ($m/m_{vir} = 0.199$). For this mode, $k_{z,max} = 0.165$ and $-\omega^2(4\pi G\rho_c)^{-1} = 0.0081$. The figures represent a) (left panel) density contours with superimposed poloidal velocity vectors. We note that there is no toroidal velocity when the field is purely toroidal. and b) (right panel) The magnetic field. We always represent the magnetic field as a split-frame figure, with poloidal field vectors shown on the right, and contours to represent the toroidal field on the left. Since no poloidal field is generated in this case, the right side of the figure is left blank.

4.9 Stability of Filamentary Clouds With Helical Magnetic Fields

In this Section, we consider the stability of models that best agree with the observational constraints found in Paper I:

$$0.11 \leq \frac{m}{m_{vir}} \leq 0.43$$
$$0.012 \leq \frac{P_S}{\langle P \rangle} \leq 0.75.$$
$$0.2 \leq X \leq 5, \tag{4.23}$$
$$\tag{4.24}$$

where the reader is refered to Paper I for a description of the various quantities. We used a Monte Carlo exploration of our three dimensional (Γ_z, Γ_ϕ, and C) parameter space to find a set of models that agree with these constraints. We use the same set of models here to determine the stability properties of filamentary clouds threaded by helical fields. It is not necessary to show full dispersion relations for all models, since most of the useful information is contained in the dispersion parameters $k_{z,max}$, $k_{z,crit}$, and $-\omega^2_{max}$. Thus, we try to determine which combination of model parameters Γ_z, Γ_ϕ, and C controls the stability properties.

We find that the dispersion parameters $k_{z,max}$, $k_{z,crit}$, and $-\omega^2_{max}$ are best correlated with the ratio Γ_ϕ/Γ_z. Figures 4-12 to 4-14 show scatter plots of these dispersion parameters as functions of Γ_ϕ/Γ_z. It is obvious from these figures that we have found two types of unstable mode in our calculation; the two types of unstable mode are mostly well separated in Figures 4-12 to 4-14, but join together when $\Gamma_\phi/\Gamma_z \approx 2$. The first, which occurs when Γ_ϕ/Γ_z is small, is a gravity-driven instability, which is analogous to the modes found for purely hydrodynamic models (Section 4.7), and MHD models in which the field is purely poloidal or toroidal (Section 3.4.1). We note that increasing Γ_ϕ/Γ_z substantially decreases the growth rate of the instability. This is in accord with the findings of Section 3.4.1, where we found that increasing Γ_ϕ and Γ_z both stabilize gravity driven modes, but Γ_ϕ is much more effective. In fact, virtually all of the gravity-driven modes in Figure 4-13 have growth rates that are significantly lower than the growth rates of unmagnetized filaments, as well as filaments with purely poloidal fields (shown in figures 4-1 and 4-5 respectively). Typically, we find

$$\begin{aligned} 0.0005 &\lesssim -\tilde{\omega}^2_{max} \lesssim 0.03 \\ 0.1 &\lesssim \tilde{k}_{z,max} \lesssim 0.3 \\ 0.2 &\lesssim \tilde{k}_{z,crit} \lesssim 0.6, \end{aligned} \tag{4.25}$$

where the tildes refers to the dimensionless growth rates and wave numbers, as defined in equation 4.20.

By taking the inverse of $\sqrt{-\omega^2}$, we find a growth timescale of

$$\tau_{frag} = 1.8 \left(\frac{-\tilde{\omega}^2_{max}}{0.01} \right)^{-1/2} \left(\frac{n_c}{10^4\ cm^{-3}} \right)^{-1/2}\ Myr. \tag{4.26}$$

where n_c is the central number density of the filament. We have chosen a fiducial central density of $10^4\ cm^{-3}$ because radially extended (0.5 pc diameter) filamentary structure is clearly visible in $C^{18}O$ maps of Taurus (Onishi et al. 1998). $C^{18}O$ molecules require a density of at least $\sim 2 \times 10^3\ cm^{-3}$ for excitation, and our models predict that the central density should be several times higher than the bulk of the filament. Nevertheless, the central densities of filaments have not yet been accurately measured, so this fiducial central density should be treated with caution. The radial signal crossing time is approximately given by

$$\tau_x \approx \frac{Rs}{\sigma} = 0.49 \left(\frac{R_S}{0.25\ pc} \right) \left(\frac{0.5\ km\ s^{-1}}{\sigma} \right)\ Myr. \tag{4.27}$$

Since the signal crossing time is somewhat longer than the fragmentation timescale, we expect filamentary clouds to achieve radial quasi-equilibrium before fragmentation destroys the filament in a few times τ_{frag}; thus, our analysis is consistent with the assumption of quasi-equilibrium used in Paper I.

The second type of unstable mode is driven by the magnetic field. These MHD-driven instabilities are triggered when $\Gamma_\phi/\Gamma_z \gtrsim 2$. Figures 4-12 to 4-14 show that this mode joins onto the gravity-driven modes, but extends to very high growth rates and very large wave numbers. Since large wave numbers correspond to small wavelengths, gravity cannot be important, as a driving force, for these modes. They are, however, most unstable when the toroidal flux wrapping the filament is large, compared to the poloidal flux. This suggests that the mode is an MHD instability. In fact the criterion that we have found is analogous to the famous stability criterion for MHD "sausage" modes:

$$B_{\phi S} > \sqrt{2} B_z \tag{4.28}$$

(cf. Jackson 1975). The analogy is far from perfect because equation 4.28 applies to the case of a uniform plasma cylinder threaded by a constant poloidal magnetic field, and surrounded by a toroidal field produced by a thin axial current sheet along the surface of the plasma. However, the axial current distribution in our case is distributed throughout the filament. Nevertheless, the similarity between equation 4.28 and our own instability criterion is very suggestive.

We do not find MHD-driven instabilities for models with purely toroidal fields. We note that the stability criterion for a non-self-gravitating plasma column pinched by a purely toroidal field can be

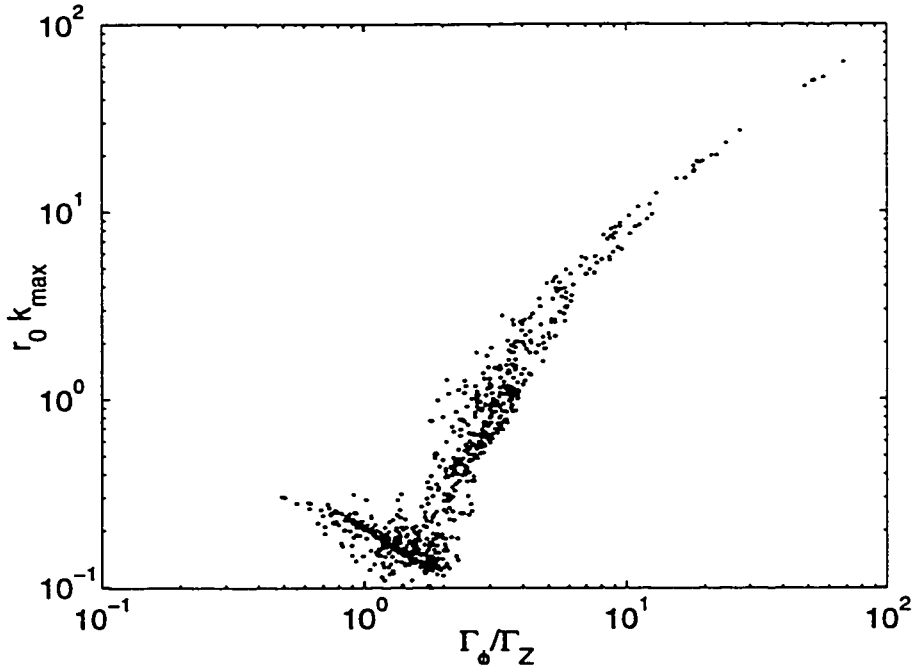

Figure 4-12: The most unstable wave numbers for a random sample of helically magnetized models that agree with our constraints.

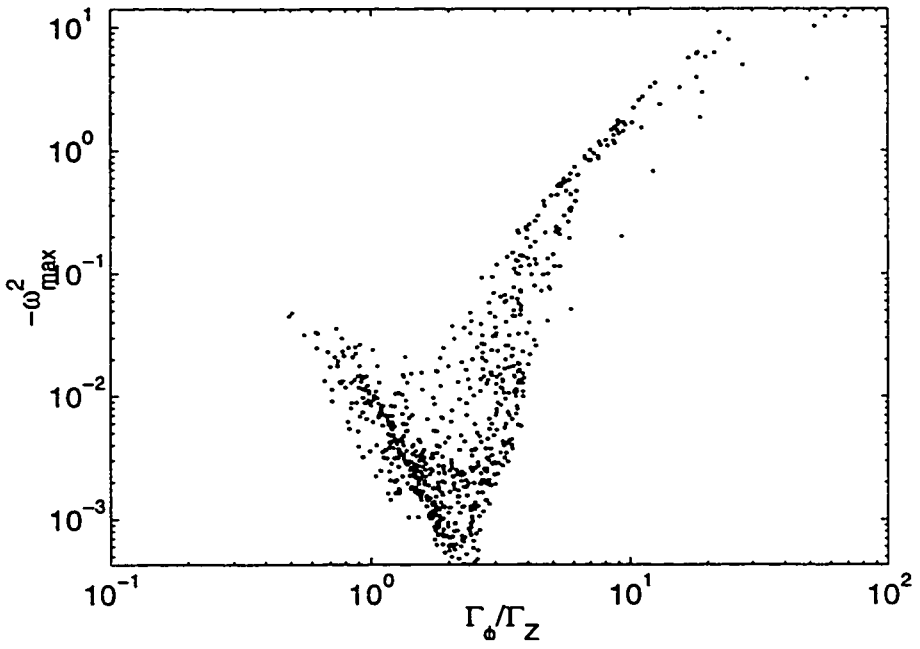

Figure 4-13: The growth rates for a random sample of helically magnetized models that agree with our constraints.

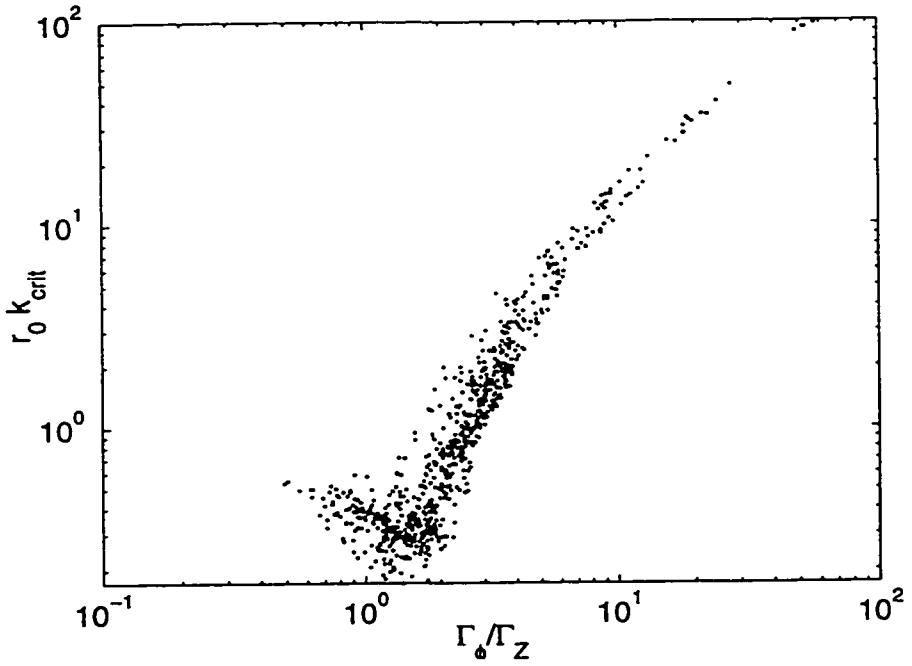

Figure 4-14: The critical wave numbers for a random sample of helically magnetized models that agree with our constraints.

expressed analytically as

$$-\frac{d\ln P}{d\ln r} < \frac{4}{2+\beta} \tag{4.29}$$

for an isothermal perturbation, where β is the usual plasma β, defined by $\beta = 8\pi P/B_\phi^2$ (cf. Sitenko & Malnev 1995). We have checked, numerically, that our equilibria obey equation 4.29, and, therefore, should be stable against "sausage" modes. It may appear that equation 4.28 is violated for any model with a purely toroidal field, but we remind the reader that equation 4.28 strictly applies to situations in which the toroidal field is generated by a current sheet at the plasma surface, and thus resides entirely outside of the plasma column. Equation 4.29 is, however, appropriate for the more distributed fields in our models.

It seems paradoxical that models with purely toroidal fields are stable against "sausage" modes, while those with a poloidal field component may be unstable. However, we note that helical fields are topologically different from purely toroidal fields. Flux tubes in purely toroidal models form closed loops, while the loops of toroidal flux are all linked in the case of a helical field. When the field is helical, twisting motions in the filament may enhance the toroidal field, while no amount of twisting can amplify a purely toroidal field. Thus, we argue that it is at least possible for modes to exist that simultaneously generate twisting motions and toroidal field, which could destabilize the filament.

We note that the gravity-driven modes join continuously with the MHD-driven modes in Figures 4-12 to 4-14; the intersection of the two branches, when $\Gamma_\phi/\Gamma_z \approx 2$, represents a transition between gravity and the toroidally dominated magnetic field as the main driving force of the instabilty. Some of the modes that we have labeled as magnetic have growth rates that are similar to gravity modes, except that the wavelength is somewhat shorter. These may represent reasonable modes of fragmentation for filamentary clouds. However, the more unstable modes of the MHD branch probably cannot, since they grow too rapidly and would probably disrupt the filament on timescales that are much shorter than the timescale on which equilibrium can be established (See equations 4.26 and 4.27). Therefore, a subset of the models allowed by the observational constraints of FP1 are actually highly unstable.

In Figure 4-15, we show an example of an unstable gravity-driven mode. As in the previously considered cases of hydrodynamic filaments (Section 4.7) and filaments with only one field component (Section 3.4.1), gravity drives a purely poloidal flow of gas towards the fragments. However, a helical field results in a toroidal component of the velocity field which alternates in sign from one side of the fragment to the other. The reason is that the helical field exerts oppositely directed torques on the gas flowing towards the fragment from opposite directions. The mode shown in Figure 4-16 is driven by the MHD "sausage" instability. The dominant wavelength of the instability is much shorter than either the filament radius or the dominant wavelength of the gravity-driven modes; therefore gravity is relatively unimportant compared to the magnetic stresses. The actual structure of the mode is quite similar to that of the gravity-driven modes, except that the mode is confined to the most central parts of the filament, where the B_ϕ gradient is steepest. This is consistent with our claim that this mode is a "sausage" instability, because "sausage" modes are driven by outwardly increasing toroidal fields with strong gradients. The filament is crushed where the toroidal field is strongest, which forces gas out along the axis and towards the fragments. As in the case of the gravity-driven modes, toroidal motions are generated as the helical field exerts torques on the gas.

Figure 4-17 shows the effect of Γ_ϕ/Γ_z on the ratio of the fragmentation wavelength λ_{max} to the filament diameter D, which we define as twice the filament radius R_S; we note that gravity-driven and MHD-driven modes cannot be easily separated on this diagram. In all cases, we find that more toroidally dominated modes have smaller λ_{max}/D. The Schneider and Elmegreen (1979) Catalogue of Dark Globular Filaments shows that $\lambda_{max}/D \approx 3.0$ for most filaments in their sample. Interestingly, this value is consistent with $\Gamma_\phi/\Gamma_z \approx 2$, which is near the transition from gravity to MHD-driven modes, and is near the lowest possible growth rate. We postulate that most filamentary clouds may be observed to reside near this maximally stable configuration because such objects would survive the longest. Although suggestive, this conclusion will also depend on the non-axisymmetric stability of filamentary clouds, to be discussed in a forthcoming paper.

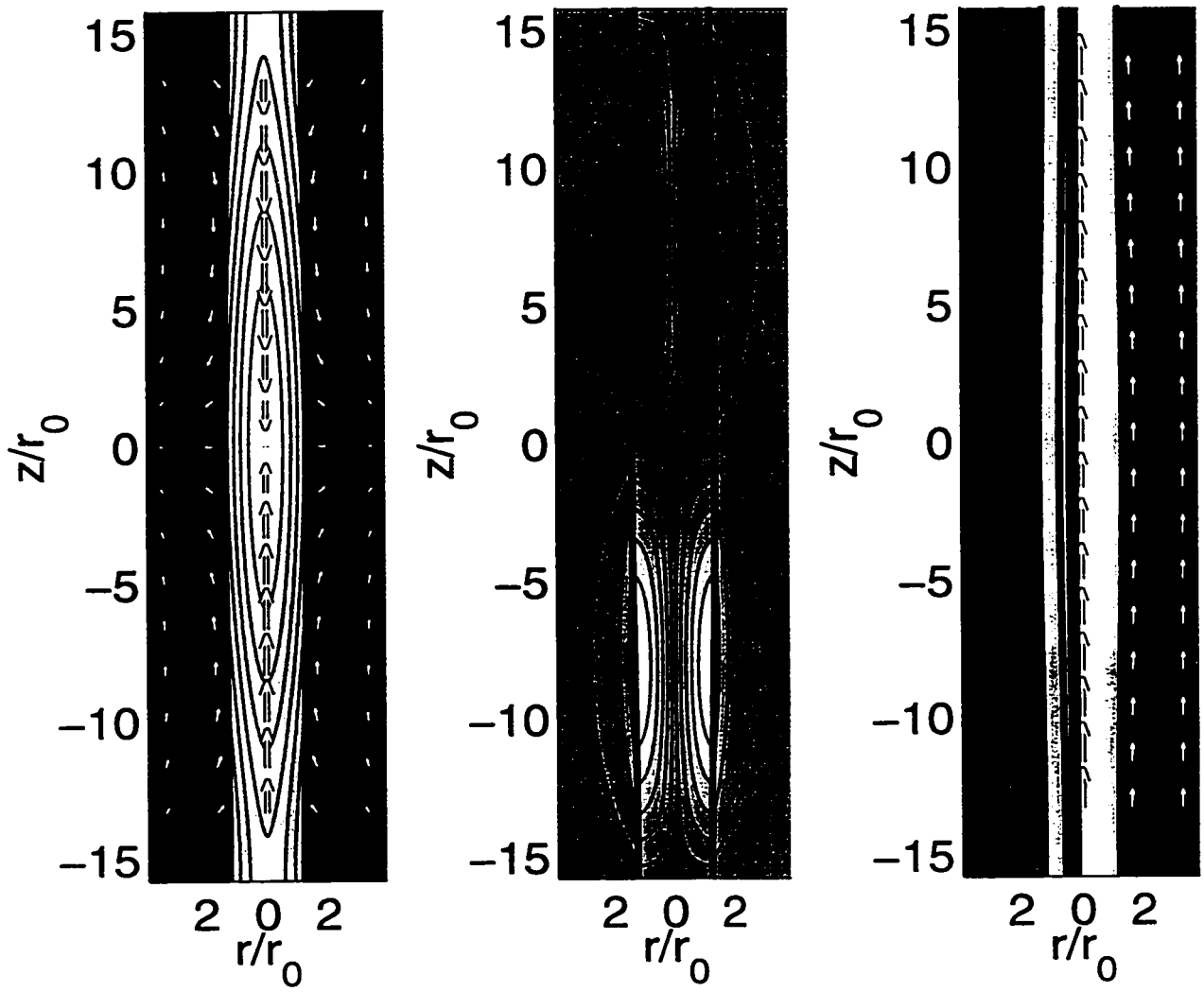

Figure 4-15: An example of a gravity-driven mode for a model with a helical magnetic field. For this mode, $k_{z,max} = 0.199$ and $-\omega^2(4\pi G\rho_c)^{-1} = 0.0081$. The figures represent a) (left panel) density contours with superimposed poloidal velocity vectors. b) (middle panel) Contours of toroidal velocity. Light coloured contours represent positive v_ϕ, while dark coloured contours represent negative v_ϕ. and c) (right panel) The magnetic field. We always represent the magnetic field as a split-frame figure, with poloidal field vectors shown on the right, and contours to represent the toroidal field on the left.

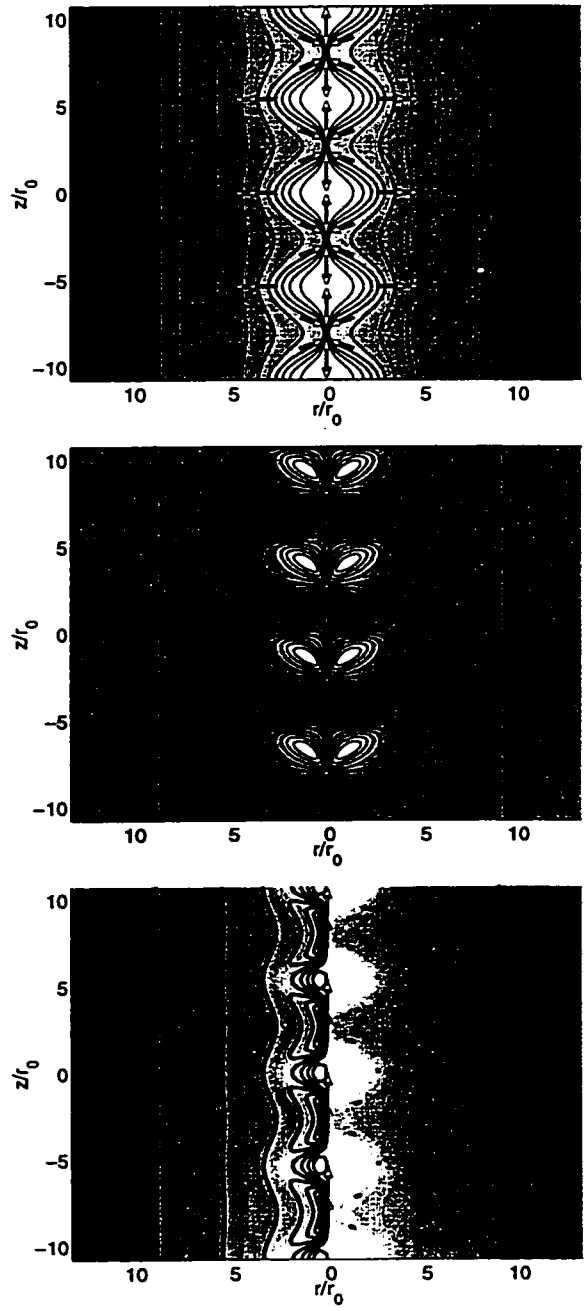

Figure 4-16: An example of an MHD-driven mode for a model with a helical magnetic field. For this mode, $k_{z,max} = 1.17$ and $-\omega^2(4\pi G\rho_c)^{-1} = 0.0390$. The figures represent a) (top panel) density contours with superimposed poloidal velocity vectors. b) (middle panel) Contours of toroidal velocity. Light coloured contours represent positive v_ϕ, while dark coloured contours represent negative v_ϕ. and c) (bottom panel) The magnetic field. We always represent the magnetic field as a split-frame figure, with poloidal field vectors shown on the right, and contours to represent the toroidal field on the left.

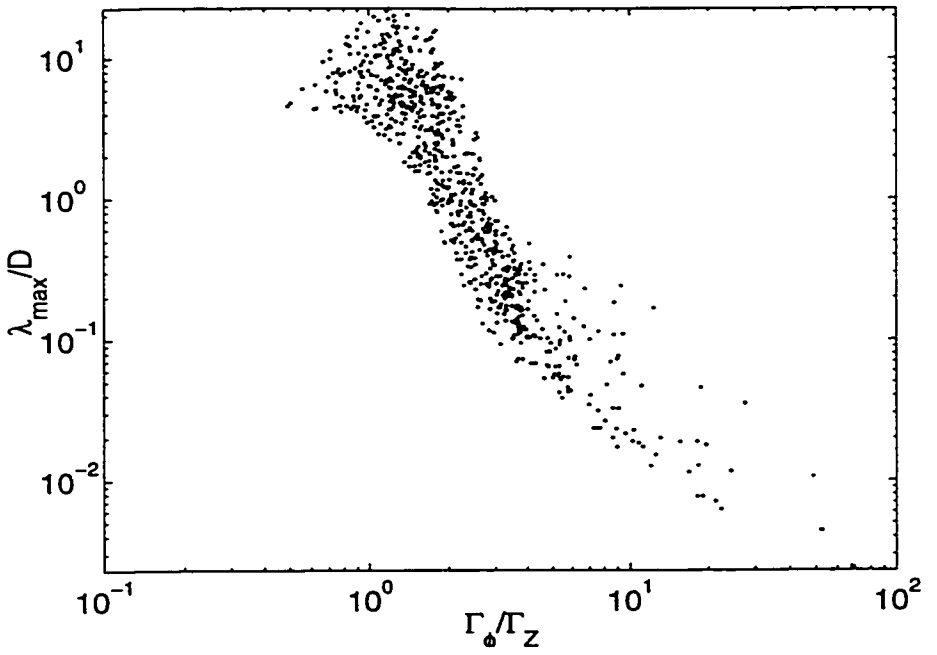

Figure 4-17: The ratio of fragment separation $\lambda_{max} = 2\pi/k_{max}$ to filament diameter $D = 2R_S$ for a random sample of models that agree with our constraints.

Finally, in Figure 4-18, we show the masses of fragments that might form from filamentary clouds. We note that we have computed the fragment masses simply by multiplying the equilibrium mass per unit length by the wavelength of the most unstable mode. This procedure implicitly assumes that there is no sub-fragmentation as fragments evolve. Thus, these masses should be regarded with caution. We find that fragment masses, computed in this way, fall in a rather large range; in dimensionless units we find

$$100 \lesssim M_{frag}(4\pi G)^{3/2}\rho_c^{1/2}\sigma^{-3} \lesssim 400 \tag{4.30}$$

for gravity-driven modes, which have $\Gamma_\phi/\Gamma_z \lesssim 2$. Thus, we obtain masses of

$$M_{frag} = 41.5\left(\frac{\bar{M}_{frag}}{100}\right)\left(\frac{\sigma}{0.5km\ s^{-1}}\right)^3\left(\frac{n_c}{10^4\ cm^{-3}}\right)^{-1/2} M_\odot. \tag{4.31}$$

4.10 Discussion and Summary

We have determined how pressure truncation and helical fields affect the stability of our models against axisymmetric modes of fragmentation, which are ultimately responsible for the formation of cores. Our analysis differs from previous work on filaments in a number of respects. Firstly, and most importantly,

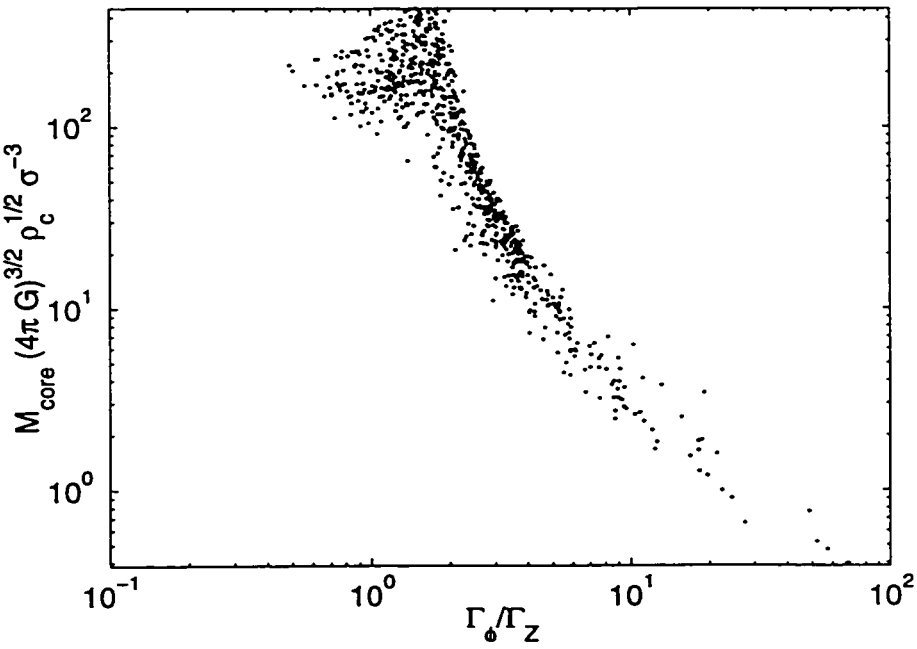

Figure 4-18: The expected mass of fragments for a random sample of models that agree with our constraints. Here we assume that $M_{frag} = m\lambda_{max}$.

we have made at least a first attempt to observationally constrain our models; thus, our modes of fragmentation pertain to equilibria that are truncated by realistic external pressures and have magnetic fields that are consistent with the observations. Moreover, our models have density gradients of $r^{-1.8}$ to r^{-2}, in good agreement with observational data (Alves et al 1998, Lada et al. 1998). Secondly, we have treated the external medium self-consistently by considering it to be a perfectly conducting gas of finite density.

We found, in Paper I, that filaments that are highly truncated by the external pressure have lower masses per unit length than untruncated filaments. We have shown, in Section 4.7, that such pressure dominated equilibria are more stable than their less truncated gravitationally dominated counterparts. We also found that the finite density of the external medium, in our calculation, slightly stabilizes filaments due to inertial effects. This effect vanishes when the external medium is "hot", with a velocity dispersion $\gtrsim 10\ \sigma$.

Both the poloidal and toroidal fields were shown to stabilize filaments against gravity-driven fragmentation in Section 3.4.1. The poloidal field stabilizes the filament by resisting motions perpendicular to the poloidal field lines. This stabilization eventually saturates, when the field is strong enough ($\Gamma_z \gtrsim 10$) to disallow radial motions altogether. Surprisingly, the toroidal field is much more effective at stabilizing filaments against gravitational fragmentation. As the filaments begins to fragment, the toroidal

flux tubes are pushed together near the fragments; this results in a gradient in the magnetic pressure ($1/8\pi\ \partial B_\phi^2/\partial z$) that opposes fragmentation. In the unrealistic limit of purely toroidal fields, the filament is stable to fragmentation when $\Gamma_\phi \gtrsim 7$. One might expect that these models would be highly unstable against MHD "sausage" modes. However, we have verified that our equilibria satisfy the stability condition given in equation 4.29.

In Section 4.9, we demonstrated that our models with helical fields are subject to both gravity-driven and MHD-driven instabilities. The two types of modes blend together in Figures 4-12 to 4-14, with the transition from gravity-driven to MHD-driven largely determined by the ratio Γ_ϕ/Γ_z; when $\Gamma_\phi/\Gamma_z \lesssim 2$, the instability is driven by gravity, with MHD-driven modes triggered only for more tightly wrapped helical fields. We provided evidence, in Section 4.9, that the MHD-driven mode is probably is an MHD "sausage" mode. These instabilities can have extremely high growth rates compared to gravity driven modes; therefore, we may interpret our stability condition as an additional theoretical constraint on our models. We note that the most stable of all equilibria are near the transition from gravity-driven to MHD-driven modes. Thus, we find that there is a regime in which filamentary clouds fragment very slowly. For gravity-driven modes, we find that $-\omega_{max}^2$, $k_{z,max}$, and $k_{z,crit}$ fall within the ranges

$$\begin{aligned} 0.0005 &\lesssim -\omega_{max}^2(4\pi G\rho_c)^{-1} \lesssim 0.03 \\ 0.1 &\lesssim r_0 k_{z,max} \lesssim 0.3 \\ 0.2 &\lesssim r_0 k_{z,crit} \lesssim 0.6, \end{aligned} \tag{4.32}$$

where r_0 is the core radius for filamentary clouds (see Paper I), and ρ_c is the central density. We may also write the expected wavelength for the separation of fragments and the growth timesacale as

$$\begin{aligned} \lambda_{max} &= 2.8 \left(\frac{\tilde{k}_{max}}{0.2}\right)^{-1} \left(\frac{\sigma_c}{0.5\ km\ s^{-1}}\right) \left(\frac{n_c}{10^4\ cm^{-3}}\right)^{-1/2} pc \\ \tau_{frag} &= 1.8 \left(\frac{-\tilde{\omega}_{max}^2}{0.01}\right)^{-1/2} \left(\frac{n_c}{10^4\ cm^{-3}}\right)^{-1/2} Myr. \end{aligned} \tag{4.33}$$

We note that the growth time for gravity-driven modes is significantly longer than the radial signal crossing time (equation 4.27), on which radial equilibrium is established. Therefore, our stability analysis is consistent with the assumption of radial quasi-equilibrium used in Paper I.

We find that the fragmentation of filamentary clouds with helical fields leads to a toroidal component of the velocity field, whose direction alternates with every half wavelength of the perturbation. These motions are comparable to, and in some cases exceed the poloidal velocities, at least in linear theory. These motions could, in principal, be detected, which would provide considerable evidence for helical

fields.

We find that the fiducial growth time for gravity-driven modes is on the order of 1.8 Myr, which is longer than the signal crossing time, on which radial equilibrium is established. Therefore, our stability analysis is consistent with the assumption of radial quasi-equilibrium used in Paper I.

Throughout this analysis, we have focussed on axisymmetric modes that lead to fragmentation, ignoring any non-axisymmetric modes that might be present. Some of our models may be unstable to at least the $m = 1$ "kink" instability. However, we do not expect gross instability for most models. While they do contain significant toroidal fields, the poloidal field is actually much stronger throughout most of the filament, particularly in the central regions, where B_z is maximal and B_ϕ vanishes. This "backbone" of poloidal field should largely stabilize our models against kink modes. In any case, the non-axisymmetric modes of fragmentation will be addressed in a forthcoming paper.

4.11 Acknowledgements

J.D.F. acknowledges the financial support of McMaster University and an Ontario Graduate Scholarship. The research grant of R.E.P. is supported by a grant from the Natural Sciences and Engineering Research Council of Canada.

Appendix A

The Equations of Linearized MHD

The equations of linearized, self-gravitating, perfect MHD in our dimensionless units are as follows:
Momentum Equation:

$$\begin{aligned} i\omega\rho_0\mathbf{v_1} &+ \nabla P_1 + \rho_0\nabla\Phi_1 + \rho_1\nabla\Phi_0 \\ &- \frac{1}{4\pi}\left[(\nabla\times\mathbf{B_0})\times\mathbf{B_1} + (\nabla\times\mathbf{B_1})\times\mathbf{B_0}\right] = 0 \end{aligned} \tag{A.1}$$

Mass conservation:

$$i\omega\rho_1 + \nabla\cdot(\rho_0\mathbf{v_1}) = 0 \tag{A.2}$$

Induction equation:

$$i\omega\mathbf{B_1} = \nabla\times(\mathbf{v_1}\times\mathbf{B_0}). \tag{A.3}$$

Poisson's equation:

$$\nabla^2\Phi_1 = \rho_1. \tag{A.4}$$

Equation of state:

$$P_1 = \gamma\sigma_0^2\rho_1, \tag{A.5}$$

where γ is the polytropic index of the gas ($\gamma = 1$ within the filament.) and $\sigma_0^2 = P_0/\rho_0$ is the one-dimensional velocity dispersion.

By introducing a "modified" gravitational potential $\varphi_1 = i\omega\Phi_1$, it is straightforward to combine equations A.1 to A.5 to form the eigensystem given by equations 4.8 and 4.9. Equations 4.8 and 4.9 represent the eigensystem, written entirely in terms of φ_1 and the components of ρv_1. We now define

differential operators $\hat{A}$, $\hat{B}$, $\hat{C}$, and $\hat{D}$ in a way that is obvious from equations 4.8 and 4.9 to write our eigensystem in closed symbolic form:

$$-\omega^2 \rho_0 \mathbf{v_1} = \hat{A}(\rho_0 \mathbf{v_1}) + \hat{B}\varphi_1 \tag{A.6}$$

$$0 = \hat{C}(\rho_0 \mathbf{v_1}) + \hat{D}\varphi_1. \tag{A.7}$$

We obtain an approximate matrix representation of operators $\hat{A}$, $\hat{B}$, $\hat{C}$, and $\hat{D}$ by finite differencing over a one-dimensional grid of N cells ($N \approx 500$ usually). From this point forward, we shall assume that all operators have been finite differenced, and shall make no distinction between matrix and operator forms. We note that equation A.7 applies to both the HI envelope and the molecular filament; thus, of the N cells, some portion (usually $\sim 2/3$) are within the filament, while the remainder are in the HI envelope. Since the density is discontinuous at the interface, care must be taken not to difference any equations across the boundary. Section 4.4 describes the boundary conditions that link the perturbation in the filament to the external medium. Matrix $\hat{C}$ is a 1×3 block of $N \times N$ sparse tridiagonal matrices, while $\hat{D}$ is a sparse tridiagonal $N \times N$ matrix. Matrices $\hat{A}$ and $\hat{B}$ each take the form of 3×3 blocks of $N \times N$ sparse tridiagonal sub-matrices (The 3×3 block structure occurs because these matrices operate on $\rho_0 \mathbf{v_1}$, which has 3 vector components.). If we consider "eigenvector" Ψ given by equation 4.13, then equation A.7 takes the form of the standard eigenvalue problem given by equation 4.12, where

$$\hat{L} = \begin{bmatrix} \hat{A} & \hat{B} \\ \hat{C} & \hat{D} \end{bmatrix}. \tag{A.8}$$

Appendix B

The Boundary Conditions at the Molecular Filament/HI Envelope Interface

Equations 4.15 to 4.18 give the boundary conditions at the interface between the molecular and atomic gas. We note that these jump conditions apply in a Lagrangian frame that is co-moving with the deformed surface. Equations 4.15 and 4.16 demand that the gravitational potential and its first derivative (the gravitational field) must be continuous aross the interface. Equation 4.17 is the usual condition on the normal magnetic field component from electromagnetic theory. It is easily derived from the divergence-free condition of the magnetic field. The final condition, equation 4.18 states that the normal component of the total stress is continuous across the boundary.

We must now transform the boundary conditions (equations 4.15), into an Eulerian frame appropriate to our fixed grid. We assume that the deformed surface is defined by the equation

$$r = R_S + \epsilon e^{i(\omega t + m\phi + k_z z)}, \tag{B.1}$$

where $|\epsilon| \ll R_S$ for a small perturbation. We note that $m = 0$ for the axisymmetric modes considered in this paper. However, we retain m in our equations, since we will examine non-axisymmetric modes in a forthcoming paper. To first order, the unit normal vector to this surface is given by

$$\hat{n} = \hat{\mathbf{r}} - \epsilon \left[\frac{im}{R_S} \hat{\phi} + ik_z \hat{\mathbf{z}} \right] e^{i(\omega t + m\phi + k_z z)}. \tag{B.2}$$

Since this is a contact discontinuity, and not a shock, the velocity field must be consistent with the motion of this surface; thus,

$$v_{r1} = \frac{\partial r}{\partial t} = i\omega\epsilon e^{i(\omega t + m\phi + k_z z)}, \tag{B.3}$$

which implies that

$$[v_{r1}] = 0 \tag{B.4}$$

in the Eulerian frame. Solving equation B.3 for ϵ and substituting into equation B.2, we obtain an expression for $\hat{n}$ that involves only the radial velocity:

$$\hat{n} = \hat{\mathbf{r}} - v_{r1}\left[\frac{m}{\omega R_S}\hat{\phi} + \frac{k_z}{\omega}\hat{z}\right]. \tag{B.5}$$

We insert the expression for the normal vector $\hat{n}$ (equation B.5) into equations 4.15 to 4.18, and evaluate all zeroth order quantities, at the position of the deformed surface, by a first order Taylor expansion. We also make use of equations A.1 to A.5 in order to express all quantities in terms of the momentum density and the potential φ. After some algebra, we obtain the explicit form of the boundary conditions that apply at the surface of the filament:

$$[\varphi_1] = 0 \tag{B.6}$$

$$\left[\frac{\partial \varphi_1}{\partial r} + \rho_0 v_r\right] = 0. \tag{B.7}$$

$$\left[\frac{1}{\rho_0}(\rho_0 v_r)\right] = 0. \tag{B.8}$$

$$\left[-\gamma\sigma_0^2 \nabla\cdot(\rho_0 \mathbf{v_1}) - \frac{\mathbf{B_0}}{4\pi}\cdot\nabla\times\left(\frac{\mathbf{B_0}}{\rho_0}\times\rho_0\mathbf{v_1}\right) + \frac{1}{\rho_0}\frac{dP_{tot}}{dr}(\rho_0\mathbf{v_1})\right] = 0, \tag{B.9}$$

where P_{tot} is the total gas plus magnetic pressure in zeroth order: $P_{tot} = P_0 + B_0^2/8\pi$.

For completeness, we also study the stability of untruncated filaments, for which there is no external pressure. When untruncated filaments extend radially to infinity, we simply do not include an internal boundary. We also consider the limit of an infinitely hot, zero density external medium. In these cases, we assume that the external medium is a non-conducting vacuum and use the boundary conditions prescribed by Nagasawa (1987).

Appendix C

Matrix Representation of the Boundary Conditions

The four boundary conditions given by equation B.6 to B.9 must now be inserted into the eigensystem given by equation 4.12. Assuming that there are N elements in our computational grid, with the interface between the molecular and atomic gas between elements I^* and $I^* + 1$, we may write a matrix representation of our boundary conditions in the form

$$\hat{a}\Psi^* + \hat{b}\Psi = 0, \tag{C.1}$$

where

$$\Psi^* = \begin{bmatrix} \Psi_1 \\ \Psi_{I^*} \\ \Psi_{I^*+1} \\ \Psi_N \end{bmatrix} \tag{C.2}$$

contains all of the boundary cells, and Ψ now contains the remaining $4(N-1)$ elements. We likewise separate our eigensystem (equation 4.12) into regular and boundary grid cells:

$$-\omega^2\Psi = \hat{L}_1\Psi^* + \hat{L}_2\Psi. \tag{C.3}$$

We may solve equation C.1 for the boundary values by elementary matrix algebra:

$$\Psi^* = -\hat{a}^{-1}\hat{b}\Psi. \tag{C.4}$$

Substituting into equation C.3, we eliminate 4 equations to obtain our eigensystem (of size $4(N-1) \times 4(N-1)$), which takes into account all boundary conditions:

$$-\omega^2 \Psi = (\hat{L}_2 - \hat{L}_1 \hat{a}^{-1} \hat{b}) \Psi. \tag{C.5}$$

This is the final form of our eigensystem, which we solve in Section 4.5.

References

Alves J., Lada C.J., Lada E.A., Kenyon S.J., Phelps R., 1998, Ap.J., 506, 292

Bally J., 1987, Ap.J., 312, L45

Bally J., 1989, in Proceedings of the ESO Workshop on Low Mass Star Formation and Pre-main Sequence Objects, ed. Bo Reipurth; Publisher, European Southern Observatory, Garching bei Munchen

Bateman G., 1978, "MHD Instabilities", The MIT Press, Cambridge, Massachusetts

Bertoldi F., McKee C.F., 1992, Ap.J., 395, 140

Bonnor W.B., 1956, MNRAS, 116, 351

Carlqvist P., 1998, Ap.&S.S., 144, 73

Carlqvist P., Gahm G., 1992, IEEE Trans. on Plasma Science, vol. 20, no. 6, 867

Caselli P., Myers P.C., 1995, Ap.J., 446, 665

Castets A., Duvert G., Dutrey A., Bally J., Langer W.D., Wilson R.W., 1990, A&A, 234, 469

Chandrasekhar S., 1961, "Hydrodynamic and Hydromagnetic Stability", Oxford University Press, London

Chandrasekhar S., Fermi E., 1953, Ap.J. 118, 116

Dutrey A., Langer W.D., Bally J., Duvert G., Castets A., Wilson R.W., 1991, A&A, 247, L9

Ebert R., 1955, Z.Astrophys., 37, 217

Elmegreen B.G., 1989, Ap.J., 338, 178

Fiege J.D, Pudritz R.E., 1999 (FP1), MNRAS, in Press (see also astro-ph/9901096)

Goodman A.A., Bastien P., Myers P.C., Ménard F., 1990, Ap.J., 359, 363

Goodman A.A., Jones T.J., Lada E.A., Myers P.C., 1995, Ap.J., 448, 748

Hanawa T., et al., 1993, Ap.J., 404, L83

Heiles C., 1987, Ap.J., 315, 555

Heiles C., 1990, Ap.J., 354, 483

Heiles C., 1997, Ap.J.Supp., 111, 245

Jackson J.D., 1975, "Classical Electrodynamics", John Wiley & Sons, New York

Lada C.J., Alves J., Lada E.A., 1998, Ap.J. in Press

McCrea W.H., 1957, MNRAS, 117, 562

McKee C.F., Zweibel E.G., Goodman A.A., Heiles C., 1993, in Protostars and Planets III, ed. Levy E.H., Lunine J.I., University of Arizona Press, Tucson, Arizona

McLaughlin D.E., Pudritz R.E., 1996, Ap.J., 469, 194

Myers P.C., Goodman A.A., 1988a, Ap.J., 326, L27

Myers P.C., Goodman A.A., 1988b, Ap.J., 329, 392

Nagasawa M., 1987, Prog. Theor. Phys., 77, 635

Nakamura F., Hanawa T., Nakano T., 1993, PASJ, 45, 551

Nakamura F., Hanawa T., Nakano T., 1995, Ap.J., 444, 770

Nakamura S., 1991, "Applied Numerical Methods With Software", Prentice Hall, New Jersey

Onishi T., Mizuno A., Kawamura A., Ogawa H., Fukui Y., 1998, Ap.J., 502, 296

Ostriker J., 1964, Ap.J., 140, 1056

Ouyed R., Pudritz R.E., 1997, Ap.J., 482, 712

Schneider S., Elmegreen B.G., 1979, Ap.J., 41, 87

Sitenko A., & Malnev V., 1995, "Plasma Physics Theory", Chapman & Hall, London

Chapter 5

Dense Cores in Molecular Clouds

We argued in Chapters 2 and 3 that molecular clouds are often filamentary, and we found indirect evidence that some filamentary clouds might be wrapped by helical magnetic fields. This motivated us to construct detailed magnetohydrostatic equilibrium models of filaments threaded by helical fields, whose fragmentation we studied in Chapter 4. In the next chapter, we construct detailed models of the cloud *cores* that might form within filamentary clouds, taking our helically magnetized filamentary cloud models as initial conditions. This approach allows us to address several important questions. What is the density structure of the cores that form as a result of our models? What magnetic geometries might be inherited from the parent filament? What are their stability properties? What are their *shapes*? The main purpose in this chapter is to discuss previous models of cloud cores, highlighting some of the differences and similarities between them and our models.

Cores are the dense ($\gtrsim 10^4\ cm^{-3}$), compact ($few \times 0.1\ pc$), strongly self-gravitating regions within molecular clouds. They are also the sites of star formation. The high densities of cores and their strong self-gravity distinguish them from clumps (discussed in Section 2.8), which are typically an order of magnitude lower in density, and are often only weakly self-gravitating.

Like molecular clouds as a whole, cores exist in an interesting regime where self-gravity, internal pressure, and magnetic fields are all about equally important. Clouds and cores are also both truncated by the pressure of an external medium. For clouds, this pressure is provided by the interstellar medium or by an envelope of HI gas at somewhat higher pressure (see Section 2.6). However, the surface pressure on a core is due to the total (thermal plus non-thermal) pressure exerted by the surrounding cloud or clump material. [1]

[1] By the "surface" of a core, we mean the surface where the core blends in to the surrounding molecular gas. However, recent observations suggest that cores might actually have quite sharp boundaries where the density falls rapidly to that of the ambient cloud material (Ward Thompson 1994, see also review by André et al. 1999). Bok globules certainly do

An important difference between clouds and cores is their mechanism of support against self-gravity. Cores, and the structurally similar (though more isolated) Bok globules, are probably the only places in the ISM where the thermal component of the pressure is often dynamically important compared to the non-thermal motions of the gas. Low mass cores are particularly quiescent, with relatively large thermally dominated (subsonic) central regions (Fuller & Myers 1992, Myers & Fuller 1992). Even massive cores appear to be thermally dominated at small radii (Caselli & Myers 1995). As a result, most cores seem to have a relatively simple internal structure compared to clouds (see Section 2.8). There is no observational evidence that the highly textured structure often seen in clouds extends to the scale of cores. On the contrary, many cores seem to have quite smoothly varying density profiles (Ward-Thompson et al. 1994, see also review by André et al. 1999). [2]

Many of the arguments developed in Section 2.11 in the context of clouds, applies to their cores as well. These specifically include our discussion of magnetic criticality (Section 3.2), the Bonner-Ebert stability of magnetized clouds (Section 2.11.2), and our demonstration that nearly Bonnor-Ebert critical clouds should obey Larson's laws (Section 2.11.4). We discuss the line width-size relation for cores in Section 5.4.2, which is analogous to Larson's first law for clouds (equation 2.44).

Models of cloud cores generally fall into two categories. The first category includes models that assume cores to be spherical, self-gravitating equilibria. These models, which we discuss in Section 5.6, concentrate on how the total (thermal plus non-thermal) pressure support determines the density structure and stability properties of cores. Often an effective equation of state (EOS) is assumed for the gas, which describes how the total pressure depends on the density. Spherical models generally do not include ordered magnetic fields because they generally result in non-isotropic forces, except if the field is force-free or current-free. [3] Such field configurations would offer no support to the gas, which does not fit in with the current paradigm of ambipolar diffusion regulated star formation in cores (Section 5.7.3). As we discuss in Section 5.5.1 below, observations of the Zeeman effect in cores, show that the ordered magnetic field in some cores is much higher (up to 3 orders of magnitude) than in the surrounding gas. These observations would be difficult to reconcile with force-free configurations. We discuss non-spherical models in Section 5.7, which focus on a self-consistent treatment of the ordered magnetic field. On the other hand, most non-spherical models of cores assume the simplest, isothermal (in the sense of constant total velocity dispersion) equation of state for the gas. They concentrate instead on the effects of the ordered magnetic field on the shapes of cores, and their stability. This is also the emphasis of our

have sharp edges where they are truncated by the ISM.

[2] Filaments also sometimes have smooth radial density profiles (eg. Alves et al. 1998, Lada et al. 1999). However, we are unaware of any filaments that are completely unfragmented along their lengths.

[3] An example of a current-free magnetic field is the field structure that we assumed in the last chapter for the HI envelope surrounding our models of filamentary clouds. The structure of the envelope was therefore determined from purely hydrostatic equations.

prolate core models in the next chapter.

The magnetic structure of cores plays an important role in the sequence of events that ultimately leads to collapse and star formation. A commonly held view is that the gradual loss of magnetic support by ambipolar diffusion controls the quasi-static evolution of a core until a final critical state is reached. Past this point, no equilibrium is possible, the core collapses, and a star or several stars form. Therefore, the magnetic field in cores plays a crucial role in establishing the initial conditions for star formation. We discuss some of the details of ambipolar diffusion and calculate a timescale for the quasi-static evolution of cores in Section 5.7.3.

5.1 Observational Properties of Cores and Bok Globules

Cores are the dense, strongly self-gravitating, and relatively quiescent regions within molecular clouds, which ultimately collapse to form stars. There is strong observational evidence to support this claim, since cores are often associated with the signposts of recent and ongoing star formation, including proto-stellar objects and embedded T-Tauri stars observed at infra-red wavelengths (Beichman et al. 1986) and molecular outflows (Myers et al. 1988). Therefore, good theoretical models of molecular cloud cores play an essential role in setting the initial conditions for star formation.

There is another class of objects called Bok globules, which are similar in many ways to cores, but differ primarily in that they are relatively isolated from larger molecular clouds. Bok globules often occur together, strung like beads along "globular filaments," often with striking periodicity (Schneider & Elmegreen 1979). Our model of filamentary clouds (Chapters 3 and 4) applies equally well to globular filaments as to filaments embedded in molecular clouds. Likewise, our model of prolate cores, presented in the next chapter, is applicable to Bok globules.

Our knowledge of molecular cloud cores can be attributed mainly to intensive observations of sub-millimetre and centimetre wavelength spectral lines of molecules that trace molecular gas at high ($\gtrsim 10^4\ cm^{-3}$) densities (see Section 3.2.4). The 1.3 cm inversion line of ammonia (NH_3) was first detected by Cheung et al. (1968) toward several sources. Detections of the rotational lines of many other high density tracer molecules were first reported in a rapid series of discovery papers in 1970 and 1971: cyanide (CN) (Jeffert, Penzias & Wilson 1970), formaldehyde (H_2CO) (Kutner & Thaddeus. 1971), carbon monoxide ($C^{18}O$) (Penzias, Jefferts, & Wilson 1971), carbon monosulfide (CS) (Penzias et al. 1971), and methyl cyanide (CH_3CN). Of these molecules, NH_3, CS, and $C^{18}O$ are most commonly used to study cores (eg. Myers & Benson 1983, Lada et al. 1991, Onishi et al. 1998). In recent years, our ability to study cores has been augmented by sub-millimetre continuum observations (eg. Chini et al. 1997, Johnstone & Bally 1999, Wilson et al. 1999).

Cores are operationally defined as the emission peaks of a molecular cloud, in one or more lines, where the density exceeds $\sim 10^4\ cm^{-3}$ (see review by Myers 1985). Most of the molecules listed above trace gas at densities higher than about $10^4\ cm^{-3}$; hence the operational definition of a core as regions of molecular clouds that exceed this density. Mean core densities are therefore about two orders of magnitude higher than the densities traced by CO emission ($\gtrsim 300\ cm^{-3}$, See review by Genzel 1992). Observations in NH_3 reveal central densities of up to $\sim 10^6\ cm^{-3}$ for many cores (Genzel 1992). Cores are relatively compact, with sizes of $\lesssim few \times 0.1\ pc$, and tend to be moderately elongated in shape, with axis ratios typically of about 2:1 (Myers et al. 1991). An important point about cloud cores is that their observed sizes vary significantly with the choice of line used to make the observations. The reason is that different molecules trace gas at different densities, as discussed in Section 3.2.4. Generally, NH_3 traces the most compact regions with the highest densities, while CS and $C^{18}O$ trace progressively less dense gas and more extended emission. ^{13}CO traces clumps (see Section 2.8), which have lower densities and many contain several cores.

Cores are often classified according to their masses and whether or not they contain stars (IRAS infra-red sources, which are protostars or somewhat more evolved T-Tauri stars; see Beichman et al. (1986)). Table 1 in Myers (1985) summarizes the properties of low versus high mass cores. Low mass cores have masses of $\sim 1\ M_\odot$, are generally $\sim 0.1\ pc$ in size, have mean densities of $\sim 10^4\ cm^{-3}$, and temperatures of $\sim 10\ K$. High mass cores are $10 - 10^3$ times more massive, $1 - 30$ times larger, and $3 - 10$ times warmer. Bok globules are similar to intermediate-sized cores in mass, size, density, and temperature. We compare some of the properties of "starless" cores with those with embedded stars in Section 5.4.2.

5.2 Cores are Self-Gravitating

It is a well-known fact that most cores are strongly self-gravitating. Self-gravitating virial equilibrium requires that $M \approx M_{vir}$ to within a factor of order unity, where M_{vir} is the virial mass discussed in Section 2.9 (equation 2.17). Equivalently,

$$\sigma^2 \sim \frac{GM}{R} \tag{5.1}$$

where R is the radius of the core (Larson 1981). Larson demonstrated that this relation holds well for clouds ranging over 3 decades in size, from $\sim 0.1\ pc$ (core scales) to $100\ pc$ (giant molecular clouds). Larson's data contained only a few core-sized objects, however. Leung, Kutner, and Mead (1982) and Myers (1983) respectively demonstrated that equation 5.1 holds for Bok globules and molecular cloud cores. Subsequently, Myers and Goodman (1988a,b) provided considerable observational evidence that many clouds and cores are in approximate equilibrium between self-gravity, pressure support, and

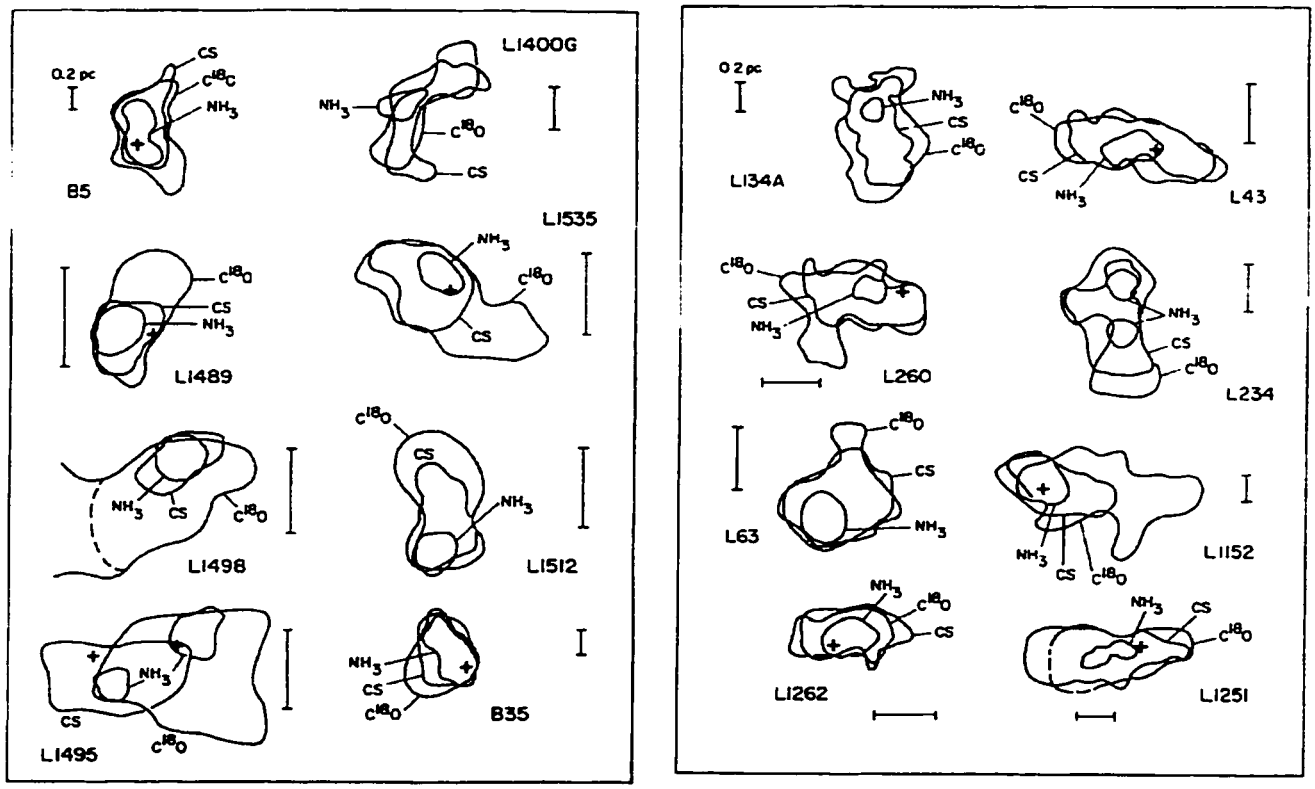

Figure 5-1: (From Myers et al. 1991) Half peak emission contours of the cores used by Myers et al. (1991) in their analysis of the shapes of cores.

magnetic fields. Therefore, theoretical models that assume equilibrium *a priori* are probably justified in many cases.

5.3 The Shapes of Cores

There is considerable observational evidence that cores are predominantly prolate in shape. Myers et al. (1991) first suggested that this might be the case, based on a sample of 16 cores, which were each observed in lines of $C^{18}O$, CS, and NH_3. These three molecules trace different densities (see Section 5.1) and therefore different size scales within cores. We show the maps from Myers et al. in Figure 5-1 below. The contour maps in each line are somewhat irregular in shape, but most cores appear to be significantly elongated in all three lines. There is also overall agreement in both the direction and degree of elongation between lines for each core. Therefore, the cores observed by Myers et al. are probably not spherical in shape.

Since we can only observe cores in projection, how is it possible to determine whether the observed elongation is due to prolate cores or oblate cores seen nearly edge on? Myers et al. attempted to deter-

mine the shapes of cores by considering the average elongations expected for ensembles of intrinsically prolate and oblate cores, assuming that they are oriented randomly relative to the observer. They found that the prolate hypothesis is consistent with the data for relatively modest axis ratios of $0.4 - 0.5$. However, rather extreme flattening is necessary, with mean axis ratios less than $0.1 - 0.3$ if cores are intrinsically oblate. Thus, they concluded that cores are most likely prolate.

Ryden (1996) performed a more elaborate statistical analysis of the shapes of cores and Bok globules, based on several larger data sets. She also found that cores and Bok globules are most likely prolate, sometimes rejecting the oblate hypothesis at a very high ($> 99\%$) confidence level.

The statistical analyses of Myers et al. (1991) and Ryden (1996) both rely on the same assumption that cores are oriented randomly on the plane of the sky. However, significant correlations could possibly exist in the orientations of cores, particularly if some fraction of the cores were aligned by large-scale magnetic fields or structures in the gas. Therefore, the statistical arguments presented by Myers et al. and Ryden probably should not be regarded as conclusive. However, Myers et al. also argued that some of the cores in their sample appear to be embedded within larger filamentary structures, and that the major axes of these cores generally align with the symmetry axes of their parent filaments. These cases represent fairly clear examples of prolate cores that have formed within filaments. Many other examples of elongated cores embedded in filamentary clouds can be found in the Schneider and Elmegreen (1979) "Catalogue of Dark Globular Filaments".

If cores truly are prolate, then this would probably have significant implications for their magnetic structures. Core models that include only the poloidal field component always result in oblate equilibria (Mouschovias 1976b, TIN, Tomisaka, Ikeuchi, and Nakamura, 1988b, 1989, 1990; See also Section 5.7), contrary to the observations. However, we show in Section 5.7 that prolate cores might naturally arise from filamentary clouds, as a natural consequence of helical magnetic fields. The full analysis of our prolate core models is the subject of the next chapter.

5.4 The Velocity Structure of Cores

The internal motions of cores can be broken down into four general categories; these are infall, outflow, rotation, and random (ie. turbulent) motions. Infall and outflow pertain to relatively evolved protostellar cores that are actively forming stars, which are beyond the scope of this thesis. Therefore, we limit our discussion to rotation and random motions, which are of direct importance to the structure of pre-protostellar cores.

5.4.1 Rotational Motions in Cores and Bok Globules

The rotation of molecular clouds and their cores reveals itself by a gradient in the line of sight component of the velocity across the cloud, as detected by Doppler shifted molecular lines. The velocity gradient $\mathcal{G}$, measured in $km\ s^{-1}\ pc^{-1}$, is related to the angular velocity ω, in $rad\ s^{-1}$, by

$$\omega = \frac{\mathcal{G}}{\sin i}\hat{\omega}, \tag{5.2}$$

where i is the (usually unknown) angle of inclination, and $\hat{\omega}$ is the direction of the axis of rotation (Goodman et al. 1993). Observations of rotation are inherently limited to the component of the angular momentum that lies in the plane of the sky, since gas motions transverse to the line of sight are undetectable by the Doppler effect. Therefore, velocity gradients provide only a lower limit to the angular momentum of an individual cloud. However, it is possible to correct statistically for inclination effects for an ensemble of randomly oriented cores: $\langle \mathcal{G}/\sin i \rangle = (4/\pi)\langle \mathcal{G} \rangle$, where angle brackets denote ensemble averages (see Goodman et al. 1993 and references therein).

The most comprehensive analysis of rotational motions in cores was provided by Goodman et al. (1993), who fit velocity gradients to 43 cores observed in NH_3. Assuming solid-body rotation, they found the best-fitting magnitude and orientation angle for the component of the angular momentum in the plane of the sky. They detected statistically significant (better than 3σ) rotation in about 2/3 of the cores in their sample. However, their analysis conclusively shows that rotation does not play a dynamically significant role in the support of molecular cloud cores against self-gravity. They provide two strong arguments to support this conclusion, which we discuss below.

Firstly, and perhaps most significantly, Goodman et al. demonstrate that the ratio of the rotational energy to the gravitational energy is less than or equal to 0.18 for *all* of the cores in their sample, and usually less than or equal to 0.05. Therefore, rotation cannot play a significant role in the support of cores, which would require this ratio to be close to unity.

The second argument relies on the well known fact that rotational stresses result in flattened, oblate equilibria (Tassoul 1978, Tomisaka et al. 1988a, hereafter TIN). One might postulate that rotational flattening accounts for the elongation of cores, but cores would appear to be elongated perpendicular to their rotational axes, if this were. However, Goodman et al. find no statistical correlation between the directions of elongation and rotation. Nor do they find any correlation between the degree of elongation and the magnitude of the velocity gradient. Thus, there appears to be no observational justification for the shapes of cores being related to rotation.

A recent study on the rotation of Bok globules (Kane & Clemens 1997) shows that they are also

slowly rotating, although not rapidly enough to provide significant support against self-gravity. [4] It is interesting that Kane and Clemens *did* find a strong correlation between the axis of rotation and the direction of elongation for Bok globules. They found that 10 out of the 15 globules in their sample are significantly elongated in the direction of the axis of rotation, exactly opposite the orientation that would be expected if globules were elongated by rotation stresses. One object in their data (CB67) is actually a striking example of a filament, which shows clear kinematic evidence of rotation about its axis of symmetry.

5.4.2 Random Motions and Thermal Support in Cores and Globules

Having argued in the previous subsection that rotation provides insufficient support against the self-gravity of cores and Bok globules, only pressure gradients and magnetic fields remain as possible means of support. In this subsection, we discuss the observational evidence for non-thermal motions in cores, and their importance relative to thermal pressure. As we shall see, the variation of the non-thermal velocity dispersion with radius has important consequences for the density structure of cores.

The Line Width-Size Relation

Recalling the relationship discovered by Larson (1981) between the observed line widths of molecular clouds and their sizes (Section 2.11.4), an obvious question is whether or not there is a similar relation that applies to cores. The total observed line width Δv_{tot} is directly related to the velocity dispersion σ of the molecular gas: [5]

$$\sigma = \frac{\Delta v_{tot}}{\sqrt{8 \ln 2}}. \tag{5.5}$$

---

[4] Kane and Clemens (1997) do not directly compare the rotational and gravitational energies of their sample of Bok globules. However, Myers and Goodman (1993) show that a related criterion for rotational support to be important is that $\beta_{vir} \sim 1$, where

$$\beta_{vir} \approx 0.92 \frac{GR}{\Delta v}, \tag{5.3}$$

where R is the radius of the core (or globule) and Δv is the line width (ie. The rotational and random kinetic energies must be comparable.). The velocity dispersions and Bok globule rotation curves presented by Kane and Clemens reveals that $\beta_{vir} \ll 1$, indicating that rotational support is unimportant.

[5] The total line width Δv_{tot} is corrected for the difference in mass between the observed molecule, of molecular weight μ and the particle of average molecular weight $\langle \mu \rangle \approx 2.33$:

$$\Delta v_{tot}^2 = \Delta v_{obs}^2 + 8 \ln(2) \frac{kT}{m_h} \left(\frac{1}{\langle \mu \rangle} - \frac{1}{\mu_{obs}} \right), \tag{5.4}$$

where Δv_{obs} is the observed line width, T is the kinetic temperature, k is Boltzmann's constant, and m_h is the mass of a hydrogen atom (Myers 1983).

The velocity dispersion measures the combined thermal and turbulent motions in the molecular gas, which is related to the pressure support within clouds and cores by the usual relation

$$P = \sigma^2 \rho. \tag{5.6}$$

Hence, the variation of the velocity dispersion with radius largely determines the pressure support and radial density structure of cores.

All of the clouds studied by Larson were dominated by supersonic (ie. non-thermally dominated) velocity dispersions. In fact, Larson speculated that the observed relation between the velocity dispersion and size of molecular clouds (see Section 2.11.4) might end on sufficiently small scales, where the motions become thermally dominated. (ie. A purely thermal cloud, with constant temperature, would have a line width-size relation of $\Delta v \propto R^0$.) The first indication that this might not be the case was in the line width-size relation obtained by Leung, Kutner, and Mead (1982) for Bok globules. Several of the Bok globules in their study have slightly subsonic velocity dispersions; yet all appear to obey a line width size relation similar to that found by Larson.

Myers (1983) determined the line width-size relation for a sample of 27 cores within dark clouds and 16 isolated globules, which are substantially smaller and less turbulent than the clouds in Larson's sample. He found a line width-size relation $\Delta v_{tot} \propto R^{0.3}$, which is slightly shallower than the 0.38 exponent found by Larson, probably due to the greater importance of the thermal component of the line width in dark clouds. Most importantly, Myers demonstrated that subsonic non-thermal motions persist even in very small dense cores. This is most clearly seen when Δv_{tot} is separated into thermal and non-thermal contributions: [6]

$$\begin{aligned} \Delta v_T^2 &= 8 \ln(2) \frac{kT}{\mu m_h} \\ \Delta v_{NT}^2 &= \Delta v_{obs}^2 - \Delta v_{th}^2. \end{aligned} \tag{5.7}$$

Myers found that

$$\Delta v_{NT} = 0.76 R^{0.52}, \tag{5.8}$$

where Δv_{NT} is in $km\ s^{-1}$ and R is in parsecs, so that $\Delta v_{turb} = \Delta v_{th}$ at a radius of $\sim 0.13\ pc$, assuming a temperature of $10\ K$. This radius marks the transition between predominantly thermal and non-thermal support, which plays a central role in the TNT (Thermal-Non-Thermal) models of cloud cores discussed in Section 5.6.4 below.

The most comprehensive analyses of the line width-size relation in cores have been in studies by Fuller

[6] Velocity dispersions and line widths add in quadrature. For example, $\Delta v_{tot}^2 = \Delta v_T^2 + \Delta v_{NT}$.

and Myers (1992), for low mass cores, and by Caselli and Myers (1995) for high mass cores. Casselli and Myers find a significant difference between the width-size relations for low and high mass cores:

$$\Delta v_{NT} \approx 0.18 R^{0.53} \tag{5.9}$$

for low mass cores, but

$$\Delta v_{NT} \approx 0.23 R^{0.21} \tag{5.10}$$

for high mass cores, in the same units as equation 5.8. Interestingly, the line width-size relation does not seem to be significantly affected by the presence of embedded stars in some of the cores (Caselli & Myers 1995). Therefore, the observed relations probably represent the initial conditions within cores at the onset of star formation.

Both of these studies confirm Myers' earlier (1983) findings, but provide improved estimates for the line width-size relations, based on a larger set of cores. They differ from Larson's earlier work, however, by distinguishing between *cloud-cloud* correlations, obtained from an ensemble of clouds measured in a single spectral line, and *line-line* correlations obtained from several spectral lines tracing different densities within a single core. Both studies find that the line-line correlations are in good agreement with the core-core correlations. Therefore, the line width-size relation probably reflects a true increase in the velocity dispersion with radius within individual cores, and should not be interpreted as a systematic variation of the velocity dispersion between isothermal (constant σ) clouds of various sizes. Several models of cloud cores are based on non-isothermal equations of state that reflect the observed line width-size relation. These models are discussed in Sections 5.6.4 and 5.6.5.

5.5 The Ordered Magnetic Field in Molecular Cloud Cores

Observations pertaining to the magnetic field strength and geometry in dense cores are rather sparse, compared to complementary studies of the magnetic field in the lower density regions of molecular clouds. We have already discussed the available techniques, namely Zeeman measurements and polarimetry, for studying the magnetic fields in molecular clouds (see Section 2.2). These same general techniques also apply to cloud cores.

5.5.1 The Zeeman Effect in Cores

Most measurement of the line of sight component of the magnetic field in molecular clouds have relied on the HI and OH Zeeman effects (see Section 2.2.1). However, observations of the Zeeman effect using transitions in these molecules are generally not suitable for cores, because HI is almost completely

absent in dense molecular gas, and OH is severely depleted at densities $\gtrsim 10^4\ cm^{-3}$ that are typical of cloud cores (Crutcher et al. 1996). Therefore, Zeeman observations must rely on other molecular species. Of these, only CN Zeeman observations have met with limited success.

The first attempt to measure the CN Zeeman effect in molecular cloud cores was by Crutcher et al. (1996). They observed two cores: OMC-N4 near the Orion KL region (see Section 2.2), and S106-CN. These two regions were selected because previous observations had detected both strong CN lines and strong magnetic fields in lower density gas, by the OH Zeeman effect. Nevertheless, they failed to detect a magnetic field in either region. The authors attribute this failure to either field reversals in their beam, or possibly an unfortunate near alignment of the field with the plane of the sky.

Subsequent observations by Crutcher et al. (1999) detected magnetic fields by the CN Zeeman effect toward three cores, including the OMC1 core in Orion A and two cores in the $DR21OH$ molecular cloud. The observed field strengths are much higher than those found by previous Zeeman measurements in OH and HI (see Section 2.2.1), with the line of sight magnetic field ranging from 33 to 71 mG in magnitude. Their results imply that the magnetic energy is only 1/10 to 1/3 of the internal kinetic energy within these cores. The cores are found to be magnetically super-critical (by a factor of $2 - 3$), but also in approximate virial equilibrium (see Section 2.11.2). It is mainly the non-thermal motions, not the field, responsible for supporting the gas in these cores.

Future CN Zeeman measurements hold much promise for revealing the field strengths and structures within cloud cores, especially in combination with far infra-red and sub-millimetre polarimetry, which we discuss next.

5.5.2 Sub-Millimetre and Far Infra-Red Polarimetry in Cores

In Section 2.2, we discussed the observational evidence that optical and near infra-red polarimetry does not trace the magnetic field in the dense regions of molecular clouds, which certainly includes their cores. Therefore, reliable polarimetry measurements of the magnetic field direction in cores require measurements at far infra-red and sub-millimetre wavelengths.

Greaves at al. (1994, 1995) obtained several 800 μm polarization vectors for three cores in the W3 cloud, Rho Ophiuchus, and Monoceros. They found that the magnetic field is well-ordered in all three cores, although the field lines in the W3 and Monoceros cores are noticeably curved. The authors suggest that the field structure in these regions might be consistent with "pinched-in" magnetic fields, resulting from the gravitational contraction of the cores. However, too few polarization vectors were obtained for this interpretation to be conclusive.

The most detailed far-infrared polarization map of a core is by Schleuning (1998), who combined 100 μm and 350 μm observations of the massive OMC-1 core in Orion, centred on the Kleinmann-Low

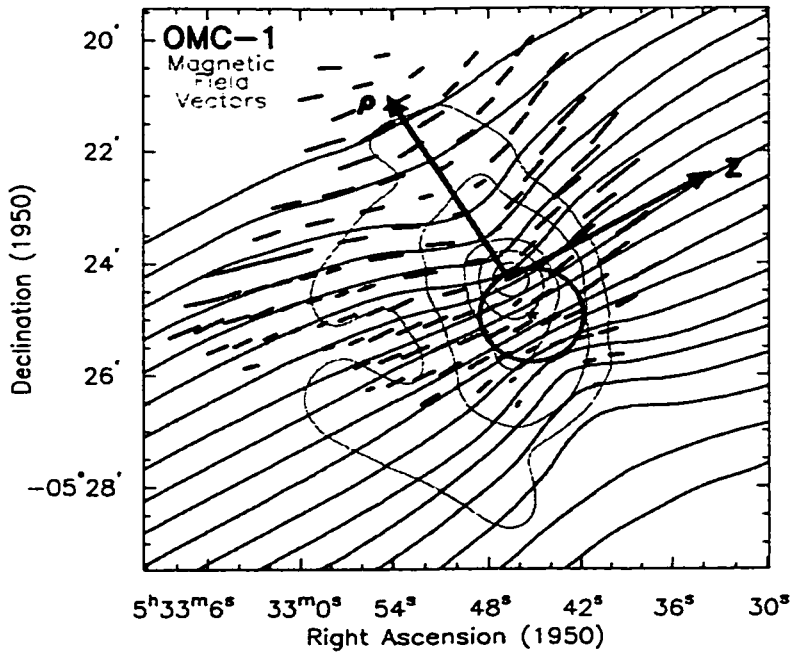

Figure 5-2: (From Schleuning 1998) The magnetic field vectors in the Orion KL region, inferred from 100 μm polarization data by rotating the vectors by 90°. The ρ and z axes are drawn to indicate the cylindrical symmetry of the field lines. The arrows are ~ 0.5 pc long.

(KL) region. His map, which we show in Figure 5-2, and subsequent analysis suggest a provocative picture of the magnetic field in this region. Schleuning found that the magnetic field is remarkably well-ordered and structured on a 1 pc scale. The field is not uniform, however. Rather, the field is symmetrically pinched in on either side of the KL Nebula. Schleuning suggested that an hourglass shaped magnetic field aligned perpendicular to the flattened KL core could explain the observations. This pinched field structure is expected for a core threaded by a predominantly poloidal field that has contracted under self-gravity (eg. TIN), which is consistent with modern ideas of magnetically regulated star formation in molecular cloud cores (Section 5.7.3). We note, however, that this data does not entirely rule out the possibility that there is some toroidal component of the magnetic field. Carlqvist and Kristen (1997) modeled the polarization patterns (in absorption) due to helical magnetic fields. For reasons that we discuss in the next chapter, they found that only only one field component, either poloidal or toroidal, dominated the polarization patterns. A helical field could exist in the KL region without being detected in the polarimetry, although we concede that this particular massive core is most consistent with a poloidally dominated magnetic field.

Several other studies are presently underway to map the 850 μm polarization in several of the cores along the integral-shaped filament in Orion A (Matthews & Wilson 1999) and a number of cores in Rho Ophiuchus and Orion B (Mitchell et al. 1999, private communication). These observations are briefly

discussed in Chapter 7.1.

5.6 Spherical Models of Molecular Cloud Cores

Generally, ordered fields are not consistent with spherical models (except for trivial cases where the field is either uniform or force-free; see discussion on page 141). We describe several spherical non-magnetic models in this section, before embarking on a discussion of non-spherical models in Section 5.7.

In spherical coordinates, the equation of hydrostatic equilibrium and Poisson's equation are respectively

$$\frac{dP}{dr} + \rho \frac{d\Psi}{dr} = 0 \tag{5.11}$$

$$\frac{1}{r^2}\frac{d}{dr}\left(r^2 \frac{d\Psi}{dr}\right) = 4\pi G\rho, \tag{5.12}$$

where r is spherical radius, ρ is the density, P is the total pressure (including thermal and non-thermal contributions), Ψ is the gravitational potential, and G is the gravitational constant. We note that equations 5.11 and 5.12 are two equations in three unknowns: ρ, P, and Ψ. Therefore, a third equation is required to close the system of equations. This is most simply specified as a "barotropic" equation of state relating the pressure to the density: $P = P(\rho)$. All of the models discussed in this chapter, as well as our models in the next, are of this type. [7]

It is often useful to define a core radius r_0 for non-singular models defined by

$$r_0^2 = \frac{\sigma_c^2}{4\pi G \rho_c}, \tag{5.13}$$

where ρ_c is the central density. [8] Generally, non-singular models are found to have a core-envelope structure in which the core ($r \lesssim r_0$) has relatively uniform density, which falls off in the envelope ($r \gtrsim r_0$), often as a power law. We have already seen examples of filaments with core-envelope density profiles in Chapter 3, the simplest example being the Ostriker (1964) solution for unmagnetized isothermal filaments.

[7] Note that this definition also includes the isothermal equation of state $P = \sigma^2\rho$, where σ is constant

[8] Often, a factor of 9 is included in the numerator of equation 5.13 (eg. Binney & Tremaine 1987 (equation 4-124b), McLaughlin & Pudritz 1996), which identifies r_0 with the radius where the projected surface density of an isothermal sphere falls to roughly half of its central value. We do not include this factor in our prolate core models in the next chapter.

5.6.1 Bonnor-Ebert Spheres

The Bonnor-Ebert (1956, 1955) model is the simplest model for spherical, pressure-truncated cores. Being isothermal, these models are not described by the line width-size relation discussed in Section 5.4.2. Bonnor-Ebert spheres are pressure-truncated solutions to equations 5.11 and 5.12, with constant σ, which cannot be expressed in closed form and must be found numerically. Bonner-Ebert spheres are characterized by a core-envelope structure with the density varying as $\sim r^{-2}$ in the envelope, as shown by the dark solid line in Figure 5-3. Note that we also show several polytropic models (dashed lines) on the same figure, which we discuss in Section 5.6.3. We have shown the Bonnor-Ebert model out to a large radius in Figure 5-3. However, the solution is to be truncated at the unique radius where the internal pressure is equal to that of the external medium.

The Bonnor-Ebert model has proven extremely useful to our understanding the stability of molecular clouds and their cores. The stability analysis presented in Section 2.11 for magnetized molecular clouds is the approximate virial theorem version of the exact calculation by Bonnor (1956) and Ebert (1955) for unmagnetized, self-gravitating, pressure-truncated gas clouds. Exact calculations find that isothermal spheres are unstable to gravitational collapse when the mass is greater than the critical Bonnor-Ebert mass

$$\mathcal{M}_{B.E.} = 1.18 \frac{\sigma^4}{G^{3/2} P_S^{1/2}}. \tag{5.14}$$

An important feature of the Bonnor-Ebert picture is that the critical mass of a core is determined by its velocity dispersion and the pressure of the surrounding cloud material. In the next chapter, we use the Bonnor-Ebert critical mass as a convenient reference point with which to compare our isothermal models of prolate cloud cores.

5.6.2 The Singular Isothermal Sphere

The equations of self-gravitating hydrostatic equilibrium (equations 5.11 and 5.12) admit a very simple singular isothermal solution, which is often called the singular isothermal sphere (SIS):

$$\rho = \frac{\sigma^2}{2\pi G r^2}, \tag{5.15}$$

where σ is constant.

Equation 5.15 is the initial state for several models of gravitational collapse (eg. Larson 1969, Penston 1969, Shu 1977), and hence plays a central role in our understanding of the collapse phase that leads to the formation of a central protostar. While useful, the SIS model does not take into account the fact that cores must be truncated by the pressure of the surrounding gas (the molecular cloud for cores, or

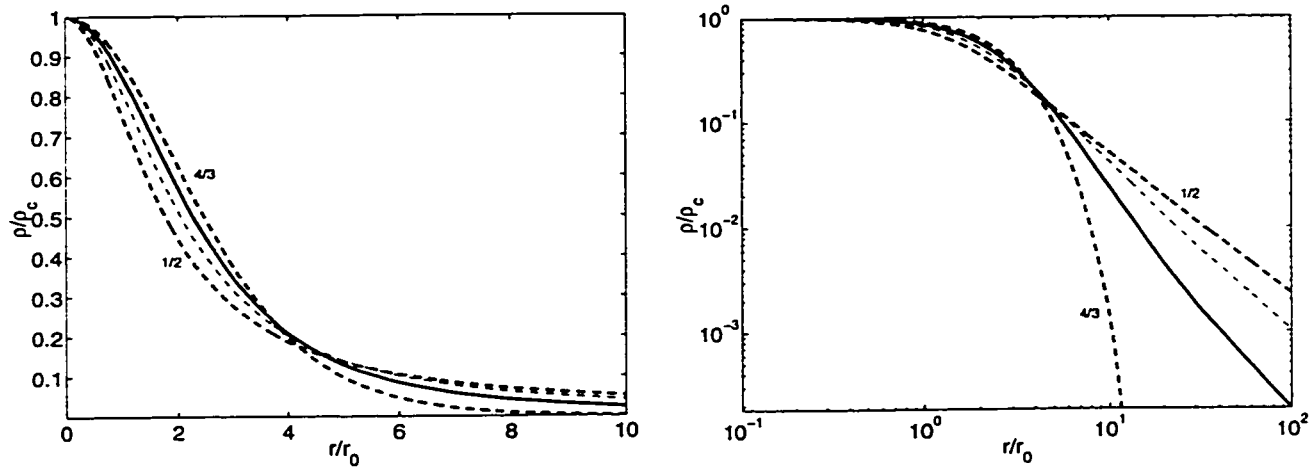

Figure 5-3: The Bonnor-Ebert isothermal sphere model (heavy solid line) and several polytropic models (dashed lines). The heavy dashed lines are for the polytropic indices indicated on the figure. The thin dashed line is for $\gamma_p = 0.73$, which obeys the same line width-size relation as high mass cores (equation 5.10). Bonnor Ebert spheres are discussed in Section 5.6.1, and polytropes are discussed in Section 5.6.3.

the ISM for isolated globules). In principle, however, the SIS model can be truncated at the radius where the internal pressure matches that of the external medium. Note, however, that recent sub-millimetre observations suggest that many starless cores have flat inner density profiles that are not consistent with singular models (Ward-Thompson et al. 1994; see also review André et al. 1999). Therefore, the SIS model, and singular models in general, may be most appropriate for cores that have already begun to form protostellar objects at their centres.

5.6.3 Polytropic Models of Cloud Cores

It is straightforward to construct polytropic models of cloud cores, in much the same way as the Bonnor-Ebert spheres discussed in Section 5.6.1. The polytropic equation of state assumes that the pressure is related to the density by an equation of the form

$$\frac{P}{P_c} = \left(\frac{\rho}{\rho_c}\right)^{1+1/n}, \tag{5.16}$$

where P_c and ρ_c are respectively the pressure and density at the centre of the core, and n is the polytropic index (assumed to be constant). Often, the exponent in equation 5.16 is replaced by γ_p, so that $P = \propto \rho^{\gamma_p}$, which is more convenient for our purposes. Equation 5.16 closes the equations of hydrostatic equilibrium (equations 5.11 and 5.12), which can be solved numerically to obtain self-gravitating polytropes. We show examples of polytropes in Figure 5-3, for $\gamma_p = 1/2$, 4/3, and 0.73. Each of these values of γ_p has a special significance, which we discuss below.

By comparing the four curves in Figure 5-3, we note that the polytropic index controls the radial structure of the core. (Note that the Bonnor-Ebert sphere can be thought of as a $\gamma_p = 1$ polytrope.) Models with small values of γ_p have small core regions and shallow density gradient in the outer envelope. Models with larger values of γ_p have extended core regions and steep density gradients in their envelopes.

Equation 5.16 implies that the velocity dispersion of the gas is related to the density by

$$\sigma^2 \propto \rho^{\gamma_p - 1}. \tag{5.17}$$

If $\gamma_p \geq 1$, it is clear that the velocity dispersion must decrease with increasing radius (decreasing density), which is opposite to the observed line width-size relation for cores. On the other hand, if $\gamma_p < 1$ (eg. Maloney 1988), then the velocity dispersion increases with radius, in better agreement with the observations. [9]

Chandrasekhar (1957, Chapter 4) shows that polytropes admit a singular solution for all $\gamma_p < 4/3$, which is analogous to the SIS model discussed in Section 5.6.2. The density structure of a singular polytrope is a power law in radius:

$$\rho \propto r^{-2/(2-\gamma_p)}, \tag{5.18}$$

so that the pressure and velocity dispersion vary with radius as

$$P \propto r^{-(2\gamma_p)/(2-\gamma_p)} \tag{5.19}$$

$$\sigma \propto r^{(1-\gamma_p)/(2-\gamma_p)} \tag{5.20}$$

by equations 5.16 and 5.17. Singular polytropic models should be thought of mainly as describing the asymptotic structure of non-singular polytropes. This is particularly evident when $\gamma_p < 1$, because the central velocity dispersion (equation 5.20) vanishes for these models.

Comparing equation 5.20 with the observed line width-size relations for cores (equations 5.9 and 5.10) suggests that high mass cores might be reasonably described by singular polytropes with $\gamma_p = 0.73$, so that $\rho \propto r^{-1.6}$ by equation 5.18. Similarly, we find that $\gamma_p = -0.13$ and $\rho \propto r^{-0.94}$ for low mass cores. Notice that the pressure increases monotonically with radius when $\gamma_p < 0$, which is clearly unrealistic. We must conclude that singular polytropic models do not suitably describe the structure of low mass cores. The $\gamma_p = 0.73$ solution for high mass cores is one of the special solutions shown in Figure 5-3.

It is well-known that polytropic spheres are unconditionally stable to adiabatic radial oscillations when $\gamma_p > 4/3$ (cf. Chandrasekhar 1957, Chapter 2), and that Bonner-Ebert instabilities are possible only when $\gamma_p < 4/3$ (see McKee & Holliman 1999). (Note that the critical case of $\gamma_p = 4/3$ is one of the

[9] The case of $\gamma_p < 1$ is often referred to as a negative index polytrope, since $n < 1$ for these models.

cases shown in Figure 5-3.) However, this conclusion depends on the type of perturbation being applied. McLaughlin and Pudritz (1996) assume that the velocity dispersion at the centre of a core remains constant during radial perturbations, which might be justified for the thermally dominated centres of cores. They find that all "negative index polytropes," with $\gamma_p < 1$, are unconditionally stable to this type of perturbation, and therefore can never collapse to form stars.

The final special case shown in Figure 5-3 is for $\gamma_p = 1/2$. This case corresponds to a core that is supported by purely Alfvén wave pressure, which we discuss in Section 5.6.5 below.

5.6.4 The TNT Model

As we discussed in Section 5.4.2, the non-thermal component of the velocity dispersion in a core is observed to increase monotonically with radius, from zero (or nearly zero) at the centre to supersonic velocities in the outer regions. At any radius, the total one-dimensional velocity dispersion is given by

$$\sigma^2 = \sigma_T^2 + \sigma_{NT}^2, \tag{5.21}$$

where σ_T is the constant thermal velocity dispersion $(kT/\mu m_h)^{1/2}$ and σ_{NT} is approximately a power law in radius (see Section 5.4.2): $\sigma_{NT} = ar^b$, where a and b are constants that can be obtained from the line width-size relations for low and high mass cores (equations 5.9 and 5.10). Note that there is a unique radius

$$r_{TNT} = \left(\frac{\sigma_T}{a}\right)^{1/b} \tag{5.22}$$

which divides the thermally dominated interior region from the non-thermally dominated outer layers of the core.

We considered singular polytropic models in Section 5.6.3, where we showed that the asymptotic structure (ie. well away from the isothermal central region) of high mass cores might be consistent with a $\gamma_p = 0.73$ polytrope. Obviously, this simple model does not apply at small radius, since the velocity dispersion in equation 5.18 vanishes at the origin (provided $b > 0$), where observations indicate that σ approaches its constant thermal value σ_T. Clearly, the SIS model is more applicable than equation 5.18 at radii less than r_{TNT}.

The TNT models of Myers and Fuller (1992) and Caselli and Myers (1995) essentially join together the radial dependence of the SIS model at small radius and equation 5.18 at large radius:

$$\rho = \frac{\sigma_T^2}{2\pi G r_0^2}\left[\left(\frac{r}{r_0}\right)^{-2} + \left(\frac{r}{r_0}\right)^{-\alpha}\right], \tag{5.23}$$

where r_0 and α are free parameters that are fit to the data. By substituting equation 5.23 into the

equations of self-gravitating hydrostatic equilibrium (equations 5.11 and 5.12), Caselli and Myers (1995) obtained the radial dependence of the non-thermal component of the velocity dispersion $\sigma_{NT}(r)$. They fit $\sigma(r)$ to the observed line width-size relations for low and high mass cores, obtaining $\alpha = 1.6$ for high mass cores, which is identical to the value that we obtained by considering singular polytropes. They obtained $\alpha = 1.1$ for low mass cores, which is somewhat higher than the value of 0.94 that we obtained from our simple argument. The pressure inferred from the TNT model decreases monotonically with radius for both high and low mass cores. Therefore, the asymptotic pressure structure of the TNT model for low mass cores is clearly more suitable than the singular polytrope that we derived in Section 5.6.3.

Although the TNT models accurately reproduce the line width-size relations for both low and high mass cores, their singular density profiles do not agree with the recent results discussed in Section 5.6.2, which suggest that pre-protostellar cores have flat inner density profiles. It is also perhaps not very satisfying that low and high mass cores are not fit by the same model. The logatropic model of McLaughlin and Pudritz (1996), discussed in Section 5.6.6 below, addresses both of these concerns.

5.6.5 Multi-Pressure Polytropes

McKee and Holliman (1999) have recently presented a comprehensive analysis of equilibria that are based on a generalization of the polytropic models discussed above. Specifically, they assume that a core consists of a single self-gravitating fluid whose pressure can be resolved into several partial pressure components P_i, each of which behaves as a polytrope:

$$P(r) = \sum_i P_i(r) = \sum_i K_{pi}\rho^{\gamma_{pi}}(r), \tag{5.24}$$

where γ_{pi} is the polytropic index associated with P_i. The advantage of their formalism is that each partial pressure models a known contribution to the overall pressure support of a core. These include the thermal gas pressure ($\gamma_{pi} = 1$), Alfvén waves ($\gamma_{pi} = 1/2$), and the magnetic pressure ($\gamma_{pi} = 4/3$).

McKee and Holliman point out that polytropic equilibria are not necessarily *isentropic*. What this means is that a core whose *equilibrium* structure is described by a polytropic equation of state need not respond *dynamically* to pressure changes by the same polytropic law. [10] Rather, McKee and Holliman assume that pressure changes are adiabatic:

$$\frac{\delta P}{P} = \gamma\frac{\delta\rho}{\rho}, \tag{5.25}$$

[10] As a simple example, consider adiabatic sound waves propagating in an isothermal ($\gamma_p = 1$) Bonnor-Ebert core.

where the adiabatic index γ might be different from the polytropic index γ_p. [11]

Not all combinations of γ_p and γ are allowed, however. If $\gamma_p > \gamma$, convective instabilities rapidly drive the core to an isentropic ($\gamma_p = \gamma$) configuration. [12] However, equilibria with $\gamma_p < \gamma$ are convectively stable, and therefore allowed as possible models of cloud cores (McKee & Holliman 1999).

There is a distinction between locally and globally adiabatic perturbations in McKee and Holliman's analysis. Locally adiabatic perturbations (equation 5.25) apply when perturbations are rapid enough that no heat is transferred internally between different parts of the cloud. On the other hand, globally adiabatic perturbations assume that no heat flows between a core and its environment, but that different parts of a core are in good thermal contact.

The most important result of McKee and Holliman's formulation is for the case of Alfvén waves, which they model as a globally adiabatic pressure component ($\gamma_p = 1/2, \gamma = 3/2$, McKee & Zweibel 1995). [13] They find that the critical mass for a cloud supported by Alfvén wave pressure alone is

$$M_w = 0.65 \frac{\langle \sigma_{NT}^2 \rangle^{3/2}}{G^{3/2} \rho_s^{1/2}}, \tag{5.26}$$

where $\langle \sigma^{NT} \rangle$ is the mean non-thermal velocity dispersion associated with the Alfvén waves and ρ_s is the density at the edge of the cloud. Comparing this with equation 2.40, Alfvén waves are somewhat less effective at supporting a cloud against self-gravity than the isothermal pressure component assumed in the Bonnor-Ebert analysis. For a cloud that is supported by a combination of thermal pressure and globally adiabatic wave pressure, McKee and Holliman find that equation 2.40 can still be used to obtain the critical mass, provided that σ is replaced by an effective velocity dispersion defined by

$$\sigma_{eff}^2 = \sigma_T^2 + 0.67 \langle \sigma_{NT}^2 \rangle. \tag{5.27}$$

5.6.6 The Pure Logatrope

McLaughlin and Pudritz (1996) have recently proposed that the line width-size relations for both low and high mass cores can be described by a single empirical equation of state for the gas:

$$P = \sigma_c^2 \rho_c \left[1 + A \ln \left(\frac{\rho}{\rho_c} \right) \right], \tag{5.28}$$

[11] Note that we implicitly assumed isentropic ($\gamma_p = \gamma = 1$) perturbations in our stability analysis in the last chapter.

[12] This is analogous to the adiabatic temperature gradient set up in the convective zone of the sun by the efficient convective transport of energy (see Collins 1989).

[13] Alfvén waves provide an isotropic pressure (Dewar 1970). See also Section 2.5.1

where A is a constant, and ρ_c and σ_c are respectively the central density and the central, purely thermal, velocity dispersion. Using this equation of state, which they refer to as a "pure logatrope", they numerically integrate equations 5.11 and 5.12, which allows them to constrain $A \approx 0.2$ by comparing with line width-size data for both low and high mass cores ***simultaneously.*** They find that the density varies as approximately r^{-1} outside of the core radius of their models. This is significantly more shallow than the r^{-2} density profile of an isothermal sphere.

McLaughlin and Pudritz emphasize that realistic models of cloud cores should be based on a non-isothermal equation of state, like their logatrope, which reflects the observational fact that the velocity dispersion rises with radius in cloud cores. McLaughlin and Pudritz' logatrope has been criticized since its origin is phenomenological (McKee 1999). However, this is equally true for polytropes, or the isothermal (including the non-thermal pressure) equation of state, for that matter. At present, we simply do not understand the origin of the observed line width-size relation in cloud cores. Models like the multiple-pressure polytropes of McKee and Holliman (1999) are promising because they attempt to derive the equation of state of molecular clouds from established physical principles. However, it remains to be shown that multiple-pressure polytropes can account for the observations as well as the pure logatrope.

5.7 Non-Spherical Models and Ordered Magnetic Fields

Models that include ordered magnetic fields are generally non-spherical as a result of non-isotropic stresses produced by the field. From a computational standpoint, magnetized models are therefore substantially more difficult to compute than their unmagnetized, spherical counterparts. Mouschovias (1976a) originally devised the Self Consistent Field Method (SCFM) which has been used by several authors (Mouschovias 1976b, TIN, Tomisaka, Ikeuchi, & Nakamura 1988b, 1989, 1990, Tomisaka 1991) to construct magnetized models of self-gravitating clouds and cores. These models are all isothermal, which is the usual assumption for models based on the SCFM. However, Mouschovias (1976) pointed out that the method could be generalized to include non-isothermal equations of state. The only place where this has actually been done is in Lizano and Shu (1989), who study the evolution of logatropic clouds by ambipolar diffusion.

We outline the SCFM in the next chapter. However, the essence of the method is that one finite differences Poisson's equation and the equation of magnetohydrostatic equilibrium, subject to appropriate boundary conditions, and iteratively solves the resulting matrix equations for the density ρ, the gravitational potential Ψ, the toroidal component of the magnetic vector potential A_ϕ (associated with the poloidal field), and the toroidal field B_ϕ. At each step, the core model is truncated at the surface

where the pressure drops to that of the ambient medium, so that the external cloud material is modelled as a source of pressure, but not gravity. Care is taken to ensure that the total mass of the core, the flux threading it, and the poloidal current associated with the toroidal field remain constant. Eventually, models either converge to a solution, or diverge if no equilibrium state is available. An example of non-convergence is the situation where the mass is chosen higher than the critical Bonnor-Ebert mass. [14]

5.7.1 The Shapes of Cores

Most magnetic models of cloud cores have concentrated on purely poloidal magnetic fields, including all of those listed above except for Tomisaka (1991), who included a toroidal field component (Tomisaka's model is discussed in detail in the next chapter). Magnetic fields exert no force in the direction of the field lines, but tend to support the gas perpendicular to the field lines. For poloidal fields, the support is predominantly in the radial direction, in cylindrical coordinates. Therefore, equilibria that employ poloidal magnetic fields are necessarily oblate, and often significantly flattened in the direction of the field (see TIN for several examples). However, observational evidence indicates that cores and Bok globules are predominantly prolate, as we discussed in Section 5.3.

We show in the next chapter that this probable discrepancy with the observations is resolved if cores inherit modest toroidal fields from their parent filamentary clouds, so that their magnetic fields are helical in general. [15] Cores are prolate in our model because the "hoop stress" of the toroidal field component squeezes the gas radially, just as it does in our models of filaments. Almost all of our core models are prolate, with a wide range of intrinsic axis ratios from $\sim 0.1 - 0.9$. We have also considered the mean projected axis ratios of our models, assuming random orientations on the sky. We find that the projected axis ratios range from $\sim 0.3 - 1$. Many of our models are in agreement with the observations, which find projected axis ratios widely distributed about a mean value, which is between 0.5 and 0.6.

Our models of prolate cores, presented in the next chapter, resemble pressure-truncated Bonnor-Ebert spheres that are squeezed into a prolate shape by the toroidal component of the magnetic field. In fact, we have verified that our models become almost identical to Bonnor-Ebert spheres (except for near their surfaces) in the high mass limit, when they are so strongly self-gravitating that the magnetic field has little effect on the density structure (see Figure 10 of Chapter 6).

[14] The Bonnor-Ebert mass is modified by the magnetic field, however. See Sections 2.11.2 and 2.11.5

[15] The field lines in our core models are not really helices in the mathematically correct sense of the word. For lack of a better word, we use the term "helical" in our discussion of core models to describe any twisted field configuration that contains both poloidal and toroidal fields.

5.7.2 The Critical Mass of Magnetized Cores

Mouschovias and Spitzer (1976) first obtained a numerical estimate of the critical Bonnor-Ebert mass for non-rotating clouds (or cores) threaded by purely poloidal fields:

$$M_{crit} \approx 1.18 M_{B.E} \left[1 - \frac{M_\Phi^2}{M_{crit}^2}\right]^{-3/2}, \tag{5.29}$$

where the magnetic critical mass is given by $M_\Phi = 0.13\ \Phi G^{-1/2}$. Note that we obtained a similar equation (without the coefficent) from our simple virial analysis in Section 2.11.2 (equation 2.41), which we graphed in Figure 2-9. Tomisaka et al. (1988b) confirmed Mouschovias' result in their analysis.

What is the effect of the toroidal field on the critical Bonnor-Ebert mass of cloud cores? Our simple virial analysis in Section 2.11.5 demonstrates that toroidal fields decrease the critical mass by squeezing cores, in concert with the external pressure (see also Habe et al. 1991). Our numerical results in the next chapter confirm this. We find that the toroidal field decreases the critical mass by about 20% for the cases that we have studied.

5.7.3 The Evolution of Cores by Ambipolar Diffusion

It was realized as early as 1956 by Mestel and Spitzer that magnetic fields in astrophysical plasmas can decay by the process of ambipolar diffusion. While flux-freezing ensures that the magnetic field is almost perfectly coupled to the ions in a molecular cloud, the vastly more common neutrals are coupled to the field only through collisions with the ions. Ambipolar diffusion occurs because neutral atoms and molecules gradually slip past the ions, allowing the cloud to contract and the magnetic field to escape.

A modern paradigm of star formation in molecular cloud cores assumes that cores begin in a magnetically sub-critical state (see Section 2.11.2), and evolve by a slow and quasi-static contraction (eg. TIN). Cores may eventually become magnetically super-critical by this process. When this happens, the magnetic field is insufficient to support the core against self gravity, and the core rapidly evolves to a Bonnor-Ebert critical state (equation 2.41). Once the Bonnor-Ebert critical state is reached, the combined pressure and magnetic forces can no longer support the core against self-gravity, and collapse is inevitable.

Following McKee (1993), we estimate the ambipolar diffusion timescale in a magnetically supported, self-gravitating core. Assuming equilibrium between ionization due to cosmic rays and recombinations, the ion density within a core is related to the density of hydrogen nucleons by the formula

$$n_i = K_i n_H^{1/2}, \tag{5.30}$$

where $K_i \approx 10^{-5} cm^{-3/2}$ is a constant. The ion-neutral collision frequency is given by

$$\nu_{ni} = n_i \langle \sigma v \rangle, \tag{5.31}$$

where $\langle \sigma v \rangle \approx 1.5 \times 10^{-9} cm^3 s^{-1}$ is the effective collision rate coefficent. Combining equations 5.30 and 5.31, the mean time between collisions is

$$\tau_{ni} = \frac{1}{\nu_{ni}} \approx (K_i \langle \sigma v \rangle)^{-1} n_H^{-1/2}. \tag{5.32}$$

The density of hydrogen nucleons is related to total mass density by $\rho = \mu_H n_H$, where $\mu_H = 2.34 \times 10^{-24} g$ is the average mass per hydrogen nucleon (McKee 1993). Therefore, equation 5.32 can be expressed in terms of ρ as

$$\tau_{ni} = C \rho^{-1/2}, \tag{5.33}$$

where

$$C \equiv \frac{\mu_H^{1/2}}{K_i \langle \sigma v \rangle} \approx 102\ g^{1/2} cm^{-3/2} s. \tag{5.34}$$

Assuming that the neutrals accelerate due to the local gravitational acceleration g, between collisions with ions, the drift speed of the neutrals is given by

$$v_d \approx g \tau_{ni} \approx C \frac{GM}{R^2} \rho^{-1/2}, \tag{5.35}$$

where M is the mass of the core, R is its radius, and G is the gravitational constant. The ambipolar diffusion timescale is the time required for neutrals to slip through a distance comparable to R:

$$\tau_{A.D.} = \frac{R}{v_d} = \frac{3}{4\pi G^{1/2} C} (G\rho)^{-1/2} \approx 9.1 (G\rho)^{-1/2} \approx 5.6 \left(\frac{n}{10^4\ cm^{-3}} \right)^{-1/2}\ Myr, \tag{5.36}$$

after some manipulations. Notice that the ambipolar diffusion timescale is proportional to the dynamical timescale for free-fall collapse defined by

$$t_{ff} = \sqrt{\frac{3\pi}{32}} (G\rho)^{-1/2} \approx 3.4 \times 10^5 \left(\frac{n}{10^4\ cm^{-3}} \right)^{-1/2}\ years, \tag{5.37}$$

where we have scaled n by a density that is typical of cores. Therefore, the ambipolar diffusion timescale is given in terms of t_{ff} by

$$\tau_{A.D.} \approx 17\ t_{ff}. \tag{5.38}$$

The most important result from this analysis is that ambipolar diffusion is slow compared to the

dynamical timescale of cloud cores. Therefore, the often made assumption of quasi-static evolution is justified, at least until the very late super-critical stages of evolution, which are much more rapid. How would a core threaded by a helical field evolve by ambipolar diffusion? To the best of our knowledge, this problem has not been addressed, but might be quite different from the simple picture presented here. The difference might arise because a helical field with a sufficiently strong toroidal component exerts a net force on the ions that is radially *inward*. It is possible that this would cause ions and field lines to drift inward initially, as a result of the magnetic stresses. However, this would increase the gradient of the poloidal field, which would probably halt the inward drift. Detailed calculations would be required to determine the long term evolution of a helically magnetized core by ambipolar diffusion.

5.8 Models of Cloud Cores - Limitations and Possibilities

We have shown in the previous section that most magnetized models of cloud cores ignore the observational fact than line widths rise with radius within individual cores, and that the gas is therefore not isothermal. [16] This criticism applies to our models presented in the next chapter as well. An equally valid criticism of spherical models (Section 5.6) is that they do not include ordered magnetic fields, which almost certainly play an important, and possibly dominant, role in the equilibrium of cloud cores. Non-isothermal models that include ordered magnetic fields are a likely future direction for models of cores.

The non-thermal motions in molecular clouds and their cores are almost certainly magnetic in origin (see Section 2.5), so it should be possible to combine magnetic fields and non-thermal motions in a self-consistent fashion that does not require an empirically determined equation of state such as McLaughlin and Pudritz' pure logatrope (Section 5.6). It is not clear at present how this degree of self-consistency can be accomplished. The next generation of models will need to question how ordered magnetic fields and MHD turbulence are related to one another. This is a very complex problem that will need to be overcome if fundamental progress is to be made.

[16] One exception is the model of Lizano and Shu (1989), which studies the process of ambipolar diffusion in logatropic cores. Their logatrope has a different form than the McLaughlin and Pudritz (1996) logatrope, however.

Chapter 6

Prolate Cores in Filamentary Molecular Clouds

This chapter is a preprint of the paper "Prolate Cores in Filamentary Molecular Clouds" by Fiege J.D. and Pudritz R.E., which has been accepted for publication by The Astrophysical Journal.

Abstract

We present a new model of molecular cloud cores that originate from filamentary clouds that are threaded by helical magnetic fields. Only modest toroidal fields are required to produce elongated cores, with intrinsic axis ratios in the range $0.1 \lesssim q \lesssim 0.9$ and mean projected axis ratios in the range $0.3 \lesssim \langle p \rangle \lesssim 1$. Thus many of our models are in good agreement with the observed shapes of cores (Myers et al 1991, Ryden 1996), which find axis ratios distributed about the mean values $\langle p \rangle \approx 0.5 - 0.6$ and $q \approx 0.4 - 0.5$. We find that the Bonnor-Ebert critical mass is reduced by about 20% by the helical field threading our models. We also find that models are generally most elongated when the mass is significantly less than the Bonnor-Ebert critical mass for unmagnetized cores.

6.1 Introduction

There is considerable observational evidence that most molecular cloud cores and Bok globules are elongated structures that may be approximately prolate in shape. Myers et al. (1991) measured the projected axis ratios of 16 cores in line intensity maps of NH_3, CS, and $C^{18}O$ and found that the mean projected axis ratio $\langle p \rangle$, defined as the ratio of the minor to major axis, is in the range $0.5 - 0.6$. They assumed that the cores are randomly oriented on the sky and calculated the allowed values of the intrinsic axis ratio q. Their analysis showed that modest elongation with $q = 0.4 - 0.5$ can account for the projected axis ratios if the cores are intrinsically prolate, but rather extreme flattening, with

$q < 0.1 - 0.3$ is required if they are intrinsically oblate. Moreover, 6 of the 16 cores appear to be inside of and aligned with larger filamentary structures of lower density observed in CO or dust extinction. They argued that cores must almost certainly be prolate in such cases, which are actually quite common. The Schneider and Elmegreen (1979) Catalogue of Dark Globular Filaments shows many other examples of elongated cores contained within filamentary structures.

Ryden (1996) extended the pioneering work of Myers et al. (1991) by analyzing the distribution of axis ratios for a large sample of Bok globules and cloud cores taken from several independent data sets (See Ryden for references). She found that randomly oriented oblate cores are inconsistent with the observed axis ratios for most samples to a high confidence level ($> 99\%$ in some cases). On the other hand, she found that prolate cores are almost always consistent with the data. Her analysis predicts that the mean intrinsic axis ratio for cores is typically 0.4-0.5, in agreement with Myers et al. (1991), but also that there should be significant numbers of cores that are either significantly more elongated or more nearly spherical.

If cores are truly prolate, then several interesting questions are raised about the non-isotropic forces responsible for their shapes. It is well established that rotation is negligible compared to magnetic and gravitational forces (Goodman et al. 1993), and tends to make cores oblate in any case (Tomisaka, Ikeuchi, and Nakamura 1988a, hereafter TIN). It is known, however, that large scale magnetic fields play a central role (Myers and Goodman 1988a,b) in supporting cores against self-gravity. Considerable theoretical effort has gone into producing magnetized, non-spherical models of cloud cores (Mouschovias 1976a,b, TIN, Tomisaka, Ikeuchi, and Nakamura 1988b, 1989, 1990 (hereafter TIN88b, TIN89, and TIN90), and Tomisaka 1991). Most of these models assume that the magnetic field threading the core is purely poloidal. However, purely poloidal fields result in oblate structures which, as we have seen, do not seem to explain the observations.

We show that prolate models of cores, whose shapes are in better agreement with the observations, are readily produced by including a toroidal component of the magnetic field, so that the field is helical in general [1]. The basic point is that the radial pinch of the toroidal field helps to squeeze cores radially into a prolate shape, while helping to support the gas along the axis of symmetry. Tomisaka (1991) finds that toroidal fields can result in moderately prolate equilibria with intrinsic axis ratios of $\gtrsim 2/3$. Therefore, his most prolate models are less elongated than the mean axis ratio predicted by the observations. His prolate equilibria are also only obtained when the cores are not very centrally concentrated, with a density contrast of only ~ 3 between the centre and the surface. We shall show that our models are both more elongated and more centrally concentrated.

[1] We use the term "helical" rather loosely to describe any field geometry that includes both poloidal and toroidal field components. The field lines in our prolate core models are not true helices in the mathematically correct sense.

One way that a core could acquire a helical field is by inheriting it from its parent filamentary cloud. We previously derived models of filamentary clouds threaded by helical magnetic fields in Fiege and Pudritz 1999a, (hereafter FP1). We showed that helical fields with constant poloidal and toroidal flux to mass loading are consistent with both the virial properties of filaments and the existing data on their density profiles (Alves et al. 1998, Lada et al. 1998). Our main goal in this paper is to determine the equilibrium states that are accessible to cores that might form from elongated fragments of these magnetized filaments. Three parameters are required to specify our filament models, which we discuss in the next section. In addition to these three parameters, we only need to specify the mass of a core to calculate its equilibrium structure in our model.

Our main findings are that a large range of core models with projected axis ratios $\langle p \rangle$ ranging from ~ 0.3 to ~ 1 can be obtained from our models of filamentary clouds threaded by helical fields. Our converged solutions define the prolate magnetic analogues of Bonnor-Ebert (1956, 1955) spheres. Their magnetic structure is characterized by a relatively strong "backbone" of poloidal flux surrounded by a region where the toroidal field dominates, but usually does not exceed the peak poloidal field.

We rather completely map out our parameter space by searching for models whose parent filaments obey the observational constraints discussed in FP1, and whose fragmentation is driven predominantly by self-gravity rather than by MHD sausage instabilities (See Fiege & Pudritz 1999b for details, hereafter FP2). The prolate core models that converge are found to occupy a well-defined region of parameter space. The failure of models to converge outside of this region can be traced to non-equilibrium resulting from gravitational and MHD instabilities. We also show that the magnetic analogue of the Bonnor-Ebert critical mass is somewhat reduced by the helical field in our models.

A brief outline of our paper is as follows. In Section 6.2 we outline the self-consistent field method that we use to generate our equilibria. We describe our numerical method in Section 6.3, and show a gallery of representative models in Section 6.4. In Section 6.5, we show sequences of models with varying mass and external pressure, and show that the Bonnor-Ebert critical mass is reduced by the magnetic field. We derive a singular model of isothermal cores wrapped by purely toroidal fields in Section 6.6, and discuss our results in Section 6.7.

6.2 The Self-Consistent Field Method

Our basic strategy is to use a relatively minor generalization of the self-consistent field method originally developed by Mouschovias (1976a), (subsequently used by Mouschovias 1976b, TIN, TIN88b, TIN89, TIN90, and Tomisaka 1991) to follow the relaxation of finite fragments of the filamentary clouds discussed in FP1. The reader is referred to TIN for a full derivation of the equations. We briefly outline the method

and discuss our modifications in this section.

The self-consistent field method iteratively solves Poisson's equation and the equations of magneto-hydrostatic equilibrium for a self-gravitating cloud threaded by a magnetic field and truncated by an external pressure. The source of the external pressure, which is presumably relatively low density molecular or atomic gas, is assumed to be non-self-gravitating and of negligible density. Thus, the external pressure P_S serves mainly to define the surface of the cloud in our model.

The self-consistent field method separates the equations of magnetohydrostatic equilibrium into equations describing the detailed balance of gravitational, magnetic, and hydrostatic forces parallel to the poloidal field lines and perpendicular to them. Following TIN, we use the flux quantity Φ which is proportional to the true magnetic flux Φ_{mag}:

$$\Phi_{mag} = 2\pi\Phi. \tag{6.1}$$

The equation of magnetohydrostatic equilibrium is given by

$$\nabla P + \frac{\mathbf{B}\times(\nabla\times\mathbf{B})}{4\pi} + \rho\nabla\Psi = 0. \tag{6.2}$$

Writing the toroidal field as

$$B_\phi = \frac{b_\phi}{r}, \tag{6.3}$$

it follows directly from the azimuthal component of equation 6.2 that b_ϕ is constant along field lines (See TIN for proof); hence b_ϕ is a function of Φ alone.

The magnetic field exerts no force in the direction parallel to the poloidal field lines. Thus the equation of magnetohydrostatic equilibrium reduces to the hydrostatic equation along a field line:

$$\frac{\partial P}{\partial s} + \rho\frac{\partial\Psi}{\partial s} = 0, \tag{6.4}$$

where s is the distance along the field line ($s = 0$ at the symmetry plane defined by $z = 0$), P is the effective pressure, which may contain a contribution due to non-thermal motions of the gas, ρ is the density, and Ψ is the gravitational potential (We do not include the effects of rotation in our analysis.). We assume that the gas is "isothermal" in the sense that the total velocity dispersion σ is constant:

$$P = \sigma^2\rho. \tag{6.5}$$

In this case, equation 6.4 can be integrated to obtain

$$\rho = \frac{Q(\Phi)}{\sigma^2} e^{-\Psi/\sigma^2}, \tag{6.6}$$

where $Q(\Phi)$ is constant along any field line [2], but may vary across them. We note that our Q is identical to the q used by TIN; we use this different notation to avoid confusing Q with the intrinsic axis ratio q of a core. The poloidal components of the magnetic field are related to the flux Φ by

$$\begin{aligned} B_r &= -\frac{1}{r}\frac{\partial \Phi}{\partial r} \\ B_z &= \frac{1}{r}\frac{\partial \Phi}{\partial z}. \end{aligned} \tag{6.7}$$

With the help of equations 6.3 and 6.6, the magnetostatic equilibrium equation (equation 6.2) can be re-arranged to give an elliptic type partial differential equation for the azimuthal component of the magnetic vector potential A_ϕ (see TIN, equation 2.26):

$$\Delta_1(rA_\phi) = -4\pi r^2 \frac{dQ}{d\Phi} e^{-\Psi/\sigma^2} - \frac{1}{2}\frac{db_\phi^2}{d\Phi}, \tag{6.8}$$

where A_ϕ is related to the flux by

$$A_\phi = \frac{\Phi}{r}, \tag{6.9}$$

and the differential operator Δ_1 is given by

$$\Delta_1 = \frac{\partial^2}{\partial z^2} + r\frac{\partial}{\partial r}\left(\frac{1}{r}\frac{\partial}{\partial r}\right). \tag{6.10}$$

We write the left hand side of equation 6.8 in terms of A_ϕ, rather than Φ, since this is the form of equation 6.8 that we actually finite difference in Section 6.3 and solve in Sections 6.4 and 6.5.

Finally, we require Poisson's equation for the gravitational potential:

$$\nabla^2 \Psi = 4\pi G\rho, \tag{6.11}$$

where ρ is related to Q and Ψ by equation 6.6.

It remains only to specify the functions $Q(\Phi)$ and $b_\phi(\Phi)$ to close the system of equations given above. TIN derive the functional form of $Q(\Phi)$ by assuming that cores relax to equilibrium from initially uniform, spherical clouds threaded by a constant poloidal magnetic field. We assume instead that cores

[2] The field constant Q is related to the Bernoulli integral along a field line, which is just $\sigma^2 \ln Q$.

relax from ellipsoidal fragments of a parent filamentary cloud that is threaded by a helical magnetic field (See FP1). Therefore, we extend the work of Mouschovias (1976a,b) and TIN by examining the equilibrium states of cores that relax from filamentary, rather than spherical, initial clouds.

The mass contained between poloidal flux surfaces defined by Φ and $\Phi + \delta\Phi$ is given by

$$\delta M = \int_0^{s_m} 4\pi r \rho \delta w \, ds, \tag{6.12}$$

where s is the distance along the field line, and s_m is its maximum value at the surface of the core, where the pressure drops to P_S. The thickness δw of the flux tube varies along its length in such a way that the flux $\delta\Phi$ between the flux surfaces remains constant:

$$\delta w = \frac{\delta\Phi}{r|B_{pol}|} \tag{6.13}$$

where $|B_{pol}| = \sqrt{B_r^2 + B_z^2}$ is the magnitude of the poloidal magnetic field. Combining this equation with equations 6.6 and 6.12, we easily obtain the mass to flux ratio:

$$\frac{dM}{d\Phi} = \frac{4\pi Q(\Phi)}{\sigma^2} \int_0^{s_m} \frac{e^{-\Psi/\sigma^2}}{|B_{pol}|} ds, \tag{6.14}$$

where we have used the fact that Q is constant along field lines to take it outside the integral. Solving for $Q(\Phi)$ and replacing the integration over s with an equivalent integral over z, we obtain

$$Q(\Phi) = \frac{\sigma^2 dM/d\Phi}{4\pi} \left[\int_0^{z_m} \frac{e^{-\Psi/\sigma^2}}{B_z} dz \right]^{-1}, \tag{6.15}$$

where the integral is to be performed along a poloidal field line, and $z = z_m$ at the surface of the cloud.

In order to use equation 6.15, we need to evaluate the mass to flux ratio $dM/d\Phi$ as a function of Φ for the initial filament, since this function is preserved by flux-freezing as the core settles toward its equilibrium state. As discussed in FP1, our models of magnetized filamentary molecular clouds require 3 parameters, namely the poloidal and toroidal flux to mass ratios Γ_z and Γ_ϕ and a third parameter C that determines the radial concentration of the cloud. The poloidal and toroidal magnetic fields are given by our filamentary cloud model as

$$\begin{aligned} B_z &= \Gamma_z \rho \\ B_\phi &= \Gamma_\phi r \rho. \end{aligned} \tag{6.16}$$

The surface of the filament, where the pressure drops to that of the ISM, is located at radius

$$R_S = r_0 e^C. \tag{6.17}$$

where r_0 is the core radius defined by

$$r_0 = \frac{\sigma^2}{4\pi G \rho_c} \tag{6.18}$$

and ρ_c is the central density of the filament. We consider an ellipsoidal "fluctuation" centred on the axis of the filament and assume that all of the gas initially inside of the ellipsoid becomes part of the core in its equilibrium state. We assume that the semiminor axis of the ellipsoid is equal to the radius R_S of the filament. The semimajor axis Z_0 (in the direction of the filament axis) is then determined by the mass chosen for the core, as we now demonstrate.

The poloidal field lines threading a filament run parallel to the filament axis since there is no radial magnetic field. Therefore, surfaces of constant flux are concentric cylinders centred on the filament axis. The mass and flux contained within the ellipsoidal fluctuation between cylindrical radii r and $r + \delta r$ are given respectively by

$$\delta M = 4\pi r \rho Z_0 \sqrt{1 - r^2/{R_S}^2}\,\delta r \tag{6.19}$$

$$\delta \Phi = \Gamma_z r \rho\, \delta r. \tag{6.20}$$

The second of these equations can be integrated to give the total flux Φ threading the ellipsoid. We find that Φ is related to the mass per unit length m of the filament by

$$\Phi_{cl} = \frac{\Gamma_z m}{2\pi}. \tag{6.21}$$

The mass to flux ratio is obtained by combining equations 6.19 and 6.20:

$$\frac{dM}{d\Phi} = \frac{4\pi Z_0}{\Gamma_z} \sqrt{1 - r^2/{R_S}^2}. \tag{6.22}$$

We note that this equation gives $dM/d\Phi$ as a function of Φ alone (numerically), as required by equation 6.15, if we consider r to be a function of Φ within the filament. The semimajor axis Z_0 which appears in equation 6.22 is obtained in terms of the mass and flux by integrating this equation and rearranging:

$$Z_0 = \frac{\Gamma_z M}{4\pi} \left(\int_0^{\Phi_{cl}} \sqrt{1 - r^2/{R_S}^2}\; d\Phi \right), \tag{6.23}$$

which is calculated numerically.

Ampère's law shows that the function $b_\phi(\Phi)$ is directly proportional to the total poloidal current passing through the flux surface threaded by flux Φ. Since b_ϕ is a function of Φ alone, the poloidal currents associated with the toroidal field must flow only in the direction of the poloidal field. Tomisaka (1991) assumed that $b_\phi \propto \Phi$. However, we obtain the function $b_\phi(\Phi)$ in our model by assuming that cores form without dissipation from the initial filamentary state, so that the current flowing between any two flux surfaces is a conserved quantity. Specifically, the functional form of $b_\phi(\Phi)$ follows from equations 6.3 and 6.16:

$$b_\phi(\Phi) = \Gamma_\phi r^2 \rho, \tag{6.24}$$

where r and ρ are the radius and density of the parent filament, considered to be functions of the flux Φ.

6.2.1 Dimensionless Equations

Following FP1, we write our equations in dimensionless form by normalizing all quantities with respect to the velocity dispersion σ_{fil} of the filament and the density ρ_c at its centre. The dimensional scale factors can then be written as follows:

$$\begin{aligned}
\sigma_0^2 &= \sigma_{fil} \\
\rho_0 &= \rho_c \\
r_0^2 &= \frac{\sigma_{fil}^2}{4\pi G \rho_c} \\
\Psi_0 &= \sigma_{fil}^2 \\
P_0 &= Q_0 = \sigma_{fil}^2 \rho_c \\
B_0 &= P_0^{1/2} \\
A_0 &= b_{\phi,0} = r_0 B_0 \\
\Phi_0 &= r_0^2 B_0 .
\end{aligned} \tag{6.25}$$

The dimensionless forms of the flux to mass ratios Γ_z and Γ_ϕ are given in FP1 (equation 33) as

$$\begin{aligned}
\tilde{\Gamma}_z &= \sqrt{\frac{\rho_c}{\sigma^2}} \left(\frac{B_z}{\rho} \right) \\
\tilde{\Gamma}_\phi &= \frac{1}{\sqrt{4\pi G}} \left(\frac{B_\phi}{r\rho} \right) .
\end{aligned} \tag{6.26}$$

Normalizing all quantities with respect to these dimensional scaling factors, only Poisson's equations

changes form:

$$\nabla^2 \Psi = \rho. \tag{6.27}$$

The dimensionless forms of the remaining equations are identical to their dimensional forms given by equations 6.3, 6.5, 6.6, 6.7, 6.8, 6.9, and 6.15, where (dimensionless) $\sigma = 1$ is specified as an input parameter [3] , and ρ, P, Ψ, A_ϕ, Φ, B, and Q are all solved self-consistently.

6.2.2 Boundary Conditions

We assume that the poloidal magnetic field threading the original filament is continuous at its surface and constant in the external medium, so that $A_\phi \propto r$ in the external medium. The total flux threading our grid, of radius $r_{max} \gg R_S$, is given by

$$\Phi_{max} = \frac{\Gamma_z}{2\pi} \left[m + \pi (r_{max}^2 - {R_S}^2) P_S / \sigma^2 \right]. \tag{6.28}$$

Therefore, $A_{\phi,max}$ is given by

$$A_{\phi,max} = c r_{max}, \tag{6.29}$$

where c is a constant:

$$c = \frac{Gz}{2\pi r_{max}^2} \left[m + \pi (r_{max}^2 - {R_S}^2) P_S / \sigma^2 \right]. \tag{6.30}$$

We find it convenient, for computational reasons, to define a "modified" vector potential A such that

$$A = A_\phi - cr. \tag{6.31}$$

It is easily verified that A satisfies the same equation (equation 6.8) as A_ϕ. However, A vanishes at the outer radius of our grid, where $r = r_{max}$.

To obtain the boundary condition on A at large z, we assume only that there is no radial component of the magnetic field at the edge of our grid corresponding to $z = z_{max}$ [4]. The boundary conditions on Ψ and A (in our dimensionless variables) are as follows.

$r = 0$:

$$\partial \Psi / \partial r = 0, \quad A = 0 \tag{6.32}$$

$r = r_{max}$:

$$\Psi = \frac{M}{4\pi \sqrt{r_{max}^2 + z^2}}, \quad A = 0 \tag{6.33}$$

[3] We only consider the case where σ is the same in the core as in the parent filament (dimensionless $\sigma = 1$). However, we leave σ in our equations so that this condition might be relaxed in future work.

[4] This differs slightly from TIN, who assume that the magnetic field connects to their initially uniform field at large z.

$z = 0$:

$$\partial\Psi/\partial z = 0, \quad \partial A/\partial z = 0 \tag{6.34}$$

$z = z_{max}$:

$$\Psi = \frac{M}{4\pi\sqrt{r^2 + z_{max}^2}}, \quad \partial A/\partial z = 0 \tag{6.35}$$

6.3 Numerical Method

We briefly describe our numerical implementation of the self-consistent field method in this section. We work in modified radial coordinates defined by

$$\begin{aligned} r &= S_r \tan\xi \\ z &= S_z \tan\eta \end{aligned} \tag{6.36}$$

so that radial infinity and infinity along the axis of symmetry are respectively mapped to $\xi = \pi/2$ and $\eta = \pi/2$. Our grid is uniformly spaced in ξ and η and contains $2^7 + 1 = 129$ points in each dimension. The advantage of working in these modified coordinates is that they provide a good dynamical range (spatially) for our calculation. We obtain good resolution within the core by keeping a large fraction (typically $\sim 1/3 - 1/2$) of the grid cells within its boundary, but our grid still extends to large radius where the boundary conditions stated in the previous section apply.

We begin by initializing our numerical method as follows. We find an equilibrium solution for a magnetized filament using the method discussed in FP1. From this solution, we calculate $dM/d\Phi$, Z_0, and $b_\phi(\Phi)$ using equations 6.22, 6.23, and 6.24 respectively. We begin with a initial guess of the density distribution $\rho(r,z)$ (eg, truncated Gaussian), as well as the magnetic vector potential $A(r,z)$, which gives $\Phi(r,z)$ by equations 6.9 and 6.31. We then solve our system of equations iteratively as follows:

1) We finite difference equation 6.27, and solve for the gravitational potential $\Psi(r,z)$

2) Next, we calculate the poloidal magnetic field using equation 6.7, and accurately locate the surface of the core by finding the surface where the pressure drops to P_S.

3) We integrate along poloidal field lines (level surfaces of Φ) to solve equation 6.15 for $Q(\Phi)$. We differentiate $Q(\Phi)$ to obtain $dQ/d\Phi$, which is one of the source terms in equation 6.8.

4) We interpolate the functions $Q(\Phi)$, $dQ/d\Phi$, and $db_\phi^2/d\Phi^2$ over our grid, using the current value of Φ at each grid point.

5) We update $A(r,z)$ by solving the finite difference equation obtained from equation 6.8, using the functions calculated in steps 1 and 5.

We repeat steps 1-5 until the solution either converges or is rejected. We keep track of the maximum

relative change in density for all cells whose density is greater than half of the central density. We consider a solution to have converged when this quantity either becomes less than 1×10^{-5}, or it remains below 1×10^{-4} for 50 consecutive iterations. A solution is rejected if the central density falls below that of the original filament ($\rho = 1$ in our dimensionless units), or appears to be growing without bound. Our code allows a maximum of 750 iterations; this limit is never reached in practice since solutions that converge usually do so within ~ 250 iterations.

6.4 Exploration of the Parameter Space

In this section we explore the range of equilibrium models that are accessible to finite segments of the filament models described in FP1. We have selected those models from FP1 that agree with the observational constraints obtained from our virial analysis of the available observational data (see FP1 equation 22), and whose kinetic and magnetic energies are nearly in equipartition, with $0.5 \leq M/K \leq 2$. Moreover, we have selected only filaments that fragment slowly, with growth timescales

$$\tau_{frag} \geq 1.8 \left(\frac{n_c}{10^4 \ cm^{-3}} \right)^{-1/2} \ Myr \tag{6.37}$$

We refer the reader to FP2 for a discussion of fragmentation in filamentary clouds and the normalization used in equation 6.37. The reason for this selection is to exclude filament models that are dominated by rapidly growing MHD-driven sausage instabilities, rather than gravitational instabilities. A total of 71 filament models from FP1 and FP2 meet these criteria and are considered as initial conditions for our core models.

The Bonnor-Ebert (1956, 1955) critical mass for unmagnetized cores bounded by surface pressure P_s is given by

$$M_{B.E.} = 1.18 \frac{\sigma^4}{G^{3/2} P_s^{1/2}}. \tag{6.38}$$

Although the ordered magnetic field in our models modifies the critical mass from its hydrostatic value, we nevertheless find $M_{B.E.}$ to be a useful fiducial mass scale to compare with our magnetized models. We find that an equilibrium state is likely to be found if the mass of a core is chosen to be comparable to, but generally not in excess of the Bonnor-Ebert critical mass for non-magnetic cores. Therefore, we attempt to compute core models with masses ranging from 0.3 to 0.8 (in steps of 0.1) times $M_{B.E.}$ for each of the 71 filaments chosen as possible initial states. Models that are more massive than $\sim 0.8 \ M_{B.E.}$ generally do not converge because the central density grows without bound until the numerical calculation is halted. Models less massive than $\sim 0.3 \ M_{B.E.}$ may converge numerically, but they do not meet our selection criterion that the central density of the core should be at least that of the initial filament

(See Section 6.3). Even within our chosen mass range, only 152 of the 426 attempted models ($\sim 1/3$) converged and satisfied our condition on the central density.

Figure 6-1 shows 6 cuts through our parameter space made by holding $M/M_{B.E.}$ constant. The solid dots represent models that converged, while the open circles represent failed or rejected models. It is apparent from the figure that most of the converged models have $0.4 \leq M/M_{B.E.} \leq 0.7$, with only 4 models found with $M/M_{B.E.} = 0.8$ and 5 with $M/M_{B.E.} = 0.3$. Within each cut of constant $M/M_{B.E.}$, we find that our converged models are separated from those that did not converge by a fairly sharp boundary, with little intermixing. This suggests that models that fail to converge likely represent genuine non-equilibrium or unstable states. Models do not converge when $M \gtrsim 0.8\ M_{B.E.}$ because the Bonnor-Ebert critical mass is reduced in our model by the toroidal field, which works in concert with gravity and surface pressure in squeezing the cores. This result is in agreement with Tomisaka (1991) and Habe et al. (1991). We also find that Γ_ϕ never exceeds Γ_z by more than a factor of ~ 1.7 for any converged model. This suggests that MHD instabilities might be preventing the convergence of models with very strong toroidal fields, since we found in FP2 that MHD sausage instabilities were triggered in filaments when $\Gamma_\phi/\Gamma_z \gtrsim 2$ (See also discussion in McKee 1999).

6.4.1 A Gallery of Models

We have computed a total of 152 models scattered throughout our parameter space. Figure 6-2 shows a gallery of representative models, with a range of intrinsic axis ratios q ranging from 0.2 to 0.8, shown in order of increasing mass. The density contours are linearly spaced from the central density (given in each panel) to the density at the surface of pressure truncation. We find that the density contours near the centre of our models are nearly circular, but become increasingly elongated towards the surface. This is explained by the dominance of gravity near the centre, and the increasing importance of the toroidal magnetic field in the outer regions. The density contours in our models are therefore somewhat more complex than in the empirical model used by Myers et al. (1991) and Ryden (1996), who assume that the density contours of cores can be described by nested ellipses of constant axis ratio.

Our models have a central "core" region of nearly uniform density, surrounded by an outer "envelope," where the density gradually decreases with radius. Figure 6-2 shows that our models are generally quite truncated by the external pressure, typically extending to only $\sim 2r_0$ in cylindrical radius. Therefore, they are truncated before they attain the r^{-2} density profile (or any other power law) that characterizes the outer envelope of a Bonnor-Ebert sphere.

For each of our models, we have computed the intrinsic axis ratio q by calculating the best-fitting ellipse (in a least squares sense) to the half maximum density contour. We have also calculated the mean projected axis ratio $\langle p \rangle$ for each model using the procedure outlined in Appendix A. (Essentially, $\langle p \rangle$ is

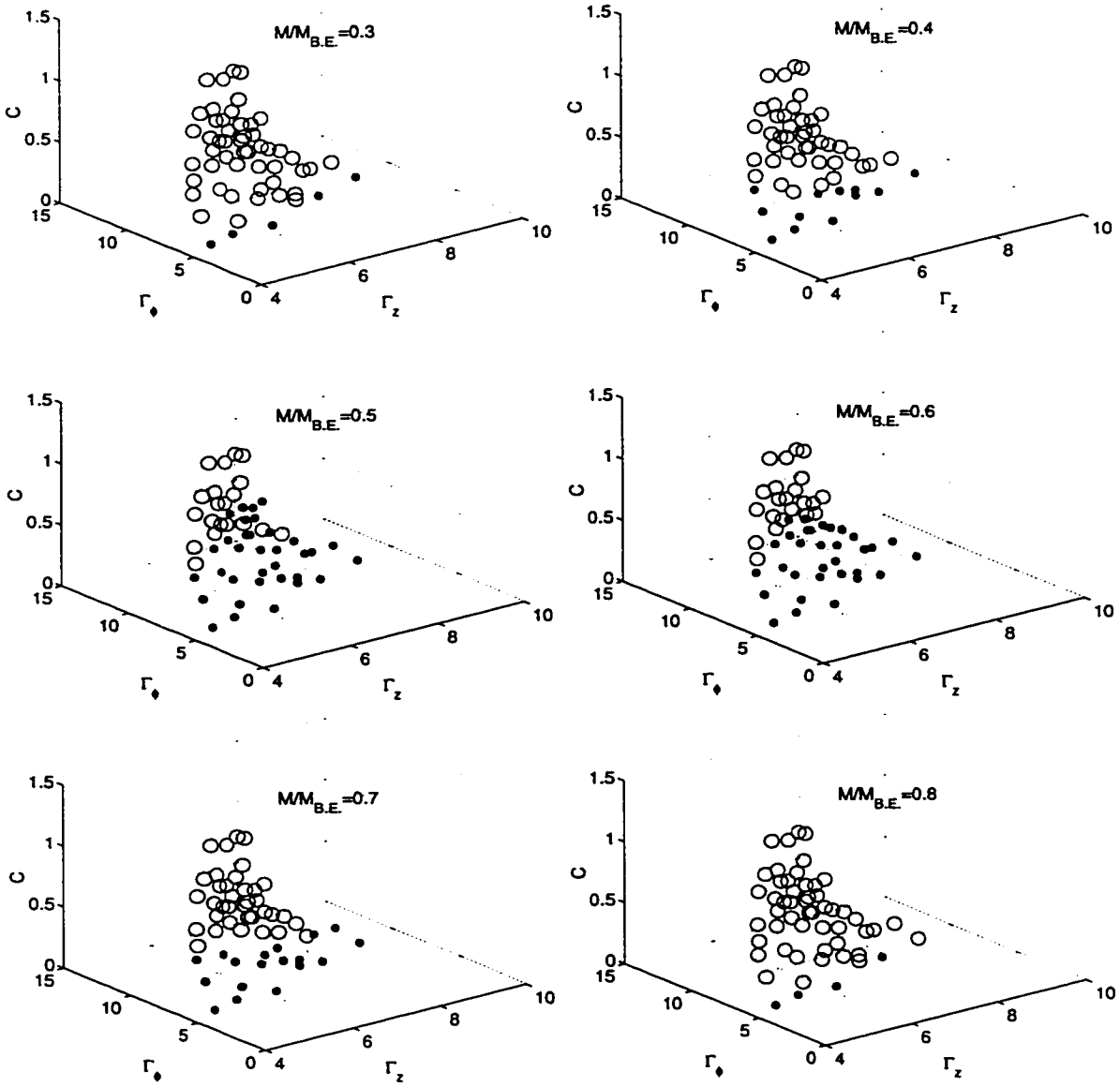

Figure 6-1: We show the regions of parameter space where our models converge (black dots) or fail to converge (open circles). Each attempted solution is consistent with a parent filament obeying the observational constraints established in FP1 and having rather low fragmentation growth rates, as given by equation 6.37.

the expectation value of the projected axis ratio of the half maximum surface density contour for a core oriented at a random inclination angle relative to the plane of the sky.)

We show histograms of the intrinsic and mean projected axis ratios in Figure 6-3 below, where we find that $0.1 \lesssim q \lesssim 0.9$ and $0.3 \lesssim \langle p \rangle \lesssim 1$. These histograms should not be interpreted as a prediction

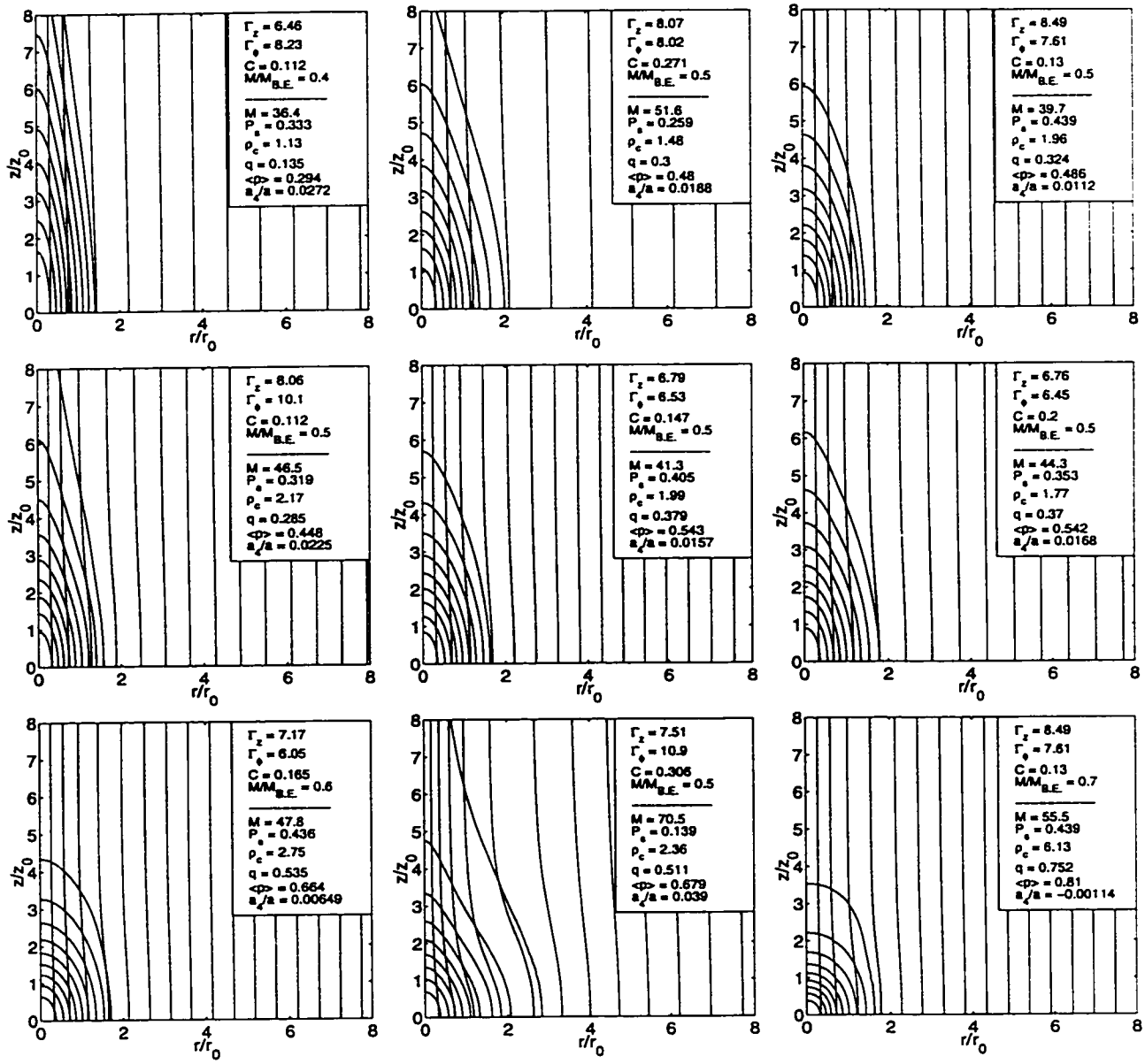

Figure 6-2: We show density contours and poloidal field lines for a set of representative models to illustrate the range of equilibria that we obtain. Models are shown in order of increasing q.

of the distribution of axis ratios for a sample of cores, as shown in Ryden (1996) for example. What they do show is the distribution of axis ratios that was actually obtained by our sample of converged models, which provides an indication of the relative ease or difficulty in producing core models with a given axis ratio. The mean value of q derived from observations is probably between 0.4 and 0.5 (Myers et al. 1991, Ryden 1996), but the predicted distributions are quite broad, containing significant numbers of cores that are much more elongated or more nearly spherical (Ryden 1996). Therefore, Figure 6-3

shows that our models cover the likely range of axis ratios.

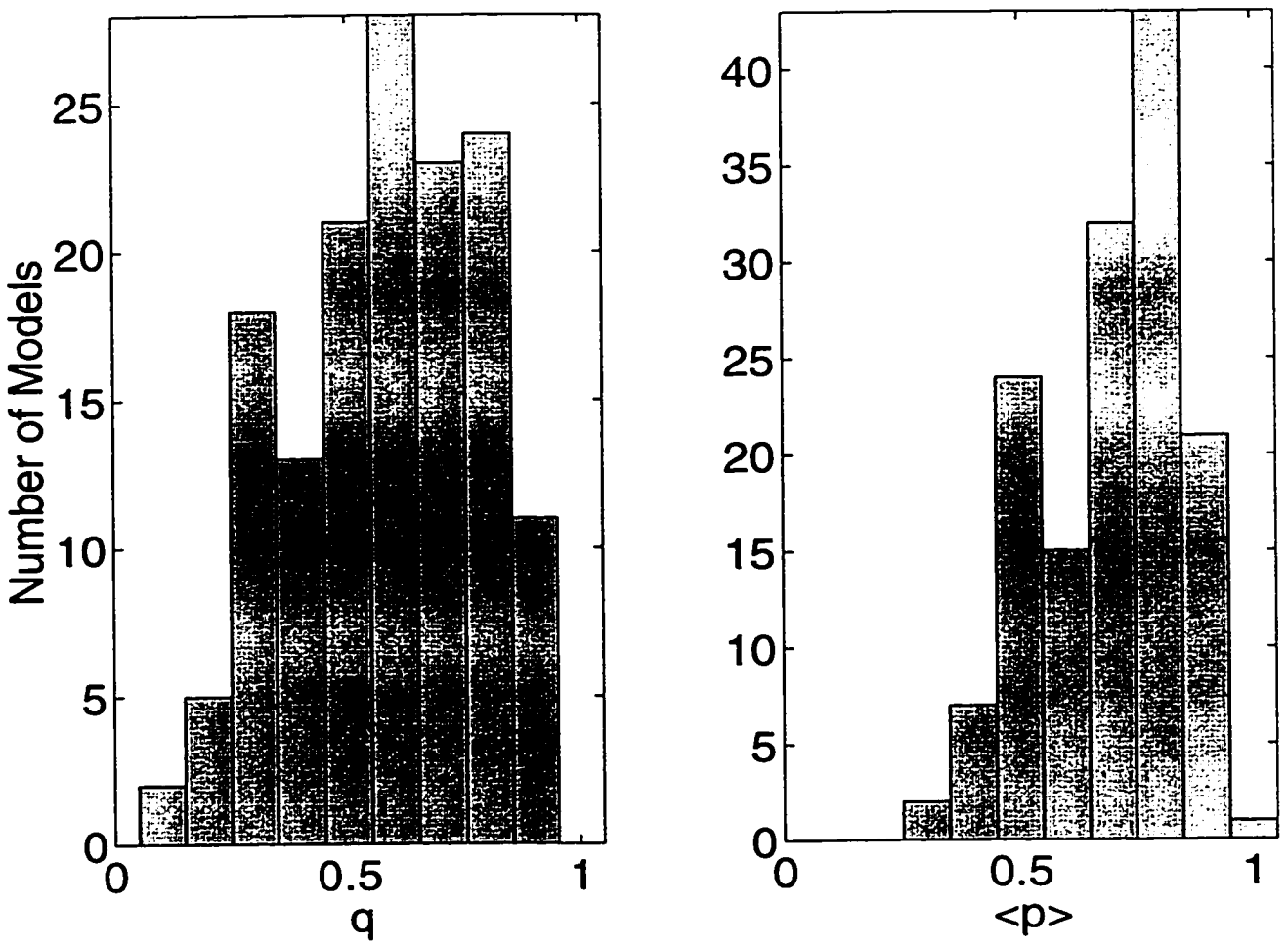

Figure 6-3: We show the distribution of intrinsic and mean projected axis ratios obtained for our converged models. All 152 models are elongated, many with axis ratios in good agreement with the observed values.

Figure 6-4 shows that the relationship between $\langle p \rangle$ and q, numerically determined by our model, is in reasonable agreement with the analytical relation (dashed line) used by Myers et al. (1991, their equation 1), even though the internal structure of our models is quite different from theirs. The relation between q and $\langle p \rangle$ is clearly not very sensitive to the detailed internal structure of cores. The error bars

represent the standard deviation in $\langle p \rangle$ for a sample of cores with axis ratio q, oriented randomly relative to the observer.

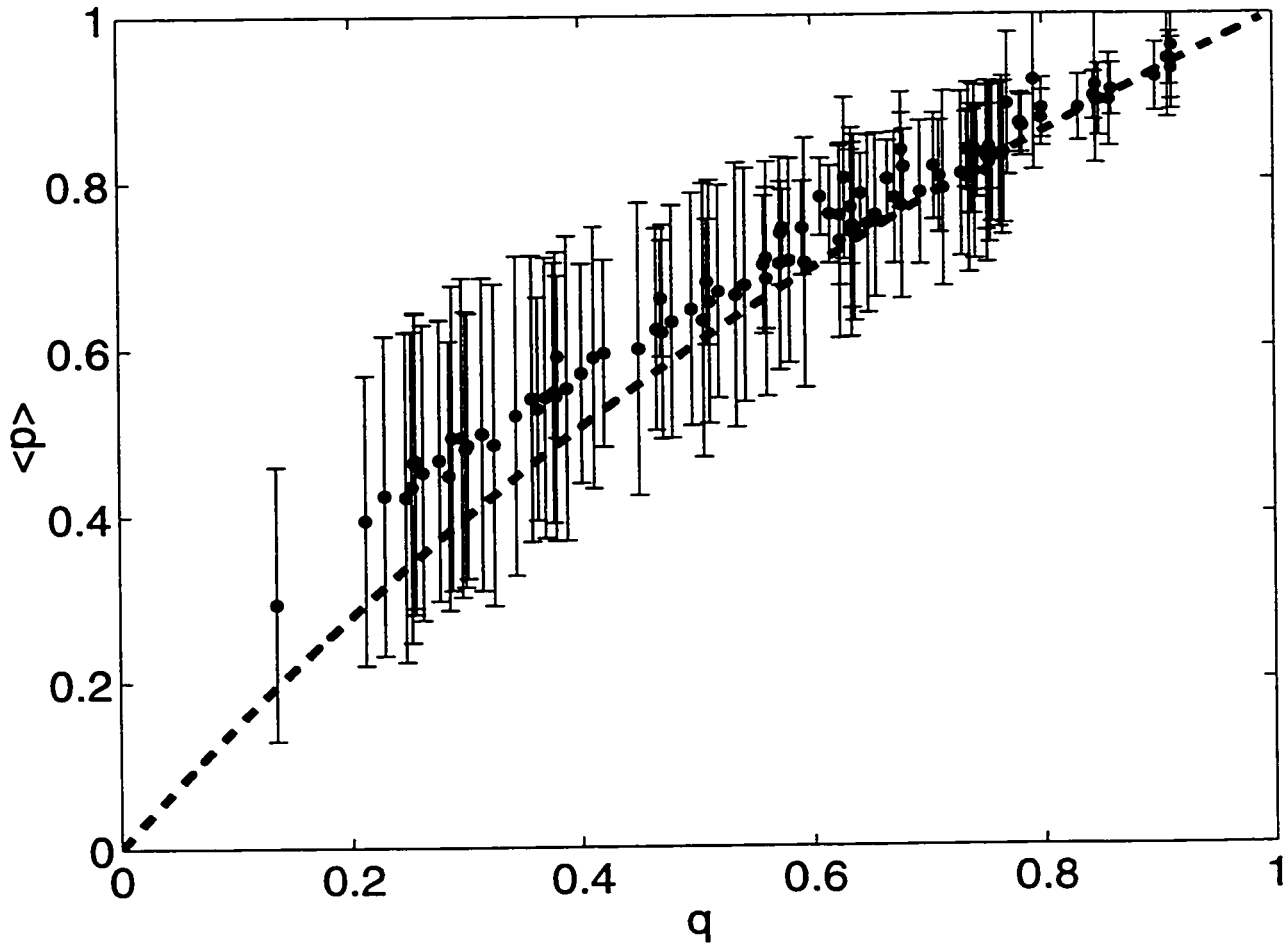

Figure 6-4: We show the relationship between the intrinsic and mean projected axis ratios for our model. We find reasonable agreement with the formula (dashed line) given by Myers et al. (1991) for an empirical model of prolate cores. The error bars represent the standard deviation of p about $\langle p \rangle$, assuming that cores are oriented randomly on the sky.

We also estimate the degree to which the half maximum density and surface density contours of our models deviate from a pure ellipse. Our method for this analysis is the Fourier method developed

by Bender and Möllenhoff (1987), who used the method to quantify the "diskiness" or "boxiness" of elliptical galaxy isophotes. Their method works by finding the best-fitting (in a least squares sense) ellipse to an isophote and Fourier analysing the residual. Their analysis shows that the fourth Fourier component a_4 of the residual dominates the Fourier spectrum, and when normalized with respect to the semimajor axis a provides an excellent indication of the deviation from an ellipse. For our purposes, $a_4/a > 0$ describes density or surface density contours that are more peaked than an ellipse along the axis of symmetry (ie: shaped like a North-American football or lemon), while $a_4/a < 0$ describes contours that are more flattened than an ellipse.

For each of our models, we calculate both an intrinsic a_4/a parameter for the half maximum density contour, and a mean projected $\langle a_4/a \rangle$ parameter for the half maximum surface density contour, averaging over all possible orientations using the procedure described in Appendix A. We show the distributions of these shape parameters for our models in Figure 6-5. We find that all of our models have intrinsic and projected shape parameters that are greater than or equal to zero, but usually less than ~ 0.05. Therefore, many of our models are slightly football-shaped. This might provide one way to distinguish observationally between our models and flattened models threaded by purely poloidal fields (eg. TIN).

We find no clear correlation between a_4/a and q. However, very few elongated models (with $\langle p \rangle \lesssim 0.6$) are significantly peaked ($\langle a_4/a \rangle \gtrsim 0.02$). Conversely, those with a high value of a_4/a are never very elongated.

An interesting feature found in many of our models is that the field lines bulge slightly outward around the core (See Figure 6-2 for several examples.). This is opposite the hourglass shaped field lines found by Mouschovias (1976b), TIN, TIN88b, TIN89, TIN90, and Tomisaka (1991). Physically, this field structure is mainly due to the radial pinch of the toroidal field, which most significantly affects the density and field line structure near the tips of cores (where the symmetry axis intersects the surface of the core). The gas pressure is lowest and the gravitational forces are weakest near the tips, so the toroidal field can squeeze in further than in the midplane.

We find a continuum of models that range considerably in shape and ellipticity. We discuss two representative models chosen because of their contrasting behaviour. The model shown in Figure 6-6 is dominated by the B_z component of the magnetic field nearly everywhere. The toroidal field vanishes at the axis of symmetry and increases radially outward, becoming comparable to the poloidal field only very near the edge of the core. It is strongest near the tips of the cores rather than in the midplane. The radial field component is much smaller than B_z everywhere within the core. Many models like the one shown in Figure 6-6, with a strong "backbone" of poloidal flux, are very elongated. We find models similar to the one shown, but with intrinsic axis ratios as low as ~ 0.1 and mean projected axis ratios as low as ~ 0.3. The density contours are usually quite nearly elliptical when a strong poloidal field is

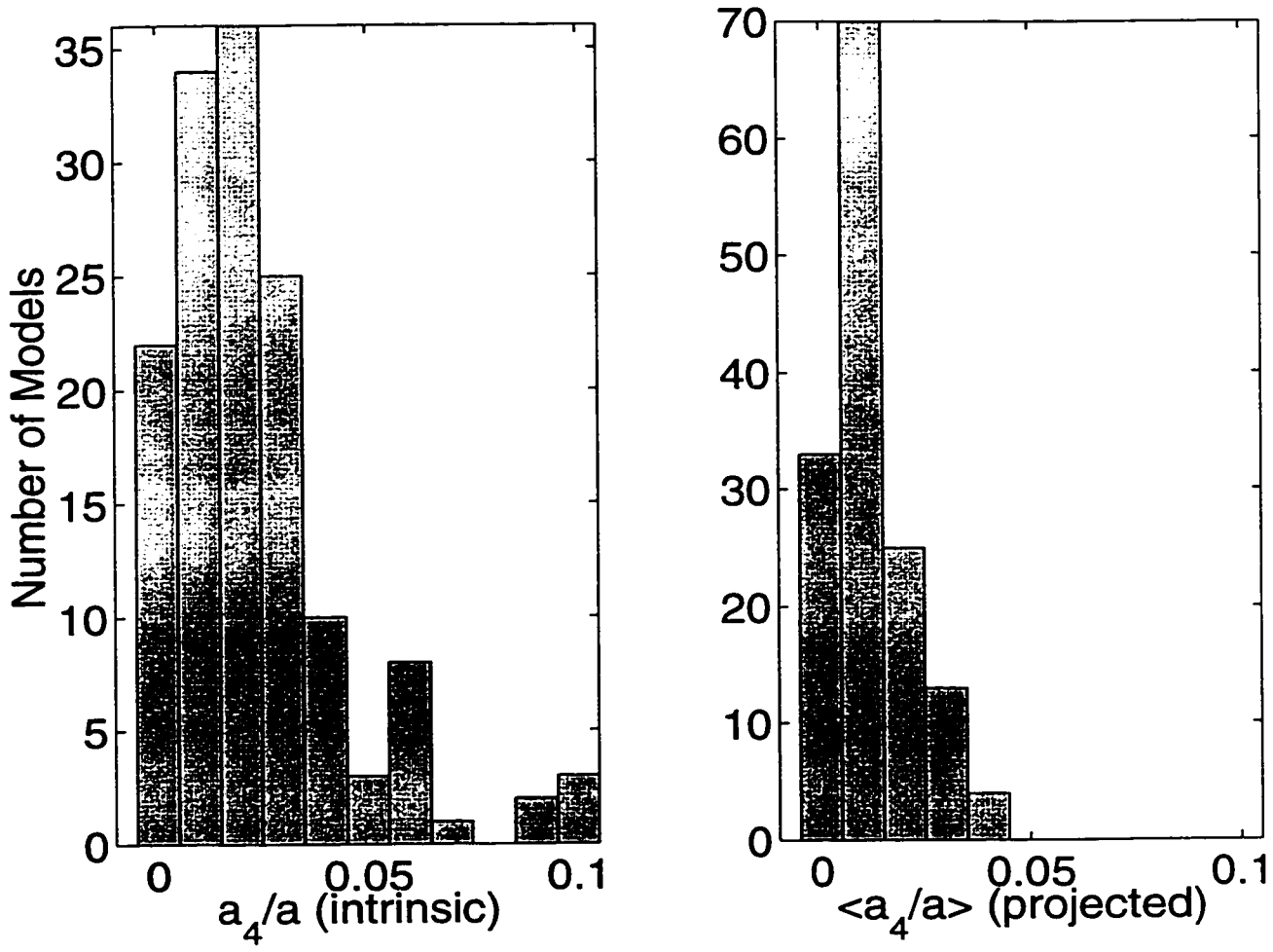

Figure 6-5: We show the distribution of the intrinsic and mean projected a_4/a shape parameters for our converged models.

present, with $0 < a_4/a \lesssim 0.03$ in most cases.

The model shown in Figure 6-7 contains regions where the toroidal field becomes significantly stronger than the poloidal field. The density contours are quite peaked towards the axis of symmetry, with $a_4/a > 0.04$ for some models like the one shown. While some models with this sort of behaviour are fairly elongated, it is interesting that most are actually less elongated than those with strong poloidal fields.

6.4.2 Trends in the Model Parameters

Figures 6-8 and 6-9 illustrate that our models generally become more elongated as the mass is decreased or as $P_S/\langle P \rangle$ is increased. The reasons for these trends are straightforward. Given that rotation is

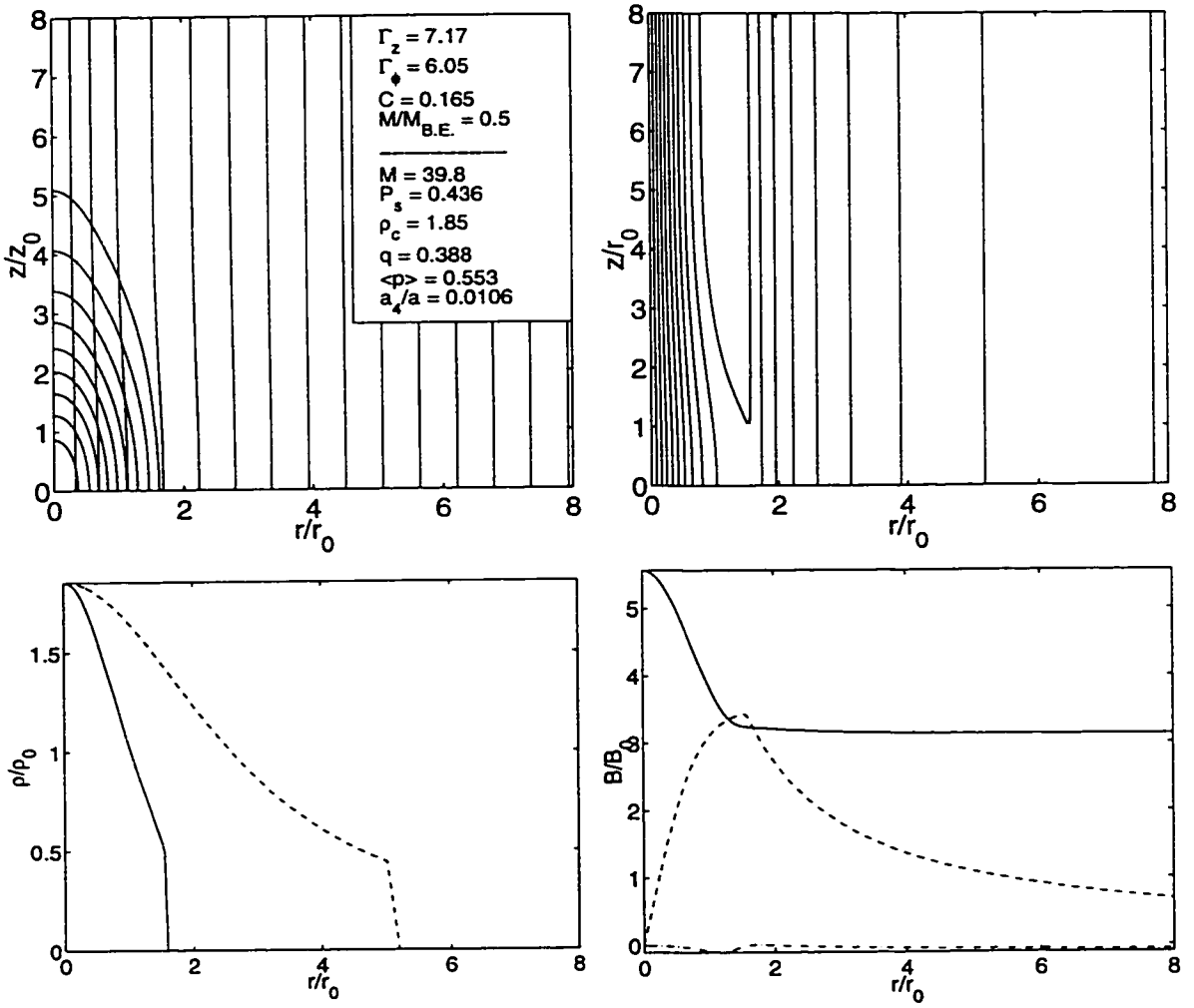

Figure 6-6: We show the structure of a representative model whose toroidal field is relatively weak compared to its poloidal field nearly everywhere. **panel (a)** (upper left): density contours and poloidal field lines. **panel (b)** (upper right):
Contours of toroidal field intensity. **panel (c)** (lower left): Density cuts taken radially in the midplane (solid line) and along the asymmetry axis (dashed line). **panel (d)** (lower right): The variation of B_z (solid line), B_ϕ (dashed line), and B_r (dot-dashed line) taken along a radial cut in the midplane.

negligible and the velocity dispersion is isotropic, gravitationally dominated cores should be spherical. We find nearly spherical, gravitationally dominated cores when the mass is large and the central density is high. The helical magnetic field can most effectively shape low mass cores, in which self-gravity is less important and the surface pressure is a significant fraction of the central pressure. The most massive core in our sample of converged solutions is shown in Figure 6-10. We show the radial density structure of a purely hydrostatic isothermal sphere overlaid on radial and axial cuts of the density from our massive solution. We find that the inner, most gravitationally dominated regions are described by an isothermal

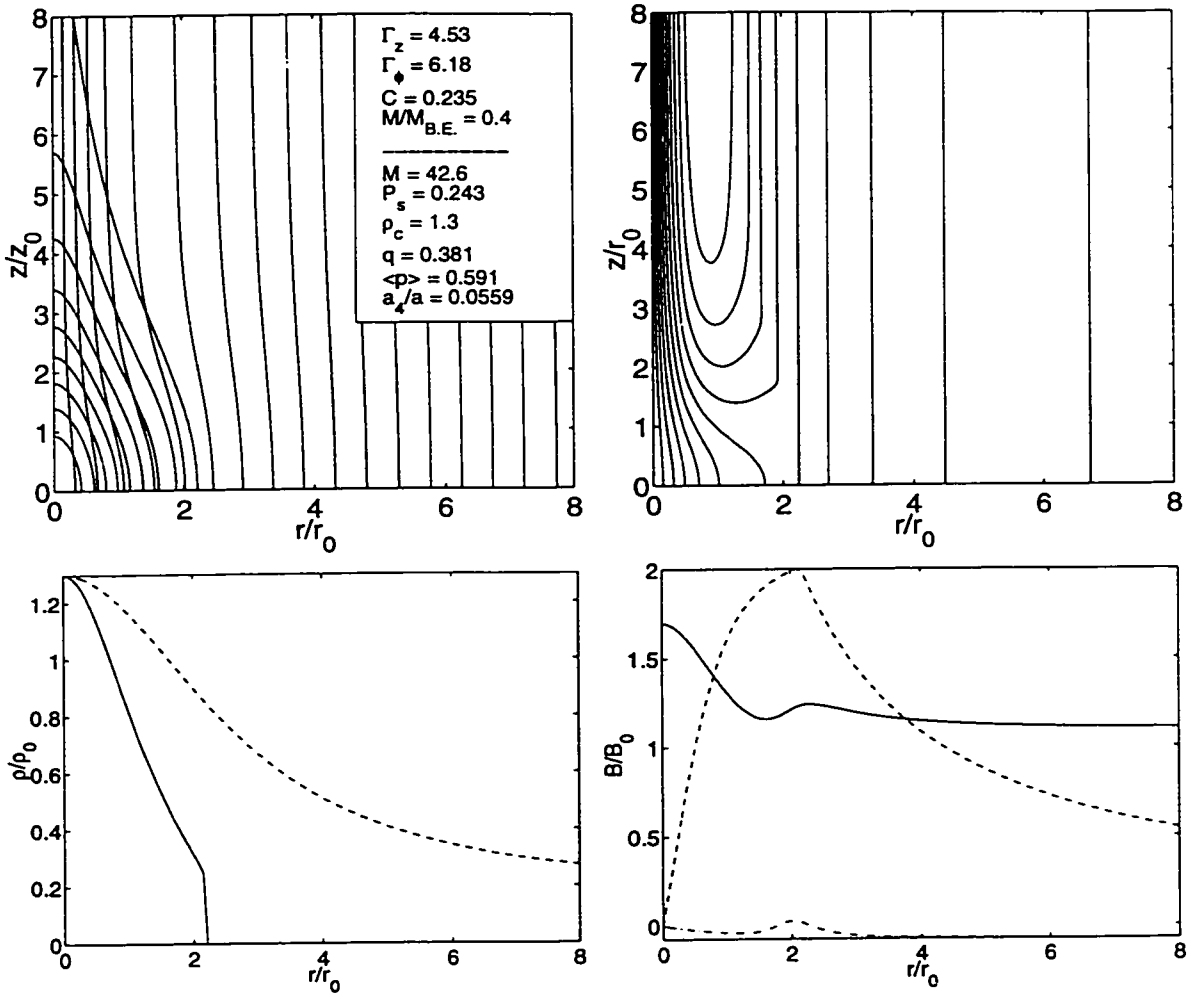

Figure 6-7: Same as Figure 6-6, but for a solution whose toroidal field component is stronger than the poloidal field over much of the core.

sphere to a high degree of accuracy within $\sim 0.5\ r_0$ of the centre (maximum deviation = 1.3%). Beyond this radius, the magnetic field becomes important relative to gravity, resulting in an axis ratio of 0.64 for the contour describing the surface of the core.

Figure 6-11 verifies our assertion in Section 6.4.1 that only modest toroidal fields are required to produce substantially elongated cores. In panel (a), we show that the projected axis ratio $\langle p \rangle$ decreases as the ratio M_{tot}/K increases, where M_{tot} and K are respectively the total magnetic energy [5] and the

[5]The magnetic energy M_{tot} is not the full magnetic energy term from the virial theorem, since we do not include any surface terms. Our definition is more relevant to Zeeman measurements, since M_{tot} is related to the total average field strength within the core. We also note that M_{tot}/K is analogous to our parameter X in FP1.

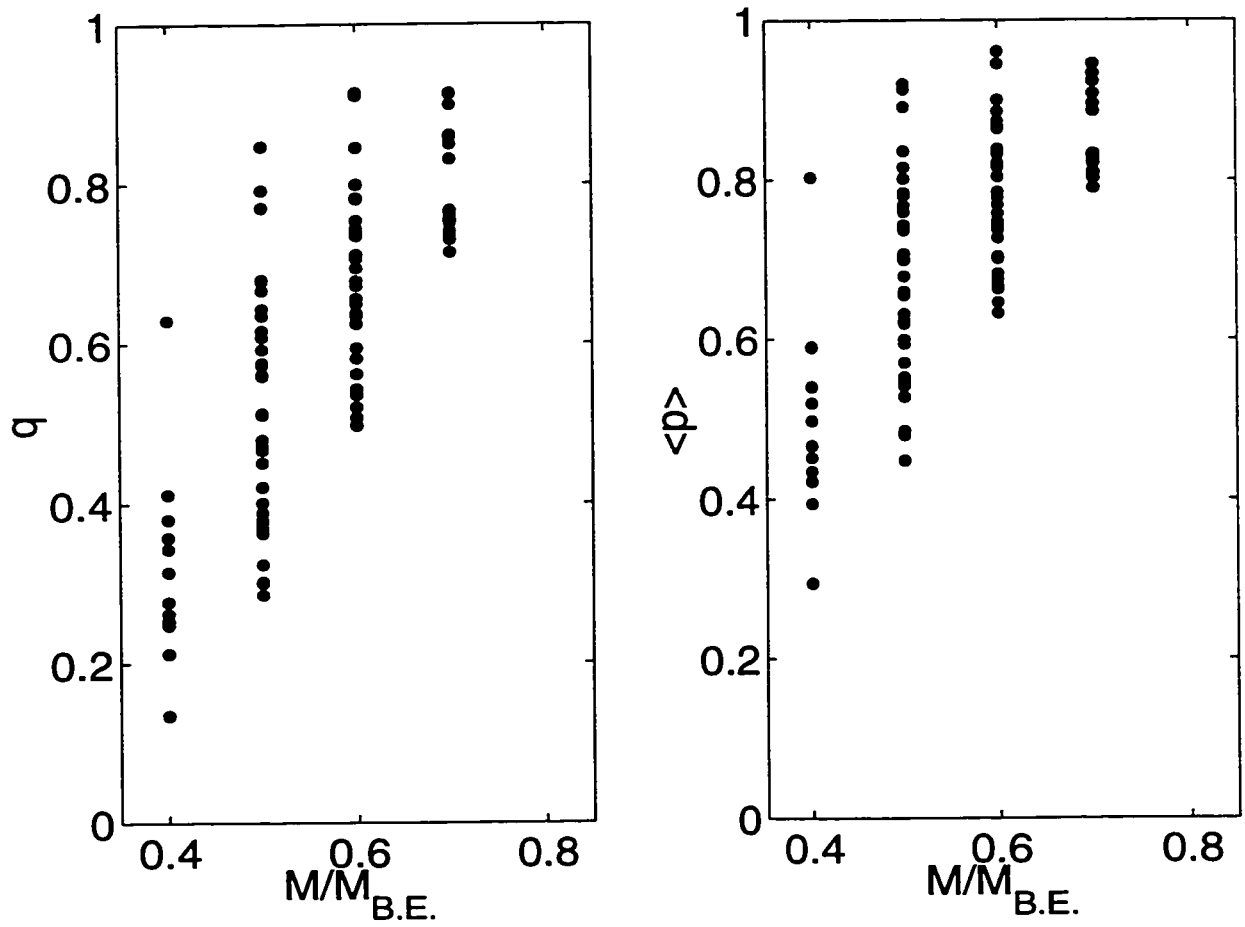

Figure 6-8: We show how the intrinsic and mean projected axis ratios depend on the ratio of the mass to the critical mass $M_{B.E.}$ for non-magnetic cores. Gravitationally dominated cores with masses near $M_{B.E.}$ are much less elongated than those with smaller masses. The error bars on p are suppressed for clarity.

kinetic energy, defined by

$$\begin{aligned} M_{tot} &\equiv \frac{1}{8\pi}\int_V B^2\, dV \\ K &\equiv \frac{3}{2}\int_V P\, dV. \end{aligned} \tag{6.39}$$

Models with $\langle p\rangle < 0.6$ have $M_{tot}/K \gtrsim 0.4$ in our model, but $M_{tot}/K \lesssim 2$ even for our most elongated models. Therefore, the field strengths required by our model are consistent with approximate equipartition between kinetic and magnetic energies, which has often been inferred from observations (eg. Myers & Goodman 1988a,b). Panel (b) shows that most of the magnetic energy is in the poloidal component of the field for significantly elongated cores, with $\langle p\rangle < 0.6$. We plot $\langle p\rangle$ against M_ϕ/M_{pol}, where M_ϕ and

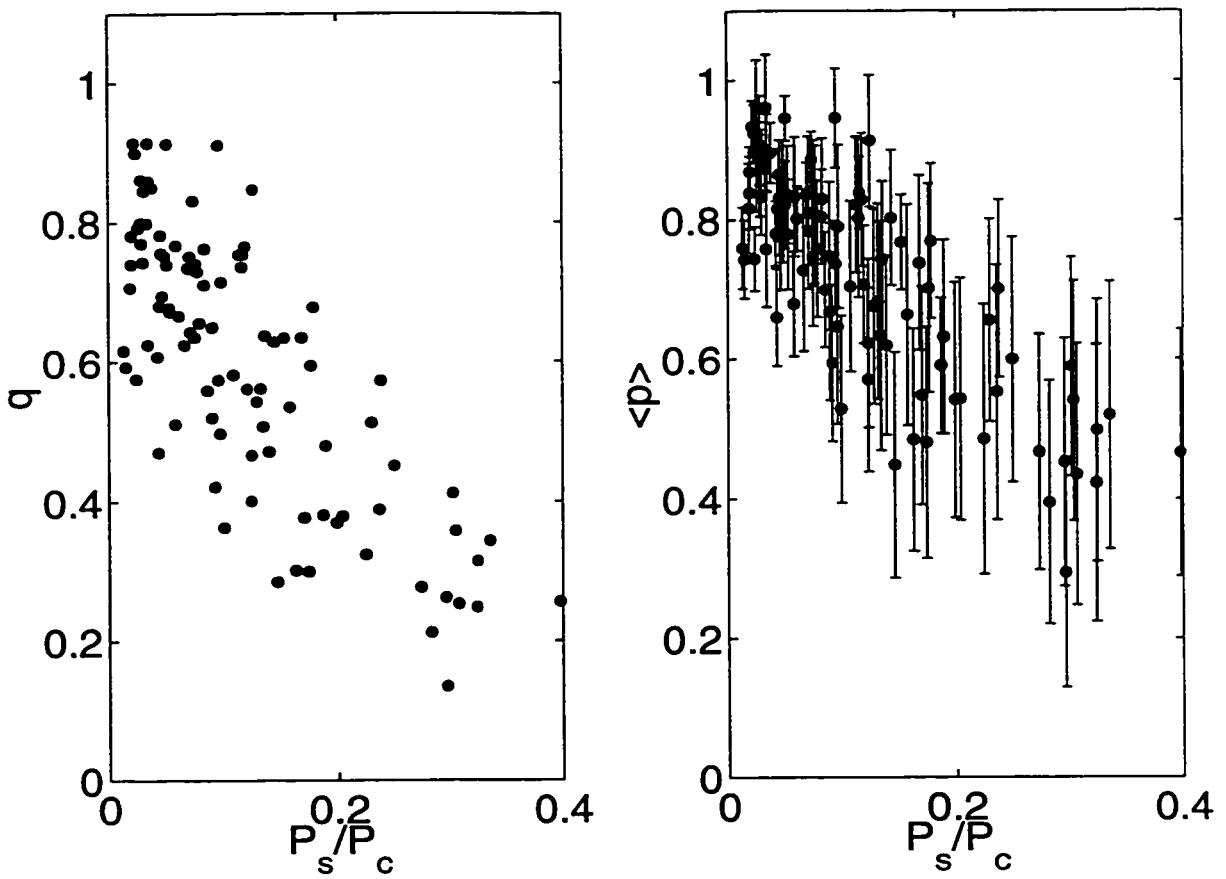

Figure 6-9: We show how the intrinsic and mean projected axis ratios depend on the ratio of the external pressure to the pressure at the centre of the core. Pressure dominated cores with relatively large values of $P_S/\langle P \rangle$ are more elongated than less pressure dominated models.

M_{pol} are respectively the toroidal and poloidal contributions to the total magnetic energy in equation 6.39. As a general trend, we find that the most elongated models have the lowest values of M_ϕ/M_{pol}, and that most models with $\langle p \rangle < 0.6$ have $0.3 \lesssim M_\phi/M_{pol} \lesssim 1$. This trend might seem paradoxical because the toroidal field is responsible for the elongation. However, models with energetically significant toroidal fields must also have strong poloidal fields to suppress MHD instabilities.

6.5 Sequences of Models with Varying Mass and External Pressure

Our emphasis in Sections 6.4.1 and 6.4.2 was on exploring the full range of equilibrium states that are accessible to our models. In this section, we select a few filament models and examine sequences of core

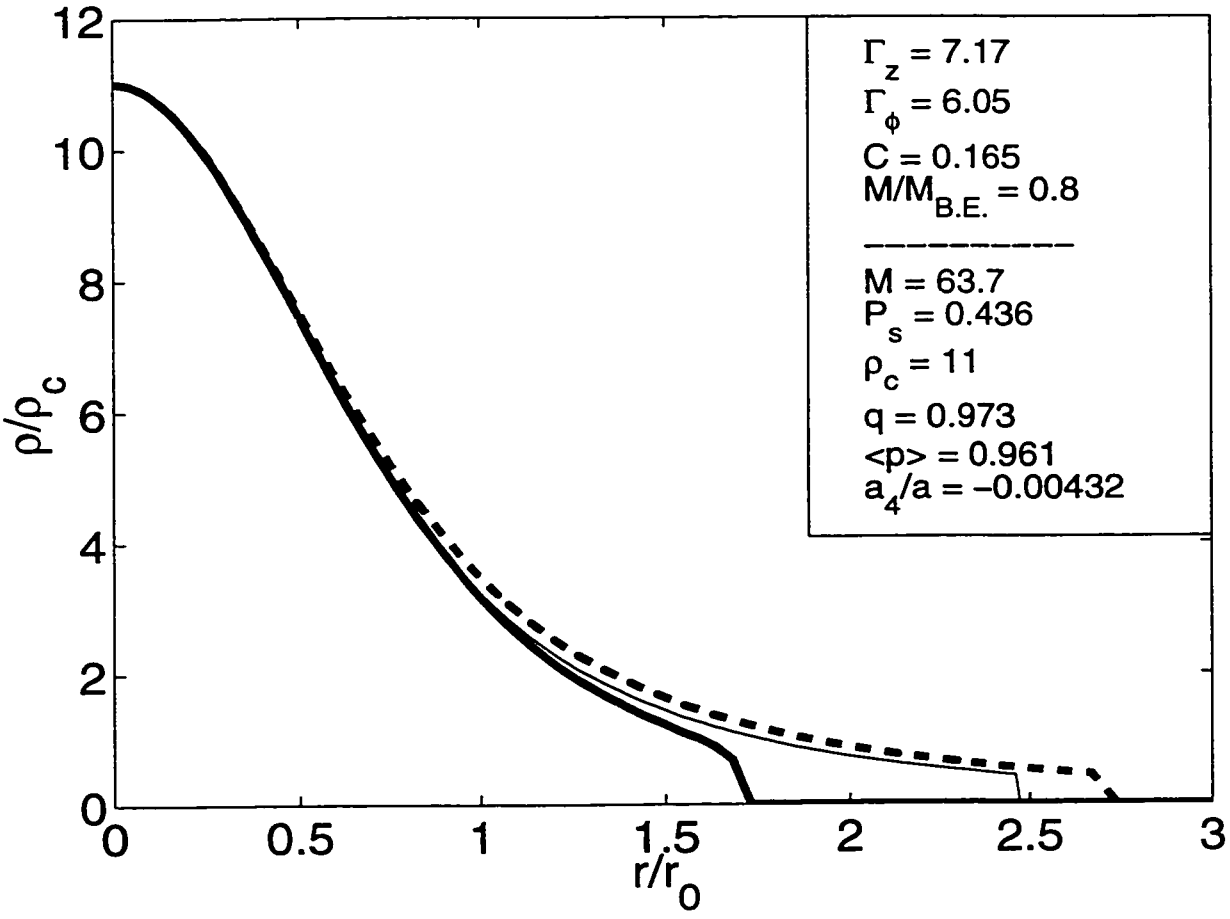

Figure 6-10: We show the most massive core obtained in our sample of 152 converged solutions. The heavy solid line and dashed line represent density cuts taken radially in the midplane and along the axis of symmetry respectively. Both cuts agree well with an isothermal sphere (thin solid line) in the inner, gravitationally dominated region, but deviate significantly in the pressure dominated region near the surface.

models that are obtained by gradually increasing the mass and the external pressure.

The sequences shown in this section terminate when the mass or pressure become sufficiently high that no equilibrium can be found due to a central density that increases with each iteration of our numerical code, apparently without bound. The maximum mass or pressure found in this way clearly represents the Bonnor-Ebert critical mass or pressure, which are both reduced by the magnetic field. These findings are consistent with the results of Tomisaka (1991) and Habe et al (1991).

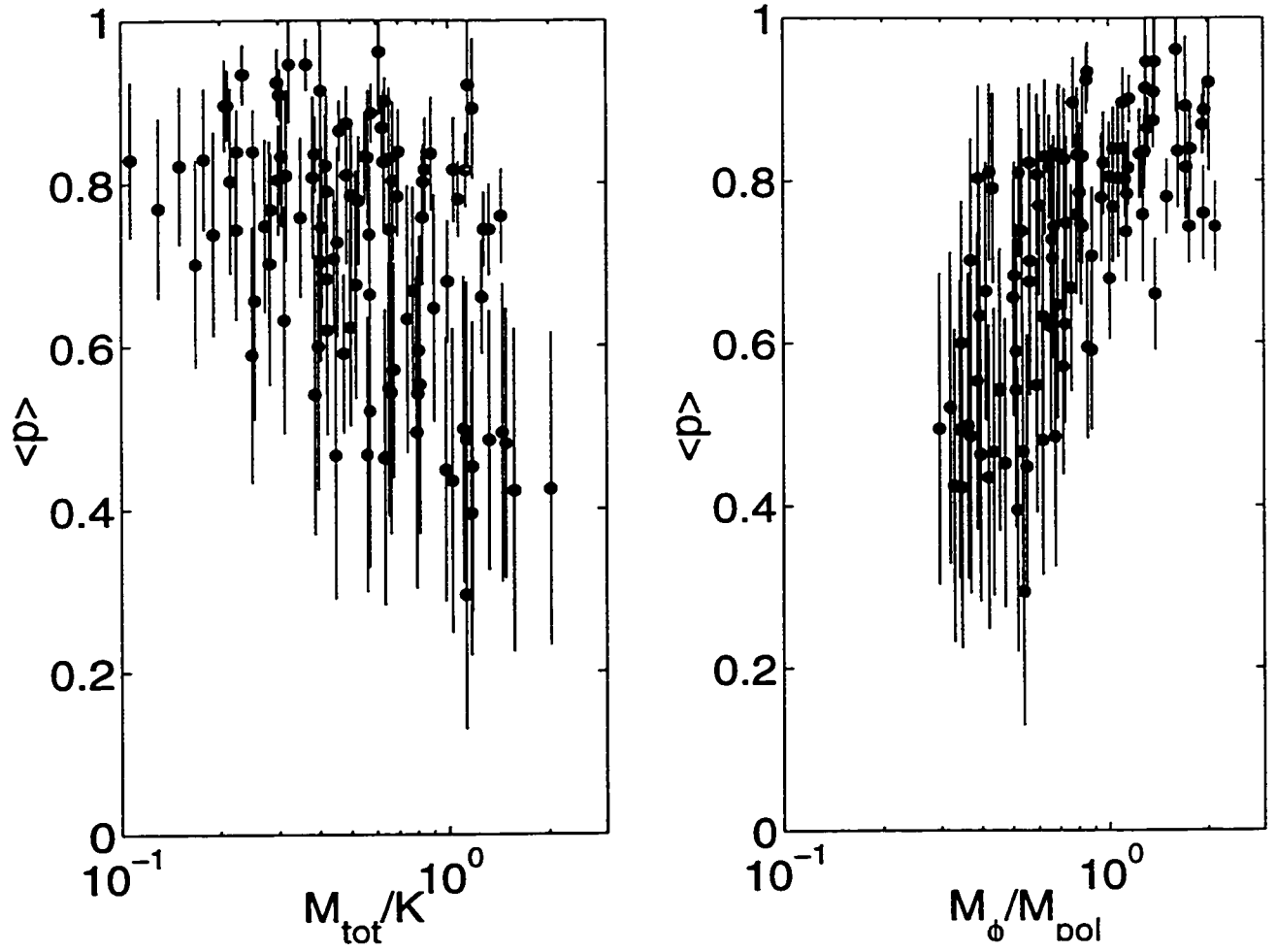

Figure 6-11: **Panel (a)** (left): we show how the projected axis ratio $\langle p \rangle$ depends on the ratio of the magnetic to kinetic energy M_{tot}/K. M_{tot} does not exceed $\sim 2K$ for any of our models. **Panel (b)** (right): We show how $\langle p \rangle$ depends on ratio of the toroidal to poloidal magnetic energy M_{ϕ}/M_{pol}. Significantly elongated models have $M_{\phi} < M_{pol}$.

6.5.1 Effect of Mass

Figure 6-12 shows how the intrinsic axis ratio q varies with mass for core models obtained from 3 different parent filaments. We have normalized the mass by the Bonnor-Ebert critical mass $M_{B.E.}$, to provide a convenient reference point for the mass. The filament parameters Γ_z, Γ_{ϕ}, and C are given in Table 6.1, as well as the external pressure P_{ext} and $M_{B.E.}$. We find that the axis ratio q decreases with increasing mass, when the mass is very low (less than a few tenths of $M_{B.E.}$). These weakly self-gravitating equilibria are strongly pinched by the toroidal field and more closely resemble short filaments than cores. Once self-gravity becomes important (when the mass is a significant fraction of $M_{B.E.}$), the axis ratio

decreases with increasing mass. Our models become nearly spherical when $M_{core} \gtrsim 0.75 M_{B.E.}$.

The sequences shown in Figure 6-12 all terminate at masses that are about 20% less than $M_{B.E.}$, although we have attempted to compute models with greater masses. This is consistent with our finding that very few models converge when $M_{crit}/M_{B.E.} > 0.8$ (see Figure 6-1). Therefore, the critical mass $M_{crit} < M_{B.E.}$ for our models, as a result of the pinch provided by the helical magnetic field.

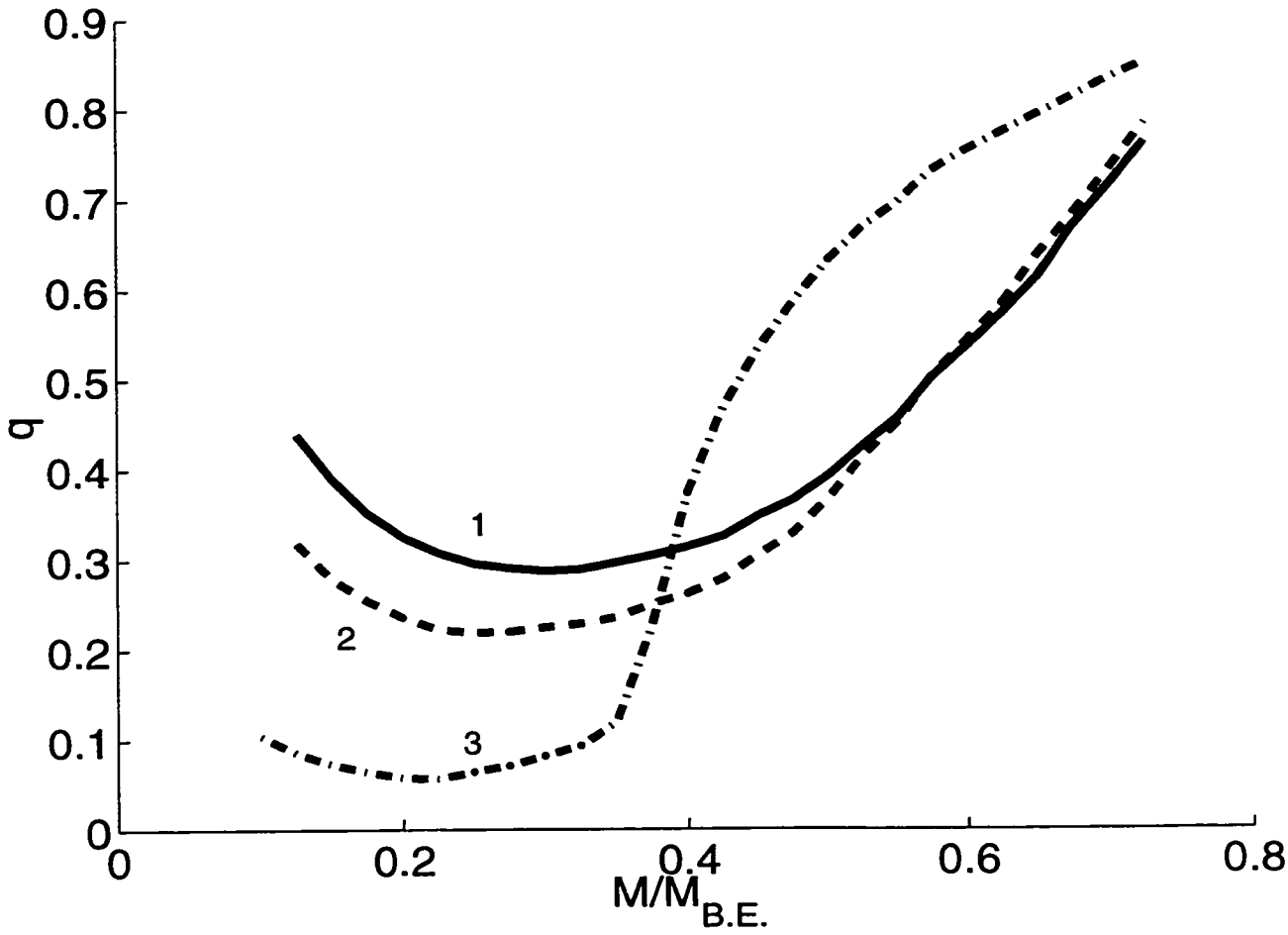

Figure 6-12: We show the effect of varying the masses of cores on q while holding all other parameters fixed. The curves are labeled to correspond with the column labeled "Sequence" in Table 6.1.

Sequence	Γ_z	Γ_ϕ	C	P_{ext}	$M_{B.E.}$
1	7.17	6.05	0.165	0.436	79.6
2	6.76	6.45	0.200	0.353	88.6
3	4.53	6.18	0.235	0.243	106.6

Table 6.1: We give the dimensionless parameters used to compute the sequences of models shown in Figure 6-12. Parameters to the left of the double vertical line are input parameters, while the quantities to the right are derived parameters of the model.

Sequence	Γ_z	Γ_ϕ	C	M_{core}	$P_{B.E.}$
1	7.17	6.05	0.165	39.8	0.519
2	4.53	6.18	0.235	42.6	0.496
3	6.76	6.45	0.200	44.3	0.484

Table 6.2: We give the dimensionless parameters used to compute the sequences of models shown in Figure 6-13. Parameters to the left of the double vertical line are input parameters, while the quantity to the right is a derived parameter of the model.

6.5.2 Bonnor-Ebert Stability and the Effect of the External Pressure

We have previously considered the external pressure bounding the core to be the same as that bounding the parent filament. However, for these sequences only, we vary the external pressure to determine how squeezing prolate cores affects their shapes. This procedure also allows us to determine the Bonnor-Ebert stability of our models.

Figure 6-13 shows how the shape of a core with fixed mass, Γ_z, Γ_ϕ, and C changes as the external pressure is varied. We have held the mass fixed and varied the external pressure, which we have normalized by the Bonnor-Ebert critical pressure $P_{B.E.}$, defined by

$$P_{B.E.} = 1.39\frac{\sigma^8}{G^3 M_{core}^2} \tag{6.40}$$

for convenience. The parameters describing the parent filament are given in Table 6.2, as well as the mass M_{core} and $P_{B.E.}$. We find that our models are most elongated when the surface pressure P_S is well below the Bonnor-Ebert critical pressure $P_{B.E.}$. Cores become strongly self-gravitating, and therefore nearly spherical, when P_S is comparable to $P_{B.E.}$.

We find that all of the sequences terminate at pressures that are well below the Bonnor-Ebert critical pressure. Therefore, the critical pressure $P_{crit} < P_{B.E.}$, as a result of the helical field squeezing our models in concert with the external pressure.

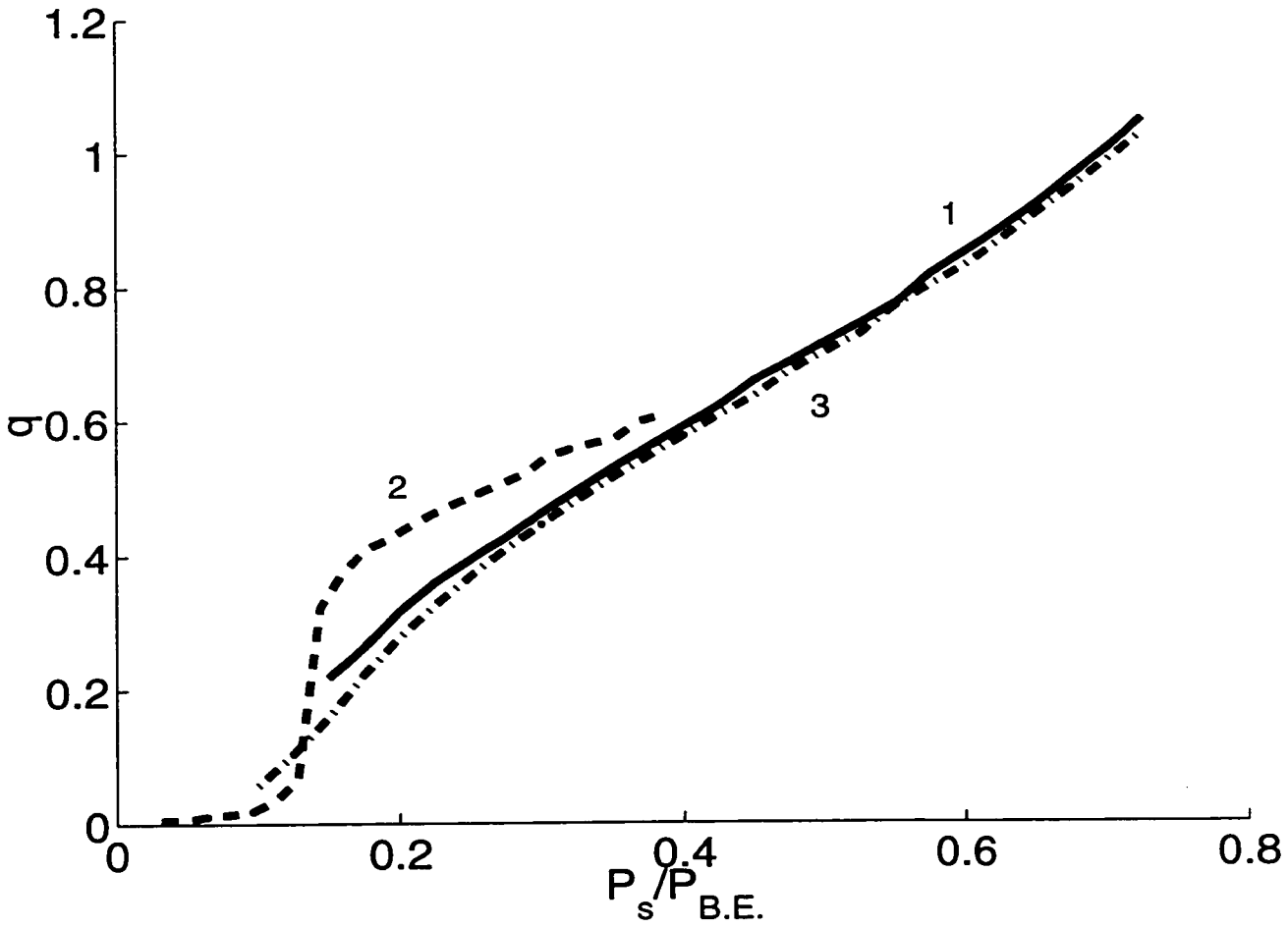

Figure 6-13: We show the effect of varying the external pressure on q for cores of constant mass. The curves are labeled to correspond with the column labeled "Sequence" in Table 6.2.

6.6 A Singular Model for Prolate Cores

We have found a very simple singular isothermal solution for a prolate core containing a purely toroidal magnetic field. While a purely toroidal field is admittedly not very realistic, the solution is interesting because it probably represents the simplest possible model of a magnetized prolate core, and is in fact a generalization of the well-known singular isothermal sphere. From a physical standpoint, this model is useful because it demonstrates that a relatively moderate toroidal field, with plasma $\beta \geq 1$ everywhere, can result in elongated cores with axis ratios that are in good agreement with the observations.

We assume a logarithmic gravitational potential, in cylindrical coordinates (r, ϕ, z), of the form

$$\Psi = \sigma^2 \ln \frac{(r^2 + \epsilon^2 z^2)}{2} \tag{6.41}$$

where ϵ is the axis ratio of the isopotential surfaces, and σ is assumed to be constant [6]. This is the potential of a singular isothermal sphere when $\epsilon = 1$, and describes singular prolate models when $\epsilon < 1$. In Appendix B, we show that the corresponding density and toroidal magnetic field are given by

$$\rho = \frac{\sigma^2}{2\pi G} \frac{\epsilon^2 \left[r^2 + (2-\epsilon^2)z^2\right]}{(r^2 + \epsilon^2 z^2)^2} \tag{6.42}$$

$$B_\phi = \frac{2\sigma^2}{G^{1/2}} \frac{r\sqrt{1-\epsilon^2}}{(r^2 + \epsilon^2 z^2)}, \tag{6.43}$$

where all quantities are the same as in our numerical models (See Section 6.2). It is clear that more elongated solutions (smaller values of ϵ) are consistent with larger values of B_ϕ.

We note that choosing $\epsilon = 1$ recovers the well-known singular isothermal sphere solution, for which B_ϕ vanishes. It is interesting that the density vanishes when $\epsilon = 0$. Therefore, the solution does not reduce to a singular model for filaments in this limit (See also FP1). An important feature of equation 6.43 is that there is no solution when $\epsilon > 1$. Hence, there are no oblate solutions that are consistent with our singular model.

The plasma β parameter is given by

$$\beta = \frac{\epsilon^2}{1-\epsilon^2} \left[1 + \frac{(2-\epsilon^2)z^2}{r^2}\right], \tag{6.44}$$

which has a maximum of $\epsilon^2/(1-\epsilon^2)$ in the midplane, where $z = 0$. Therefore, $\epsilon = 1/\sqrt{2}$ results in a moderately magnetized model with $\beta \geq 1$ everywhere, which we show in Figure 6-14. We find that the density contours of this singular model have an axis ratio of ≈ 0.46 (See Section 6.4 and Appendix A for a discussion of our method of estimating axis ratios.). This result is in good agreement with the mean intrinsic axis ratios that are typically derived for samples of cores (See Ryden 1996).

A simple numerical example illustrates that relatively moderate toroidal fields can result in significant elongation. We consider the magnetic field at a distance of 0.1 pc from the centre of the $\epsilon = 1/\sqrt{2}$ model discussed above. This distance corresponds to the radius at which the thermal and non-thermal velocity dispersions are approximately equal for low mass cores (Fuller & Myers 1992, Casseli & Myers 1996). Therefore, $\sigma \approx 0.26\ km\ s^{-1}$, assuming a temperature of 10 K for the gas. Equation 6.43 requires a maximum strength of only $\approx 12\ \mu G$ for B_ϕ at this distance.

The toroidal field in the singular model is strongest in the midplane, which squeezes the gas so that the constant density surfaces are slightly pinched in. This is markedly different from our non-singular numerical solutions, which have their maximum toroidal field off the midplane. However, models with purely toroidal fields, such as our singular solution, are a separate class of solutions that cannot be

[6] See Binney and Tremaine (1994) equation 2-54a for a similar potential used in the context of galactic disks.

obtained from the self-consistent field equations (discussed in Section 6.2), even in the limit of a vanishing poloidal field. The reason for this difference is that azimuthal component of the magnetohydrostatic equilibrium equation (equation 6.2) is automatically satisfied for purely toroidal field geometries. In the more general case of a helical field, torsional equilibrium requires b_ϕ to be constant along poloidal field lines, so that the class of allowed solutions is somewhat more restricted.

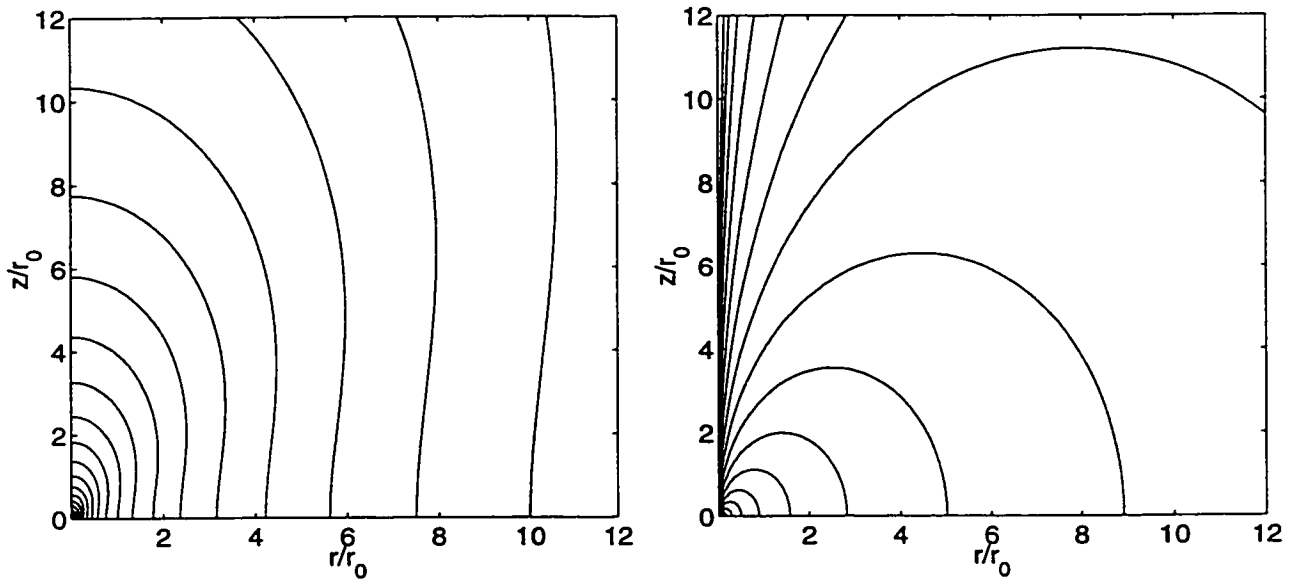

Figure 6-14: We show density contours (top, panel a) and toroidal field intensity contour (bottom, panel b) for the singular model for prolate cores with a purely toroidal field.

6.7 Discussion and Conclusions

We have previously (FP1) suggested that some filamentary molecular clouds may contain helical magnetic fields, and that such filaments are unstable against fragmentation along their lengths (FP2). Some fragments may dynamically evolve into equilibrium states that can be identified as cloud cores. The central point of the present work is to demonstrate that most of the possible equilibrium states that arise from our filament models are prolate, and that many have realistic axis ratios.

It is very encouraging that we are able to explain several of the observed features of filamentary

clouds and their cores within a self-consistent theoretical framework. Future tests of our models may be provided by measurements of polarized dust grain emission. A useful test of our models will be to predict the polarization due to both our filament models (FP1) and the prolate core models derived in this paper. This is done in a forthcoming study. Perhaps even more importantly, the central assumption of our model, which posits a constant flux to mass loading, requires direct confirmation. This could one day be feasible with sufficiently high spatial resolution Zeeman measurements.

Previous observations of the shapes of cores have concentrated mainly on their axis rations (Myers et al. 1991, Ryden 1996). However, we have found that the shapes of cores can usefully be described by a second observable parameter a_4/a, which quantifies the deviation of the density contours from ellipses. The toroidal field in our model results in $a_4/a > 0$, which is consistent with surface density contours that are somewhat football-shaped (ie. peaked along the major axis). Therefore a detailed isophotal analysis of cores may provide important clues to their internal magnetic structures.

Core models that exceed the critical mass for stability in the sense of Bonnor (1956) and Ebert (1955) are doomed to collapse. The dynamical collapse of one of our prolate core models from a critical initial state is a difficult problem that should be addressed by future numerical simulations.

6.8 Summary

1. Most of the core models that are consistent with our previous models of filamentary molecular clouds are found to be prolate. A wide range of axis ratios is possible, with $0.1 \lesssim q \lesssim 0.9$ and $0.3 \lesssim \langle p \rangle \lesssim 1$.
2. Both density and surface density profiles are found to be slightly football-shaped (ie. peaked toward the symmetry axis) in our models, as quantified by the a_4/a parameter of Bender & Möllenhoff (1987).
3. The Bonnor-Ebert critical mass is reduced by about 20% in our models by the toroidal field.
4. We find that models are generally more elongated for low values of the mass ratio $M/M_{B.E.}$ and the pressure ratio $P_S/P_{B.E.}$.
5. Only modest toroidal fields are required to produce elongated cores. Most of our models have $B_\phi < B_z$ nearly everywhere.

6.9 Acknowledgements

J.D.F. acknowledges the financial support of McMaster University during this research. The research of R.E.P. is supported by a grant from the Natural Sciences and Engineering Research Council of Canada.

Appendix A

The Mean Projected Axis Ratio and a_4/a Shape Parameter

For each of the models discussed in the previous sections, we have calculated the surface density at various angles of inclination. By assuming that cores are oriented randomly, we calculate a distribution function for the axis ratio and the a_4/a shape parameter of the half maximum surface density contour, from which we obtain their mean values and standard deviations. We work in Cartesian coordinates (x', y', z'), with the origin at the centre of the core, the y' axis along the line of sight to a distant observer, and the $x' - z'$ plane parallel to the plane of the sky. We define a second set of Cartesian coordinates (x, y, z) fixed relative to the core, with z corresponding to the axis of symmetry. The z axis is assumed to be tilted by an inclination angle i relative to the plane of the sky and towards the observer. The coordinates are then related by

$$\begin{aligned} x' &= x \\ y' &= y\cos i - z\sin i \\ z' &= y\sin i + z\cos i. \end{aligned} \tag{A.1}$$

Since the cylindrical radius (relative to the symmetry axis) is given simply by $r = \sqrt{x^2 + y^2}$, we interpolate $\rho(r, z)$ over the primed coordinates to obtain $\rho(x', y', z')$. The surface density $\Sigma(x', z')$ is then obtained by integrating over y'. We then compute the contour of the half maximum surface density, from which we estimate the axis ratio by fitting an ellipse as described in Section 6.4. We also compute the a_4/a shape parameter, using the method discussed in Bender and Möllenhoff (1987). We repeat this procedure at many different inclination angles to determine the projected axis ratio p and a_4/a as

a function of i.

The z axis is assumed to be oriented in a random direction (θ, ϕ) relative to the z' axis. The inclination angle is related to θ and ϕ by

$$\cos i = 1 - \sin^2\theta \sin^2\phi. \tag{A.2}$$

The probability dp_ϕ of the z axis being oriented between ϕ and $\phi + d\phi$ is

$$dp_\phi = \frac{d\phi}{2\pi}. \tag{A.3}$$

Integrating, the probability of the z axis being oriented between 0 and ϕ is given by $\phi/2\pi$, so that

$$\phi = 2\pi\xi \tag{A.4}$$

if ξ is a uniformly distributed random variable. Similarly, it is easy to show that

$$\cos\theta = 1 - 2\xi \tag{A.5}$$

for another random variable ξ. We generate a large number of realizations (typically 10^5) of the orientation (θ, ϕ), from which we calculate the orientation i by equation A.2. We interpolate to find p and a_4/a for each realization, and calculate the mean values and standard deviations of the resulting distributions.

Appendix B

Derivation of the Singular Isothermal Model for Prolate Cores

Working in the dimensionless variables introduced in equation 6.25 and assuming that the magnetic field is purely toroidal, the equation of magnetohydrostatic equilibrium (equation 6.2) can be written as

$$8\pi r^2 e^{-\Psi} \nabla Q = \nabla b_\phi^2 \tag{B.1}$$

where b_ϕ is related to B_ϕ by equation 6.3. The variable Q has the same form as in equation 6.6, but is no longer contsrained to be a function of Φ:

$$Q = \rho e^{\Psi}. \tag{B.2}$$

We note that the r and z components of equation B.1 can be combined into the form of a Jacobian determinant, which implies that b_ϕ can be considered as a function of Q alone.

The potential for the singular isothermal sphere model, in our dimensionless variables, is given by $\Psi = \ln(R^2/2)$, where R is the spherical radius. Therefore, we consider distorted logarithmic potentials of the form

$$\Psi = \ln\left(\frac{r^2 + \epsilon^2 z^2}{2}\right) \tag{B.3}$$

where ϵ is the axis ratio of the isopotential surfaces. The density is easily obtained from Poisson's equation (equation 6.27):

$$\rho = 2\epsilon^2 \frac{\left[r^2 + (2-\epsilon^2)z^2\right]}{(r^2 + \epsilon^2 z^2)^2}, \tag{B.4}$$

which appears in dimensional form as equation 6.42.

Inserting equations B.3 and B.4 into equation B.2, we find that Q can be written in the form

$$Q(\zeta) = \frac{\epsilon^2 \left[1 + (2 - \epsilon^2)\zeta^2\right]}{1 + \epsilon^2 \zeta^2}, \tag{B.5}$$

where

$$\zeta \equiv z/r. \tag{B.6}$$

Since b_ϕ is a function of Q alone, we can consider both Q and b_ϕ to be functions of ζ in equation B.1. This equation becomes an ordinary differential equation in for $b_\phi(\zeta)$:

$$\frac{db_\phi}{d\zeta} = -\frac{8\pi}{1 + \epsilon^2 \zeta^2} \frac{dQ}{d\zeta}. \tag{B.7}$$

Substituting $Q(\zeta)$ into this equation and integrating, we find that

$$b_\phi^2 = \frac{16\pi(1 - \epsilon^2)}{(1 + \epsilon^2 \zeta^2)^2}. \tag{B.8}$$

The toroidal field B_ϕ is directly obtained from this equation by replacing both ζ and b_ϕ with their respective definitions (equations B.6 and 6.3). The final dimensional form is written out in equation 6.43.

References

Alves J., Lada C.J., Lada E.A., Kenyon S.J., Phelps R., 1998, Ap.J., 506, 292

Bender R., Möllenhoff C., 1987, A&A, 177, 71

Binney J., Tremaine S., 1994, *Galactic Dynamics* (Princeton: Princeton University Press)

Bonnor W.B., 1956, MNRAS, 116, 351

Caselli P., Myers P.C., 1995, Ap.J., 446,665

Ebert R., 1955, Z.Astrophys., 37, 217

Fiege J.D, Pudritz R.E., 1999 (FP1), MNRAS, in Press (see also astro-ph/9901096)

Fiege J.D, Pudritz R.E., 1999 (FP2), MNRAS, in Press (see also astro-ph/9902385)

Fuller G.A., Myers P.C., 1992, Ap.J., 384, 523

Goodman A.A., Benson P.J., Fuller G.A., Myers P.C., 1993 Ap.J., 406, 528

Habe A., Uchida Y., Ikeuchi S., Pudritz R.E., 1991, PASJ, 43, 703

Lada C.J., Alves J., Lada E.A., 1999, Ap.J., 512, 250

McKee C.F., 1999, in *NATO Advanced Study Institute on The Physics of Star Formation and Early Stellar Evolution*, eds. Kylafis N., Lada C. (see also astro-ph 9901370) Mouschovias T., 1976, Ap.J., 206, 753

Mouschovias T., 1976, Ap.J., 207, 141

Myers, P.C., Fuller, G.A., Goodman, A.A., Benson P.J., 1991, Ap.J., 376, 561

Myers P.C., Goodman A.A., 1988a, Ap.J., 326, L27

Myers P.C., Goodman A.A., 1988b, Ap.J., 329, 392

Ryden, B.S., 1996, Ap.J., 471, 822

Schneider S., Elmegreen B.G., 1979, Ap.J.S., 41, 87

Tomisaka K., 1991, Ap.J., 376, 190

Tomisaka K., Ikeuchi S., Nakamura T., 1988a, Ap.J., 326, 208

Tomisaka K., Ikeuchi S., Nakamura T., 1988b, Ap.J., 335, 239

Tomisaka K., Ikeuchi S., Nakamura T., 1989, Ap.J., 341, 220

Tomisaka K., Ikeuchi S., Nakamura T., 1990, Ap.J., 362, 202

Chapter 7

Discussion and Summary

7.1 General Discussion of Our Models - Strengths, Weaknesses, and Future Directions

We have shown that our models capture many of the observed features of filamentary clouds and their cores, within a single, reasonably self-consistent theoretical framework. This should be regarded as the principle success of our models. However, our models of filaments and cores suffer from the same difficulty as any equilibrium model. While we can predict the *structure* of filaments and cores within the framework of our models, and perhaps even observationally constrain the model parameters, we can only speculate on the *origins* of the structures that we predict. Our basic strategy has been to demonstrate that such models might describe the observations before considering their origins in detail. Future dynamical models or simulations could potentially address the formation of filamentary clouds, but we can only speculate for now.

We have suggested two possible scenarios from which helically magnetized filamentary clouds might originate. The first of these scenarios involves the fragmentation of magnetized supershells that sweep up material of non-uniform angular momentum from different radii of the Galactic disk (See Section 2.3.2). It is conceivable that poloidal field lines threading a filamentary cloud might be twisted into a helical geometry by the resulting differential rotation. The second scenario relies on the well-known fact that turbulent flows are characterized by their kinematic vorticity and magnetic helicity. Simulations also show that the regions of highest vorticity are often associated with high density clouds where molecular gas would likely form (See Section 2.5.5 and references therein). Therefore, it seems possible that a turbulent ISM could generate the magnetic helicity required by our models.

Our models also suffer from the opposite problem to the question of their origins, namely that we

do not know how our models evolve dynamically. The stability analysis in Chapter 4 partly addresses this concern, but the analysis there strictly applies only to the linear phase of fragmentation. We simply cannot predict how the fragments that form in the linear regime evolve and eventually settle down to form cores. It is for this very reason that we needed to specify the mass of the cores in Chapter 6 as a fourth parameter beyond the three that are required for our model of filaments. A more self-consistent treatment would dynamically evolve our filamentary initial conditions, seeded by an initial perturbation (perhaps corresponding to the mode of maximum instability from our linear stability analysis), to determine the range of core models that emerge. This type of simulation could probably be accomplished using existing MHD codes (eg. ZEUS-2D and ZEUS-3D).

7.1.1 The Evolution of Filamentary Molecular Clouds

Our models of filamentary clouds implicitly assume that they are in a state of radial quasi-equilibrium and that fragmentation is the main process driving their evolution. Although we can prove neither of these assumptions, we can offer an *a posteriori* argument for the self-consistency of our models.

There are four important timescales that determine the evolution of a helically magnetized filamentary molecular cloud. These are the radial signal crossing time, the fragmentation timescale, the timescale for the decay of the magnetic field by ambipolar diffusion, and the timescale on which the helical field can be lost from the filament as a torsional Alfvén wave. We discuss and compare these timescales to demonstrate that radial equilibrium is a reasonable (or at least self-consistent) assumption, and that fragmentation is probably the dominant process in the evolution of filamentary clouds.

Radial Signal Crossing Time

The radial signal crossing time τ_x in a filamentary cloud of radius R is approximately equal to R/v_A, where v_A is the Alfvén speed (equation 2.9). We assume here that disturbances can propagate radially outward as magnetosonic waves, [1] so that τ_x is the timescale on which radial equilibrium can be established in a magnetized filament. For our models, the kinetic and magnetic energies are in approximate equipartion. Therefore the Alfvén speed is related to the velocity dispersion by $v_A \approx \sqrt{3}\sigma$. It is useful to note that the dynamical timescale τ_{dyn} for the gravitational collapse of a filamentary cloud is $\tau_{dyn} = c_{dyn}(G\langle\rho\rangle)^{-1/2}$, where $\langle\rho\rangle$ is the average density of the filament, and c_{dyn} is a coefficient that depends on the radial density distribution. The radial signal crossing time is therefore proportional to

[1] The fast magnetosonic wave propagates perpendicular to field lines (ie:radially outward in our filament model) at a speed $v_{fast} = \sqrt{v_A^2 + c_s^2}$. However, the sound speed is negligible in molecular clouds (except for in dense cores) compared to the Alfvén speed.

τ_{dyn}:

$$\tau_x \approx 0.46 \left(\frac{m}{m_{vir}}\right)^{1/2} (G\langle\rho\rangle)^{-1/2}, \tag{7.1}$$

where we have used the definition of m_{vir} (equation 3.12), and the identity $m = \pi R^2 \langle\rho\rangle$.

Fragmentation Timescale

The fragmentation timescale for our models is given by equation 4.26, which is also proportional to the dynamical timescale:

$$\tau_{frag} = 2.8 \left(\frac{-\tilde{\omega}^2_{max}}{0.01}\right)^{-1/2} \left(\frac{\langle\rho\rangle}{\rho_c}\right)^{1/2} (G\langle\rho\rangle)^{-1/2}, \tag{7.2}$$

where ρ_c is the central density in the notation of Chapter 3, and we have normalized the dimensionless squared growthrate $-\tilde{\omega}^2_{max}$ by values that are "typical" of models that are dominated by gravitational instabilities rather than magnetic ones (See Chapter 4). Therefore, τ_{frag} is usually considerable longer than τ_x, which allows radial equilibrium to be established before filaments fragment.

Ambipolar Diffusion Timescale

In Section 5.7.3, we calculated a timescale for ambipolar diffusion in cores. We now calculate the ambipolar diffusion timescale for filamentary clouds, using the same argument presented in Section 5.7.3. A fiducial value for the gravitational acceleration g within a filamentary cloud of mass per unit length m and radius R is given by

$$g = \frac{2mG}{R}. \tag{7.3}$$

Using this expression in equations 5.35 and 5.36, and ignoring any complications that might arise as a result of the toroidal field (See discussion in Section 5.7.3), it is easy to show that

$$\tau_{A.D.} \approx 6.0(G\langle\rho\rangle)^{-1/2}, \tag{7.4}$$

which is only slightly shorter than the equivalent expression for spheroidal clouds (See equation 5.36). Comparing with equation 4.27, we find that ambipolar diffusion requires many signal crossing times to weaken the magnetic field in our models. It is also longer than the fragmentation timescale (equation 4.26) for most of our models. However the timescale for ambipolar diffusion might be comparable to the fragmentation timescale of our most stable filaments, where $-\tilde{\omega}^2_{max} \ll 0.01$.

Torsional Alfvén Wave Timescale

Torsional Alfvén waves are a type of Alfvén wave that propagate as helical disturbances along poloidal magnetic field lines, which could "radiate" away the toroidal component of the magnetic field. The timescale on which this could happen is given by $\tau_\phi \approx L/v_A$, where L is the length of a filamentary cloud. This can also be expressed as

$$\tau_\phi \approx \frac{L}{R}\tau_x. \tag{7.5}$$

Since $L/R \gtrsim 10$ for filamentary clouds, by definition, it is clear that torsional Alfvén waves cannot significantly weaken the toroidal field for many signal crossing times. Comparing to equations 4.27 and 7.2, the timescale for torsional waves is also significantly longer the fragmentation scale.

To summarize, fragmentation is likely to be the dominant process in the evolution of most filamentary clouds, since the fragmentation timescale is shorter than the torsional Alfvén wave transit timescale, or the ambipolar diffusion timescale for most models. However, our most stable models might live long enough for ambipolar diffusion to have significant effects. All of these timescale are substantially longer than the radial signal crossing timescale. Therefore, the assumption of radial quasi-equilibrium seems to be justified.

7.1.2 Observational Tests of Our Models

We have placed a major emphasis on comparing and constraining our models with observational data throughout this thesis. Our models are now at a stage where they can be thoroughly tested by the observations. We briefly discuss some of the possible observational tests below.

The most direct test of our models would be to fit our models to the surface density structures derived from observational data. This might be most easily done at sub-millimetre wavelengths for the reasons discussed in Section 2.1.2, although line data would also be useful. For example, a useful test of our model of filamentary molecular clouds would be to fit our models to the surface density structure of the integral-shaped filament in Orion A, which has recently been mapped in sub-millimetre continuum emission at $450\mu m$ and $850\mu m$ by Johnstone and Bally (1999). [2]

Other data may also soon be available to test our models. A Consortium of Canadian astronomers [3] is presently using SCUBA to map several nearby molecular clouds, namely Orion B, Taurus, and Rho Ophiuchus, at $450\mu m$ and $850\mu m$ sub-millimetre wavelengths, as well obtaining some complementary molecular line data from other telescopes. Preliminary results indicate the presence of several filaments and numerous cores that could be used to test our models. The large quantity of data that is emerging

[2] Johnstone and Bally have provided us with their data for this purpose.
[3] The author of this thesis is a member.

from this project will allow us to test our models very thoroughly.

Carlqvist and Kristen (1997) have recently modelled the polarization, in absorption, due to an empirical model of a magnetized filament (See Section 2.2.4 and Chapter 3). It would be useful to apply a technique like theirs to model the sub-millimetre polarization patterns that would be expected for our models of filaments and cores threaded by helical magnetic fields. The predicted polarization patterns could then be compared with the Matthews and Wilson (1999) polarization data for the integral-shaped filament (also discussed in Section 2.2.4), as well as the filaments and cores that are being mapped in polarimetry by the Canadian Consortium.

7.2 Summary

7.2.1 A Model For Helically Magnetized Filamentary Clouds

Molecular clouds are known to be both magnetized and truncated by the pressure of the surrounding ISM. Observations have revealed that they are also highly filamentary. The main objective of the original work in this thesis has been to develop a reasonably self-consistent picture of filamentary molecular clouds and their cores.

In Chapter 3, we derived a virial equation that is appropriate for filamentary clouds that are threaded by both poloidal and toroidal fields, so that the field lines are helical in general. Comparing with existing observational data compiled form the literature, we demonstrated that the global properties (mass, length, surface pressure, and internal velocity dispersion) of many filamentary clouds are consistent with equilibrium models that are threaded by helical magnetic fields. In fact, the global properties of many filamentary clouds would be very difficult to explain without the magnetic "pinch" provided by a modest toroidal field component.

Our virial analysis also demonstrated that equilibrium models of magnetized filamentary clouds are consistent with Larson's laws. This can also be demonstrated for spheroidal clouds from the virial theorem (See Section 2.11.4.), but with one important difference. A necessary step in our derivation of Larson's laws for spheroidal clouds was the assumption that clouds are nearly critical in the sense of the Bonnor-Ebert stability analysis presented in Section 2.11.2. However, no corresponding assumption was required to obtain Larson's laws for filamentary clouds. Therefore, Larson's laws are obtained for filamentary clouds under more general circumstances than for their spheroidal clouds.

We considered the Bonnor-Ebert stability of our models, finding that filamentary clouds, whether magnetized or not, behave very differently from spheroidal clouds. We showed that there is an upper limit m_{mag} ($\equiv m_{vir}$ for unmagnetized models) for the mass per unit length of a filamentary cloud, which depends on the magnetic field, past which collapse is inevitable. If $m < m_{mag}$, a filamentary

cloud can never be made to collapse gravitationally, no matter how high the external pressure. Any magnetically super-critical spheroidal cloud, on the other hand, can be made to collapse under self-gravity by increasing the external pressure past a critical value.

The suggestion of a helical field from our virial results in Chapter 3 motivated us to proceed with the second part of the analysis (also in Chapter 3), where we constructed detailed magnetohydrostatic models of filamentary clouds, considering only the subset of models that are in agreement with our virial constraints. We found that nearly all of our isothermal models, and some of our logatropic models, are consistent with the observed $\sim r^{-2}$ density profiles (Alves et al. 1998, Lada et al. 1999) of filamentary clouds. A necessary caveat to this success is that our models are not completely general, since we assumed constant magnetic flux to mass ratios for the poloidal and toroidal field components. It is likely that different radial profiles could be obtained if the flux to mass ratios were allowed to vary with radius. However, it is encouraging that this simplest case results in density profiles that are in apparent agreement with the observational data. Our choice of constant flux to mass loading might be natural for filamentary clouds because neighbouring helical flux tubes can be interchanged in this configuration with no change to the energy of the magnetic field. Such a configuration is clearly stable against interchange instabilities, while other choices might not be.

The overall conclusion of Chapter 3 was that our models of helically magnetized filamentary clouds appear to be consistent with the existing observational data, and have interesting stability properties. In many ways, filamentary clouds represent the opposite extreme of the more traditionally studied spherical clouds. Both filaments and spheroids should be studied as complementary models of molecular cloud structure.

7.2.2 The Fragmentation of Filamentary Clouds

We considered the stability of our models against axisymmetric modes of fragmentation in Chapter 4. We found that our models are subject to two distinct types of instability. Many models are dominated by long wavelength gravitationally dominated modes of fragmentation, as have been previously found by several authors (eg. Chandrasekhar & Fermi 1953b, Nakamura et al. 1993, Gehman et al. 1996) for different models of filamentary clouds. Others are dominated by short wavelength MHD-driven instabilities, which we attribute to MHD sausage instabilities (although modified by self-gravity). Some of the models on this branch are extremely unstable, and therefore probably do not represent realistic models of filamentary clouds. Since these models are allowed by our virial constraints from Chapter 3, we conclude that our virial analysis provides necessary, but probably not sufficient conditions to fully constrain our models of filamentary clouds.

The timescale for fragmentation is given by

$$\tau_{frag} = 1.8 \left(\frac{-\tilde{\omega}^2_{max}}{0.01} \right)^{-1/2} \left(\frac{n_c}{10^4\ cm^{-3}} \right)^{-1/2}\ Myr, \tag{7.6}$$

where we have normalized by fiducial values for the central number density n_c of the filament (The reasons for the normalization in this equation are discussed in Chapter 4, following equation 4.26.), and the dimensionless squared growth rate $-\tilde{\omega}^2_{max} \approx 0.01$ (See Figure 4-13). The most interesting result of our stability analysis is that there is a regime at intermediate wavelengths between the gravitationally-driven and MHD-driven modes where clouds fragment very slowly, with fragmentation timescales on the order of $\sim 5.7\ Myr$, corresponding to $-\tilde{\omega}^2_{max} \approx 10^{-3}$. This very stable regime exists because toroidal fields actually *suppress* gravity-driven modes. Gravity-driven modes grow increasingly slowly as the strength of the toroidal field is increased, until MHD-driven sausage modes are triggered when $\Gamma_\phi \approx 2\Gamma_z$.

We did not consider non-axisymmetric modes in our analyis. The most rapidly growing, and therefore most dangerous, non-axisymmetric, MHD-driven instability for magnetically pinched cylindrical plasma columns is often the $m = 1$ "kink" instability. Kink instabilities cause cylindrical plasmas to distort into helices which eventually break up. However, kink instabilities are strongly suppressed by the poloidal field. Plasma columns are stable to all kink modes with wavelengths shorter than ~ 14 times the radius of the plasma column, when the poloidal field is comparable to the toroidal field (Jackson 1975). Our filament models are threaded by a rather strong "backbone" of poloidal flux, which should help to prevent kink instabilities, especially at short wavelengths. We therefore expect mainly long wavelength kink instabilities to be active in our models, which would only apply to real filaments of sufficient length. Nevertheless, it would be useful (and reassuring) to study the non-axisymmetric stability of our models, using the same techniques as in Chapter.

7.2.3 Prolate Cores in Filamentary Clouds

In Chapters 5 and 6, we discussed considerable observational evidence that cores and Bok globules are prolate, with mean projected axis ratios of $\sim 0.5 - 0.6$, and a wide range of allowed values distributed about the mean (Myers et al. 1991, Ryden 1996). In Chapter 6, we relaxed finite segments of helically magnetized filamentary clouds to equilibrium, using the well-known Self Consistent Field Method that was originally developed by Mouschovias (1976a). Our main result was that finite segments of helically magnetized filamentary clouds easily lead to elongated prolate cores, with projected axis ratios in the range $0.3 \lesssim \langle p \rangle \lesssim 1$. Therefore, we find that many of our models are in good agreement with the range of axis ratios allowed by the data.

Our models are prolate as a result of the radial "pinch" provided by a modest toroidal magnetic field component. By "modest", we mean that the magnetic energy in our models is always comparable to or less than the kinetic energy, and that the energy of the toroidal field never greatly exceeds that of the poloidal field. In fact, the toroidal field energy is considerably lower than the poloidal field energy for our most elongated models. Substantially elongated cores do not require large toroidal fields in our model.

We also considered the Bonnor-Ebert stability of our models, finding that the critical mass is decreased by about 20%. This is in qualitative agreement with the simple virial argument that we presented in Chapter 5, where we showed that the toroidal field acts like an extra surface "pressure" that works in concert with the external medium to squeeze cores. Note that we also demonstrated in Chapter 3 that toroidal fields squeeze filaments only through a surface term in the virial equation (See equation 6 of Chapter 3).

7.3 Concluding Remarks

We have argued that good models of molecular clouds and their cores are necessary to establish the initial conditions for star formation. Our models of clouds as intrinsically filamentary, helically magnetized objects are very different from the more usual models of molecular clouds as spheroidal equilibria that are supported by a poloidal magnetic field. Our prolate models of cloud cores are also very different from the oblate models that result from purely poloidal fields.

How do our models change our overall picture of star formation in molecular clouds? We addressed this question by showing that our models have very different stability properties, compared to spheroidal models. In particular, there is no analogue of the Bonnor-Ebert instability in filaments. As long as the mass per unit length of a magnetized filamentary cloud is below a critical value m_{mag}, the filament cannot be made to collapse radially under self-gravity. Therefore, star formation in filamentary clouds must begin by the filament fragmenting along the axis of symmetry. These fragments might eventually form spheroidal, self-gravitating clumps and cores, which would be subject to the magnetic analogue of the Bonnor-Ebert instability. We demonstrated that toroidal fields tend to decrease the magnetic critical mass by $\sim 20\%$ in our models, which is opposite to the effect of the poloidal field.

Some cores might eventually become Bonnor-Ebert unstable and collapse to form stars. This might be driven by ambipolar diffusion, as in models that include only poloidal fields. However, ambipolar diffusion might work somewhat differently in our models, as we discussed in Section 5.7.3. An important point is that toroidal fields result in an overall compression of cores, so that the loss of the toroidal field cannot, by itself, trigger collapse. Rather, the weakening of the poloidal field by ambipolar diffusion

would be in direct competition with the loss of the toroidal field. Cores might become Bonnor-Ebert unstable if the poloidal field were lost more rapidly than the toroidal field. Otherwise, prolate cores would evolve toward less magnetized and more nearly spherical, Bonner-Ebert stable states. If this were to happen, cores would probably remain stable against collapse, unless one of two events were to occur. A core in a stable state could become unstable by accreting more mass from the surrounding cloud material. Alternatively, a torsional Alfvén wave could effectively decrease the magnetic analogue of the Bonnor-Ebert critical mass, thus inducing collapse (Habe et al. 1991).

In conclusion, we emphasize that this thesis provides a self-consistent and highly testable model for filamentary molecular clouds and their prolate cores. We are hopeful that sufficient observational data will soon be available to thoroughly put our models to the test.

Appendix A

Computer Code

This appendix contains a listing of the essential code used to used to calculate models of filamentary clouds and prolate cores. All of the code runs under Matlab version 5.2 for unix. We do not include graphics routines or some of the routines that were used for analysis after the solutions were found. Also, the driver programs SIMPLEFILAMENT.m and SIMPLECORE.m have been substantially modified to provide a simpler interface to the user, compared to the version that we actually used in Chapters 3 and 6 to explore the parameter space of our models.

We do not include a listing of the code used in Chapter 4 to analyze the stability of our models, since the finite difference method used was absolutely standard and discussed thoroughly in many books (See Press et al. (1986) for example, or Nakamura (1991)). The program is also very lengthy due the the complex equations that are solved.

Any code used in this thesis is available by contacting the author. (This, of course, does not include any proprietary Matlab software owned by The MathWorks.)

A.1 Prolate Cores - Numerical Considerations

We briefly discuss our code for computing core models, since this was by far the most elaborate code written for for the purpose of this thesis.

A number of numerical difficulties were overcome in the development of the code used in Chapter 6 to compute the equilibrium structure of magnetized prolate cores. The purpose of this chapter is to briefly discuss our version of the self-consistent field method (SCFM), with particular attention to some the difficulties that were encountered and overcome. The program SIMPLECORE.m in Section A.2 below initializes all parameters, computes an initial filament model, and calls the main program PR.m, which solves the equations.

We must ensure that a sufficient number of grid cells are within the the boundaries of the core, while also ensuring that that the grid extends far enough out that the boundary conditions at infinity are satisfied adequately. This problem of dynamic range can be satisfied by a non-linear grid, but it is simpler to use the coordinate transformations given by equations 6.36 and work in the coordinates ξ and η. We note that a similar transformation was used in Chapter 4 in our stability analysis of filamentary clouds. The scale factors S_r and S_z are dynamically optimized by the code to ensure that $\sim 1/3 - 2/3$ of the grid cells fall within the core. Specifically, we require

$$\begin{aligned} 0.6 \times \pi/2 \leq \xi_{max} \leq 0.8 \times \pi/2 \\ 0.6 \times \pi/2 \leq \eta_{max} \leq 0.8 \times \pi/2 \end{aligned} \tag{A.1}$$

where ξ_{max} and η_{max} are the extreme values of ξ and η on the surface of the core. (Note that ξ and η have maximum values of $\pi/2$ on our grid.)

A notable difference between our method and that of Mouschovias (1976) or TIN is that we work with the "modified" vector potential A, given by equation 6.31 rather than the true vector potential A_ϕ. We noted in Chapter 6 that both A and A_ϕ obey the same partial differential equation (equation 6.8) but that A vanishes on the outer radial boundary, while $A_\phi \propto r$. Note that a very large radius is contained within a few radial grid cells near the outer grid boundary because of our transformation to (ξ, η) coordinates. We found it easier to work with A since the accuracy of the finite differencing is poor when r is very large, which makes non-vanishing boundary conditions difficult to satisfy. No difficulties are encountered when A is used instead of A_ϕ.

The most significant difficulty encountered involves the relatively poor convergence and the numerical stability of the self-consistent field method, particularly when a significant toroidal field is present. We found it necessary to under-relax $\rho(r,z)$, $P(r,z)$, $A(r,z)$, $\Psi(r,z)$, and $Q(\Phi)$ between successive iterations. This means that instead of directly using the updated values of these quantities in the next iteration, we "blend" the new values with the values of the previous iteration:

$$f(r,z) = W f_{new} + (1 - W) f_{old} \tag{A.2}$$

for example, where f is to be replaced with any of the quantities given above, and W is the under-relaxation parameter. We found it necessary to make W as low as ~ 0.25 for numerical stability in some cases, which seriously degrades the convergence of the method.

We took two important steps to improve the convergence. First of all, we adjusted W dynamically between iterations to optimize the convergence. When our solution is allowed to relax too quickly, oscillatory behaviour results, which is analogous to an under-damped mechanical system. Therefore, the

program (PR.m) monitors the converging sollution for signs of oscillation, decreasing the under-relaxation parameter for the oscilating variable if any are detected. Secondly, we found that the numerical instabilities are worst in the outer most pressure dominated regions of the core, while the central gravitationally dominated regions are usually more stable. This motivated us to use a non-constant under-relaxation parameter $W(r,z)$ for each quantity so the central regions were allowed to converge more rapidly than the edges. Using these techniques, solutions were sometimes found to converge to 10^{-5} accuracy (ie. maximum step-step drift in the density) within ~ 100 iterations, although $\sim 200-250$ was typical.

The function $Q(\Phi)$ is defined by the integral given in equation 6.15. Normally, we obtain Q_i for ~ 50 discrete values of Φ_i and interpolate to obtain any value of Q between the Φ_i. However, it is actually the first derivative of $Q(\Phi)$ with respect to Φ that enters as a source term into equation 6.8 for the vector potential A. There is always some numerical "noise" in $Q(\Phi)$, particularly during the first few iterations, which makes straightforward finite differencing inadequate. We fit a relatively low order Chebyshev polynomial to $Q(\Phi)$, which acts as a low pass filter to slightly smooth the function. Moreover, the derivative $dQ/d\Phi$ is a smooth function that can be obtained analytically from the Chebyshev series approximation (See Press et al. 1986). Since $Q(\Phi)$ is generally quite a featureless function, we find that 12th to 16th order Chebyshev polynomials provide adequate smoothing without loss of accuracy.

A further numerical difficulty is encountered when calculating $Q(\Phi)$ near the last field line, which encloses the total flux threading the core Φ_{cl} and just touches the radial edge of the core. It becomes increasingly difficult to calculate $Q(\Phi)$ by equation 6.15 because both the numerator and denominator vanish when $\Phi = \Phi_{cl}$. The numerator vanishes because $\Phi \to \Phi_{cl}$ as $r \to R_s$ within the parent filament. The denominator vanishes because the last field line threading the core intersects the core surface at a single point in the midplane, driving the integral in equation 6.15 to zero. The solution to this problem is straightforward. The pressure P within the core becomes equal to P_s at the surface, which allows us to obtain a limit for Q:

$$Q(\Phi_{cl}) = P_s e^{\Psi_0/\sigma^2}, \tag{A.3}$$

where Ψ_0 is the gravitational potential at the point where the last field line crosses the midplane. Our procedure is to calculate $Q(\Phi)$ using equation 6.15 for $N-s$ equally spaced field lines within the core, where N is the total number of field line (typically ~ 50) and $s \approx 2-4$. (s is the variable called "STANDOFF" in program PR.m) The value of Q for the last (N*th*) field line is calculated by equation A.3, and the Chebyshev interpolation described above ensures that the remaining values of Q_i (Q_{N-s+1} to Q_{N-1}) are interpolated smoothly. We note that this region where Q_i must be interpolated involves only a very thin annulus passing near the radial edge of the core, since flux surfaces that are equally spaced in Φ become very closely spaced in radius near the surface.

A.2 Code Listings

```
% ************************************************************************
% ************************************************************************
% SIMPLEFILAMENT.m - A SIMPLE DRIVER PROGRAM FOR CALCULATING FILAMENT MODELS
% ************************************************************************
% ************************************************************************
%
global EOS Gphi Gz A ds S Y;

% ========================================================================
% FILAMENT PARAMETERS
%
Gz=10;
Gphi=10;
C=1;
EOS='isothermal';
%EOS='logatrope'; A=0.2;
%
% ========================================================================
%
RMIN=1e-5; s0=log(RMIN);
RMAX=10^C; send=log(RMAX);
%
% NUMBER OF POINTS AND STEPSIZE
N=500;
ds=(send-s0)/(N-1);
%
% TOLERANCE
tol=1e-8;
%
% ========================================================================
%
% CALL MAIN PROGRAM
%
CYLBASIC;


% ************************************************************************
% ************************************************************************
% SIMPLECORE.m - A SIMPLE DRIVER PROGRAM
% TO RUN PR.m (TO MAKE PROLATE CORE MODELS.)
% ************************************************************************
% ************************************************************************
%
clear all;
```

```
global XIg ETAg RHO PAR;
%
% ========================================================================
%
% GLOBAL PARAMETERS
%
global XIg ETAg APHISOURCE PAR;
global ds S Y;
global EOS Gphi Gz A gamma;
global BO RO CONST PHICL;
%
% ========================================================================
% GRID SIZE
%
l=7; Nr=2^l+1;
l=7; Nz=2^l+1;
rmin=1e-3; rmax=1e2;
zmin=0;
NFL=60;
%
% ========================================================================
% OTHER COMPUTATIONAL PARAMETERS -
% NORMALLY DO NOT CHANGE.
%
STANDOFF=4; SMOOTHSURFACE=0;
dPfac=0.001; dPHIRHOfac=0.001; dPHIPfac=0.5;
verbose=0; method='linear';
AXIS=[0 8 0 8];

MAXIT=750; TOL=1e-5;
KillCurrentReversals=1;
AllowBreaks=0;
RejectLowMass=1;
periodic=0;
Srmax=5; Szmax=10;
%
% ========================================================================
% FILAMENT PAPRAMETERS.
%
Gz=10;
Gphi=10;
C=0.5; RO=10^C;
%
% ========================================================================
% CORE MASS - RELATIVE TO BONNOR-EBERT MASS
%
MASSFRAC=0.5;
```

```
%
% ============================================================================
% SCALE FACTORS AND GRID SIZE
%
Sr=4;
Sz=6;
lambda=200; zmax=lambda/2;
%
% ============================================================================
% THESE PARAMETERS ARE FIXED - DO NOT CHANGE
SIGMA=1;
PSFACTOR=1;
FixedMass=0;
%
% ============================================================================
% UNDER-RELAXATION PARAMETERS
%
ORPSI=0.4;
ORAPHI=0.25;
ORRHO=0.4;
ORP=0.4;
ORQ=0.25;
ORB=0.25;
W_edge=0.2;
%
% ============================================================================
%
% MAKE EQUILIBRIUM....
%
PR;


% ****************************************************************************
% ****************************************************************************
% PR.m - MAIN PROGRAM FOR MAKING PROLATE CORES
% ****************************************************************************
% ****************************************************************************
% START BY MAKING INITIAL FILAMENT MODEL
%
RMIN=1e-4; s0=log(RMIN);
RMAX=10^C; send=log(RMAX);
tol=10^(-8);
EOS='isothermal'; % ONLY ISOTHERMAL EOS HERE!
N=200; R=[]; ML=[]; P=[];
ds=(send-s0)/(N-1);
CYLBASIC;
MLint=2*pi*R.*RHO.*R; mstar=d01gaf(S,MLint)
```

```
Rs=R(end); Ps=PSFACTOR*P(end);

send=log(RO-1e-10);
N=1000; ds=(send-s0)/(N-1);
R=[]; ML=[]; P=[];
CYLBASIC;
%
% ============================================================================
% CALCULATE MASS/LENGTH
%
MLint=2*pi*R.*RHO.*R;
ML=[];
for i=4:length(S);
   S1=S(1:i);
   MLint1=MLint(1:i);
   [ML(i),er,ifail] = d01gaf(S1,MLint1);
end;

index=find(ML>0);
S=S(index); R=R(index); ML=ML(index); RHO=RHO(index);
MLcore=ML(end);
%
% ============================================================================
% CALCULATE FLUX THREADING CORE (PHICL), AND TOTAL FLUX THROUGH
GRID (PHIINF) % Phi=Gz*ML/2/pi;
PHICL=Gz*MLcore/2/pi;
PHIINF=Gz*(mstar+pi*(rmax^2-Rs^2)*Ps/SIGMA^2)/2/pi;
X=Phi/PHICL;
Zint=sqrt(1-R.^2/RO^2);
%
% THIS IS JUST IN CASE NUMERICAL NOISE RESULTS IN PHI NOT BEING MONOTONIC.
% WOULD MESS UP INTERPOLATIONS LATER.
index=find(diff(X)>0); X=X(index); Zint=Zint(index); R=R(index); RHO=RHO(index);

% THE BONNER-EBERT MASS IN MY UNITS...
G=1/4/pi; Mbe=1.18*SIGMA^4/G^1.5*Ps^-.5;
if ~FixedMass;
   MASS=MASSFRAC*Mbe;
end;

% NOW CALCULATE THE MAXIMUM Z FOR AN ELLIPSOIDAL FRAGMENT.
ZO=Gz*MASS/4/pi/PHICL/d01gaf(X,Zint);

% ABORT IF ZO>ZMAX=LAMBDA/2 (IE. INITIAL FRAGMENT IS OFF THE GRID).
OUTRANGE=0;
if RO>10^C | ZO>lambda/2;
   disp('ERROR - OUT OF RANGE!');
```

```
   OUTRANGE=1;
   break;
end;

% ============================================================================
% DO NOT PROCEED IF OUT OF RANGE!
%
if ~OUTRANGE;

% NOW CALCULATE MASS/FLUX FUNCTION MPRIME0, AND TOROIDAL FIELD FUNCTION b0=b_\phi.
Z=Z0*sqrt(1-R.^2/R0^2);
Mprime0=4*pi/Gz*Z;

index=find(Mprime0<0); Mprime0(index)=0;
X=X(4:end); Mprime0=Mprime0(4:end);
index=find(diff(X)>0)+1;
X=X(index); Mprime0=Mprime0(index); R=R(index); RHO=RHO(index); RHOc=RHO(1);

b0=Gphi*R.^2.*RHO;

% USE CHEBYSHEV POLYNOMIALS TO SLIGHTLY SMOOTH AND DIFFERENTIATE b0.
[b0,DB0]=CHEBYFIT(X,b0,X,8); DB0=DB0/PHICL; DB0=2*b0.*DB0;
eps=1e-10; X2=[X,X(end)+eps 1e6*PHIINF]; b0=[b0,b0(end),b0(end)]; DB0=[DB0,0 0];
%
% ============================================================================
%
MASS=PHICL*d01gaf(X,Mprime0);
PHI0min=0.1*PHICL/NFL;
dP=dPfac*Ps; dPHIRHO=dPHIRHOfac*PHICL;
%
% ============================================================================
% DEFINE (XI,ETA) COODINATES.
%
XImin=atan(rmin/Sr); XImax=atan(rmax/Sr); dXI=(XImax-XImin)/(Nr-1);
ETAmin=atan(zmin/Sz); ETAmax=atan(zmax/Sz); dETA=(ETAmax-ETAmin)/(Nz-1);

XI=XImin:dXI:XImax;
ETA=ETAmin:dETA:ETAmax;
R=Sr*tan(XI);
Z=Sz*tan(ETA);
% OTHER USEFUL FUNCTIONS - USED IN FINITE DIFFERENCING EQ'S
CR=cos(XI).^2/Sr; CR2=-2*sin(XI).*cos(XI).^3/Sr^2;
CZ=cos(ETA).^2/Sz; CZ2=-2*sin(ETA).*cos(ETA).^3/Sz^2;
%
% ============================================================================
% INITIAL GUESS... ARBITRARY, BUT THIS CHOICE WORKS WELL...
%
```

```
[Rg,Zg]=meshgrid(R,Z);
[XIg,ETAg]=meshgrid(XI,ETA);
ONE=ones(Nz,Nr);
RHO0=1.5/SIGMA^2*max(RHOc,Ps/SIGMA^2); P0=SIGMA^2*RHO0;
ROP=RO/sqrt(log(P0/Ps)); P=P0*(exp(-(Rg.^2+Zg.^2)/ROP^2) );
RHO=P; index=find(P<Ps);
RHO(index)=0;
CONST=Gz/2/pi/rmax^2*(mstar+pi*(rmax^2-Rs^2)*Ps/SIGMA^2);
BO=min(3,Gz*RHOc);
ROB=fzero('func',ROP); if isnan(ROB); ROB=ROP; end;
fac=1.1; A2=BO*ROB^2/2*(1-exp(-Rg.^2/ROB^2))./Rg; A2=A2*fac;

dPHIO=(PHICL-PHIOmin)/(NFL-1);
PHIO=[0, PHIOmin:dPHIO:PHICL];
%
% ============================================================================
% THESE ARE THE ''OSCILLATION PARAMETERS.'' THEY WATCH THE SOLUTION FOR
% OSCILLATIONS AND ADJUST THE UNDER-RELAXATION PARAMETERS OR* ACCORDINGLY.
%
converge=0; it=1; OSC=[0,0,0]; OSCEDGE=[0,0,0]; OSCA=[0,0,0];
OSCQ1=[0,0,0]; OSCQ2=[0,0,0]; OSCQ3=[0,0,0]; OSCQ4=[0,0,0];
NOSC=0; NNOOSC=0; NEDGEOSC=0; NNOEDGEOSC=0; NAOSC=0; NNOAOSC=0; NQOSC=0; NNOQOSC=0;
FREEZErelerr=0;

IFAIL=0; INCREASABLE=1; lastaverelerr=1e6; relerr=1; relerrvec=[]; NFRtotal=0;
while converge==0 & it<MAXIT;

dPHIP=dPHIPfac*PHICL;
oraphi=ORAPHI; orpsi=ORPSI;
%
% ============================================================================
% OCCASIONALLY FIELD REVERSALS OCCUR AT INTERMEDIATE STEPS SO THAT PHI
% IS NOT MONOTONIC. PROGRAM TRIES TO BACK OUT OF THESE SITUATIONS,
% SINCE IT CAN'T INTERPOLATE OVER A NON-MONOTONIC PHI.
%
FieldReversal=1; NFR=0;
while FieldReversal==1;

   PAR=[Sr Sz XImin XImax ETAmin ETAmax dXI dETA RO ZO MASS];

   if ~isreal(RHO) | ~isempty(find(isnan(RHO)));
      IFAIL=1; disp('FAIL POINT 1'); converge=0; break;
   end;
   % FINITE DIFFERENCE LAPLACIAN OPERATOR.
   [D,rhs]=LAPFAST(Nr,Nz,dXI,dETA);
   % JUST WORKSPACE FOR EQUATION SOLVER...
   WORKlength=(round(length(D/2)));
```

```
WORKSPACE1=zeros(WORKlength,7);
WORKSPACE2=zeros(WORKlength,1);
ub=zeros(Nr*Nz,1); tol=1e-7; maxit=1000;
% SOLVE POISSON'S EQUATION - THIS IS FROM THE NAG LIBRARY.
[a,rhs2,us,u,numit,ub,ifail] = d03edf(Nr,Nz,[D;WORKSPACE1],...
   [rhs;WORKSPACE2],ub,maxit,tol);

% NOW STORE TO GRID...
PSInew=[];
for I=1:Nr;
for J=1:Nz;
   PSInew(J,I)=u(I+(J-1)*Nr);
end;
end;
PSInew=PSInew-PSInew(1,1);

% UNDER-RELAX PSI
if it>1;
   PSI2=(1-orpsi*WEIGHT).*PSI2+orpsi*WEIGHT.*PSInew;
else;
   PSI2=PSInew;
end;

% BACK OUT IF PSI CONTAINS A NAN OR BLEW UP.
if it>1;
if ~isempty(find(isnan(PSInew))) | max(max(abs(PSInew)))>=10*max(max(abs(PSI)));
   PSI2=PSI;
end;
end;

% NOW I CAN GET THE DENSITY, PRESSURE, ETC. - UNDER-RELAX
% THESE USING THEIR OR* PARAMETERS.
if it>1;
   Pnew=Q.*exp(-PSI/SIGMA^2);
   RHOnew=Pnew/SIGMA^2; RHOuntrunc=RHOnew;
   RHOc=RHOnew(1,1); alpha=-log(W_edge)/log(RHOc*SIGMA^2/Ps);
   if alpha<0; alpha=1; end;
   % WEIGHT FUNCTION FOR NON-UNIFORM UNDER-RELAXATION.
   % HELPS WITH CONVERGENCE.
   WEIGHT=max(W_edge,(RHOnew/RHOc).^alpha);
   RHO=ORRHO*WEIGHT.*RHOnew+(1-ORRHO*WEIGHT).*RHOuntrunc;
   P=ORP*WEIGHT.*Pnew+(1-ORP*WEIGHT).*P;
else;
   RHOc=RHO(1,1); alpha=-log(W_edge)/log(RHOc*SIGMA^2/Ps);
   if alpha<0; alpha=1; end; WEIGHT=max(W_edge,(RHO/RHOc).^alpha);
   RHOuntrunc=RHO; P=RHO;
end;
```

```
   % VERY SLIGHT 5 POINT SMOOTHING...
   P(2:Nz-1,2:Nr-1)=0.5*P(2:Nz-1,2:Nr-1)+0.125*(P(1:Nz-2,2:Nr-1)+...
   P(3:Nz,2:Nr-1)+P(2:Nz-1,1:Nr-2)+P(2:Nz-1,3:Nr));
   P(1,2:Nr-1)=0.5*P(1,2:Nr-1)+0.25*(P(1,1:Nr-2)+P(1,3:Nr));
   P(Nz,2:Nr-1)=0.5*P(Nz,2:Nr-1)+0.25*(P(Nz,1:Nr-2)+P(Nz,3:Nr));
   P(2:Nz-1,1)=0.5*P(2:Nz-1,1)+0.25*(P(1:Nz-2,1)+P(3:Nz,1));
   P(2:Nz-1,Nr)=0.5*P(2:Nz-1,Nr)+0.25*(P(1:Nz-2,Nr)+P(3:Nz,Nr));
   P(:,1)=P(:,2);

   if it>1;

      % THE SOURCE FUNCTION FOR THE VECTOR POTENTIAL.
      APHISOURCE=-4*pi*Rg.*DQ.*exp(-PSI2/SIGMA^2)-DB./2./Rg;
      APHISOURCE(:,1)=0;
% ========================================================================

      % VERY SLIGHT 5 POINT SMOOTHING...
      APHISOURCE(2:Nz-1,2:Nr-1)=0.5*APHISOURCE(2:Nz-1,2:Nr-1)+...
         0.125*(APHISOURCE(1:Nz-2,2:Nr-1)+APHISOURCE(3:Nz,2:Nr-1)+...
         APHISOURCE(2:Nz-1,1:Nr-2)+APHISOURCE(2:Nz-1,3:Nr));
      APHISOURCE(1,2:Nr-1)=0.5*APHISOURCE(1,2:Nr-1)+0.25*(APHISOURCE(1,1:Nr-2)+...
         APHISOURCE(1,3:Nr));
      APHISOURCE(Nz,2:Nr-1)=0.5*APHISOURCE(Nz,2:Nr-1)+...
         0.25*(APHISOURCE(Nz,1:Nr-2)+APHISOURCE(Nz,3:Nr));
      APHISOURCE(2:Nz-1,1)=0.5*APHISOURCE(2:Nz-1,1)+0.25*(APHISOURCE(1:Nz-2,1)+...
         APHISOURCE(3:Nz,1));
      APHISOURCE(2:Nz-1,Nr)=0.5*APHISOURCE(2:Nz-1,Nr)+...
         0.25*(APHISOURCE(1:Nz-2,Nr)+APHISOURCE(3:Nz,Nr));

      % BACK OUT IF APHISOURCE HAS A NAN.
      if ~isreal(APHISOURCE) | ~isempty(find(isnan(APHISOURCE)));
         IFAIL=1; disp('FAIL POINT 2'); converge=0;  break;
      end;
      % FINITE DIFFERENCE DELTA1 OPERATOR.
      [D,rhs]=DELTA1FAST(Nr,Nz,dXI,dETA);
      % SOME WORKSPACE FOR SOLVER.
      WORKlength=(round(length(D/2)));
      WORKSPACE1=zeros(WORKlength,7);
      WORKSPACE2=zeros(WORKlength,1);
      ub=zeros(Nr*Nz,1); tol=1e-6; maxit=1000;
      % SOLVE FOR THE VECTOR POTENTIAL.
      [a,rhs2,us,u,numit,ub,ifail]=...
         d03edf(Nr,Nz,[D;WORKSPACE1],[rhs;WORKSPACE2],ub,maxit,tol);

      % PUT APHI ON THE GRID.
      Anew=[];
```

```
   for I=1:Nr;
   for J=1:Nz;
      Anew(J,I)=u(I+(J-1)*Nr);
   end;
   end;

   % UNDER-RELAX.
   if it>0;
      A2=(1-oraphi*WEIGHT).*A+oraphi*WEIGHT.*Anew;
   else;
      A2=Anew;
   end;
   if it>1
   if ~isempty(find(isnan(A2)))
      A2=A;
   end
   end;

   % SLIGHT 5-POINT SMOOTHING.
   A2(2:Nz-1,2:Nr-1)=0.5*A2(2:Nz-1,2:Nr-1)+0.125*(A2(1:Nz-2,2:Nr-1)+...
      A2(3:Nz,2:Nr-1)+A2(2:Nz-1,1:Nr-2)+A2(2:Nz-1,3:Nr));
   A2(1,2:Nr-1)=0.5*A2(1,2:Nr-1)+0.25*(A2(1,1:Nr-2)+A2(1,3:Nr));
   A2(Nz,2:Nr-1)=0.5*A2(Nz,2:Nr-1)+0.25*(A2(Nz,1:Nr-2)+A2(Nz,3:Nr));
   A2(2:Nz-1,1)=0.5*A2(2:Nz-1,1)+0.25*(A2(1:Nz-2,1)+A2(3:Nz,1));
   A2(2:Nz-1,Nr)=0.5*A2(2:Nz-1,Nr)+0.25*(A2(1:Nz-2,Nr)+A2(3:Nz,Nr));

   A2(:,1)=A2(:,2).*Rg(:,1)./Rg(:,2);

   CONST=Gz/2/pi/rmax^2*(mstar+pi*(rmax^2-Rs^2)*Ps/SIGMA^2);
end;

% THIS IS THE REAL VECTOR POTENTIAL -
% SEE PAPER FOR DIFFERENCE BETWEEN A AND APHI.
Aphi2=A2+CONST*Rg; PHI2=Rg.*Aphi2;
index=find(PHI2<0 & abs(PHI2)<1e-2); PHI2(index)=0;

% Make Field - Convert to derivatives wrt XI and ETA later...
% CALCULATE POLOIDAL MAGNETIC FIELD - NEED GRADIENTS.
[DR,dummy]=gradient(XIg); DR=DR.*(Sr*sec(XIg).^2);
[dummy,DZ]=gradient(ETAg); DZ=DZ.*(Sz*sec(ETAg).^2);

[DrA,DzA]=gradient(A2);
DrA=DrA./DR; DzA=DzA./DZ;
BR=-DzA; ONE=ones(Nz,Nr); BZ=A2./Rg+DrA+2*CONST*ONE;
BMAG=sqrt(BR.^2+BZ.^2);
% A UNIT FIELD LINE VECTOR.
BRNORM=BR./BMAG; BZNORM=BZ./BMAG;
```

```
   % CHECK FOR FIELD REVERSALS.
   index=find(P>Ps);
   BZmin=min(min(BZ(index))); PHImin=min(min(PHI2(index)));
   PHI2=PHI2(1,:);  monotonic=isempty(find(diff(PHI2)<=0));
   if BZmin>0 & PHImin>0 & monotonic & isreal(A2);
      FieldReversal=0;
   else;
      oraphi=oraphi/5;
      orpsi=orpsi/5;
      disp(['Field Reversal']);
      NFR=NFR+1; NFRtotal=NFRtotal+1;
      if NFR>=10; IFAIL=1; disp('FAIL POINT 3'); break; end;
   end;
% End (If Field Reversal) While
end;

% ABORT IF IFAIL...
if IFAIL; break; end;

A=A2; Aphi=A+CONST*Rg; PHI=Rg.*Aphi;
PSI=PSI2;

if it<5;
   % If initial radius was too small, allow initial guess (Rinit) to be increased.
   % GIVES PROGRAM A SECOND CHANCE IF A PROBLEM OCCURED IN FIRST FEW ITERATIONS.

   XICLmin=interp1(PHI(1,:),XIg(1,:),PHICL);
   while max(max(XIg( find(P>Ps) )))<XICLmin;
      ROP=ROP*2;
      P=P0*(exp(-(Rg.^2+Zg.^2)/ROP^2) ); RHO=P;

      index=find(P<Ps);
      RHO(index)=0;

      % Of course, the gravitational potential must then be re-calculated.
      [D,rhs]=LAPFAST(Nr,Nz,dXI,dETA);
      WORKlength=(round(length(D/2)));
      WORKSPACE1=zeros(WORKlength,7);
      WORKSPACE2=zeros(WORKlength,1);
      ub=zeros(Nr*Nz,1); tol=1e-6; maxit=1000;
      [a,rhs2,us,u,numit,ub,ifail] =...
      d03edf(Nr,Nz,[D;WORKSPACE1],[rhs;WORKSPACE2],ub,maxit,tol);
      PSI=[];
      for I=1:Nr;
      for J=1:Nz;
         PSI(J,I)=u(I+(J-1)*Nr);
```

```
      end;
      end;
      PSI=PSI-PSI(1,1);

   end;
end;

% ============================================================================
% Ensure correct behaviour on symmetry axis.
% THIS IS A LITTLE HEAVY-HANDED BUT IT HELPS...
%
BZ(:,1)=BZ(:,3); BZ(:,2)=BZ(:,3);
BR(:,1)=0*BR(:,1);
% ============================================================================
%
% Columns correspond to R, rows to Z.
PHI2=PHI(1,:);

% ============================================================================
% ACCURATELY LOCATE THE SURFACE OF THE CORE BY THE P=PS CONTOUR.
%
SURFACE=contourc(XI,ETA,P,[Ps Ps]);
IFAIL=1;
XISmin=Inf;
%
% THIS IS JUST IN CASE AN EARLY STEP PRODUCES MORE THAN ONE
% P=PS CLOSED CONTOURS - RARELY HAPPENS, BUT TAKE THE ONE CLOSEST TO THE
% ORIGIN IF IT DOES.
while ~isempty(SURFACE);
   pairs=SURFACE(2,1);
   XIS1=SURFACE(1,2:pairs+1);
   ETAS1=SURFACE(2,2:pairs+1);
   if min(XIS1)<XISmin & min(ETAS1)<0.1;
      XIS=XIS1;
      ETAS=SURFACE(2,2:pairs+1);
      XISmin=min(XIS);
      IFAIL=0;
   end;
   SURFACE=SURFACE(:,pairs+2:end);
end;
% ABORT IF SURFACE COULD NOT BE FOUND.
if IFAIL; disp('FAIL POINT 4'); end;

% PUT IT IN THE ''RIGHT'' ORDER...
if XIS(1)>XIS(end); XIS=fliplr(XIS); ETAS=fliplr(ETAS); end;
if XIS(1)>0 & ETAS(1)~=ETAmax; XIS=[0,XIS]; ETAS=[ETAS(1),ETAS]; end;
```

```
% ========================================================================
%
% THIS IS WHERE WE DO THE FIELD LINE INTEGRATIONS - THE MOST COMPLICATED PART OF
% THE PROGAM.  STANDOFF CONTROLS THE FLUX LEVEL OF THE LAST FIELD LINE NEAR THE
% EDGE OF THE CORE.  NOTE THAT WE CAN'T GO ALL THE WAY TO THE EDGE.
% THE INTEGRAL DEFINING Q IS UNDEFINED THERE.
%
% MAKE FLUX CONTOURS - THESE ARE THE SAME AS FIELD LINES (AND FASTER TO GENERATE
% THAN INTEGRATING)
%
CC=contourc(XI,ETA,PHI,PHI0(2:end-STANDOFF));
PHIfl=[]; IQ=[]; PSI0fl=[]; XI0fl=[]; IsOpen=[];
NFLPT=100; ANYOPEN=0;
while ~isempty(CC);
   pairs=CC(2,1);
   % SURFACE IS GIVEN PARAMETRICALLY BY (XIfl,ETAfl)
   XIfl=CC(1,2:pairs+1);
   ETAfl=CC(2,2:pairs+1);
   [ETAfl,index]=sort(ETAfl);
   XIfl=XIfl(index);
   % NOTE THAT FIELD LINES CAN BE OPEN, SINCE OUR GRID IS PERIODIC
   % (WITH A VERY LONG WAVELENGTH) - NO PROBLEM.
   if max(ETAS)==ETAmax & XIfl(end)<min(XIS);
      OPEN=1; ANYOPEN=1; INTERSECT=0;
   else
      OPEN=0;
   end;
   % CHECK THAT FIELD LINE DOESN'T ''DOUBLE BACK''.
   monotonic=isempty(find(diff(ETAfl)<=0));
   if max(XIfl(end))>=min(XIS) & ~OPEN & monotonic;  % Find the cloud surface.
      q=diff(diff(XIS)>0); endpts=1+find(q~=0); endpts=[1,endpts,length(XIS)];
      for region=1:length(endpts)-1;
         index=endpts(region):endpts(region+1);
         index2=find(XIfl>min(XIS(index)) & XIfl<max(XIS(index)));
         ETAS2=interp1(XIS(index),ETAS(index),XIfl(index2),'linear');
         ZERO=ETAfl(index2)-ETAS2;
         if min(ZERO)<=0 & max(ZERO)>=0; break; end;
      end;
      ETAfl2=ETAfl(index2); XIfl2=XIfl(index2);
      if min(ZERO)<0 & max(ZERO)>0;
         q=diff(diff(ZERO)>0); endpts=1+find(q~=0); endpts=[1,endpts,length(ZERO)];
         for region=1:length(endpts)-1;
            index=endpts(region):endpts(region+1);
            if min(ZERO(index))<=0 & max(ZERO(index))>=0;
               break;
            end;
         end;
```

```
         % INTERPOLATE TO FIND SURFACE.
         ETAs=interp1(ZERO(index),ETAfl2(index),0);
         XIs=interp1(ETAfl(index2),XIfl(index2),ETAs);
         index=find(ETAfl<=ETAs); ETAfl=ETAfl(index); XIfl=XIfl(index);
         XIfl=[XIfl(index),XIs];
         ETAfl=[ETAfl(index),ETAs];
         INTERSECT=1;
      else;
         INTERSECT=0;
      end;
   end;
   % IF EVERYTHING IS OK WITH THIS FIELDLINE...
   if (INTERSECT | OPEN) & monotonic;
      if length(ETAfl)>=4;
         PSIfl=interp2(XIg,ETAg,PSI,XIfl,ETAfl);
         BZfl=interp2(XIg,ETAg,BZ,XIfl,ETAfl);

         IQint=exp(-PSIfl/SIGMA^2)./BZfl.*Sz.*sec(ETAfl).^2;
         Rfl=Sr*tan(XIfl);

         PHIfl=[PHIfl,CC(1,1)];
         PSIOfl=[PSIOfl,PSIfl(end)];
         XIOfl=[XIOfl,XIfl(1)];
         % PERFORM FIELDLINE INTEGRAL REQ'D FOR Q.
         IQ=[IQ,dO1gaf(ETAfl,IQint)];
         if OPEN; IsOpen=[IsOpen,1]; else; IsOpen=[IsOpen,0]; end;
      end;
   end;
   CC=CC(:,pairs+2:end);
end;
if length(PHIfl)<5; IFAIL=1; disp('FAIL POINT 5'); break; end;
lastfl=find(PHIO==PHIfl(end));
PSI1=interp1(PHIfl,PSIOfl,PHICL);

x=PHIfl/PHICL;
Mprime=interp1(X,MprimeO,x);
%
% NOW WE'VE GOT THE Q(PHI) FUNCTION...
QOnew=SIGMA^2*Mprime./(4*pi)./IQ;
%
% ========================================================================
%
% TWIDDLE THE SOLUTION A LITTLE (EXTEND, SMOOTH, ETC.)
%
if it>5;
% Reject any obviously bad points.
dq=diff(QOnew);
```

```
[dq,position]=sort(dq); position=position+1;
index=find(abs(dq)<min(10,50*mean(abs(dq))));
position=sort([1,position(index)]);
PHIfl=PHIfl(position);
QOnew=QOnew(position);
IsOpen=IsOpen(position);
end;

if length(PHIfl)<5; IFAIL=1; disp('FAIL POINT 5.5'); break; end;

% EXTEND Q BACK TO ORIGIN - VERY SLIGHT EXTRAPOLATION.
slope=(QOnew(2)-QOnew(1))/(PHIfl(2)-PHIfl(1));
QO1=max(0, QOnew(1)+slope*(0-PHIfl(1)) );

% I CAN FIND AN ANALYTIC FORM FOR Q RIGHT AT THE EDGE OF THE CORE...
% Q=QSTAR1=PS/EXP(PSISTAR).
PSIstar=interp1(PHI(1,:),PSI(1,:),PHICL);
if (it>5 | relerr<0.25); Qstar1=Ps*exp(PSIstar); else; Qstar1=QOnew(end); end;
if it==1;
   Qstarvec=Qstar1*ones(1,5);
else;
   Qstarvec=[Qstarvec(2:end),Qstar1];
end;
Qstar=mean(Qstarvec);

PHIfl=[PHIfl,PHICL];
QOnew=[QOnew,Qstar];
IsOpen=[IsOpen,0];

% SOME TRICKY BUSINESS - REFLECT Q ABOUT PHI=0.  THIS HELPS ELIMINATE EDGE
% EFFECTS IN THE CHEBYSHEV SMOOTHING AND DIFFERENTIATION BELOW.
n=min(1,length(PHIfl)); st=min(100,length(PHIfl)-n);
bigPHIfl=[0 PHIfl]; flip=-fliplr(PHIfl(1+st:n+st)); bigPHIfl=[flip,bigPHIfl];
bigQOnew=[QO1,QOnew]; flip=QOnew(1)*ones(1,n); bigQOnew=[flip,bigQOnew];

index=max(find(IsOpen==1));
if isempty(index);
   LastOpenFl=0;
else;
   LastOpenFl=find(PHIO==PHIfl(index));
   bigLastOpenFl=find(bigPHIfl==PHIfl(index));
end;

% CHEBYSHEV SMOOTHING AND DIFFERENTIATION...
ORDER=14;
if AllowBreaks & LastOpenFl>=6 & LastOpenFl<=length(PHIfl)-6;
   order=min(ORDER,round(0.5*length(bigPHIfl(1:bigLastOpenFl))));
```

```
   [Q0new1,DQ0new1]=CHEBYFIT(bigPHIfl(1:bigLastOpenFl),...
      bigQ0new(1:bigLastOpenFl),PHI0(1:LastOpenFl),order);
   order=min(ORDER,round(0.5*length(bigPHIfl(bigLastOpenFl+1:end))));
   [Q0new2,DQ0new2]=CHEBYFIT(bigPHIfl(bigLastOpenFl+1:end),...
      bigQ0new(bigLastOpenFl+1:end),PHI0(LastOpenFl+1:end),order);
   Q0new=[Q0new1,Q0new2];
   DQ0new=[DQ0new1,DQ0new2];
else;
   order=min(ORDER,round(length(bigQ0new)/2));
   [Q0new,DQ0new]=CHEBYFIT(bigPHIfl,bigQ0new,PHI0,order);
end;

% EXTEND FUNCTIONS PAST EDGE OF CORE, SO THERE'S NO TROUBLE INTERPOLATING.
% (HOW FAR WE EXTEND THINGS WON'T MATTER, SINCE WE TRUNCATE AT THE CORE
% SURFACE ANYWAYS)
%
PHI0full=[PHI0,10*PHICL];
Q02=Q0new(end);
Q0new=[Q0new,Q02]; Q0new=max(0,Q0new); % Q0new(end-1:end)=Q0new(end-2);
DQ0new=[DQ0new,DQ0new(end)];

% Set realistic limits on Q0, etc.
% JUST IN CASE...
index=find(abs(Q0new)>0); limit=20*median(abs(Q0new(index)));
index=find(abs(Q0new)>limit); Q0new(index)=sign(Q0new(index))*limit;
%
% ============================================================================
%
% Under-relax Q0.
% USE NON-UNIFORM UNDER-RELAXATION HERE TOO - HELPS...
%
if it==1;
   Q0=Q0new;
   DQ0=DQ0new;
else;
   half=round(length(Q0)/3);

   if relerr<0.1; MIN=0.25; else; MIN=0.1; end;
   dQ0=abs(Q0new)-abs(Q0); w1=1;
   wend=MIN+min(1-MIN,mean(abs(dQ0(1:half)))/max(abs(dQ0(end-5:end-1))));
   pos=(0:length(Q0)-1)/(length(Q0)-1); weight=ORQ*(w1+pos*(wend-w1));
   index=find(dQ0<0); weight(index)=min(3*weight(index),ORQ);
   Q0=weight.*Q0new+(1-weight).*Q0;

   dQ0=abs(DQ0new)-abs(DQ0); w1=1;
   wend=MIN+min(1-MIN,mean(abs(dQ0(1:half)))/max(abs(dQ0(end-5:end-1))));
   weight=ORQ*(w1+pos*(wend-w1)); index=find(dQ0<0);
```

```
   weight(index)=min(3*weight(index),ORQ);
   DQO=weight.*DQOnew+(1-weight).*DQO;

if 0;
   QO=ORQ*QOnew+(1-ORQ)*QO;
   DQO=ORQ*DQOnew+(1-ORQ)*DQO;
end;
%
% ================================================================================
%
end;

index=find(PHI>PHICL | PHI<0);
index2=find(PHI>max(PHIOfull) | PHI<0);
%
% ================================================================================
%
% INTERPOLATE FUNCTIONS OF PHI OVER GRID...
Q=reshape(interp1(PHIOfull,QO,reshape(PHI,1,Nr*Nz),method),Nz,Nr);
DQ=reshape(interp1(PHIOfull,DQO,reshape(PHI,1,Nr*Nz),method),Nz,Nr);
index=find(isnan(Q));
Q(index)=0;
DQ(index)=0;
b=reshape(interp1(X2*PHICL,bO,reshape(PHI,1,Nr*Nz),method),Nz,Nr);
BPHI=b./Rg;
DB=reshape(interp1(X2*PHICL,DBO,reshape(PHI,1,Nr*Nz),method),Nz,Nr);

% H IS LIKE A FERMI FUNCTION - BUT BETTER FOR MY PURPOSES.
% IT IS GOOD TO BLUR THE EDGE OUT A LITTLE.
%
% KILL ANY DENSITY ON BNDY AND PUT IN PRESSURE TRUNCATION.
x=(P+dP-Ps)/dP; H1=0.5+0.5*tanh(tan(0.9999*pi/2*sign(x).*min(abs(x),1)));
RHO=H1.*RHO;
x=(PHICL+dPHIP-PHI)/dPHIP;
H=0.5+0.5*tanh(tan(0.9999*pi/2*sign(x).*min(abs(x),1)));
Q=H.*Q;
x=(PHICL+dPHIRHO-PHI)/dPHIRHO;
H=0.5+0.5*tanh(tan(0.9999*pi/2*sign(x).*min(abs(x),1)));
DQ=H1.*H.*DQ;

if it<5;
   x=(atan(5/Sz)-ETAg)/0.1;
   H=0.5+0.5*tanh(tan(0.9999*pi/2*sign(x).*min(abs(x),1)));
   Q=H.*Q;
   RHO=H.*RHO;
   P=H.*P;
elseif it<15;
```

```
   x=(ETAmax-0.1-ETAg)/0.04;
   H=0.5+0.5*tanh(tan(0.9999*pi/2*sign(x).*min(abs(x),1)));
   Q=H.*Q;
   RHO=H.*RHO;
   P=H.*P;
end;
%
% ============================================================================
% THE REST IS ALL ABOUT CONTROLLING THE CONVERGENCE....
% Test for Convergence:
%
RHOc=RHO(1,1);
if it>1;
   if RHOc>Ps/SIGMA^2;
      index=find(RHO>(RHOc+Ps/SIGMA^2)/2 );
   else;
      index=find(RHO);
   end;
   if ~FREEZErelerr;
      relerr=max(max(abs( (RHO(index)-RHOlast(index))./RHO(index) )));
   else;
      FREEZErelerr=0;
   end;
   if relerr<TOL; converge=1; end;
else;
   relerr=1;
end;

OSC=[OSC(2:3),RHOc];
index=find(RHO>=Ps/SIGMA^2 & RHO<(1*RHOc+2*Ps/SIGMA^2)/3);
if ~isempty(index);
   OSCEDGE=[OSCEDGE(2:3),mean(mean(RHO(index)))];
end;

OSCA=[OSCA(2:3),A((Nr-1)/2,(Nz-1)/2)];

n=round(NFL/2.5);
OSCQ1=[OSCQ1(2:3),mean(Q0(1:n))];
OSCQ2=[OSCQ2(2:3),mean(Q0(lastfl-n+1:lastfl))];
OSCQ3=[OSCQ3(2:3),mean(DQ0(1:n))];
OSCQ4=[OSCQ4(2:3),mean(DQ0(lastfl-n+1:lastfl))];

% Test for Oscillations:
if it>5;
   Oscillating=prod(diff(OSC))<0;
   if Oscillating;
      NOSC=NOSC+1;
```

```
      NNOOSC=0;
   else;
      NOSC=0;
      NNOOSC=NNOOSC+1;
   end;

   EdgeOscillating=prod(diff(OSCEDGE))<0;
   if EdgeOscillating;
      NEDGEOSC=NEDGEOSC+1;
      NNOEDGEOSC=0;
   else;
      NEDGEOSC=0;
      NNOEDGEOSC=NNOEDGEOSC+1;
   end;

   AOscillating=prod(diff(OSCA))<0;
   if AOscillating;
      NAOSC=NAOSC+1;
      NNOAOSC=0;
   else;
      NAOSC=0;
      NNOAOSC=NNOAOSC+1;
   end;

   QOscillating=prod(diff(OSCQ1))<0 | prod(diff(OSCQ2))<0 |...
       prod(diff(OSCQ3))<0 | prod(diff(OSCQ4))<0;
   if QOscillating;
      NQOSC=NQOSC+1;
      NNOQOSC=0;
   else;
      NQOSC=0;
      NNOQOSC=NNOQOSC+1;
   end;
end;

if NOSC>=3;
   fac=0.9;
   ORPSI=fac*ORPSI;
   ORRHO=fac*ORRHO;
   ORP=fac*ORP;
   NOSC=0;
   disp(['Reducing Relaxation Parameters: ORPSI=' num2str(ORPSI)...
      'ORRHO=' num2str(ORRHO) ', ORP=' num2str(ORP)]); end;
if NEDGEOSC>=3;
   W_edge=max(0.1,0.9*W_edge);
   NEDGEOSC=0;
   disp(['Reducing W_edge to ' num2str(W_edge)]);
```

```
end;
if NAOSC>=2;
   ORAPHI=0.9*ORAPHI;
   NAOSC=0;
   disp(['Reducing ORAPHI to 'num2str(ORAPHI) ]);
end;
if NQOSC>=2;
   ORQ=0.9*ORQ;
   NQOSC=0;
   disp(['Reducing ORQ to ' num2str(ORQ)]);
end;

if it>10;
if relerr>3*relerrlast; % ie) Something catastrophic happened...
   fac=2/3;
   ORPSI=fac*ORPSI;
   ORRHO=fac*ORRHO;
   ORP=fac*ORP;
   W_edge=max(0.1,fac*W_edge);
   ORAPHI=fac*ORAPHI;
   ORQ=fac*ORQ;
   disp('Catastrophic Step! Reducing All Relaxation Parameters.');
end;
end;

if INCREASABLE;
   if NNOOSC>=5;
      fac=1.05;
      ORPSI=min(1,fac*ORPSI);
      ORRHO=min(1,fac*ORRHO);
      ORP=min(1,fac*ORP);
      NNOOSC=0;
      disp(['Increasing Relaxation Parameters: ORPSI=' num2str(ORPSI) '...
         ORRHO=' num2str(ORRHO) ', ORP=' num2str(ORP)]);
   end;
   if NNOEDGEOSC>=5;
      W_edge=min(0.5,1.05*W_edge);
      NNOEDGEOSC=0;
      disp(['Increasing W_edge to ' num2str(W_edge)]);
   end;
   if NNOAOSC>=5;
      ORAPHI=min(0.8,1.05*ORAPHI);
      NNOAOSC=0;
      disp(['Increasing ORAPHI to 'num2str(ORAPHI) ]);
   end;
   if NNOQOSC>=5;
      ORQ=min(1,1.05*ORQ);
```

```
      NNOQOSC=0;
      disp(['Increasing ORQ to ' num2str(ORQ)]);
   end;
end;
%
% ================================================================================
%
relerrlast=relerr;
RHOlast=RHO;

CALCMASS;
TEXT=['iteration: ' num2str(it) ', relerr=' num2str(relerr) ', RHO_c='...
    num2str(RHO(1,1)) ', MASS=' num2str(M) ', TRUEMASS=' num2str(MASS)];
disp(TEXT);

it=it+1;

if max(max(RHO))>50;
   converge=0;
   IFAIL=1;
   break;
end;
%
% ================================================================================
%
% IF SOLUTION GROWS TO BIG OR SHRINKS TOO SMALL IN ONE DIRECTION, ADAPT THE
% COORDINATE SYSTEM AND RE-GRID THE SOLUTIONS AS IT CONVERGES.
%
REGRID=0;
if mod(it,3)==0 & it>5 & it<=50;
   if max(ETAS)<0.6*ETAmax; Sz=0.75*Sz;
      disp(['Decreasing Sz: Sz=' num2str(Sz)]); REGRID=1;
   end;
   if ~ANYOPEN;
      if max(ETAS)>0.8*ETAmax; Sz=min(Szmax,1.25*Sz);
         disp(['Increasing Sz: Sz=' num2str(Sz)]); REGRID=1;
      end;
   end;
   if max(XIS)<.6*XImax; Sr=0.75*Sr;
      disp(['Decreasing Sr: Sr=' num2str(Sr)]); REGRID=1;
   end;
   if max(XIS)>0.8*XImax; Sr=min(Srmax,1.25*Sr);
      disp(['Increasing Sr: Sr=' num2str(Sr)]); REGRID=1;
   end;

   if REGRID;
```

```
      XImin=atan(rmin/Sr); XImax=atan(rmax/Sr); dXI=(XImax-XImin)/(Nr-1);
      ETAmin=atan(zmin/Sz); ETAmax=atan(zmax/Sz); dETA=(ETAmax-ETAmin)/(Nz-1);

      XI=XImin:dXI:XImax;
      ETA=ETAmin:dETA:ETAmax;
      R=Sr*tan(XI);
      Z=Sz*tan(ETA);
      CR=cos(XI).^2/Sr; CR2=-2*sin(XI).*cos(XI).^3/Sr^2;
      CZ=cos(ETA).^2/Sz; CZ2=-2*sin(ETA).*cos(ETA).^3/Sz^2;

      [Rg2,Zg2]=meshgrid(R,Z);
      [XIg,ETAg]=meshgrid(XI,ETA);

      disp('Re-Gridding Functions...');
      RHO=interp2(Rg,Zg,RHO,Rg2,Zg2); RHO(:,1)=RHO(:,2);
      Q=interp2(Rg,Zg,Q,Rg2,Zg2);       Q(:,1)=Q(:,2);
      DQ=interp2(Rg,Zg,DQ,Rg2,Zg2);     DQ(:,1)=0;
      DB=interp2(Rg,Zg,DB,Rg2,Zg2);     DB(:,1)=0;
      A=interp2(Rg,Zg,A,Rg2,Zg2);       A(:,1)=0;
      P=interp2(Rg,Zg,P,Rg2,Zg2);       P(:,1)=P(:,2);
      PSI=interp2(Rg,Zg,PSI,Rg2,Zg2);   PSI(:,1)=PSI(:,2);
      index=find(isnan(RHO));
      RHO(index)=0;
      Q(index)=0;
      DQ(index)=0;
      DB(index)=0;
      A(index)=0;
      P(index)=0;
      PSI(index)=0;

      Rg=Rg2; Zg=Zg2;
      clear Rg2 Zg2;

      FREEZErelerr=1;
   end;
end;
%
% ============================================================================
%
% THE STEP-STEP DRIFT FOR THE LAST 50 ITERATIONS...
relerrvec=[relerrvec,relerr];
if mod(it,50)==0;
   averelerr=mean(relerrvec);
   % ARE WE DIVERGING?
   if averelerr>5*lastaverelerr;
      IFAIL=1; disp('FAIL POINT 6');
      converge=0;
```

```
      break;
   end;
   lastaverelerr=averelerr;
   relerrvec=[];
end;

% IS SOLUTION ''GOOD ENOUGH?''
if relerr<10*TOL; GoodEnough=GoodEnough+1; else; GoodEnough=0; end;
if GoodEnough>=50; converge=1; disp('Good Enough!'); end;

% DON'T ALLOW OR* PARAMETERS TO INCREASE IF WE'RE REALLY CLOSE TO A SOLUTION ALREADY...
if relerr<5*TOL; INCREASABLE=0; else; INCREASABLE=1; end;
if RejectLowMass & ((it>30 & RHOc<1) | (it>20 & RHOc<0.666));
   disp('Central Density Is Too Low - Exiting...'); IFAIL=1; disp('FAIL POINT 7');
   break;
end;

% ABORT IF WE'VE STALLED BECAUSE OF FIELD REVERSALS...
if NFRtotal>=50; IFAIL=1; disp('FAIL POINT 8'); break; end;

% End Main Loop.
end;
%
% ==========================================================================
%
% UH-OH.....
if IFAIL;
   disp('SOLUTION HAS FAILED.')
end;

% End if ~OUTRANGE;
end;


% **************************************************************************
% **************************************************************************
% CYLBASIC.m - MAIN PROGRAM FOR MAKING FILAMENT MODELS
% **************************************************************************
% **************************************************************************
%
% VARIABLE NAMES \APPROX SAME AS IN PAPER 1
%
% ==========================================================================
%
s=s0;
Psi=exp(2*s);
g=-exp(s)/2;
```

```
y=[Psi;g];

S=[]; Y=[];
%
% ========================================================================
%
% CALL D02BBF FROM NAG LIBRARY (CALLED THROUGH MATLAB)
%
[s,y,tol,ifail] = d02bbf(s,send,y,tol,'fcn','OUTPUT');
S=[S,s]; Y=[Y,y];
%
% ========================================================================
%
% NOW GET PHYSICAL VARIABLES
%
PSI=Y(1,:);
g=Y(2,:);

R=exp(S);
RHO=PSI./R.^2; P=RHO;
BPHI=Gphi*R.*RHO;
BZ=Gz.*RHO;

% ************************************************************************
% ************************************************************************
% LAPFAST.m - FINITE DIFFERENCE LAPLACIAN OPERATOR.
% ************************************************************************
% ************************************************************************
%
function [D,rhs]=LAP(Nx,Ny,hx,hy);
global XIg ETAg RHO PAR;

Sr=PAR(1); Sz=PAR(2);
XImin=PAR(3); XImax=PAR(4);
ETAmin=PAR(5); ETAmax=PAR(6);
dXI=PAR(7); dETA=PAR(8);

Rg=Sr*tan(XIg');
Zg=Sz*tan(ETAg');
CR=cos(XIg').^2/Sr; CR2=-2*sin(XIg').*cos(XIg').^3/Sr^2;
CZ=cos(ETAg').^2/Sz; CZ2=-2*sin(ETAg').*cos(ETAg').^3/Sz^2;

ONE=ones(size(XIg')); ZERO=zeros(size(XIg'));

% DEFINE THE PDE...
ALPHA=ONE;
BETA=ZERO;
```

```
GAMMA=ONE;
DELTA=ONE./Rg;
EPSILON=ZERO;
PHI=ZERO;
PSI=RHO';

DELTA=CR.*DELTA+CR2.*ALPHA;
EPSILON=CZ.*EPSILON+CZ2.*GAMMA;
ALPHA=CR.^2.*ALPHA;
GAMMA=CZ.^2.*GAMMA;

% ==========================================================================
% BC's
%
% TEMPLATE: dPSI+a*PSI=b;
HUGE=1e8*[1 2 3 4].^(pi/3);

MASS=PAR(11);
Rsphere=sqrt(Rg.^2+Zg.^2);
G=1/4/pi;
PSIedge=G*MASS./Rsphere;
clear Rsphere;

% i=1;  r=0;
ZERO=zeros(Ny,1); ONE=ones(Ny,1); INF=HUGE(1)*ONE;
ax1=ZERO; bx1=ZERO;

% i=Nx; r=rmax;
ZERO=zeros(Ny,1); ONE=ones(Ny,1); INF=HUGE(2)*ONE;
ax2=INF; bx2=INF.*PSIedge(Nx,:)';

% j=1;  z=0;
ZERO=zeros(Nx,1); ONE=ones(Nx,1); INF=HUGE(3)*ONE;
ay1=ZERO; by1=ZERO;

% j=Ny; z=zmax;
ZERO=zeros(Nx,1); ONE=ones(Nx,1); INF=HUGE(4)*ONE;
ay2=ZERO; by2=ZERO;
%
% ==========================================================================
%
%<<<<<<<<<<<<<<<<<<<<<<<<<<<<<<<<>>>>>>>>>>>>>>>>>>>>>>>>>>>>
%<<<<<<<<<<<<<<<<<<<<<<<<GENERIC CODE>>>>>>>>>>>>>>>>>>>>>>>>
%<<<<<<<<<<<<<<<<<<<<<<<<SEE DELTA1FAST.m>>>>>>>>>>>>>>>>>>>>>>>>
%<<<<<<<<<<<<<<<<<<<<<<<<<<<<<<<<>>>>>>>>>>>>>>>>>>>>>>>>>>>>

ONE=ones(Nx*Ny,1); ZERO=zeros(Nx*Ny,1);
```

```
n=(1:Nx*Ny)';

ALPHA=reshape(ALPHA,Nx*Ny,1);
BETA=reshape(BETA,Nx*Ny,1);
GAMMA=reshape(GAMMA,Nx*Ny,1);
DELTA=reshape(DELTA,Nx*Ny,1);
EPSILON=reshape(EPSILON,Nx*Ny,1);
PHI=reshape(PHI,Nx*Ny,1);
PSI=reshape(PSI,Nx*Ny,1);

D_0=-2*ALPHA/hx^2-2*GAMMA/hy^2+PHI;
D_1=ALPHA/hx^2+DELTA/2/hx;
D_m1=ALPHA/hx^2-DELTA/2/hx;
D_Nx=GAMMA/hy^2+EPSILON/2/hy;
D_mNx=GAMMA/hy^2-EPSILON/2/hy;
rhs=PSI;

% EDGES.

I=1; J=1:Ny; n=I+(J-1)*Nx;
a=ax1(J); b=bx1(J);
alpha=ALPHA(n); beta=BETA(n); gamma=GAMMA(n);
delta=DELTA(n); epsilon=EPSILON(n); phi=PHI(n); psi=PSI(n);
D_0(n)=-2*alpha/hx^2-2*gamma/hy^2+2*alpha.*a/hx-delta.*a+phi;
D_1(n)=2*alpha/hx^2;
D_Nx(n)=gamma/hy^2+epsilon/2/hy;
D_mNx(n)=gamma/hy^2-epsilon/2/hy;
D_m1(n)=0;
rhs(n)=psi+2*alpha.*b/hx-delta.*b;

I=Nx; J=1:Ny; n=I+(J-1)*Nx;
a=ax2(J); b=bx2(J);
alpha=ALPHA(n); beta=BETA(n); gamma=GAMMA(n);
delta=DELTA(n); epsilon=EPSILON(n); phi=PHI(n); psi=PSI(n);
D_0(n)=-2*alpha/hx^2-2*gamma/hy^2-2*alpha.*a/hx-delta.*a+phi;
D_m1(n)=2*alpha/hx^2;
D_Nx(n)=gamma/hy^2+epsilon/2/hy;
D_mNx(n)=gamma/hy^2-epsilon/2/hy;
D_1(n)=0;
rhs(n)=psi-2*alpha.*b/hx-delta.*b;

J=1; I=1:Nx; n=I+(J-1)*Nx;
a=ay1(I); b=by1(I);
alpha=ALPHA(n); beta=BETA(n); gamma=GAMMA(n);
delta=DELTA(n); epsilon=EPSILON(n); phi=PHI(n); psi=PSI(n);
D_0(n)=-2*alpha/hx^2-2*gamma/hy^2+2*gamma.*a/hy-epsilon.*a+phi;
D_Nx(n)=2*gamma/hy^2;
```

```
D_1(n)=alpha/hx^2+delta/2/hx;
D_m1(n)=alpha/hx^2-delta/2/hx;
D_mNx(n)=0;
rhs(n)=psi+2*gamma.*b/hy-epsilon.*b;

J=Ny; I=1:Nx; n=I+(J-1)*Nx;
a=ay2(I); b=by2(I);
alpha=ALPHA(n); beta=BETA(n); gamma=GAMMA(n);
delta=DELTA(n); epsilon=EPSILON(n); phi=PHI(n); psi=PSI(n);
D_0(n)=-2*alpha/hx^2-2*gamma/hy^2-2*gamma.*a/hy-epsilon.*a+phi;
D_mNx(n)=2*gamma/hy^2;
D_1(n)=alpha/hx^2+delta/2/hx;
D_m1(n)=alpha/hx^2-delta/2/hx;
D_Nx(n)=0;
rhs(n)=psi-2*gamma.*b/hy-epsilon.*b;


% CORNERS

I=1; J=1; n=I+(J-1)*Nx;
ax=ax1(J); ay=ay1(I); bx=bx1(J); by=by1(I);
alpha=ALPHA(n); beta=BETA(n); gamma=GAMMA(n);
delta=DELTA(n); epsilon=EPSILON(n); phi=PHI(n); psi=PSI(n);
D_0(n)=-2*alpha/hx^2-2*gamma/hy^2+2*alpha*ax/hx+...
   2*gamma*ay/hy-delta*ax-epsilon*ay+phi;
D_Nx(n)=2*gamma/hy^2;
D_1(n)=2*alpha/hx^2;
D_m1(n)=0;
D_mNx(n)=0;
rhs(n)=psi+2*alpha*bx/hx+2*gamma*by/hy-delta*bx-epsilon*by;

I=Nx; J=1; n=I+(J-1)*Nx;
ax=ax2(J); ay=ay1(I); bx=bx2(J); by=by1(I);
alpha=ALPHA(n); beta=BETA(n); gamma=GAMMA(n);
delta=DELTA(n); epsilon=EPSILON(n); phi=PHI(n); psi=PSI(n);
D_0(n)=-2*alpha/hx^2-2*gamma/hy^2-2*alpha*ax/hx+...
   2*gamma*ay/hy-delta*ax-epsilon*ay+phi;
D_Nx(n)=2*gamma/hy^2;
D_m1(n)=2*alpha/hx^2;
D_1(n)=0;
D_mNx(n)=0;
rhs(n)=psi-2*alpha*bx/hx+2*gamma*by/hy-delta*bx-epsilon*by;

I=1; J=Ny; n=I+(J-1)*Nx;
ax=ax1(J); ay=ay2(I); bx=bx1(J); by=by2(I);
alpha=ALPHA(n); beta=BETA(n); gamma=GAMMA(n);
delta=DELTA(n); epsilon=EPSILON(n); phi=PHI(n); psi=PSI(n);
```

```
D_0(n)=-2*alpha/hx^2-2*gamma/hy^2+2*alpha*ax/hx-...
   2*gamma*ay/hy-delta*ax-epsilon*ay+phi;
D_mNx(n)=2*gamma/hy^2;
D_1(n)=2*alpha/hx^2;
D_m1(n)=0;
D_Nx(n)=0;
rhs(n)=psi+2*alpha*bx/hx-2*gamma*by/hy-delta*bx-epsilon*by;

I=Nx; J=Ny; n=I+(J-1)*Nx;
ax=ax2(J); ay=ay2(I); bx=bx2(J); by=by2(I);
alpha=ALPHA(n); beta=BETA(n); gamma=GAMMA(n);
delta=DELTA(n); epsilon=EPSILON(n); phi=PHI(n); psi=PSI(n);
D_0(n)=-2*alpha/hx^2-2*gamma/hy^2-2*alpha*ax/hx-...
   2*gamma*ay/hy-delta*ax-epsilon*ay+phi;
D_mNx(n)=2*gamma/hy^2;
D_m1(n)=2*alpha/hx^2;
D_1(n)=0;
D_Nx(n)=0;
rhs(n)=psi-2*alpha*bx/hx-2*gamma*by/hy-delta*bx-epsilon*by;

D=[D_mNx,ZERO,D_m1,D_0,D_1,ZERO,D_Nx];

MAX=max(abs(D),[],2);
rhs=rhs./MAX;
for I=1:7;
D(:,I)=D(:,I)./MAX;
end;

MULT=ones(Nx*Ny,1);
index=find(D(:,4)<0);
MULT(index)=-1;
rhs=rhs.*MULT;
MULT=[MULT,MULT,MULT,MULT,MULT,MULT,MULT];
D=D.*MULT;


% ************************************************************************
% ************************************************************************
% DELTA1.m - FINITE DIFFERENCE DELTA1 OPERATOR.
% ************************************************************************
% ************************************************************************

function [D,rhs]=DELTA1(Nx,Ny,hx,hy);
global XIg ETAg APHISOURCE PAR;

Sr=PAR(1); Sz=PAR(2);
XImin=PAR(3); XImax=PAR(4);
```

```
ETAmin=PAR(5); ETAmax=PAR(6);
dXI=PAR(7); dETA=PAR(8);

Rg=Sr*tan(XIg');
Zg=Sz*tan(ETAg');
CR=cos(XIg').^2/Sr; CR2=-2*sin(XIg').*cos(XIg').^3/Sr^2;
CZ=cos(ETAg').^2/Sz; CZ2=-2*sin(ETAg').*cos(ETAg').^3/Sz^2;

ONE=ones(size(XIg')); ZERO=zeros(size(XIg'));

% DEFINE THE PDE...
ALPHA=ONE;
BETA=ZERO;
GAMMA=ONE;
DELTA=ONE./Rg;
EPSILON=ZERO;
PHI=-ONE./Rg.^2;
PSI=APHISOURCE';

DELTA=CR.*DELTA+CR2.*ALPHA;
EPSILON=CZ.*EPSILON+CZ2.*GAMMA;
ALPHA=CR.^2.*ALPHA;
GAMMA=CZ.^2.*GAMMA;

% ================================================================================
% BC's
% TEMPLATE: dPSI+a*PSI=b;
%
HUGE=1e8*[1 2 3 4].^pi;

% i=1;  r=0;
ZERO=zeros(Ny,1); ONE=ones(Ny,1); INF=HUGE(1)*ONE;
ax1=INF; bx1=ZERO;

% i=Nx; r=rmax;
ZERO=zeros(Ny,1); ONE=ones(Ny,1); INF=HUGE(2)*ONE;
ax2=INF; bx2=ZERO;

% j=1;  z=0;
ZERO=zeros(Nx,1); ONE=ones(Nx,1); INF=HUGE(3)*ONE;
ay1=ZERO; by1=ZERO;

% j=Ny; z=zmax;
ZERO=zeros(Nx,1); ONE=ones(Nx,1); INF=HUGE(4)*ONE;
ay2=ZERO; by2=ZERO;

% ================================================================================
```

```
% <<<<<<<<<<<<<<<<<<<<>>>>>>>>>>>>>>>>>>>>
% <<< REST OF PROGRAM IS SAME AS LAPFAST.m >>>
% <<< FOLLOWING PART LABELLED GENERIC CODE >>>
% <<<<<<<<<<<<<<<<<<<<>>>>>>>>>>>>>>>>>>>>


% ********************************************************************************
% ********************************************************************************
% CHEBYFIT.m - FIT CHEBYSHEV POLYNOMIAL AND DIFFERENTIATE DATA
% ********************************************************************************
% ********************************************************************************
%
function [Y,DY,a]=CHEBYFIT(x,y,xnew,degree);

[x,index]=sort(x);
y=y(index);
xmax=max(x); xmin=min(x);

% E02ADF AND E02AHF ARE FROM THE NAG LIBRARY
% (CALLED THROUGH MATLAB)
[a,s,ifail] = e02adf(degree+1,x,y);
a=a(degree+1,:);
[patm1,adif,ifail] = e02ahf(xmin,xmax,a);

xbar=((xnew-xmin)-(xmax-xnew))/(xmax-xmin);

for I=1:length(xnew);
[Y(I),ifail] = e02aef(a,xbar(I));
[DY(I),ifail] = e02aef(adif,xbar(I));
end;


% ********************************************************************************
% ********************************************************************************
% CALCMASS.m - CALCULATES MASS OF CORE
% ********************************************************************************
% ********************************************************************************
%
Sr=PAR(1); Sz=PAR(2); dXI=PAR(7); dETA=PAR(8);

index=find(RHO<Ps/SIGMA^2);
RHO(index)=0;

dM=2*pi*Sr*Sz*Rg.*RHO.*sec(XIg).^2.*sec(ETAg).^2*dXI*dETA;
M=2*sum(sum(dM));
```

```
% ************************************************************************
% ************************************************************************
% fcn.m - DEFINES THE FUNCTION THAT WE INTEGRATE
% REQUIRED BY D02BBF NAG LIBRARY ROUTINE
% ************************************************************************
% ************************************************************************
%
function [f]=fcn(s,y);
global EOS Gphi Gz A;

Psi=y(1,:);
g=y(2,:);

t0=exp(-2*s);
R=exp(s);
switch EOS;
   case 'isothermal'
      H1=-2;
      H2=1/Psi;
   case 'logatrope';
      t1=A./t0./Psi.^2;
      H1=-2*t1.*Psi;
      H2=t1;
end

t1=Gphi^2/(4*pi);
t2=Gz^2/(4*pi);
t3=R.*g-H1+2*t0.*t2.*Psi;
t4=H2+t1+t0.*t2;

dPsi=t3./t4;
dg=-Psi./R-g;

f=[dPsi;dg];


% ************************************************************************
% ************************************************************************
% OUTPUT.m - REQUIRED BY D02BBF FROM NAG LIBRARY (CALLED THROUGH MATLAB)
% INCREMENTS INDEPENDENT VARIABLE s AND MAKES OUTPUT VECTORS
% S AND Y.
% ************************************************************************
% ************************************************************************
%
function [s]=OUTPUT(s,y);
global ds S Y;
```

```
S=[S,s];
Y=[Y,y];

s=s+ds;


% ************************************************************************
% ************************************************************************
% func.m - USED BY PR.m TO OBTAIN INITIAL GUESS OF APHI
% (NOT THAT IMPORTANT, BUT HELPS SLIGHTLY)
% ************************************************************************
% ************************************************************************
%
function [ZERO]=func(ROB);
global BO RO CONST PHICL;

ZERO=BO*ROB^2/2*(1-exp(-RO^2/ROB^2))+CONST*RO^2-PHICL;
```

Appendix B

Copyright Information

Following are the publication agreements for the two articles contained in Chapters 3 and 4, which have been accepted for publication by the Monthly Notices of the Royal Astronomical Society (MNRAS). The entire copyright to these articles belongs to MNRAS, who have granted me permission to reprint the articles within my thesis. I hereby pass this licence on to McMaster University and to the National Library of Canada.

I am presently the copyright holder of the article contained in Chapter 6, which has been accepted for publication by the Astrophysical Journal.

BLACKWELL SCIENCE/ROYAL ASTRONOMICAL SOCIETY
COPYRIGHT ASSIGNMENT FORM

Your paper of ref MY563 has now been accepted for publication in **MONTHLY NOTICES OF THE ROYAL ASTRONOMICAL SOCIETY**

Copyright assignment
Please read the notes overleaf. Then complete parts 1 and 2(i) of this form, sign and return one to the editor, keeping the duplicate copy for yourself. If you do not own the copyright to your article, please complete part 1 and get the copyright holder to complete and sign part 2(ii). **Please use BLOCK LETTERS.**

---

1 Name: Dr J.D. Fiege

Address: Dept. of Physics & Astronomy, McMaster University, 1280 Main St. W., Hamilton, Ontario, L8S 4M1, CANADA.

Article title: Helical fields and filamentary molecular clouds

---

2 In consideration of the publication of my contribution in the above journal, I hereby warrant:

(a) I am, or am authorized to represent, the copyright owner or owners;
(b) that in the case of joint authorship I have been authorised by all co-authors to sign this agreement on their behalf, and references to the singular shall include the plural as appropriate;
(c) that this article is the author's/authors' original work, has not been previously published elsewhere for financial gain either in printed or electronic form (including World Wide Web home pages, discussion groups and other electronic bulletin boards), and is not under consideration for publication elsewhere;
(d) that this article does not infringe the copyright, moral rights or other intellectual property rights of any person and is not in breach of contract or in breach of confidence and does not contain any material of an obscene, libellous or otherwise unlawful nature, and that I will indemnify and keep indemnified the Editor, the Royal Astronomical Society and Blackwell Science Ltd against all claims and expenses (including legal costs and expenses) arising from any breach of this warranty and the other warranties on my behalf in this agreement;
(e) that I have obtained permission for and acknowledged the source of any illustrations, diagrams or other material included in the article of which I am not the copyright owner.

(i) *To be filled in if copyright belongs to you*
Declaration A - In consideration of the publication of my contribution in the above journal, I hereby assign to the Royal Astronomical Society the copyright throughout the world in any form and in any language (including without limitation on disk, transmission over the internet and other communications networks, and in any other electronic form).

Signed ..... Date Aug 11, 1999

(to be signed by corresponding or senior author on behalf of all authors)

(ii) *To be filled in if copyright does not belong to you.*
Declaration B - Please provide the complete and full title of the copyright holder. This will be printed on the copyright line on each page of the article. It is the author's responsibility to provide the correct information.

Name and address of copyright holder (if not the author) .....

.....

.....

The copyright holder hereby grants the Royal Astronomical Society non-exclusive rights to publish the above mentioned contribution and to deal with requests from third parties in the manner specified in paragraphs 4 and 7 overleaf.

..... (Signature of copyright holder)

Date .....

PLEASE RETURN ONE SIGNED COPY OF THIS FORM TO THE PRODUCTION EDITOR, MONTHLY NOTICES OF THE ROYAL ASTRONOMICAL SOCIETY, 23 AINSLIE PLACE, EDINBURGH, EH3 6AJ, UK

Notes on the Assignment of Copyright

1 The journal's policy is to acquire copyright for all contributions. There are two reasons for this:

(a) ownership of copyright by one central organisation tends to ensure maximum international protection against infringement;

(b) it also ensures that requests by third parties to reprint a contribution, or part of it, are handled efficiently and in accordance with a general policy which is sensible both to any relevant changes in international copyright legislation and to the general desirability of encouraging the dissemination of knowledge.

2 The author retains his or her moral rights in the article including the right to be identified as the author whenever and wherever the article is published, under the terms of the UK Copyright Designs and Patents Act 1988.

3 In assigning your copyright you are not forfeiting your rights to use your contribution elsewhere. This you may do after obtaining our permission (withheld only in exceptional circumstances) provided that the journal is acknowledged as the original source.

4 All requests to reprint your contribution, or a substantial part of it, or figures, tables or illustrations from it in another publication (including publications of Blackwell Science) will be subject to your approval (which we will assume is given if we have not heard from you within thirty days of your approval being sought).

5 The journal is registered with the Copyright Licensing Agency (London) and the Copyright Clearance Center (New York), non-profit making organizations which offer centralized licensing arrangements for photocopying. Any income received through these arrangements will be used to further the interests of the journal.

6 It is understood that in some cases copyright will be held by the contributor's employer (for instance the British or US Government). If so, the journal requires non-exclusive permission to deal with requests from third parties, on the understanding that any requests it receives from third parties will be handled in accordance with paragraph 4 above (i.e. you and your employer will be asked to approve the proposed use). If you are or were a UK Crown servant and the contribution is made in that capacity, the article must be submitted for clearance by the Permanent Head of the Department concerned. If you are or were a US Government employee and the contribution is made in that capacity, assignment applies only to the extent allowable by US law. In all cases, the Publishers must be informed as soon as the article is accepted for publication so that the appropriate arrangements can be made with the contributor's employer.

7 In addition to reproduction in conventional printed form, your article may be stored electronically and then printed out (e.g. from CD-ROM under the ADONIS document delivery scheme) to meet individual requests. Your assignment of copyright signifies your agreement to the journal making arrangements to include your paper in such document delivery services and electronic journal databases.

8 By signing this form you certify that your contribution is your original work, has not been published before and is not being considered for publication elsewhere; that you have obtained permission for and acknowledged the source of any excerpts from other copyright works; that to the best of your knowledge your paper contains no statements which are libellous, unlawful or in any way actionable and that you have informed any co-authors of the terms of this agreement and are signing on their behalf.

BLACKWELL SCIENCE/ROYAL ASTRONOMICAL SOCIETY
COPYRIGHT ASSIGNMENT FORM

Your paper of ref **MY948** has now been accepted for publication in **MONTHLY NOTICES OF THE ROYAL ASTRONOMICAL SOCIETY**

Copyright assignment
Please read the notes overleaf. Then complete parts 1 and 2(i) of this form, sign and return one to the editor, keeping the duplicate copy for yourself. If you do not own the copyright to your article, please complete part 1 and get the copyright holder to complete and sign part 2(ii). **Please use BLOCK LETTERS.**

---

1 Name: Dr J.D. Fiege

Address: Dept. of Physics & Astronomy, McMaster University, 1280 Main St. W., Hamilton, Ontario, L8S 4M1, CANADA.

Article title: Helical fields and filamentary molecular clouds II - Axisymmetric stability and fragmentation

---

2 In consideration of the publication of my contribution in the above journal, I hereby warrant:

(a) I am, or am authorized to represent, the copyright owner or owners;
(b) that in the case of joint authorship I have been authorised by all co-authors to sign this agreement on their behalf, and references to the singular shall include the plural as appropriate;
(c) that this article is the author's/authors' original work, has not been previously published elsewhere for financial gain either in printed or electronic form (including World Wide Web home pages, discussion groups and other electronic bulletin boards), and is not under consideration for publication elsewhere;
(d) that this article does not infringe the copyright, moral rights or other intellectual property rights of any person and is not in breach of contract or in breach of confidence and does not contain any material of an obscene, libellous or otherwise unlawful nature, and that I will indemnify and keep indemnified the Editor, the Royal Astronomical Society and Blackwell Science Ltd against all claims and expenses (including legal costs and expenses) arising from any breach of this warranty and the other warranties on my behalf in this agreement;
(e) that I have obtained permission for and acknowledged the source of any illustrations, diagrams or other material included in the article of which I am not the copyright owner.

(i) *To be filled in if copyright belongs to you*
Declaration A - In consideration of the publication of my contribution in the above journal, I hereby assign to the Royal Astronomical Society the copyright throughout the world in any form and in any language (including without limitation on disk, transmission over the internet and other communications networks, and in any other electronic form).

Signed ..... Date Aug 11, 1999

(to be signed by corresponding or senior author on behalf of all authors)

(ii) *To be filled in if copyright does not belong to you.*
Declaration B - Please provide the complete and full title of the copyright holder. This will be printed on the copyright line on each page of the article. It is the author's responsibility to provide the correct information.

Name and address of copyright holder (if not the author) .....

.....

.....

The copyright holder hereby grants the Royal Astronomical Society non-exclusive rights to publish the above mentioned contribution and to deal with requests from third parties in the manner specified in paragraphs 4 and 7 overleaf.

..... (Signature of copyright holder)

Date .....

PLEASE RETURN ONE SIGNED COPY OF THIS FORM TO THE PRODUCTION EDITOR, MONTHLY NOTICES OF THE ROYAL ASTRONOMICAL SOCIETY, 23 AINSLIE PLACE, EDINBURGH, EH3 6AJ, UK

Notes on the Assignment of Copyright

1 The journal's policy is to acquire copyright for all contributions. There are two reasons for this:

(a) ownership of copyright by one central organisation tends to ensure maximum international protection against infringement;

(b) it also ensures that requests by third parties to reprint a contribution, or part of it, are handled efficiently and in accordance with a general policy which is sensible both to any relevant changes in international copyright legislation and to the general desirability of encouraging the dissemination of knowledge.

2 The author retains his or her moral rights in the article including the right to be identified as the author whenever and wherever the article is published, under the terms of the UK Copyright Designs and Patents Act 1988.

3 In assigning your copyright you are not forfeiting your rights to use your contribution elsewhere. This you may do after obtaining our permission (withheld only in exceptional circumstances) provided that the journal is acknowledged as the original source.

4 All requests to reprint your contribution, or a substantial part of it, or figures, tables or illustrations from it in another publication (including publications of Blackwell Science) will be subject to your approval (which we will assume is given if we have not heard from you within thirty days of your approval being sought).

5 The journal is registered with the Copyright Licensing Agency (London) and the Copyright Clearance Center (New York), non-profit making organizations which offer centralized licensing arrangements for photocopying. Any income received through these arrangements will be used to further the interests of the journal.

6 It is understood that in some cases copyright will be held by the contributor's employer (for instance the British or US Government). If so, the journal requires non-exclusive permission to deal with requests from third parties, on the understanding that any requests it receives from third parties will be handled in accordance with paragraph 4 above (i.e. you and your employer will be asked to approve the proposed use). If you are or were a UK Crown servant and the contribution is made in that capacity, the article must be submitted for clearance by the Permanent Head of the Department concerned. If you are or were a US Government employee and the contribution is made in that capacity, assignment applies only to the extent allowable by US law. In all cases, the Publishers must be informed as soon as the article is accepted for publication so that the appropriate arrangements can be made with the contributor's employer.

7 In addition to reproduction in conventional printed form, your article may be stored electronically and then printed out (e.g. from CD-ROM under the ADONIS document delivery scheme) to meet individual requests. Your assignment of copyright signifies your agreement to the journal making arrangements to include your paper in such document delivery services and electronic journal databases.

8 **By signing this form you certify that your contribution is your original work, has not been published before and is not being considered for publication elsewhere; that you have obtained permission for and acknowledged the source of any excerpts from other copyright works; that to the best of your knowledge your paper contains no statements which are libellous, unlawful or in any way actionable and that you have informed any co-authors of the terms of this agreement and are signing on their behalf.**

References

The following reference list is for work cited in Chapters 1, 2, 5, and 7. Chapters 3, 4, and 6 are self-contained articles that contain their own reference lists.

1. Adam W.S., Dunham T., 1938, Ap.J., 87, 102
2. Alves J., Lada C.J., Lada E.A., Kenyon S.J., Phelps R., 1998, Ap.J.,506, 292
3. Andre P., Ward-Thompson D., & Barsony, 2000, in *Protostars and Planets IV*, ed. Mannings V., Boss A.P., Russell S.S. (Tucson: University of Arizona Press), in press
4. Arons J., Max C.E., 1975, Ap.J., 196, L77
5. Balbus S.A. & Hawley J.F., 1991, Ap.J., 376, 223
6. Ballesteros-Paredes J., Vazquez-Semadeni E., Scalo J., 1999, Ap.J., 515, 286
7. Bally J., 1989, in *Proceedings of the ESO Workshop on Low Mass Star Formation and Pre-main Sequence Objects*, ed. Bo Reipurth (ESO: Garching bei Munchen)
8. Bally J., Stark A., Wilson R.W., Langer W.D., 1987, ApJ., 312, L45
9. Beichman C.A., Myers P.C., Emerson J.P., Harris S., Mathieu R., Benson P.J., Jennings R.E., 1986, Ap.J., 307, 337
10. Benson P.J., Myers P.C., 1989, Ap.J., Supp., 71, 89
11. Bertoldi F., McKee C.F., 1992, Ap.J., 395, 140
12. Binney J., Tremaine S., 1994, *Galactic Dynamics* (Princeton: Princeton University Press)
13. Blitz L., Williams S.P., 1999, astro-ph/9903382 in *The Physics of Star Formation and Early Stellar Evolution* (Crete II) eds. Kylafis and Lada.
14. Bonnor W.B., 1956, MNRAS, 116, 351
15. Boulares A., Cox D.P., 1990, Ap.J., 365, 544

16. Carlqvist P., Kristen H., 1997, A&A., 324, 1115

17. Carruthers G.R., 1970, Ap.J., 161, 81L

18. Caselli P., Myers P.C., 1995, Ap.J., 446, 665

19. Castets A., Duvert G., Dutrey A., Bally J., Langer W.D., Wilson R.W., 1990, A&A, 234, 469

20. Chandrasekhar S., Fermi E., 1953, Ap.J., 118, 116

21. Chandrasekhar S., Fermi E., 1953, Ap.J., 118, 113

22. Cheung A.C., Rank D.M., Townes C.H., Thornton D.D., Welch W.J., 1968, Phys. Rev. Lett. 21, 1701

23. Chieze J.P., 1987, A&A, 171, 225

24. Chini R., Reipurth B., Ward-Thompson D., Bally J., Nyman L.A., Sievers A., Billawala Y., 1997, Ap.J., 474, L135

25. Chromey F.R., Elmegreen B.G., Elmegreen D.M., 1989, Ap.J., 98, 2203

26. Crutcher R.M., Troland T.H., Goodman A.A., Heiles C., Kazes I., Myers P.C., 1993 Ap.J., 407, 175

27. Crutcher R.M., Troland T.H., Lazareff B., Kazes I., 1996, Ap.J., 456, 217

28. Crutcher R.M., Troland T.H., Lazareff B., Paubert G., Kazes I., 1999, Ap.J.,514, L121

29. Cudlip W., Furniss I., King K.J., Jenings R.E., 1982, MNRAS, 200, 1169

30. Dewar R.L., 1970, Phys. Fluids, 13, 2710

31. Dunham T., 1937, PASP, 49, 26

32. Dutrey A., Langer W.D., Bally J., Duvert G., Castets A., Wilson R.W., 1991, A&A, 171, L9

33. Ebert R., 1955, Z. Astrophys., 37, 217

34. Elmegreen B.G., 1978, Ap.J., 225, L85

35. Elmegreen B.G., 1985, Ap.J., 299, 196

36. Elemgreen B.G., 1993, Ap.J., 419, L29

37. Elmegreen B.G., Elmegreen D.M, 1987, Ap.J., 320, 182

38. Elmegreen B.G., Falgarone E., 1996, Ap.J., 471, 816

39. Ferriere K.M., Mac Low M.M., Zweibel E.G., 1991, Ap.J., 375, 239

40. Fiege J.D, Pudritz R.E., 1999 (FP1), MNRAS, in Press (see also astro-ph/9901096)

41. Fiege J.D, Pudritz R.E., 1999 (FP2), MNRAS, in Press (see also astro-ph/9902385)

42. Field G.B., Saslaw W.C., 1965, Ap.J., 142, 568

43. Fuller G.A., Myers P.C., 1992, Ap.J., 384, 523

44. Gehman C.S., Adams F.C., Watkins R., 1996, Ap.J., 472, 673

45. Genzel R., 1992, in *The Galactic Interstellar Medium*, by Burton W.B., Elmegreen B.G., Genzel R. (Berlin: Springer-Verlag), 275

46. Goodman A.A., Jones T.J., Lada E.A., Myers P.C., 1992, Ap.J., 399, 108

47. Goodman A.A., Benson P.J., Fuller G.A., Myers P.C., 1993, Ap.J., 406, 528

48. Goodman A.A., Heiles C., 1994, Ap.J., 424, 208

49. Goodman A.A, Jones T.J., Lada E.A., Myers P.C., 1995, Ap.J., 448, 748

50. Goldsmith P.F., Langer W.D., 1978, Ap.J., 222, 881

51. Greaves J.S., Murray A.G., Holland W.S., 1994, A&A, 284 L19

52. Greaves J.S., Holland W.S., Murray A.G., 1995, A&A, 297, L49

53. Habe A., Uchida Y., Ikeuchi S., Pudritz R.E., 1991, PASJ, 43, 703

54. Haslam C.G.T., Salter C.J., Stoffel H., Wilson W.E., 1983, A&AS, 47, 1

55. Heiles C., 1987, Ap.J., 315, 555

56. Heiles C., 1997, Ap.J., Supp., 111, 245

57. Heiles C., 1998, in *Lecture Notes in Physics*, vol. 506, ed. Breitschwerdt D., Freyberg M.J., Truemper J. (Springer-Verlag: Berlin), pp. 229

58. Heiles C., Jenkins E.B., 1976, A&A, 46, 333

59. Heyer M.H., Brunt C. 1999, in ASP Conf. Ser. 168, in *New Perspectives in the Interstellar Medium*, ed. Taylor A.R., Landecker T.L., Joncas G. (ASP: San Fancisco), 387

60. Heyer M.H., Tereby S., 1998, Ap.J., 502, 265

61. Hildebrand R.H., Dragovan M., Novak, G., 1984, Ap.J., 284, 51L

62. Jackson J.D., 1975, *Classical Electrodynamics*, (John Wiley & Sons: New York)

63. Jefferts K.P., Penzias A.A., Wilson R.W., 1970, Ap.J., 161, L87

64. Johnstone D., Bally J., 1999, Ap.J., 510, 49L

65. Kane B.D., Clemens D.P., 1997, Ap.J., 113, 1799

66. Kolmogorov A., 1941, Dokl. Akad. Nauk SSSR, 31, 538; 32, 16

67. Kutner M., Thaddeus P., 1971, Ap.J., 168, 67

68. Kwan J., Valdes F., 1983, Ap.J., 271, 604

69. Lada E.A., Bally J., Stark A.A., 1991, Ap.J., 368, 432

70. Lada E.A., 1992, Ap.J., 393, 25

71. Lada C.J. Alves J., Lada E.A., 1999, Ap.J., 512, 250

72. Landau & Lifshitz, 1989, *Fluid Mechanics* (Permagon Press: Oxford)

73. Larson R.B., 1969, MNRAS, 145, 271

74. Larson R.B., 1981, MNRAS, 184, 809

75. Lazarian A., Draine B.T., 1997, Ap.J., 487, 248

76. Lazarian A., Draine B.T., 1997, Ap.J., 520, 67L

77. Leung C.M., Kutner M.L., Mead K.N., 1982, Ap.J., 262, 583

78. Loren R.B., 1989, Ap.J., 338, 902

79. Maddalena R.J., Morris M., Moscowitz J., Thaddeus P., 1986, Ap.J., 303, 375

80. Maloney, 1988, Ap.J., 334, 761

81. Matthews B.C., Wilson C.D., 1999, Submitted to Ap.J.

82. McCrea W.H., 1957, MNRAS, 117, 562

83. McKee C.F., 1989, Ap.J., 345, 782

84. McKee C.F., 1993, in *Protostars and Planets III*, ed. Levy E.H. & Lunine J.I. (Tucson: University of Arizona Press)

85. McKee C.F., 1999, in *NATO Advanced Study Institute on The Physics of Star Formation and Early Stellar Evolution*, eds. Kylafis N., Lada C. (see also astro-ph 9901370)

86. McKee C.F., Holliman J.H., 1999, astro-ph/9903213

87. McKee C.F., Ostriker J.P., 1977, Ap.J., 218, 148

88. McKee C.F., Zweibel E.G., 1992, Ap.J., 399, 551

89. McKee C.F., Zweibel E.G., 1995, Ap.J., 440, 686

90. McLaughlin D.E., Pudritz R.E., 1996, Ap.J., 469, 194

91. Mestel L., Spitzer L. Jr., 1956, MNRAS, 116, 583

92. Mouschovias T. C., 1976a, Ap.J., 206, 753

93. Mouschovias T. C., 1976b, Ap.J., 207, 141

94. Mouschovias T.C., Spitzer L. Jr., 1976, Ap.J., 210, 326

95. Myers P.C., 1983, Ap.J., 270, 105

96. Myers P.C., 1985, in *Protostars and Planets II*, ed. Black D.C., Matthews M.S. (Tucson: University of Arizona Press), p.81

97. Myers P.C., Benson P.J., 1983, Ap.J., 266, 309

98. Myers P.C., Fuller G.A., 1992, Ap.J., 396, 631

99. Myers P.C., Fuller G.A., Goodman A.A., Benson P.J., 1991 Ap.J., 376, 561

100. Myers P.C., Goodman A.A., 1988a, Ap.J., 326, L27

101. Myers P.C., Goodman A.A., 1988b, Ap.J., 329, 392

102. Myers P.C., Goodman A.A., Gusten R. Heiles C., 1995, Ap.J., 442, 177

103. Myers P.C., Heyer M., Snell R.L., Goldsmith P.F., 1988, Ap.J., 324, 907

104. Myers P.C., Ladd E.A., Fuller G.A., 1991, Ap.J., 372, L95

105. Nagai T., Inutsuka S., Miyama S.M., 1998, Ap.J., 506, 306

106. Nakamura F., Hanawa T., Nakano T., 1993, PASJ, 45, 551

107. Novak G., Gonatas D.P., Hildebrand R.H., Platt S.R., 1989, Ap.J.,345, 802

108. Onishi T., Mizuno A., Kawamura A., Ogawa H., Fukui Y., 1998, Ap.J., 502, 296

109. Ostriker J., 1964, Ap.J., 140, 1056

110. Passot T., Vazquez-Semadeni E., Pouquet A., 1995, Ap.J., 455, 536

111. Patel K., Pudritz R.E., 1994, Ap.J., 424, 688

112. Penston M.V., 1969, MNRAS, 144, 425

113. Penzias A.A., Jefferts K.B., Wilson R.W., 1971, Ap.J., 165, 229

114. Penzias A.A., Solomon P.M., Wilson R.W., Jefferts K.B., 1971, Ap.J., 168, 53L

115. Pouquet A., Galtier S., Politano H., 1999, in ASP Conf. Ser. 168, *New Perspectives in the Interstellar Medium*, ed. Taylor A.R., Landecker T.L., Joncas G. (ASP: San Fancisco), 417

116. Pudritz R.E., 1990, Ap.J., 350, 195

117. Pudritz R.E., Fiege J.D., 1999, in ASP Conf. Ser. 168, in *New Perspectives in the Interstellar Medium*, eds. Taylor A.R., Landecker T.L., Joncas G. (ASP: San Fancisco), 235

118. Ryden, B.S., 1996, Ap.J., 471, 822

119. Schleuning D.A., 1998, Ap.J., 493, 811

120. Schneider S., Elmegreen B.G., 1979, Ap.J., 41, 87

121. Shu F., 1977, Ap.J., 214, 488

122. Smith A.M., 1973, Ap.J., 179, L11

123. Solomon P.M., Jefferts K.B., Penzias A.A., Wilson R.W., 1971, Ap.J., 168, L107

124. Spitzer L. Jr., 1978, *Physical Processes in the Interstellar Medium* (John Wiley & Sons: New York)

125. Stodólkiewicz J.S., 1963, Acta Astron., 13, 30

126. Stone J.M., Ostriker E.C., Gammie C.F., 1998, Ap.J., 508, L99

127. Tassoul J.L., 1978, *Theory of Rotating Stars*, (Princeton University Press: Princeton)

128. Troland T.H., Crutcher R.M., Goodman A.A., Heiles C., Kazes I., Myers P.C., 1996, Ap.J., 471, 302

129. Troland T.H., Heiles C., 1982, Ap.J., 252, 179

130. Troland T.H., Heiles C., 1986, Ap.J., 301, 339

131. Tomisaka K., 1991, Ap.J., 376, 190

132. Tomisaka K., Ikeuchi S., Nakamura T., 1988a, Ap.J., 326, 208

133. Tomisaka K., Ikeuchi S., Nakamura T., 1988b, Ap.J., 335, 239

134. Tomisaka K., Ikeuchi S., Nakamura T., 1989, Ap.J., 341, 220

135. Tomisaka K., Ikeuchi S., Nakamura T., 1990, Ap.J., 362, 202

136. Vazquez-Semadeni E., Ballesteros-Paredes J., Rodriguez L.F., 1997, Ap.J., 474, 292

137. Vazquez-Semadeni E., Ostriker C., Passot T., Gammie C.F., Stone J.M., 2000, in *Protostars and Planets IV*, ed. Mannings V., Boss A.P., Russell, S.S. (Tucson: University of Arizona Press), in press

138. Vazquez-Semadeni E., Passot T., Pouquet A., 1995, Ap.J., 441, 702

139. Vazquez-Semadeni E., Passot T., Pouquet A., 1996, Ap.J., 473, 881

140. Vrba F.J., Strom S.E., Strom K.M., 1988, A.J., 96, 680

141. Ward-Thompson D., Scott P.F., Hills R.E., Andre P., 1994, MNRAS, 268, 276

142. Weintraub D.A., Goodman A.A., Akeson R.L., 2000, in *Protostars and Planets IV*, ed. Mannings V., Boss A.P., Russell, S.S. (Tucson: University of Arizona Press), in press

143. Williams J.P., Blitz L., Stark A.A., 1995, Ap.J., 451, 252

144. Wilson C.D., Avery L.W., Fich M., Johnstone D., Joncas G., Knee L.B.G., Matthews H.E., Mitchell G.F., Moriarty-Schieven G.H., Pudritz R.E., 1999, Ap.J., 513, L139

145. Wilson R.W., Jefferts K.B., Penzias A.A., 1970, Ap.J.,161, L43